INSIGHTS INTO THE GEOLOGIC HISTORY OF MARS' NORTHERN LOWLANDS FROM NEAR-INFRARED SPECTROSCOPY

Thesis by
Lu Pan

In Partial Fulfillment of the Requirements for
the degree of
Doctor of Philosophy

CALIFORNIA INSTITUTE OF TECHNOLOGY
Pasadena, California

2017
Defended May 10 2017

Lu Pan

ORCID: 0000-0002-8151-2125

ACKNOWLEDGEMENTS

First, I want to thank my thesis advisor, Bethany Ehlmann, for making this happen. I appreciate her teaching me how to use CRISM data from scratch in the very beginning; sending me to classes, workshops, and conferences in many cool places in the world; always keeping me on track and encouraging me to pursue whatever science is interesting; and always being ready to give advices when I needed them. Thanks for making the course of PhD such a wonderful experience. Oh and special thanks for carefully reading through my writings and giving me useful writing tips here and there.

I would like to thank my committee members: Yuk Yung, for first introducing me to Caltech on a skype call during the Chinese Spring Festival and later agreeing to be my academic advisor; George Rossman for always being there ready to show me a new mineral and for sharing many good stories in classes; and John Grotzinger, for sharing insights on the big picture of Mars and its sedimentary environments. I also owe my thanks to Dave Stevenson, Heather Knutson, and Andy Ingersoll for first introducing me to planetary science as I never imagined before; Mike Lamb, Ed Stopler, Rob Clayton, Mike Gurnis, John Eiler, Paul Asimow, Victor Tsai, Alex Sessions, Joe Kirshvink, and Jason Saleeby for teaching me new tools in geology, geochemistry, and geophysics and showing me great role models as scientists and leading wonderful field trips.

For my research, I benefited greatly from everyone in Ehlmann group, including Rebecca Greenberger, Daven Quinn, Jennifer Buz, Mathieu Lapôtre, Abigail Fraeman, Christopher Edwards, Ara Oshagan, Kirsten Siebach, Dana Anderson, Nancy Thomas, Ellen Leask, Peter Martin, Alistair Hayden, Nathan Stein, and Cecilia Sanders. Thanks for being so resourceful and helpful all the time. I do appreciate all the suggestions and comments on my work, scientific discussions, and advice on graduate school, as well as all the gossiping time and good food.

I am grateful for all my friends in Planetary Science, especially Captain Planets (Henry Ngo, Mike Wong, Joe O'rourke, and Danielle Piskorz) for welcoming me into the crowd and working together on the coursework in the first year. I'm deeply indebted to Xi Zhang, Cheng Li, and Qiong Zhang for giving me instructions on analytical physics and statistics, and for taking me outside to hiking/biking trips and Chinese dinners. I'm grateful for Peter Gao, Xi Zhang, Henry

Ngo, Qiong Zhang, Dana Anderson, Peter Buhler, and Ian Wong for being wonderful officemates. I am also more than lucky to have known Miki Nakajima, Da Yang, Coco Zhang, Pushkar Kopparla, Hao Cao, Siteng Fan, Ana de Oliveira Lobo, Chris Spalding, Elizabeth Bailey, Tianhao Le. Thanks for bringing much fun and laughter to the hallway of South Mudd. I am deeply grateful for our planetary science administrative staff, including Irma Black, Ulrika Terrones, Margaret Carlos, and Bronagh Glaser, who have given me help in many ways, perhaps more than I know.

Of all else that kept me happy and sane through graduate school, I have to thank volleyball and the Caltech gym for keeping me mentally and physically healthy. Among many others I met on the volleyball court, I am grateful for the volleybobo team: Yi-Chun Chen, Ho-Hsuan Wei, Chia-Wei Hsu, Chia-Hsien Shen, Shunjia Chen, and Kuangwei Yang. We met through volleyball but since then you have welcomed me like a family and become the brothers and sisters I never had. Thanks for all the amazing moments in and out of volleyball courts.

I am deeply grateful for Wen Chen for friendship and companion, for sharing the passion for good food, and for letting me shoot her *c. elegans* for fun. I thank Sally Zhang for showing me new worlds by taking me to Lang Lang's piano concert and making exotic cuisine. I also thank Min-Feng Tu for sharing an apartment and many interesting conversations in the middle of the night with me for the last three years.

Finally, I would like to thank my dad Mu Pan and my mom Ping Chen. I would not have the chance to be here without their constant trust, love, and support. I thank my grandparents Gengsheng Pan and Youyun Xiao for reminding me the home recipe of pork chop soup with lotus root. I am grateful for my aunt Fang Pan and her family for being my extended family away from home and sending food and Texas themed t-shirts once in a while. Lastly, above all else, I have to thank Zhengbin Deng for sharing every bit of the journey with me, for being my critical audience but always giving me the warmest encouragement and reassurance with his optimistic mind. Through all the best and worst moments in the last five years, I am just so ever grateful for having you.

ABSTRACT

Hydrated minerals, identified on Mars using near-infrared spectroscopy data, reveal new insights into the aqueous processes and evolution of climate in the history of Mars. Through investigations of the mineralogical record using near-infrared spectroscopy, this dissertation focuses on the geologic history and aqueous processes in the northern lowlands of Mars in order to assess the existence of a long-lived global ocean, the extent and volume of Noachian-Hesperian volcanic flows filling the northern lowlands, the nature of aqueous activity in the most recent Amazonian age, and the spectral variability of carbonates. The first chapter reports widespread and diverse mafic and hydrated mineralogy of units associated with impact craters across the northern lowlands. In the lowlands-wide survey, no pervasive carbonate or evaporative salts are found in support of a northern ocean, but we identify widespread phyllosilicates inferred to be Noachian basement materials excavated beneath 1-2 km of mafic lava flows. In the second and third chapters, combined analysis of imagery and spectral data is used to investigate local geologic processes related to liquid water in the knobby terrains of Acidalia and in the vicinity of Lyot crater. Phyllosilicates and hydrated silica are detected in the knobby terrains of Acidalia indicative of a declining prevalence of aqueous alteration through time. We also find diverse mineralogy in the vicinity of Lyot, probably formed in a hydrothermal system and later excavated by the Lyot impact. In contrast, we did not identify mineralization related to local channels that are syn- or post-impact. The fourth study analyzes the spectral properties of unshocked and impact-shocked carbonate rocks on Earth and found similar spectral characteristics between Mars carbonate detections and terrestrial carbonates in impact environments. Using near-infrared spectroscopy, we have identified and characterized the mineralogic record of Mars, and found past environments within the northern lowlands of Mars with varying style and intensity of aqueous alteration through time, with implications for the evolution of Mars climate.

PUBLISHED CONTENT AND CONTRIBUTIONS

Pan L. et al. (2017), "The Stratigraphy and History of Mars' Northern Lowlands Through Mineralogy of Impact Craters: A Comprehensive Survey." *Journal of Geophysical Research: Planets*. in revision.

L. P. participated in the conception of the project, tested and improved the noise processing algorithm, analyzed spectral data, prepared the figures, and participated in the writing of the manuscript.

-*Adapted for the contents in Chapter 2*

Pan, L., and B. L. Ehlmann (2014), Phyllosilicate and hydrated silica detections in the knobby terrains of Acidalia Planitia, northern plains, Mars. *Geophys. Res. Lett*., 41(6), 1890–1898, doi:10.1002/2014GL059423.

L. P. participated in the conception of the project, analyzed spectral data, prepared the figures, and participated in the writing of the manuscript.

-*Adapted for the contents in Chapter 3*

TABLE OF CONTENTS

LIST OF ILLUSTRATIONS

Chapter 4

Chapter 5

LIST OF TABLES

LIST OF ACRONYMS

CRISM	Compact Reconnaissance Imaging Spectrometer for Mars
DEM	Digital Elevation Model
HiRISE	High Resolution Imaging Science Experiment
ISIS	Integrated Software for Imagers and Spectrometers
OMEGA	Observatoire pour la Minéralogie, l'Eau, les Glaces, et l'Activité
MER	Mars Exploration Rover
MGS	Mars Global Surveyor
SHARAD	Mars SHAllow RADar sounder
MOLA	Mars Orbiter Laser Altimeter
MRO	Mars Reconnaissance Orbiter
MSL	Mars Science Laboratory
TES	Thermal Emission Spectrometer
THEMIS	THermal EMission Infrared Spectrometer

Chapter 1

INTRODUCTION

1.1 Overview: The geologic and aqueous history of Mars

Like our own planet Earth, Mars once hosted liquid water on its surface. Since the Mariner 9 imagery in the 1970s, numerous observations of water-carved landscapes have been identified on the Mars surface, including the widespread integrated valley networks [e.g. Carr, 1995; Hynek et al., 2010], open and closed basin lakes [e.g. Fassett and Head, 2008; Goudge et al., 2012], widespread sedimentary deposits [Malin and Edgett, 2000], as well as huge outflow channels [e.g. Baker, 1974; Masursky et al., 1977; Lucchita et al., 1981] debouching into the northern lowlands. It has also been suggested that there existed a global ocean in the northern lowlands of Mars [e.g. Parker et al., 1993; Clifford and Parker 2001; Perron et al., 2007], but investigation of later higher-resolution images found the shoreline evidence to be inconclusive [Malin and Edgett, 1999]. Most of these morphological features are late Noachian-early Hesperian in age, with the exception of outflow channels which formed later in the Hesperian. Together this evidence indicates pervasive surface water in the early history of the planet.

Liquid water is not stable on Mars surface currently given its distant orbit and thin CO_2 atmosphere (6 mbar). Due to significantly diminished solar luminosity in the past, climate models require a denser CO_2 atmosphere (1-5 bars) in early Mars to achieve elevated mean surface temperature [Pollak et al., 1987; Forget et al., 2013]. However, taking condensation into account, it remains difficult to reproduce sufficient warming in a CO_2-H_2O atmosphere to reach an equilibrium temperature of the melting point of water at any surface pressure [Kasting, 1991], without invoking events like meteorite impacts [e.g. Segura et al., 2002], sulfur dioxide emissions [e.g. Yung et al., 1997; Johnson and Stewart, 2008; Halevy and Head, 2014], obliquity variations [e.g. Wordsworth et al., 2013] or an early reducing atmosphere with H_2 or CH_4 [e.g. Ramirez et al., 2014; Wordsworth et al., 2017].

On the other hand, the polar deposits of CO_2 ice [Phillips et al., 2011], the global reservoir of carbonate deposits detected until present [Edwards and Ehlmann, 2015], and the currently understood atmospheric escape rates [Jakosky et al., 2017] are not sufficient alone to explain loss or more than 1-2 bars CO_2 atmosphere. Given the current measurement of $\delta^{13}C$ in Martian atmosphere, the atmospheric pressure of CO_2 may be less than 1 bar in the Noachian [Hu et al., 2015]. The size distribution of ancient craters in the Dorsa Aeolis region near Gale Crater also indicate low paleopressures of CO_2 (<0.9-3.8 bar) around 3.6 Ga [Kite et al., 2014]. One proposal is that the geologic observations on Martian surface may form in periodically transient warm periods in a predominantly cold climate [Wordsworth et al., 2015, 2016].

Thus, questions regarding the nature of the changing climate of Mars still remain unsolved. Further investigations into the geologic record are needed to better resolve the ambiguity regarding the prevalence, duration, and involved processes of liquid water throughout the history of Mars. The understanding of the geologic and climate history of Mars will also improve our knowledge of the origin and evolution of water in the inner solar system and climate change on our planet Earth.

1.2 Mineralogical record of Mars history from visible-near-infrared spectroscopy

New data acquired by orbital missions in the recent decades enable us to further investigate the geologic record of Mars in detail and gain insights to the evolving climate and geologic history of the planet. The characterization of surface composition using infrared spectroscopy data has established and better refined our understanding of the current paradigm of climate evolution.

In particular, visible near-infrared spectroscopy data acquired by OMEGA (Observatoire pour la Minéralogie, l'Eau, la Glace et l'Activité) on board Mars Express and CRISM (Compact Reconnaissance Imaging Spectrometer for Mars) on board the MRO (Mars Reconnaissance Orbiter) enabled identification of widespread, diverse mineralogy over the surface of the planet. Detection of olivine, high- and low-calcium pyroxene [Mustard et al., 2005; Ody et al., 2012] confirm the globally basaltic upper crust of Mars. Alteration materials,

including clay minerals, carbonate, sulfates, hydrated silica, and zeolite are also identified on Mars and preserve evidence of the history of water-rock interaction in Mars' crust. Clay minerals, especially Fe/Mg phyllosilicates and chlorite, are found to be widespread on early Noachian units on Mars [Poulet et al., 2005; Mustard et al., 2008], indicative of early weathering environments with liquid water. Fe/Mg clays have also been detected in fans and deltas in late Noachian-early Hesperian paleolakes (e.g. Jezero, Eberswalde and Holden), probably as both detrital sediments and in-situ diagenesis [e.g. Grant et al. 2008, Ehlmann et al., 2008a; Milliken & Bish 2010, Pondrelli et al., 2011, Goudge et al., 2015]. Fe-oxide and sulfate formations are found in the Hesperian units in both OMEGA and CRISM data [e.g. Bibring et al., 2007; Murchie et al. 2009, Roach et al. 2010] and in situ at Meridiani Planum [e.g. Squyres et al., 2004], consistent with acidic weathering, possibly via upwelling groundwater [Tosca et al., 2005; Andrews-Hanna et al., 2010] and consequent chemical interactions.

Though hydrated mineralogy is found to be widespread in the Noachian or Hesperian terrains in the highlands region, few detections are found in the younger terrains of the northern lowlands [Mustard et al., 2005; Carter et al., 2013; Ehlmann and Edwards, 2014]. The associations of aqueous minerals to different aged terrains in an orbital scale have been attributed to the decreasing intensity of water-rock interaction through time [Bibring et al., 2006]. The link between these aqueous alteration environments and the previous mentioned geomorphic evidence of liquid water on Mars raises an interesting question. For example, the period of widespread Fe/Mg phyllosilicate formation is not readily connected to the formation of valley networks [Fassett and Head, 2011]. The lack of hydrated alteration in the northern lowlands of Mars seems inconsistent with other geomorphic evidences which suggest existence of a global ocean [Di Achilles and Hynek, 2010]. Thus, the relationship of the mineralogical record with geomorphology on Mars presents an important clue to decipher the physical erosion and chemical alteration history of Mars. In this thesis I will focus on the geologic interpretations of Mars surface mineralogy analyzed through near-infrared spectroscopy to better constrain the geologic history and aqueous alteration of Mars with a particular focus on the understudied northern lowlands.

1.3 Northern lowlands: Key motivation and questions

One of the most striking features on the surface of Mars is the dichotomy boundary which divides the northern lowlands from the neighboring southern highlands with a contrast of mean elevation of ~5 km. The northern lowlands (or northern lowlands), which encompasses one third of Martian surface area, holds important clues to the mineralogical and morphological record of water activity on Mars. After the dichotomy formation in early Mars' history due to a giant impact [Marinova et al., 2008; Andrews-Hanna et al., 2008], several impacts [Frey, 2008], or mantle convection [Zhong and Zuber, 2001], the northern lowlands of Mars have been a depositional center throughout Mars history and recorded the geologic record of the evolution of water activity on Mars. Previous study of topographical data showed the existence of Noachian-aged, heavily cratered basement [Frey et al., 2002], widespread Hesperian-Amazonian lava flows [Head et al., 2002] and sedimentary units [Tanaka, 1997], including the Vastitas Borealis Formation (VBF) [Salvatore and Christensen, 2014].

Several lines of evidence indicate previous water activity in the northern lowlands. Outflow channels that debouch into the lowlands are thought to have deposited sediment and water into the lowlands region in the Hesperian age [Tanaka, 1997; Tanaka et al., 2001]. Putative shorelines have been proposed [Parker et al., 1993; Clifford and Parker, 2001] to have formed in the presence of a global ocean. However, these mapped shorelines do not follow an equipotential surface [Malin and Edgett, 1999; Carr and Head, 2003], and the shoreline evidence is found to be ambiguous with later high-resolution images [Malin and Edgett; 1999]. The search for the remnant deposits of the hypothesized northern ocean is still continuing. Recent work on 29 deltas along the dichotomy suggested they might have deposited in a large standing body of water [Di Achille and Hynek, 2010]. A different investigation revealed littoral deposits, backwash channels, and ice-rich lobes that propagate upslope in the circum-Chryse and northwestern Arabia Terra regions that are hypothesized to be deposits from a tsunami in the northern ocean [Rodriguez et al., 2016, Costard et al., 2017]. Thus, the existence of a global ocean remains an open question.

In addition to classic surface hydrologic features, additional processes involving liquid water have been proposed to shape the landscape of the northern lowlands. Small conical features hypothesized to be mud volcanoes have been reported in multiple locations in the northern lowlands, including Acidalia and Chryse Planitia [Farrand et al., 2005; Oehler and Allen, 2010; Komatsu et al., 2016]; Utopia Planitia [Skinner and Tanaka, 2007] and the Scandia region [Tanaka, 2005]. Glacial landforms thought to be active during the mid-late Amazonian are observed in the mid-latitude region [Head et al., 2006; Dickson et al., 2008, Levy et al., 2007, 2010] and could have been perturbed by energetic impact events [Russell and Head, 2002; Harrison et al., 2010]. However, there is still ambiguity in terms of the prevalence of water in the northern lowlands throughout Mars' history, especially given the scarcity of aqueous mineral detections. In this thesis, I would like to investigate a few questions regarding the geologic and aqueous activity in the northern lowlands of Mars, including: Are there ocean deposits in the northern lowlands sediments with minerals formed due to weathering by seawaters or precipitation from them? What is the extent of Hesperian lava plains [Salvatore et al., 2010] and their relationship to the uplifted phyllosilicates [Carter et al., 2010] in the stratigraphy? What is the extent and duration of alteration processes in the lowlands and how are they related to water activity in the southern highlands? What are the main sources and form of aqueous processes on Amazonian Mars? Is impact-induced heating an important source of climate warming in the Amazonian? Are there missing carbonates buried in the northern lowlands, and what spectral properties may keep them hidden from orbital detection?

1.4 Thesis summary

Based on the key motivation presented above, this thesis will present several research projects regarding the geological history of the northern lowlands of Mars and environmental implications of near-infrared spectroscopy. The thesis is composed of two parts. In the first part I will discuss the results of the analysis of spectral and imagery data in the northern lowlands, aiming to place better constraints on questions like the existence of a long-lived global ocean; the extent of Noachian-Hesperian volcanic flows in the northern lowlands; the nature of aqueous activity in the northern lowlands in the Amazonian age. Chapters 2, 3 and 4 include three projects focusing on different aspects of the water activity in the northern

lowlands: the stratigraphy of the northern lowlands excavated by impact craters, the knobby terrains of Acidalia Planitia, and the aqueous activity in the Amazonian-aged Lyot crater and its vicinity.

In the second part, through a different line of investigation to understand the mineralogical record of Mars surface in near infrared spectroscopy, I present a laboratory study and analysis of Mars-relevant terrestrial carbonates in impact structures and shock experiments to characterize the variation in carbonate spectra (Chapter 5). Carbonate was first identified in Nili Fossae region on Mars associated with olivine-rich rocks [Ehlmann et al., 2008b], found to be 3-5 wt. % in northern lowlands soils at the Phoenix landing site [Boynton et al., 2009], 16-34 % in localized outcrops of olivine-bearing rocks at Gusev crater [Morris et al. 2010], in mixed units excavated by an impact crater [Michalski and Niles 2010], and recently expanded to Huygens basin northwest of Hellas, in western Noachis Terra, and other individual craters [Wray et al., 2016]. The spectral properties of these carbonate detections have spectral features that are different from the terrestrial lab data of pure Mg-, Fe-, or Ca-carbonates. Furthermore, carbonate is not widespread at concentrations and scales visible from orbit in the northern lowlands. Thus it is important to understand the spectral property of carbonates and the role of impact shock loading and elevated temperature in obscuring carbonate from orbital observation. This analysis also has implications for the interpretation of the mineralogical record in northern lowlands of Mars.

Here I summarize the key points of each chapter:

In Chapter 2, I summarize the global survey of impact craters in the northern lowlands of Mars and the stratigraphy inferred from this study [Pan et al, *in revision*]. In this survey, widespread mafic and hydrated minerals associated with impact craters have been detected in all the major basins in the northern lowlands. We also find diverse hydrated mineralogy is similar to the highlands, and implies an excavated ancient basement from beneath 1-2 km of mafic materials. However, no strong evidence for pervasive carbonate or other evaporative salts has been found to support of the hypothesis of a global ocean.

In Chapter 3, I present the discovery of Fe/Mg phyllosilicate and hydrated silica in discrete stratigraphic units within the knobby terrains of Acidalia Planitia. Fe/Mg phyllosilicates are detected in knobs that were eroded remnants of southern highlands, and hydrated silica, formed in a younger unit via localized weathering [Pan and Ehlmann, 2014]. These data record a history of aqueous processes with progressively less intensive aqueous chemical alteration from the Noachian to Amazonian.

Chapter 4 follows on the survey of Chapter III to further analyze of mineralogy and morphology in Lyot crater vicinity and their implication for the Amazonian climate [Pan et al., *in prep*]. Diverse hydrated minerals including Fe/Mg phyllosilicate, chlorite, illite/muscovite, prehnite are mapped in Lyot crater and four small craters in the vicinity of Lyot. From the distribution and correlation of the minerals and their relationship to the morphological features of fluvial activity in and surrounding Lyot crater, we identify four different stages of aqueous activity, from pre-impact hydrothermal alteration in the Noachian/Hesperian to mid-late Amazonian channel formation.

In Chapter 5, I summarize the initial results of a laboratory project in which I assess the spectral effect of impact-shocked carbonates in terrestrial craters and impact shock experiments, and discuss their implications for Mars. Here I find spectral slope from 1 to 1.7 μm region in shocked carbonate clasts from Haughton impact structure and investigated the cause of spectral slope. I also present the comparison of various spectral characteristics between different terrestrial carbonate rocks and Mars carbonate spectra.

Finally, in the last chapter, I will discuss the implication for the geologic and climate history of Mars from near-infrared spectroscopy study using both orbital and laboratory data, as well as future directions.

Reference:

Andrews-Hanna, J. C., M. T. Zuber, and W. B. Banerdt (2008), The Borealis basin and the origin of the Martian crustal dichotomy, Nature, 453(7199), 1212–1215, doi:10.1038/nature07011.

Andrews-Hanna, J. C., M. T. Zuber, R. E. Arvidson, and S. M. Wiseman (2010), Early Mars hydrology: Meridiani playa deposits and the sedimentary record of Arabia Terra, J. Geophys. Res. E Planets, 115(6), 1–22, doi:10.1029/2009JE003485.

Baker, V. R., and D. J. Milton (1974), Erosion by catastrophic floods on Mars and Earth, Icarus, 23(1), 27–41, doi:10.1016/0019-1035(74)90101-8.

Bibring, J.-P. et al. (2006), Global Mineralogical and Aqueous Mars History Derived from OMEGA/Mars Express Data, Science (80-.)., 312(5772), 400–404, doi:10.1126/science.1122659.

Bibring, J.-P. et al. (2007), Coupled Ferric Oxides and Sulfates on the Martian Surface, Science (80-.)., 317(August), 1206–1211, doi:10.1126/science.1144174.

Boynton, W. V et al. (2009), Evidence for calcium carbonate at the Mars Phoenix landing site., Science, 325(5936), 61–64, doi:10.1126/science.1172768.

Carr, M. H. (1995), The Martian drainage system and the origin of valley networks and fretted channels, J. Geophys. Res., 100, 7479, doi:10.1029/95JE00260.

Carr, M. H., and J. W. Head (2003), Oceans on Mars: an assessment of the observational evidence and possible fate, J. Geophys. Res. , 108(4203), 5042, doi:10.1029/2002JE001963.

Carter, J., F. Poulet, J.-P. Bibring, and S. Murchie (2010), Detection of hydrated silicates in crustal outcrops in the northern plains of Mars., Science, 328(5986), 1682–6, doi:10.1126/science.1189013.

Carter, J., F. Poulet, J. P. Bibring, N. Mangold, and S. Murchie (2013), Hydrous minerals on Mars as seen by the CRISM and OMEGA imaging spectrometers: Updated global view, J. Geophys. Res. E Planets, 118(4), 831–858, doi:10.1029/2012JE004145.

Clifford, S. M. (1993), A Model for the Hydrologic and Climatic Behavior of Water on Mars, , 98.

Clifford, S. M., and T. J. Parker (2001), The evolution of the Martian hydrosphere: Implications for the fate of a primordial ocean and the current state of the Northern Plains, Icarus, 154(1), 40–79, doi:10.1006/icar.2001.6671.

Costard, F., A. Séjourné, K. Kelfoun, S. Clifford, F. Lavigne, I. Di Pietro, and S. Bouley (2017), Modeling tsunami propagation and the emplacement of thumbprint terrain in an early Mars ocean, J. Geophys. Res. Planets, 122, 633–649, doi:10.1002/2016JE005230.

Di Achille, G., and B. M. Hynek (2010), Ancient ocean on Mars supported by global distribution of deltas and valleys, Nat. Geosci., 3(7), 459–463, doi:10.1038/ngeo891.

Dickson, J. L., J. W. Head, and D. R. Marchant (2008), Late Amazonian glaciation at the dichotomy boundary on Mars: Evidence for glacial thickness maxima and multiple glacial phases, Geology, 36(5), 411–414, doi:10.1130/G24382A.1.

Edwards, C. S., and B. L. Ehlmann (2015), Carbon sequestration on Mars, Geology, 43(10), 863–866, doi:10.1130/G36983.1.

Ehlmann, B. L., J. F. Mustard, C. I. Fassett, S. C. Schon, J. W. Head III, D. J. Des Marais, J. a. Grant, and S. L. Murchie (2008), Clay minerals in delta deposits and organic preservation potential on Mars, Nat. Geosci., 1(6), 355–358, doi:10.1038/ngeo207.

Ehlmann, B. L. et al. (2008), Orbital identification of carbonate-bearing rocks on Mars., Science, 322(5909), 1828–1832, doi:10.1126/science.1164759.

Ehlmann, B. L., and C. S. Edwards (2014), Mineralogy of the Martian Surface, Annu. Rev. Earth Planet. Sci, 42, 291–315, doi:10.1146/annurev-earth-060313-055024.

Farrand, W. H., L. R. Gaddis, and L. Keszthelyi (2005), Pitted cones and domes on Mars: Observations in Acidalia Planitia and Cydonia Mensae using MOC, THEMIS, and TES data, J. Geophys. Res. E Planets, 110(5), 1–14, doi:10.1029/2004JE002297.

Fassett, C. I., and J. W. Head (2008), Valley network-fed, open-basin lakes on Mars: Distribution and implications for Noachian surface and subsurface hydrology, Icarus, 198(1), 37–56, doi:10.1016/j.icarus.2008.06.016.

Fassett, C. I., and J. W. Head (2011), Sequence and timing of conditions on early Mars, Icarus, 211(2), 1204–1214, doi:10.1016/j.icarus.2010.11.014.

Frey, H. V. (2002), Ancient lowlands on Mars, Geophys. Res. Lett., 29(10), 0–3, doi:10.1029/2001GL013832.

Frey, H. (2008), Ages of very large impact basins on Mars: Implications for the late heavy bombardment in the inner solar system, Geophys. Res. Lett., 35(13), doi:10.1029/2008GL033515.

Forget, F., R. Wordsworth, E. Millour, J. B. Madeleine, L. Kerber, J. Leconte, E. Marcq, and R. M. Haberle (2013), 3D modelling of the early martian climate under a denser CO 2 atmosphere: Temperatures and CO 2 ice clouds, Icarus, 222(1), 81–99, doi:10.1016/j.icarus.2012.10.019.

Goudge, T. A., J. W. Head, J. F. Mustard, and C. I. Fassett (2012), An analysis of open-basin lake deposits on Mars: Evidence for the nature of associated lacustrine deposits and post-lacustrine modification processes, Icarus, 219(1), 211–229, doi:10.1016/j.icarus.2012.02.027.

Goudge, T. A., J. F. Mustard, J. W. Head, C. I. Fassett, and S. M. Wiseman (2015), Assessing the mineralogy of the watershed and fan deposits of the Jezero crater paleolake system, Mars, J. Geophys. Res. E Planets, 120(4), 775–808, doi:10.1002/2014JE004782.

Grant, J. A., R. P. Irwin, J. P. Grotzinger, R. E. Milliken, L. L. Tornabene, A. S. McEwen, C. M. Weitz, S. W. Squyres, T. D. Glotch, and B. J. Thomson (2008), HiRISE imaging of

impact megabreccia and sub-meter aqueous strata in Holden Crater, Mars, Geology, 36(3), 195–198, doi:10.1130/G24340A.1.

Halevy, I., and J. W. Head III (2014), Episodic warming of early Mars by punctuated volcanism, Nat. Geosci., 7(12), 865–868, doi:10.1038/ngeo2293.

Harrison, T. N., M. C. Malin, K. S. Edgett, D. E. Shean, M. R. Kennedy, L. J. Lipkaman, B. A. Cantor, and L. V. Posiolova (2010), Impact-induced overland fluid flow and channelized erosion at Lyot Crater, Mars, Geophys. Res. Lett., 37(21), doi:10.1029/2010GL045074.

Head, J. W., M. A. Kreslavsky, and S. Pratt (2002), Northern lowlands of Mars: Evidence for widespread volcanic flooding and tectonic deformation in the Hesperian Period, J. Geophys. Res. Planets, 107(E1), 5004, doi:10.1029/2000JE001445.

Head, J. W., A. L. Nahm, D. R. Marchant, and G. Neukum (2006), Modification of the dichotomy boundary on Mars by Amazonian mid-latitude regional glaciation, Geophys. Res. Lett., 33(8), doi:10.1029/2005GL024360.

Hynek, B. M., M. Beach, and M. R. T. Hoke (2010), Updated global map of Martian valley networks and implications for climate and hydrologic processes, J. Geophys. Res. Planets, 115(E9), 1–14, doi:10.1029/2009JE003548.

Hu, R., D. M. Kass, B. L. Ehlmann, and Y. L. Yung (2015), Tracing the fate of carbon and the atmospheric evolution of Mars, Nat. Commun., 6, 10003, doi:10.1038/ncomms10003.

Jakosky, B. M., et al. "Mars' atmospheric history derived from upper-atmosphere measurements of 38Ar/36Ar." Science 355.6332 (2017): 1408-1410.

Johnson, S. S., M. A. Mischna, T. L. Grove, and M. T. Zuber (2008), Sulfur-induced greenhouse warming on early Mars, J. Geophys. Res. E Planets, 113(8), doi:10.1029/2007JE002962.

Kasting, J. F. (1991), CO2 condensation and the climate of early Mars, Icarus, 94(1), 1–13, doi:10.1016/0019-1035(91)90137-I.

Kite, Edwin S., et al. "Low palaeopressure of the martian atmosphere estimated from the size distribution of ancient craters." Nature Geoscience 7.5 (2014): 335-339.

Komatsu, G., C. H. Okubo, J. J. Wray, L. Ojha, M. Cardinale, A. Murana, R. Orosei, M. A. Chan, J. Orm, and R. Gallagher (2016), Small edifice features in Chryse Planitia, Mars: Assessment of a mud volcano hypothesis, Icarus, 268, 56–75, doi:10.1016/j.icarus.2015.12.032.

Levy, J. S., J. W. Head, and D. R. Marchant (2007), Lineated valley fill and lobate debris apron stratigraphy in Nilosyrtis Mensae, Mars: Evidence for phases of glacial modification of the dichotomy boundary, J. Geophys. Res. E Planets, 112(8), doi:10.1029/2006JE002852.

Levy, J., J. W. Head, and D. R. Marchant (2010), Concentric crater fill in the northern mid-latitudes of Mars: Formation processes and relationships to similar landforms of glacial origin, Icarus, 209(2), 390–404, doi:10.1016/j.icarus.2010.03.036.

Malin, Michael C., and Kenneth S. Edgett. "Oceans or seas in the martian northern lowlands: high-resolution imaging tests of proposed coastlines." Geophysical Research Letters 26.19 (1999): 3049-3052.

Malin, M. C., and K. S. Edgett (2000), Sedimentary rocks of early Mars, Science (80-.)., 290(5498), 1927–1937, doi:10.1126/science.290.5498.1927.

Marinova, M. M., O. Aharonson, and E. I. Asphaug (2008), Mega-impact formation of the Mars hemispheric dichotomy., Nature, 453(7199), 1216–1219, doi:10.1038/nature07070.

Masursky, H., J. M. Boyce, A. L. Dial, G. G. Schaber, and M. E. Strobell (1977), Classification and time of formation of Martian channels based on Viking data, J. Geophys. Res., 82(28), 4016–4038, doi:10.1029/JS082i028p04016.

Michalski, J. R., and P. B. Niles (2010), Deep crustal carbonate rocks exposed by meteor impact on Mars, Nat. Geosci., 3(11), 751–755, doi:10.1038/ngeo971.

Milliken, R. E., and D. L. Bish (2010), Sources and sinks of clay minerals on Mars, Philos. Mag., 90(17–18), 2293–2308, doi:10.1080/14786430903575132.

Morris, R. V et al. (2010), Identification of Carbonate-Rich Outcrops on Mars by the Spirit Rover, Science (80-.)., 329(5990), 421–424, doi:10.1126/science.1189667.

Mustard, J. F., F. Poulet, A. Gendrin, J.-P. Bibring, Y. Langevin, B. Gondet, N. Mangold, G. Bellucci, and F. Altieri (2005), Olivine and pyroxene diversity in the crust of Mars., Science, 307(5715), 1594–7, doi:10.1126/science.1109098.

Mustard, J. F. et al. (2008), Hydrated silicate minerals on Mars observed by the Mars Reconnaissance Orbiter CRISM instrument., Nature, 454(7202), 305–309, doi:10.1038/nature07097.Murchie, S. L. et al. (2009), A synthesis of Martian aqueous mineralogy after 1 Mars year of observations from the Mars Reconnaissance Orbiter, J. Geophys. Res. E Planets, 114(9), doi:10.1029/2009JE003342.

Ody, A., F. Poulet, Y. Langevin, J. P. Bibring, G. Bellucci, F. Altieri, B. Gondet, M. Vincendon, J. Carter, and N. Manaud (2012), Global maps of anhydrous minerals at the surface of Mars from OMEGA/MEx, J. Geophys. Res. E Planets, 117(9), doi:10.1029/2012JE004117.

Oehler, D. Z., and C. C. Allen (2010), Evidence for pervasive mud volcanism in Acidalia Planitia, Mars, Icarus, 208(2), 636–657, doi:10.1016/j.icarus.2010.03.031.

Pan, L., and B. L. Ehlmann (2014), Phyllosilicate and hydrated silica detections in the knobby terrains of Acidalia Planitia, northern plains, Mars, Geophys. Res. Lett., 41(6), 1890–1898, doi:10.1002/2014GL059423.

Pan L. et al. (2017), “The Stratigraphy and History of Mars’ Northern Lowlands Through Mineralogy of Impact Craters: A Comprehensive Survey.” Journal of Geophysical Research: Planets. in revision.

Parker, T. J., D. S. Gorsline, R. S. Saunders, D. C. Pieri, and D. M. Schneeberger (1993), Coastal geomorphology of the Martian northern plains, J. Geophys. Res., 98(93), 11061, doi:10.1029/93JE00618.

Perron, J. T., J. X. Mitrovica, M. Manga, I. Matsuyama, and M. a Richards (2007), Evidence for an ancient martian ocean in the topography of deformed shorelines., Nature, 447(June), 840–843, doi:10.1038/nature05873.

Phillips, R. J. et al. (2011), Massive CO_2 ice deposits sequestered in the south polar layered deposits of Mars., Science, 332(6031), 838–841, doi:10.1126/science.1203091.

Pollack, J. B., J. F. Kasting, S. M. Richardson, and K. Poliakoff (1987), The case for a wet, warm climate on early Mars, Icarus, 71(2), 203–224, doi:10.1016/0019-1035(87)90147-3.

Pondrelli, M., A. Baliva, S. Di Lorenzo, L. Marinangeli, and A. P. Rossi (2005), Complex evolution of paleolacustrine systems on Mars: An example from the Holden crater, J. Geophys. Res. E Planets, 110(4), 1–20, doi:10.1029/2004JE002335.

Poulet, F. et al. (2005), Phyllosilicates on Mars and implications for early martian climate, Nature, 438(7068), 623–627, doi:10.1038/nature04274.

Ramirez, R. M., R. Kopparapu, M. E. Zugger, T. D. Robinson, R. Freedman, and J. F. Kasting (2013), Warming early Mars with CO2 and H2, Nat. Geosci., 7(1), 59–63, doi:10.1038/ngeo2000.

Roach, L. H., J. F. Mustard, M. D. Lane, J. L. Bishop, and S. L. Murchie (2010), Diagenetic haematite and sulfate assemblages in Valles Marineris, Icarus, 207(2), 659–674, doi:10.1016/j.icarus.2009.11.029.

Rodriguez, J. A. P. et al. (2016), Tsunami waves extensively resurfaced the shorelines of an early Martian ocean, Sci. Rep., 6(April), 25106, doi:10.1038/srep25106.

Russell, P. S., and J. W. Head (2002), The martian hydrosphere/cryosphere system: Implications of the absence of hydrologic activity at Lyot crater, Geophys. Res. Lett., 29(17), 1–8, doi:10.1029/2002GL015178.

Salvatore, M. R., J. F. Mustard, M. B. Wyatt, and S. L. Murchie (2010), Definitive evidence of Hesperian basalt in Acidalia and Chryse planitiae, J. Geophys. Res., 115(E7), 1–16, doi:10.1029/2009JE003519.

Salvatore, M. R., and P. R. Christensen (2014), On the origin of the Vastitas Borealis Formation in Chryse and Acidalia Planitiae, Mars, J. Geophys. Res. E Planets, 119(12), 2437–2456, doi:10.1002/2014JE004682.

Segura, T. L., O. B. Toon, A. Colaprete, and K. Zahnle (2002), Environmental effects of large impacts on Mars., Science, 298(December), 1977–1980, doi:10.1126/science.1073586.

Skinner, J. A., and K. L. Tanaka (2007), Evidence for and implications of sedimentary diapirism and mud volcanism in the southern Utopia highland-lowland boundary plain, Mars, Icarus, 186(1), 41–59, doi:10.1016/j.icarus.2006.08.013.

Squyres, S. W. et al. (2004), In situ evidence for an ancient aqueous environment at Meridiani Planum, Mars., Science, 306(5702), 1709–1714, doi:10.1126/science.1104559.

Tanaka, K. L. (1997), Sedimentary history and mass flow structures of Chryse and Acidalia Planitiae, Mars, J. Geophys. Res., 102(E2), 4131–4149, doi:10.1029/96JE02862.

Tanaka, K. L., W. B. Banerdt, J. S. Kargel, and N. Hoffman (2001), Huge, CO 2 -charged debris-flow deposit and tectonic sagging in the northern plains of Mars, Geology, 29(3), 427–430.

Tanaka, K. L. (2005), Geology and insolation-driven climatic history of Amazonian north polar materials on Mars., Nature, 437(7061), 991–994, doi:10.1038/nature04065.

Tosca, N. J., S. M. McLennan, B. C. Clark, J. P. Grotzinger, J. A. Hurowitz, A. H. Knoll, C. Schr??der, and S. W. Squyres (2005), Geochemical modeling of evaporation processes on Mars: Insight from the sedimentary record at Meridiani Planum, Earth Planet. Sci. Lett., 240(1), 122–148, doi:10.1016/j.epsl.2005.09.042.

Wordsworth, R., F. Forget, E. Millour, J. W. Head, J.-B. Madeleine, and B. Charnay (2013), Global modelling of the early martian climate under a denser CO2 atmosphere: Water cycle and ice evolution, Icarus, 222(1), 1–19, doi:10.1016/j.icarus.2012.09.036.

Wordsworth, R. D., L. Kerber, R. T. Pierrehumbert, F. Forget, and J. W. Head (2015), Comparison of "warm and wet" and "cold and icy" scenarios for early Mars in a 3-D climate model, J. Geophys. Res. E Planets, 120(6), 1201–1219, doi:10.1002/2015JE004787.

Wordsworth, R. D. (2016), The Climate of Early Mars, Annu. Rev. Earth Planet. Sci., 44(1), 1–31, doi:doi:10.1146/annurev-earth-060115-012355.

Wordsworth, R., Y. Kalugina, S. Lokshtanov, A. Vigasin, B. Ehlmann, J. Head, C. Sanders, and H. Wang (2017), Transient reducing greenhouse warming on early Mars, , 1–6, doi:10.1029/.

Wray, J. J., S. L. Murchie, J. L. Bishop, B. L. Ehlmann, R. E. Milliken, M. B. Wilhelm, K. D. Seelos, and M. Chojnacki (2016), Orbital evidence for more widespread carbonate-bearing rocks on Mars, J. Geophys. Res. E Planets, 121(4), 652–677, doi:10.1002/2015JE004972.

Yung, Y. L., H. Nair, and M. F. Gerstell (1997), CO2 greenhouse in the early Martian atmosphere: SO2 inhibits condensation, Icarus, 130(1), 222–224, doi:10.1006/icar.1997.5808.

Zhong, S., and M. T. Zuber (2001), Degree-1 mantle convection and the crustal dichotomy on Mars, Earth Planet. Sci. Lett., 189(1–2), 75–84, doi:10.1016/S0012-821X(01)00345-4.

Chapter 2

THE STRATIGRAPHY AND HISTORY OF MARS' NORTHERN LOWLANDS THROUGH MINERALOGY OF IMPACT CRATERS: A COMPREHENSIVE SURVEY

Lu Pan[1], Bethany L. Ehlmann[1,2], John Carter[3], and Carolyn M. Ernst[4]

[1]Division of Geological and Planetary Sciences, California Institute of Technology, Pasadena, California, USA.

[2]Jet Propulsion Laboratory, California Institute of Technology, Pasadena, California, USA.

[3]Institut d'Astrophysique Spatiale, Orsay, France

[4]The John Hopkins University Applied Physics Laboratory, Laurel, Maryland, USA

Corresponding author: Lu Pan (lpan@caltech.edu)

Pan L. et al. (2017). "The stratigraphy and history of Mars' northern lowlands through mineralogy of impact craters: A comprehensive survey". In: *Journal of Geophysical Research: Planets (in revision)*

Abstract

The basin-filling materials of the northern lowlands, which cover ~1/3 of Mars' surface, record the long-term evolution of Mars' geology and climate. The buried stratigraphy was inferred through analyses of impact crater mineralogy, detected using data acquired by the Compact Reconnaissance Imaging Spectrometer for Mars (CRISM). Examining 1045 impact craters across the northern lowlands, we find widespread olivine and pyroxene and diverse hydrated/hydroxylated minerals, including Fe/Mg smectite, chlorite, prehnite, and hydrated silica. The distribution of mafic minerals is consistent with infilling volcanic materials across the entire lowlands (~1–4·10^7 km^3), indicating a significant volume of volatile release by volcanic outgassing. Hydrated/hydroxylated minerals occur more frequently in large craters, consistent with the scenario that the hydrated minerals are being excavated from deep basement rocks similar to the southern highlands, beneath 1-2 km thick mafic lava flows/volcaniclastic materials. In addition, select deposits with hydrated minerals may have formed through impact-induced hydrothermal alteration during the Late Hesperian-Amazonian. Meanwhile, no evidence of concentrated salt deposits has been found, that would indicate a long-lived global ocean. In this study, we also find significant geographical variations of local mineralogy and stratigraphy in different basins (geological provinces), independent of dust cover. For example, many hydrated and mafic minerals are newly discovered within the polar Scandia region (> 60°N), and Chryse Planitia has more mafic mineral detections than other basins, possibly due to a previously unrecognized volcanic source.

1 Introduction

The northern lowlands of Mars preserve a long-term record of Mars' geologic history, including heavily cratered Noachian basement [Frey et al., 2002], Hesperian outflow channels and/or possible ocean deposits [Tanaka et al., 2003; Parker et al., 1993], widespread Hesperian lava flows [Head et al., 2002], and Amazonian surface sedimentary/volcanic geomorphic structures (cones, knobs, polygons, etc.) [Frey et al., 1979; Lucchitta et al., 1986; Farrand et al., 2005, Oehler and Allen, 2012]. The surface of the northern lowlands is covered by geologic units dated from the Early Hesperian to the Amazonian and has been mapped in great detail [Tanaka et al., 2005; Tanaka et al., 2014].

However, little is known about the stratigraphic relationships between the underlying cratered basement, widespread lava flows, and subsequent units, including their thicknesses and variability across the northern lowlands. Questions also remain regarding the spatial and temporal variations of aqueous activity in the northern lowlands and the possible existence of an ancient global ocean. Study of the subsurface stratigraphy of the northern lowlands thus presents an opportunity to assess past Martian igneous and aqueous processes changing through time.

Our ability to interpret the mineralogy of the subsurface of the northern lowlands has been limited by mantling deposits and coatings that obscure the composition of surface units as well as limit exposure of earlier units. Few tectonic scarps exist that would expose materials in section. Instead, impact craters that excavate bedrock provide the key means of accessing the subsurface stratigraphy of the northern lowlands. In this study, we apply a set of improved noise reduction tools to analyze data acquired by the Compact Reconnaissance Imaging Spectrometer for Mars (CRISM) onboard the Mars Reconnaissance Orbiter (MRO). We analyze high spatial resolution, targeted data covering part or all of 1045 impact craters in the northern lowlands to assess the mineralogy of their units, which includes materials excavated from the subsurface. From the frequency and geologic context of different types of mineral-bearing units, we consider the implications for the subsurface stratigraphy and provide insights into the geologic and aqueous history of the northern lowlands of Mars.

In this paper we first review existing knowledge about the northern lowlands (Section 2); describe the CRISM processing methods and crater dataset used in this study (Section 3); present the results of mineral detections, spatial distribution and statistical relationships with crater size and other key variables (Section 4); discuss the implications for the geologic history of the northern lowlands, including igneous and aqueous activity (Section 5); and summarize key conclusions (Section 6).

2 History and Composition of the Northern Lowlands

The northern lowlands, also known as the northern plains, are divided from the southern highlands by the crustal dichotomy boundary, which has long been recognized and hypothesized to have formed early in Mars' history due to a large impact [Marinova et

al., 2008; Andrews-Hanna et al., 2008], several impacts [Frey, 2006], or mantle convection [Zhong and Zuber, 2001]. Mars Orbiter Laser Altimeter (MOLA) and gravity data from Doppler tracking on Mars Global Surveyor show that the northern lowlands have an average elevation approximately 5 km lower than the cratered southern highlands and a much thinner crust (30-40 km) than that of the highlands (70-80 km) [Smith et al., 1999; Zuber et al., 2000]. Due to its unique geologic history, the northern lowlands are also distinctive from the southern highlands of Mars with its smoother surface and younger age [Aharonson, 1998; Tanaka, 2005; 2014] as well as a different surface composition (described below).

The smoothness and low crater density indicate a surface of Late Hesperian-Amazonian age over the majority of the lowlands [Tanaka et al., 2005; Tanaka et al., 2014]. However, subtle circular depressions called Quasi Circular Depressions (QCD) have been identified in MOLA data throughout the lowlands [Frey, 2002; 2008], probably indicating a heavily-cratered Noachian or pre-Noachian surface buried underneath plains materials. Also, the topographic expression of wrinkle ridges is consistent with widespread Hesperian lava flows that may account for most of the post-Noachian fill within the northern basin [Head et al., 2002], a scenario that may have had significant influence on Mars climate due to release of volatiles as part of the volcanic eruptions. Due to the lack of good exposures in the plains, there are uncertainties regarding the relationship between the ancient basement and widespread lava flows indicated by wrinkle ridges, including whether intermediate stratigraphic units exist between the two. The composition and depth of this ancient basement may hold important clues to understanding the nature of the dichotomy, and a detailed analysis of the thickness of the surface lava unit(s) may provide better constraints for the volume of volcanic deposits in the northern lowlands.

Two proposed shorelines that follow topographic contours suggest the possible past existence of ocean(s) in the Noachian [Clifford and Parker, 2001] or Early Hesperian [Carr and Head, 2003]. Evidence for shoreline features has been challenged because later mapping shows the contacts do not follow equipotential surfaces [Malin and Edgett, 1999; Carr and Head, 2003], though these observations may be reconciled with other mechanisms like true polar wander [Perron et al., 2007]. Later, the identification of 29 putative deltaic

deposits within a 200-m topographic contour near the dichotomy also suggests a past ocean [Di Achille and Hynek, 2010]. Regardless of whether an ocean existed for long periods of time, large outflow channels certainly repeatedly debouched into the plains in the Hesperian and early Amazonian, presumably depositing large quantities of sediments [Tanaka et al., 1997; Tanaka et al., 2001]. Widespread aqueous alteration might occur given the existence of repeated outflow deposits or an ocean, which may leave evidence in the stratigraphic record [e.g., Salvatore and Christensen, 2014a]. The evaporation of a large standing body of water could also precipitate salt and carbonate in localized, if not extensive, regions as the topmost aqueous deposits in the stratigraphy. These minerals, previously unidentified in the northern lowlands, may lie deep beneath the current northern lowlands surface, so the investigation of the underlying mineralogy would add an important line of evidence to the existence/absence of an ancient global ocean.

Other sedimentary processes (e.g. aeolian, periglacial etc.) have also been observed within the northern lowlands. The Vastitas Borealis Formation (VBF), a widespread sedimentary unit on the surface of the northern lowlands, probably represents one of the final stages of water-related sedimentary activity. The VBF has been suggested to have resulted from either volatile expulsion from the compaction of a fluid-laden sedimentary unit [Salvatore and Christensen 2014a], local periglacial processes acting on outflow channel sediments and other older plains materials [Tanaka et al., 2003], sublimation residues [Krevlasky and Head, 2002], or ocean sediments [Parker et al., 1989, 1993; Baker et al., 1991]. On the surface of the Vastitas Borealis Formation many geomorphic features that could be related to aqueous activity have been identified, including polygonal troughs for ice/volatile-related processes [McGill et al., 1992; Hiesinger and Head, 2000; Yoshikawa, 2003; Mangold, 2004] and conical and domical features hypothesized to be mud volcanoes or springs [Farrand, 2005; Oehler and Allen, 2010]. Any hydrated/hydroxylated mineral associated with the unit may help to distinguish the different formation mechanisms for the Vastitas Borealis Formation.

The subsurface mineralogy of the northern lowlands may also be unevenly distributed among geographically separated basins, which have been subject to local sedimentary and volcanic resurfacing in addition to any lowlands-wide processes. For

example, outflow channel sediments may have been deposited in Chryse and Acidalia Planitiae [Tanaka et al., 2001, Salvatore et al. 2014]; continuous activity of Elysium Mons volcanic province has filled much of Elysium and Utopia Planitiae [Hartmann and Berman, 2001; Platz and Michael, 2011]; and Arcadia and Amazonian Planitiae have been resurfaced with extensive volcanic flows probably sourced from Olympus Mons [Fuller and Head, 2002]. The detailed basin-specific stratigraphy and resurfacing processes also constitute major components of the geology of the northern lowlands and will be investigated in this study.

Previous works on compositional data in the northern lowlands provide important understanding of their geologic history. Thermal infrared data acquired from Thermal Emission Spectrometer (TES) indicate a relatively silica-enriched surface (Surface type II) compared to the typical basalt (Surface type I) of the southern highlands [Christensen et al., 2001]. Therefore, the surface of the lowlands was initially interpreted to be andesitic in composition [Bandfield et al., 2000] but later reinterpreted to represent altered terrains [e.g., Wyatt & McSween, 2002; Kraft et al., 2003; Michalski et al., 2005]. Gamma Ray Spectrometer data do not show enhancement of Si in the bulk rock [Karunatillake et al., 2006, Boynton et al., 2007], thus favoring the interpretation that spectral differences may be explained by the presence of a thin silica-enriched coating or rind [e.g., Kraft et al., 2003]. Later, visible/shortwave-infrared (VSWIR) imaging spectrometers (e.g., OMEGA and CRISM) showed much of the surface of the northern lowlands has a characteristic downward slope toward longer wavelengths (the “blue” slope) [Mustard et al., 2005], which makes visible-shortwave-infrared spectral identifications of surface mineralogy more difficult. The distinct spectral features relative to the southern highlands may be due to dust cover, silica-enriched coatings, and/or a weathered glass [Ruff et al., 2002; Kraft et al., 2003; Mustard et al., 2005; Horgan and Bell, 2012].

Higher spatial resolution studies of composition have shown that the mineralogy of the northern lowlands is not completely obscured. Mesas at the margins of the dichotomy boundary and the surfaces of intervening terrains show diverse hydrated silicates, including plateaus with Fe/Mg phyllosilicates and silica in stratigraphically higher but often topographically lower units [Pan & Ehlmann, 2014]. Also using CRISM data, mafic

minerals were identified in 182 craters (0.3-62.7 km in diameter) in Acidalia Planitia [Salvatore et al., 2010], olivine was detected in multiple northern lowlands locales [Ody et al., 2013], and hydrated minerals were found in nine large northern lowlands craters (20-230 km in diameter) [Carter et al., 2010]. As previous work suggested [Head et al., 2002], the mafic detections were interpreted to indicate the excavation of materials formed during widespread volcanism [Salvatore et al., 2010; Ody et al., 2013]. Hydrated minerals were interpreted to result from excavation of altered Noachian crustal materials [Carter et al., 2010]. Additional occurrences of hydrated minerals associated with impact craters and other morphological features (e.g., cones and polygonal troughs) were found in a global survey by Carter et al. [2013] but their geologic context has not yet been examined in detail.

To gain a more complete and detailed understanding of the geologic history of the northern lowlands as indicated by compositionally distinct units, we surveyed all the CRISM images associated with impact craters in the northern lowlands. This work builds on previous successful surveys of the mineralogy of crater central peaks, largely focused on craters in the southern highlands using near-infrared data [Sun and Milliken, 2015; Caudill et al., 2012; Quantin et al., 2012]. Impact craters can excavate subsurface materials and expose them within the crater central peak/ring structure, crater walls, ejecta blanket, and on the crater floor, making it possible for us to access the subsurface stratigraphy to varying degrees using orbital data. Study of the diameters of impact craters that expose distinctive mineralogy in the ejecta reveals the minimum depth to such a unit by physical constraints on the maximum excavation depth [e.g., Budney and Lucey, 1998; Baratoux et al., 2007; Ernst et al., 2010; Barnhart & Nimmo 2011]. Central peaks of large complex craters sometimes expose the deepest stratigraphy brought to the surface by the impact [e.g., Caudill et al., 2012; Ernst et al., 2010]. Inverted flaps exposed on the crater walls access the shallow subsurface [e.g., Salvatore et al., 2010; Salvatore and Christensen, 2014a]. Impact craters into volatile-rich substrates can also initiate long-lived hydrothermal systems, if sufficient water/ice and heat are available [e.g., Rathbun & Squyres, 2002; Abramov et al., 2005; Schwenzer & Kring, 2013]. Thus, the geologic context of hydrated mineral detections must be examined to understand their origins. Through analyses of the origins of detected minerals in craters and their association with impact crater size and morphology, we will be able to construct basic stratigraphies, constrain scenarios for

lowlands-wide evolution, discover region-specific geology that was previously unknown, and unravel the buried record of geologic and aqueous activity within the northern lowlands of Mars.

3 Data and Method

3.1 Study region and CRISM coverage

To better understand the stratigraphic framework of the northern lowlands, we focus on the analysis of spectral data from the CRISM instrument on board MRO, acquired at the instrument's highest spatial sampling. CRISM L-detector targeted images cover the wavelength region from 1 μm to 3.92 μm, which includes electronic transitions of Fe and vibrational absorptions related to OH, H_2O, CO_3, SO_4, and metal-OH. CRISM targeted images cover approximately 10-km-wide areas with a spatial resolution of 15-19 m/pixel for full-resolution images (FRT, FRS) and ~36 m/pixel for half-resolution images (HRL, HRS) [Murchie et al., 2007]. Here we adapt and improve an enhanced noise reduction algorithm (see section 3.2) to examine all the CRISM targeted images in the northern lowlands over any part of an impact crater, including the central structure, crater walls, crater floor, and ejecta blanket. For the purpose of this work, we study all identified impact craters with diameters ≥1km in the northern lowlands with coverage of CRISM targeted L-detector data as of November 2015. We focus on the well-calibrated 1.0-2.6 μm channels from the L-detector because both mafic and hydrated minerals are expressed in the spectral range; in locations with hydrated mineral detections, we examined select S-detector data (covering 0.4-1.0 μm) to search for crystalline iron oxides but did not find them. The region of interest is shown in Figure 1, with the outline of the study region bounded by contour lines along the dichotomy boundary, following Tanaka et al. [2005] and excluding the northern polar cap. A total of 18,293 impact craters ranging in diameter from 1 km to 376 km lie within the proposed study region, documented in Mars' global crater database [Robbins et al., 2011]. Among these, 1,045 craters are covered by 2,257 CRISM targeted images. The craters are distributed across in the northern lowlands from the equator to ~80°N with some biases in targeting (Figure 1). Better CRISM coverage exists closer to the pole due to the higher repeat rate of observations in MRO's polar orbit. CRISM

coverage may vary significantly for different craters since more targets are placed after minerals are detected with CRISM or OMEGA.

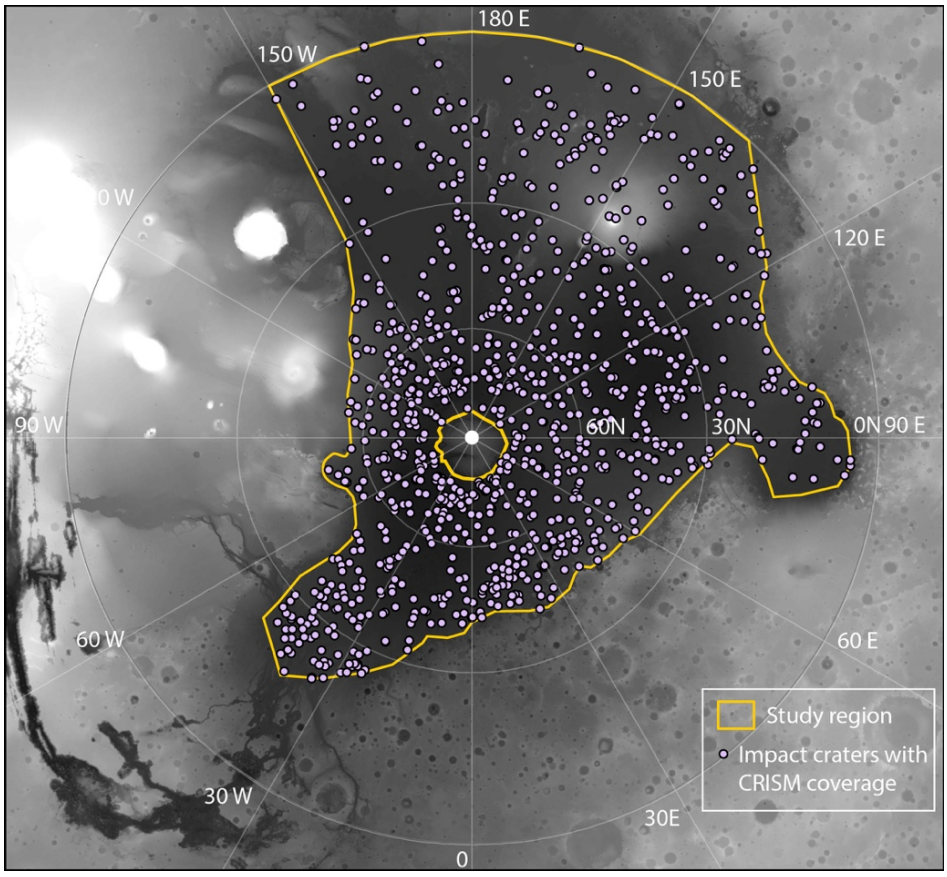

Figure 1. Study region of this investigation, which includes the area encompassed by the boundary of the dichotomy between the northern plains and the southern highlands, excluding the northern polar cap (orange line). Purple dots indicate impact craters with CRISM coverage that meet the requirements of this work: a. With crater diameter over 1 km; b. Located within the study region (outlined here); c. With CRISM L-detector data over any part of the crater, including central structure, rim, floor, and ejecta. Base map is Mars topography data from Mars Orbiter Laser Altimeter (MOLA) in Mars North Polar Stereographic Projection.

3.2 CRISM processing using a noise reduction algorithm

To fully utilize the CRISM dataset in the northern lowlands of Mars, an improved CRISM noise reduction tool has been implemented to facilitate mineral detection, adapted from a previous automated processing pipeline [Carter et al., 2012], using a subset of routines. The detailed workflow is described below (Figure 2):

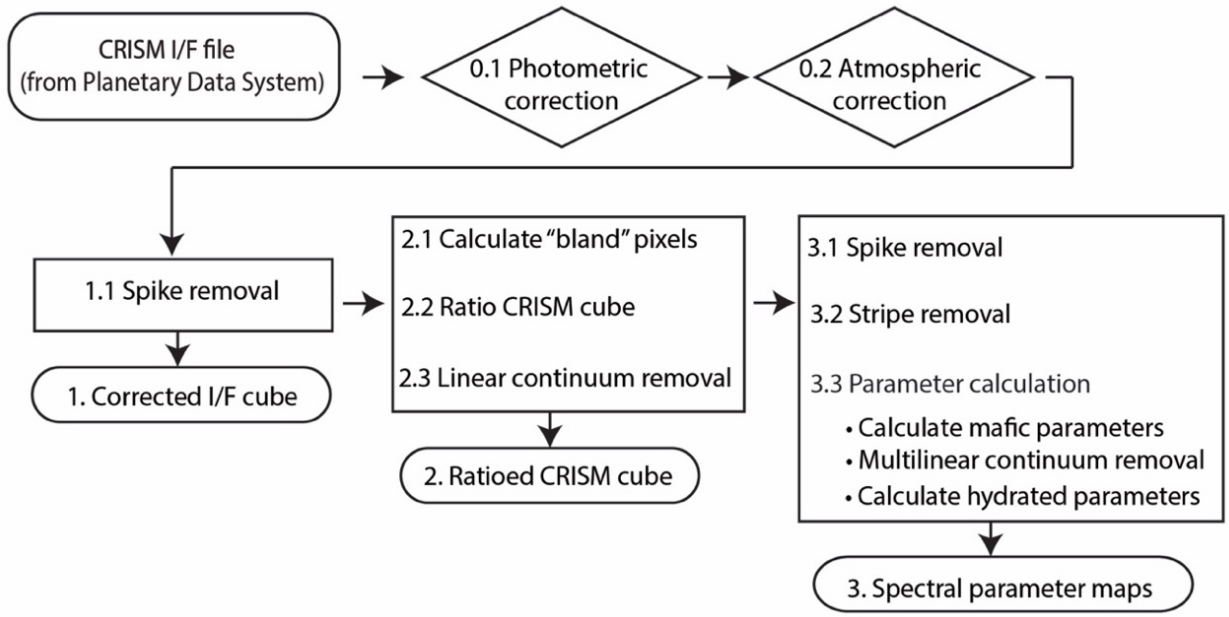

Figure 2. Flow chart and products of the pre-processing algorithm for CRISM data to reduce noise and highlight mineral detections.

- First, CRISM I/F files are downloaded from the Planetary Data System, and we use standard data processing procedures to perform atmospheric correction using volcano-scan method [Mustard et al., 2005] and photometric correction through the CRISM Analysis Toolkit (CAT) [Morgan et al., 2009].
- Then based on the atmospherically and photometrically corrected data cube, we find statistical outliers in spectral dimension in a given image, which are possibly due to the anomalous behavior of the detector (criteria: single channel offset >1.5% of predicted value based on the boxcar average of adjacent 10 channels). We then replace the spurious value with the predicted value from a boxcar average of 30

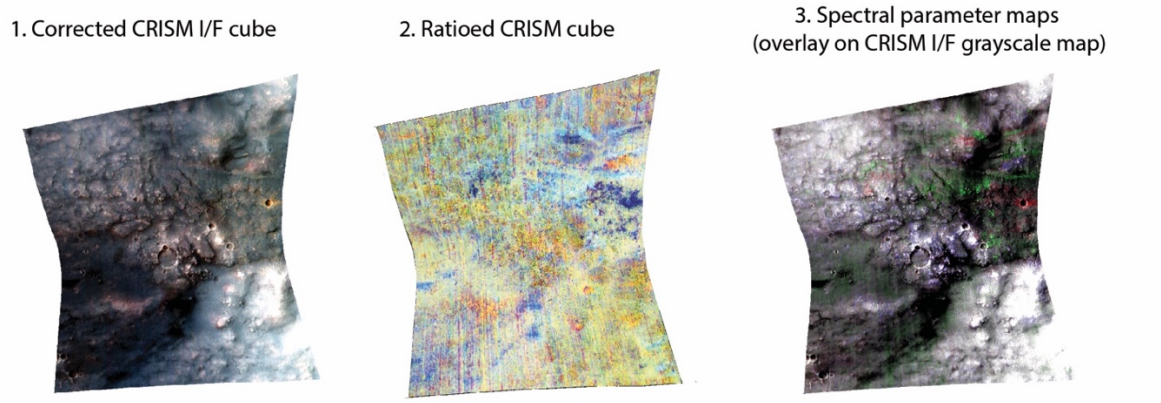

Figure 3. Data products from noise processing algorithm for a CRISM full resolution target IR image (FRT00018AEF_07_IF167L_TRR3) as sample data product form noise processing.

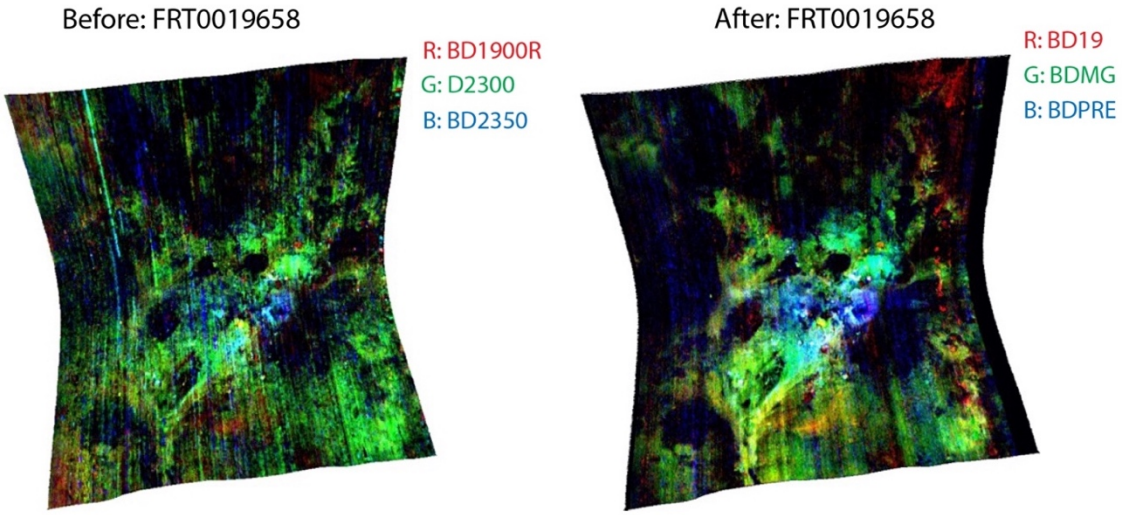

Figure 4. Example denoised parameter map (right) compared to a parameter map calculated from a non-processed CRISM I/F image (FRT0019658) that was simply photometrically and atmospherically corrected using the CRISM Analysis Tool (CAT) (left). Colors represent different spectral parameter outputs in CAT and noise reduction process (Red, Green, and Blue bands represent absorption depths at 1.9, 2.3 and 2.35 μm, respectively, indicative of hydrated minerals, Fe/Mg phyllosilicates or carbonates, and prehnite or chlorite, respectively).

adjacent channels in the spectral domain. This limits the effect of spectral spikes for later processing. This selection threshold is set so that only features with unreasonable reflectance values and single-channel spikes are selected so as to avoid over-correcting for spectral absorption features. The product of these steps is the “corrected I/F cube” product (Figure 3.1).

- Afterwards, several spectral parameters characteristic of particular mineral spectral features are computed (After Pelkey et al. [2007] and Carter et al. [2012]). Then, instead of the conventional method of handpicking in-scene denominator spectra to calculate spectral ratios for areas with strong parameter values, an algorithm automatically identifies the pixels within the same image below a threshold value (median+1.5 σ) for several spectral parameters [as benchmarked in Carter et al., 2012]. We then create column-specific "bland" spectra for the scene using the median of the selected pixels in each column. For columns with no “bland” pixel, the median spectrum of the entire column is used as denominator. This step removes most instrument artifacts and atmospheric residuals. After computing scene-derived denominator spectra, this algorithm calculates the ratio of the entire scene, which accentuates all the possible mineral detections relative to the spectrally bland regions in the same image. Each pixel in the scene is then normalized to a linear continuum based on the corrected I/F values at 1.76 and 2.14 μm, wavelengths chosen because few minerals relevant to Mars have absorptions at these wavelengths. With this normalization and continuum removal method, the effect of reflectance and illumination geometry on the spectral ratio is minimized in the “ratioed CRISM cube” (Figure 3.2), which is used for the quick-identification of spectra of regions of interest.
- To produce an improved parameter map, using more aggressive noise filtering that could influence spectral shape, we first apply empirical methods of additional despiking and destriping to the ratioed CRISM cube. As in the previous despiking step, we find statistical outliers in the spectral dimension and replace with the value of with a 30-channel boxcar average in the spectral domain. (criteria: single channel offset over 1% of predicted reflectance value based on 10 channel average) We then calculate a weighted mean corrected I/F spectrum for each image column to

construct a striping profile across detector pixels. The columns are normalized by the average value of the entire column (calculated as the mean of the median spectrum of the upper, middle and lower one third of the column) to remove the stripes in the along-track direction.

- Then, spectral parameters are calculated to emphasize the band depth (*bd*) of different wavelengths based on I/F value of the band of interest (R_{band}) and the calculated I/F value of the continuum ($R_{continuum}$):

  $$bd = 1 - \frac{R_{band}}{R_{continuum}} \quad (1)$$ [Clark and Roush, 1984]

  The band depths of absorption features of typical minerals previously found on Mars are calculated with band centers chosen to represent different chemistries in hydrated minerals (e.g., 2.29 μm for Fe-smectite; 2.31 μm for Mg phyllosilicate; 2.21 μm for Al-phyllosilicate). For hydrated minerals, instead of the usual spectral parameter maps calculated directly from the I/F cube (e.g. Viviano-Beck, 2014), we compute and examine the band depth map using the despiked and destriped ratioed CRISM cube because absorption features for hydrated minerals are accentuated and isolated from overall continuum effects (Figure 3.3). The result, the new "spectral parameter map" (Figure 3.3), is used to aid the quick identification of mineral absorption features in a hyperspectral cube.

Our tests and previous benchmarks on the northern lowlands images show that the application of the algorithm was successful in reducing noise and providing more details in spectral parameter maps (Figure 4) to further aid geologic interpretation. Limitations are understood as a result of vetting with sample images. Potential issues observed with the algorithm include a) if 2 or more adjacent channels are behaving irregularly, they will not be corrected in the despike step, a conservative choice made so as to avoid altering bands due to real mineral absorption; b) mafic absorption features can be inverted by the ratioing step in images where a mafic signature is ubiquitous; and c) absorptions present that are not considered a priori become part of the "bland" pixels used in the ratio denominator, and thus the absorptions are weakened or removed in the ratio product. Therefore, when applying this algorithm, we use the heavily processed cubes only for parameter mapping to highlight areas of interest. The ratio cubes are used for fast-evaluation of spectra and are

then compared with the original I/F spectra for validation of detections. The denoising algorithm reduces noise in the spectral domain for the northern lowlands dataset and enables fast identification of mineralogically interesting areas, subject to the limitations above. We use this processing in mineral identification.

3.3 Mineralogy analyses

In this study we processed all the CRISM targeted images in the study area covering impact craters greater than 1 km in diameter (Figure 1), using the processing procedure described above. Then all the parameter maps were examined, and the spectra of regions highlighted by parameter maps were confirmed in the ratioed cubes as well as in the I/F cubes. We recorded the detections of different mineral phases (including olivine, pyroxene, Fe/Mg phyllosilicates (smectites), hydrated silica, chlorite/prehnite, sulfate, some minor hydrated minerals, and unidentified hydrated minerals), according to their spectral characteristics and documented where they occur (central peak, crater walls, floor, or ejecta). These detections are based on reference to terrestrial spectral library [e.g., Clark et al., 2007] and prior CRISM works [e.g., Bishop et al., 2008; Ehlmann et al., 2009; Roach et al., 2010]. We also find a few hydrated materials with absorption combinations that do not belong to the above categories or do not have a good match in the spectral library (See Results: mineralogy). Detections with absorption bands that are hardly distinguishable from the noise or less certain due to the effect of dust cover or coatings on the spectral continuum are noted as "maybe" detections. Minerals detected in dark dunes, which commonly occur on crater floors or within ejecta, are not counted because these are unrelated to the local stratigraphy and rocks influenced by impact. Craters north of 40-50°N are sometimes found with spectral features of H_2O ice or CO_2 ice, which may mask some of the bedrock mineralogy. Detections (or "maybe" detections) are reported when minerals are present. Non-detection does not, however, imply absence, so our detections signify a lower bound on the prevalence of mafic and hydrated minerals in the northern lowlands.

3.4 Statistical analyses of crater detection results

To analyze the influence of crater size, dust cover, and modification, we fit a logistic regression function, *f(x),* to the mafic and hydrated mineral detections in association with one or more crater morphology parameters (*x*) (e.g., crater diameter). For example, based on the ideal excavation model, small craters with excavation depths smaller than the minimum depth of the mineral-bearing strata (x_0) will not show detection of this mineralogy (*f(x)*~0) while large craters will (*f(x)* ~1). The relationship can be expressed as:

$$f(x) = \frac{1}{1+e^{x-x_0}} \quad (2)$$

The significance of the fit shows the influence of crater diameter (or other morphologic parameters) on the outcome of mineral detection (Section 4.3.1&4.3.5).

We also delineate the northern lowlands into 8 different geological provinces and perform a Mann-Whitney U-test comparing frequencies of the mafic/hydrated mineral detections by geological province, which highlights regional differences in crater-associated mineralogy (Section 4.3.2).

4 Results

4.1 Northern lowlands impact crater demographics and mineral occurrence statistics

We analyzed 2257 images with CRISM L-detector data using the noise-reduction method, covering the central peak, crater wall, crater floor and/or ejecta blanket of 1045 impact craters in the northern lowlands. The diameters of these impact craters range from 1 to 220 km (Figure 5). Mineral detections, categorized into mafic and hydrated minerals, are widespread in the northern lowlands, though there is considerable spatial variability in occurrence not solely related to image availability (Figure 6). Here an occurrence is defined as a geological unit with a specific mineral detection in an image, e.g. several regions on the crater wall with the same mineralogy are documented as one occurrence, and each image may have more than one occurrence of each mineral. In total, 251 craters (~24%) are found with 722 occurrences of mafic minerals and 81 craters (~8%) are found with 300 occurrences of hydrated minerals, including the probable detections with less certainty ("maybe" detections; section 3.3) (Figure 6,7). Observed mineralogy varies with crater size.

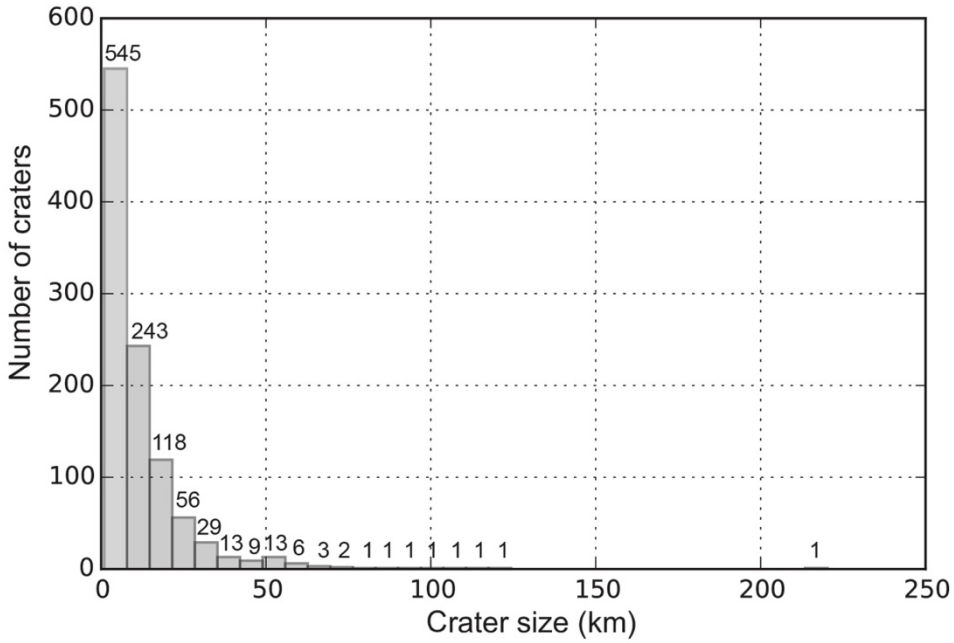

Figure 5. Size-frequency diagram for northern plains impact craters investigated in this study. The number of craters within each bin is labeled on the top of the bar.

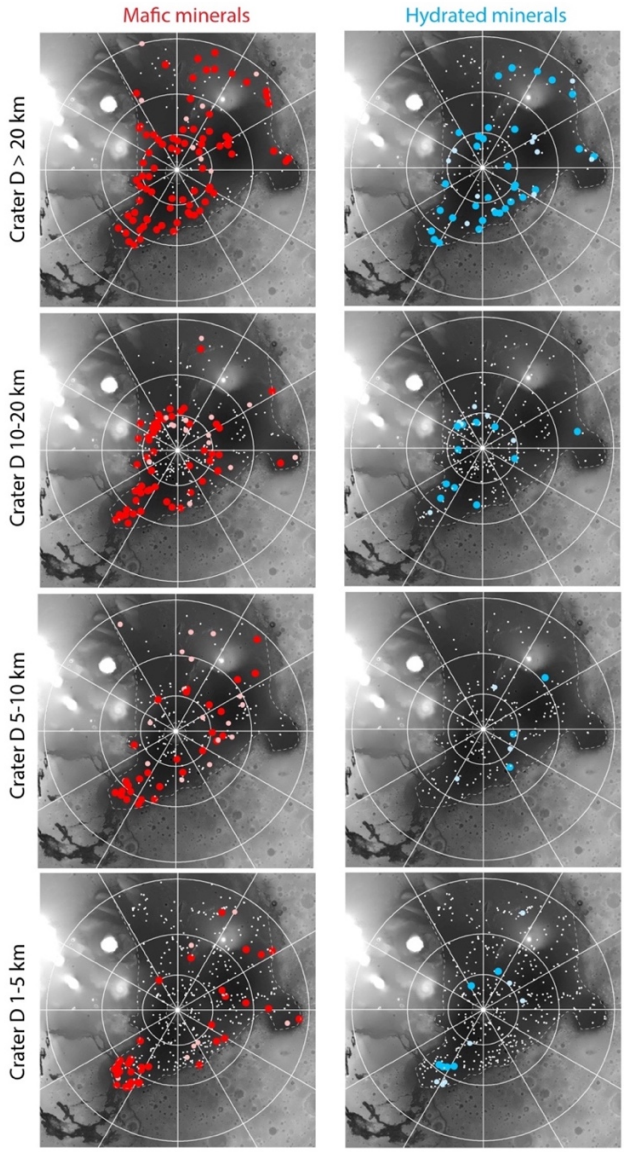

Figure 6. Distribution for all northern plains mafic and hydrated mineral detection binned by crater size. Lighter colored dots (pink, light blue) indicate craters where only absorption with less certainty ("maybe" detections) is found. Small white dots represent impact craters in the same size bin without detections. The maps showing the northern hemisphere with MOLA data as the base map in Mars North Polar Stereographic Projection.

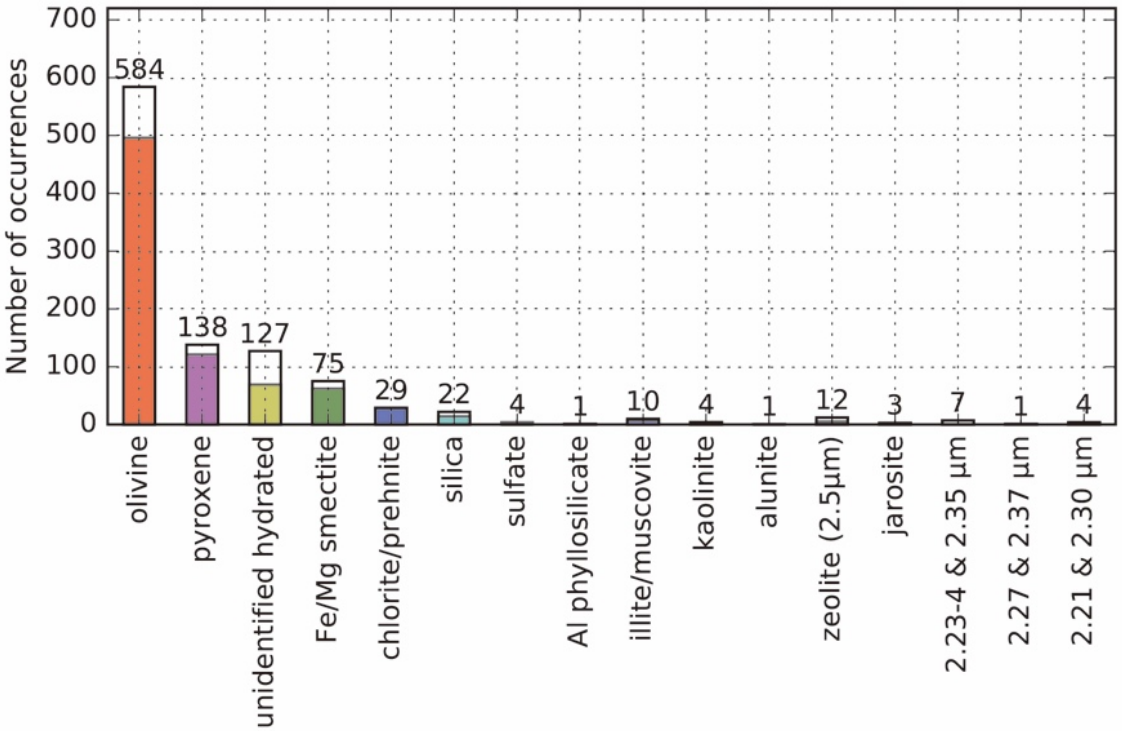

Figure 7. Histogram of major categories of mineral occurrences in northern plains impact craters (An occurrence counts for detection in a certain geological unit within a CRISM image). White color represents detections that are probable but lack certain features ("maybe"). The total number of occurrences (including "maybe" detections) of each mineral or spectral class is given on top of the column.

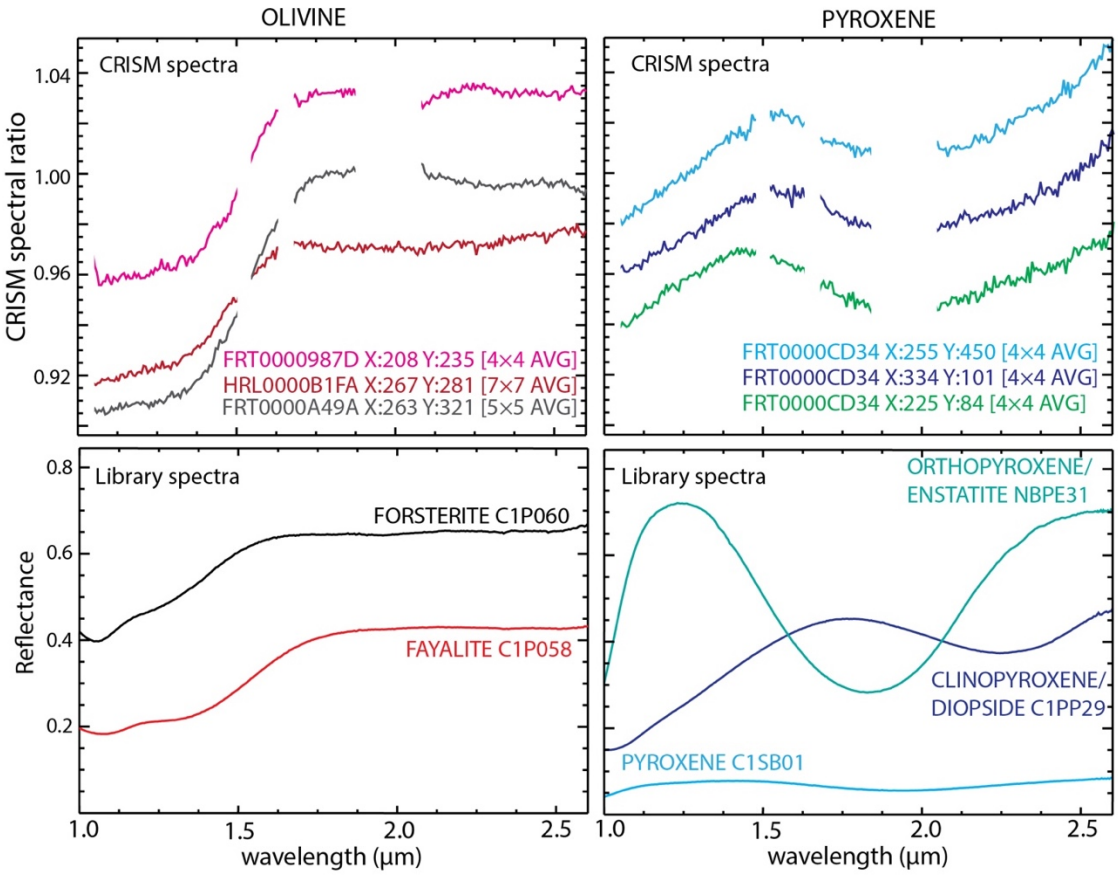

Figure 8. Laboratory reflectance spectra and CRISM ratioed spectra showing mafic minerals in the northern plains. Upper panels show example spectra extracted from CRISM images in the northern plains; lower panels show library spectra of olivine and pyroxene.

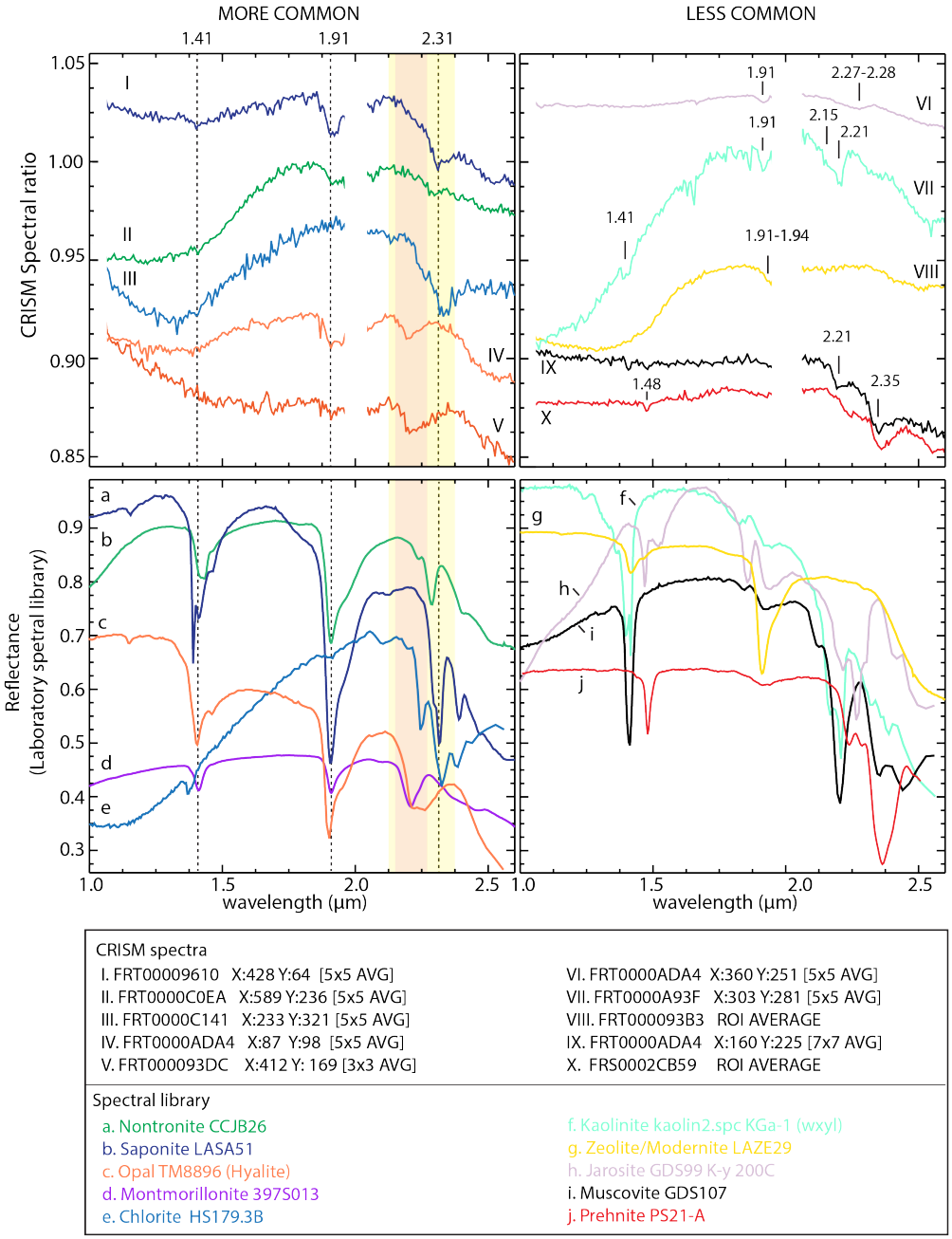

Figure 9. CRISM and laboratory reflectance spectra (From USGS spectral library [Clark et al., 2007] and the CRISM spectral library) showing hydrated silicate mineral diversity in the northern plains. Upper panels show example spectra extracted from CRISM images in the northern plains. Left: Fe/Mg phyllosilicates (I-II), chlorite (III), hydrated silica (IV-V). Dashed lines are placed at 1.41, 1.91 and 2.31 μm. Shaded bars show the different 2.2-μm band width in library spectra of montmorillonite and hydrated silica. Right: Detections

of other (less common) hydrated minerals in the northern plains including the hydrated unidentified category. Lower panels show library spectra of minerals with similar absorption features.

Both mafic minerals and hydrated minerals are identified in craters larger than 20 km distributed throughout the northern lowlands; for craters between 5-10 km and craters smaller than 5 km, mafic detections are still relatively widespread while hydrated minerals are restricted to localized regions (Figure 6). In the following text, we discuss in detail the spectral characteristics and criteria for mineral detection, the distribution of each mineral, the correlation between crater size and mineralogy, and the geographic distribution of mafic and hydrated materials throughout the northern lowlands, as well as other influencing factors including dust cover and crater modification.

4.2 Mineral identifications and spectral characteristics

4.2.1 Mafic minerals: Olivine and pyroxene

Mafic minerals are widespread in 24% of craters of different sizes, including 594 occurrences of olivine in 246 craters and 138 occurrences of pyroxene in 69 craters (Figure 7). These minerals have been identified with processed CRISM L-data from absorptions due to electronic crystal field transitions of Fe [Burns, 1970]. Olivines [$(Mg, Fe)_2SiO_4$] have a broad absorption centered at 1 μm that varies according to Fe content (Figure 4a) [Sunshine and Pieters, 1998]. Pyroxenes [$(Ca, Fe, Mg)_2Si_2O_6$] are identified by two broad absorptions around 1 and 2 μm, where the band centers shift to longer wavelengths with increasing calcium and iron content (Figure 8) [Hazen et al., 1978]. Only detections with the presence of strong Fe absorption features and the absence of other vibrational features from hydrated minerals are counted in the mafic mineral category. In this study, we do not distinguish the detailed chemistry of mafic minerals but rather focus on the geographic and depth distribution of the detections.

4.2.2 Hydrated/hydroxylated minerals

A wide range of hydrated/hydroxylated minerals has been identified in the survey in 8% of the craters (Figure 7, 9). Fe/Mg phyllosilicates (likely smectites or mixed-layered clays; 75 occurrences found in 32% of all craters with any hydrated mineral occurrences),

chlorite or prehnite (29 occurrences in 11% of the craters), and hydrated silica (22 occurrences in 17% of the craters) are the most abundant hydrated minerals that can be distinguished using spectral properties. Among the rest, kaolinite, illite or muscovite, other Al-phyllosilicates, and possible zeolites with a 2.5 μm absorption are found with 1-12 occurrences in 1-12% of craters but some of these detections with less certainty. Spectra with 1.9-μm absorption feature due to H_2O but lacking in other diagnostic absorptions constitute a significant fraction of mineral detections (with 127 occurrences). These are identified in 74% of all craters with any hydrated mineral detection and characterized as "unidentified hydrated" minerals. Each mineral class of detection is detailed below.

4.2.2.1 Fe/Mg phyllosilicates

Fe/Mg phyllosilicates – we use the term to refer to smectites and mixed-layer clay minerals but not chlorite – are identified using 1.39-1.41, 1.91, and 2.29-2.31 μm absorptions due to H_2O overtones and combination modes as well as a Fe/Mg-OH stretching mode (Figure 9). For Fe/Mg smectites, the centers of absorption features shift due to variation in Fe or Mg as cations in the phyllosilicates: 1.41 and 2.31 μm for Mg-OH and 1.39 and 2.28-2.29 μm for Fe-OH absorptions [Clark, 1999; Bishop et al., 2002], sometimes accompanied by weaker 2.4 and 2.5 μm absorption features. In Martian spectra, some 1.41 μm absorption features are weak or absent, which could be a result of an alteration rind or coating.

As with other studies, we find Fe/Mg phyllosilicates are the most abundant identifiable hydrated mineral [Ehlmann et al., 2011, Carter et al., 2013]. In the northern lowlands, they are found in 75 occurrences in 26 impact craters with diameters ranging from 5.3 km to 220 km (Figure 10a). These phyllosilicates are found in all the major basins except Isidis Basin, where the CRISM coverage is less complete. Fe/Mg phyllosilicates in the northern lowlands show some variability in absorption band centers and shapes. For example, the 2.3 μm absorption band shifts from ~2.28 μm for Fe-rich phyllosilicates to ~2.31 μm for Mg-rich phyllosilicates (Figure 9 spectra I-II).

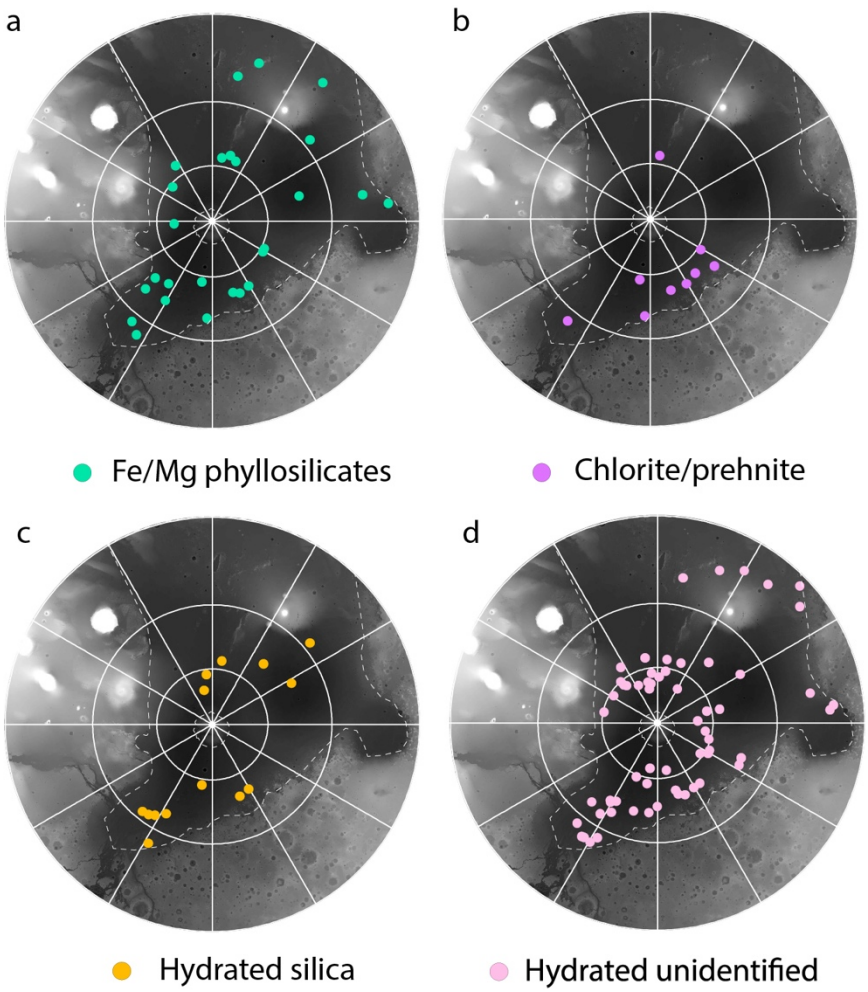

Figure 10. Northern plains hydrated mineral detection map for a) Fe/Mg phyllosilicates (exclusive of chlorite), b) chlorite/prehnite, c) hydrated silica, and d) unidentified hydrated minerals. Each dot represents a location of the center of an impact crater with at least one mineral detection. The base maps show the MOLA topography data of the northern hemisphere in Mars North Polar Stereographic Projection.

4.2.2.2 Chlorite and prehnite

Chlorite is a 2:1:1 phyllosilicate with a prominent 2.35 μm absorption due to Mg-OH combination tone and typically weaker or absent 1.9 μm absorption, sometimes accompanied by a 2.25-2.26 μm Al,Fe-OH or Al,Mg-OH stretching absorption [Bishop et al., 2008] (Figure 9 spectra III, e). It has distinctive spectral properties from other Fe/Mg phyllosilicates and thus can be discriminated. Prehnite is a Ca, Al-bearing inosilicate that is often associated with hydrothermal or low-grade metamorphic alteration on Earth. It is spectrally similar to chlorite, except with a sharp 1.48 μm absorption in addition to the 2.35 μm absorption. We found 29 occurrences with chlorite and/or prehnite detections in 9 northern lowlands craters (Figure 10b). The locations of these detections are limited to Chryse/Acidalia Planitiae, in the vicinity of Lyot crater (the largest fresh crater in the northern lowlands), and in Stokes crater. Chlorite/prehnite detections are often found to coexist with Fe/Mg smectites, and sometimes they appear in mixture with Fe/Mg smectite and form a wider absorption from 2.31 to 2.35 μm as well as deeper 1.9 and 1.4 μm absorption features. Due to the spectral similarity with chlorite, prehnite may be present but it is difficult to distinguish from chlorite with the quality of the orbital data and the concentration of the phases. In the northern lowlands, the additional 1.48 μm absorption clearly diagnostic of prehnite is observed in two occurrences, both on the outer rim of Lyot Crater [as first reported in Carter et al., 2010].

4.2.2.3 Hydrated silica

Hydrated silica has been identified in 14 craters in the northern lowlands (Figure 10c). Hydrated silica is recognized with a broad absorption feature at 2.2 μm as well as 1.9 and 1.4 μm features. The broad feature at 2.2 μm is caused by 2 types of surface hydroxyl groups [Anderson and Wickersheim, 1964]. Different types of hydrated silica (including opal-A, opal-CT, opal-AG, cristobalite, micro-quartz, chalcedony, etc.) have varying relative strengths of 2.21 and 2.26 μm bands and slightly shifting band centers between 1.39-1.41 μm due to the relative amount of water and the bonding state of OH to Si in the mineral [Milliken et al., 2008; Rice et al., 2013; Smith et al, 2013]. Hydrated silica shares a similar spectral feature with Al-phyllosilicate (e.g. montmorillonite etc.) in that both Al-OH and Si-OH vibrations cause absorptions around 2.21 μm. Hydrated silica, in general,

has a wider absorption at 2.2 μm than Al-phyllosilicate. However, in a few locations in the northern lowlands (including Stokes crater), the 2.2 μm absorptions are narrower than a typical 2.2 μm Si-OH absorption, yet wider than the Al-OH vibrational absorption (Figure 9). These are classified as hydrated silica due to the similarity in spectral continuum and shape of absorption.

Hydrated silica is less widespread than Fe/Mg phyllosilicates. They are found in relatively higher latitudes near Lyot crater, in Elysium Planitia, and in the Scandia region near Stokes crater, except for 4, lower-latitude clustered small craters in southern Acidalia Planitia (Fig 10c), with sizes range from 1 to 2.5 km. These hydrated silica detections are found on crater central peak, crater floor, crater walls and ejecta blanket. Within the northern lowlands, there are also hydrated silica detections, identified previously but not associated with craters: in the knobby terrains of Acidalia Planitia [Pan and Ehlmann, 2014] and in some of the cones and polygonal troughs in Utopia Planitia [Carter et al., 2013]. These cases probably represent materials younger than the Fe/Mg phyllosilicates and may not be genetically related to the ancient basement that is excavated by craters.

4.2.2.4 Unidentified hydrated minerals

Another major category of hydrated mineral detections, in fact the most common category (found in 74% of all craters with any hydrated mineral occurrences), show the 1.9 μm absorption, a combination tone of H_2O due to a vibrational absorption, but do not have distinguishable features from 2.1-2.5 μm and have been categorized as "unidentified hydrated" in the mineralogy survey (Figure 11). The absence of diagnostic absorption features could be due to the nature of the materials, e.g., that they are hydrated salts or zeolites. In contrast to unidentified hydrated materials in the southern highlands, a 1.4 μm absorption, also due to combination tones of H_2O, is not apparent in the northern lowlands spectra. Observational factors such as surface coatings, dust mixing, low signal-to-noise ratio, and/or influence of aerosol or surface ice on CRISM spectra may confound detections of 1.4 or 2.1-2.5 μm absorptions, which are often weaker on Mars compared to laboratory spectra of terrestrial analogs. The spatial distribution of the unidentified hydrated minerals generally overlaps that of Fe/Mg phyllosilicates and does not show particular clustering in the northern lowlands (Figure 10d).

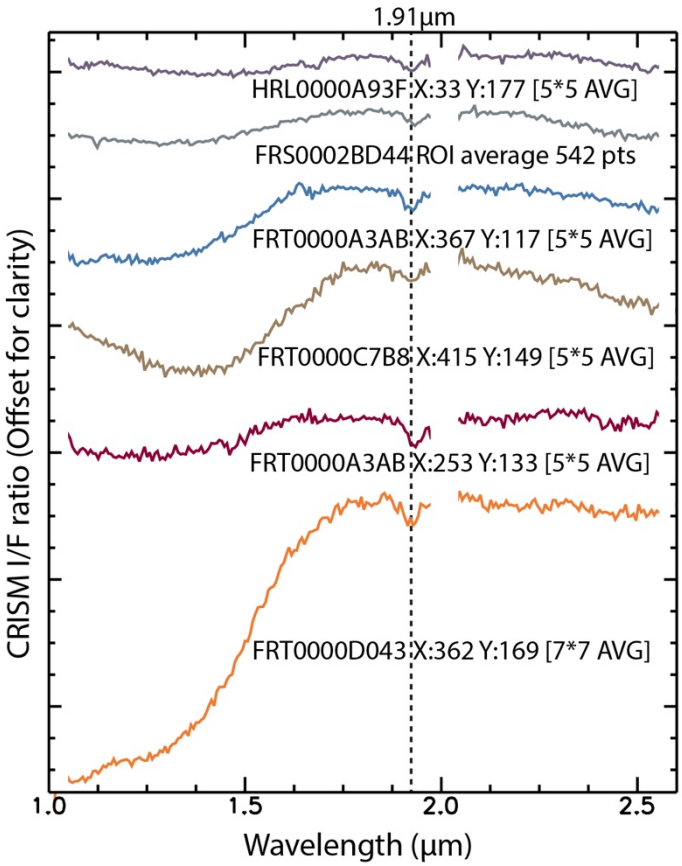

Figure 11. CRISM spectral ratio of unidentified hydrated minerals (labeled with CRISM image ID and the location/area of the region where spectra are taken from).

4.2.2.5 Minor hydrated/hydroxylated species

There are other less common species found localized to a small number of craters within the northern lowlands. These spectra show absorption bands at 1.9 µm and between 2.1-2.5 µm. These spectra include possible Al-phyllosilicate with a 2.21 µm absorption, jarosite with a weak 2.27 µm absorption; illite or muscovite with absorption bands at 2.19-2.21 µm and 2.35 µm; kaolinite with a doublet at 2.15 and 2.21 µm; possible alunite with absorption at 2.17 µm; and possible zeolite detections with features at 2.5 µm, which may also be found in sulfate or carbonate (Figure 9). The small areas (small number of pixels)

of these spectral classes hinder our ability to make further distinctions, but these spectral classes indicate geographical variations and mineral diversity in some northern lowlands localities. For example, illite/muscovite detections are only found in multiple locations at Lyot and Stokes crater. Kaolinite has only one occurrence in Stokes crater (Supplementary Materials Table 1).

4.2.2.6 Mixtures of hydrated/hydroxylated minerals

In some locations, additional bands at 2.19-2.21 μm, 2.26-2.27 μm, and 2.48-2.51 μm have been observed in addition to the 2.3 μm or 2.35 μm absorptions of Fe/Mg-OH. The combination of the spectral features cannot be matched to a specific mineralogy but may be caused by mixtures of different hydrated minerals. Three typical mixtures observed in the survey have absorption bands at 2.23-4 and 2.35 μm; 2.27 and 2.37 μm; as well as 2.21 and 2.31 μm. The combination of 2.23-4 and 2.35 μm absorptions closely resembles illite/muscovite detections but with wider and longer-wavelength absorption features around 2.23-4 μm than a typical illite/muscovite spectrum with 2.21 μm band, so the mixing of hydrated silica or Al-phyllosilicate with chlorite/prehnite is a more plausible explanation. The 2.27 and 2.37 μm absorption combination may be explained by a sulfate mineral possibly mixed with chlorite or prehnite. The combination of 2.21 and 2.31 μm does not have a good spectral match for a specific mineral either, but can be explained by the co-existence of Al- and Fe/Mg phyllosilicates. These mixtures are primarily found in Lyot crater and other smaller craters in its vicinity, Stokes crater, and one other crater east of Elysium Mons (Supplementary Materials Table 1).

4.3 Crater size, geographical distribution and other influencing factors for CRISM detection

4.3.1 Mineral detection vs crater size

For craters smaller than 20 km in diameter, the percentage of craters found with at least one occurrence of hydrated/hydroxylated minerals is only 2%, as compared to 15% for mafic minerals. On the other hand, both hydrated minerals (~38%) and mafic minerals (~55%) are not uncommon for craters larger than 40 km (Figure 12a). In evaluating whether the difference in mineral detections is significant, effects of surface obscuration and

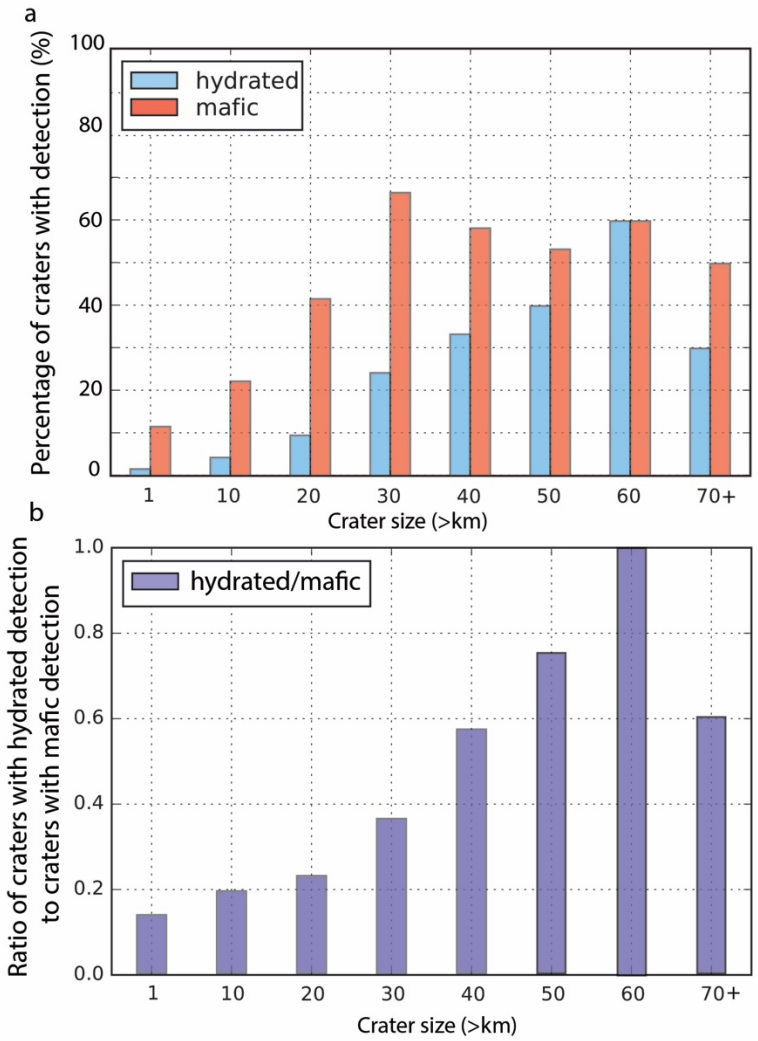

Figure 12. Histogram of impact crater mineral detections across the northern plains as a function of crater diameter. a) The percentage of craters with mineral detections in binned crater sizes; b) The ratio of craters with hydrated detections to mafic detections in binned crater sizes. Crater size is binned in intervals of 10 km diameter and the bins are labeled based on the lower limit. Craters larger than 70 km are grouped into the last bin.

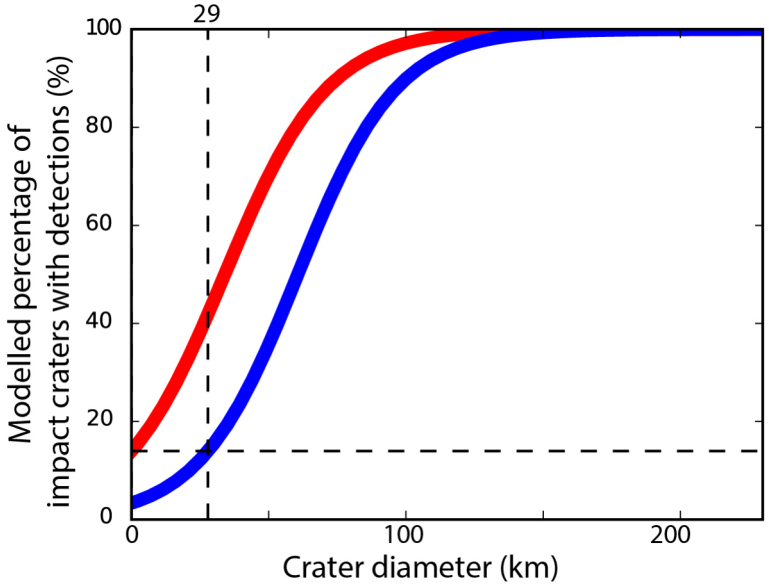

Probability of detection (X = DIAMETER)	Mafic	Hydrated
X=0 km	0.15	0.04
X=10 km	0.22	0.06
X=20 km	0.32	0.09
X=30 km	0.45	0.15
X=50 km	0.58	0.24

Figure 13. Binary logistic function model for the probability of mafic and hydrated mineral detections as a function of crater diameter in the northern plains, based on the best-fit logistic function of the observations. The table shows the predicted probability of detection for craters with different sizes in this model.

Table 1. Mann-Whitney U-test for detections in each geological province compared to the rest of the northern plains. n is the sample size of each geological province. Asterisks indicate provinces where tests are significant at the 95% confidence level.

Mineralogy	**Mafic mineral detection**		**Hydrated mineral detection**	
Geological provinces (n =1045)	**u-stat**	**p-value**	**u-stat**	**p-value**
Acidalia (n=182)	76069.5	0.18	77021.5	0.19
Arcadia (n=85)	34835.0	0.0013*	37357.5	0.0027*
Chryse (n=67)	16091.5	0.00*	30774.0	0.036*
Elysium (n=151)	64221.5	0.098	66084.0	0.19
Isidis (n=19)	9519.0	0.41	9500.0	0.34
Lyot (n=55)	26812.5	0.40	25272.5	0.027*
Scandia (n=257)	99026.5	0.24	99649.0	0.20
Utopia (n=228)	85424.0	0.048*	91219.0	0.15

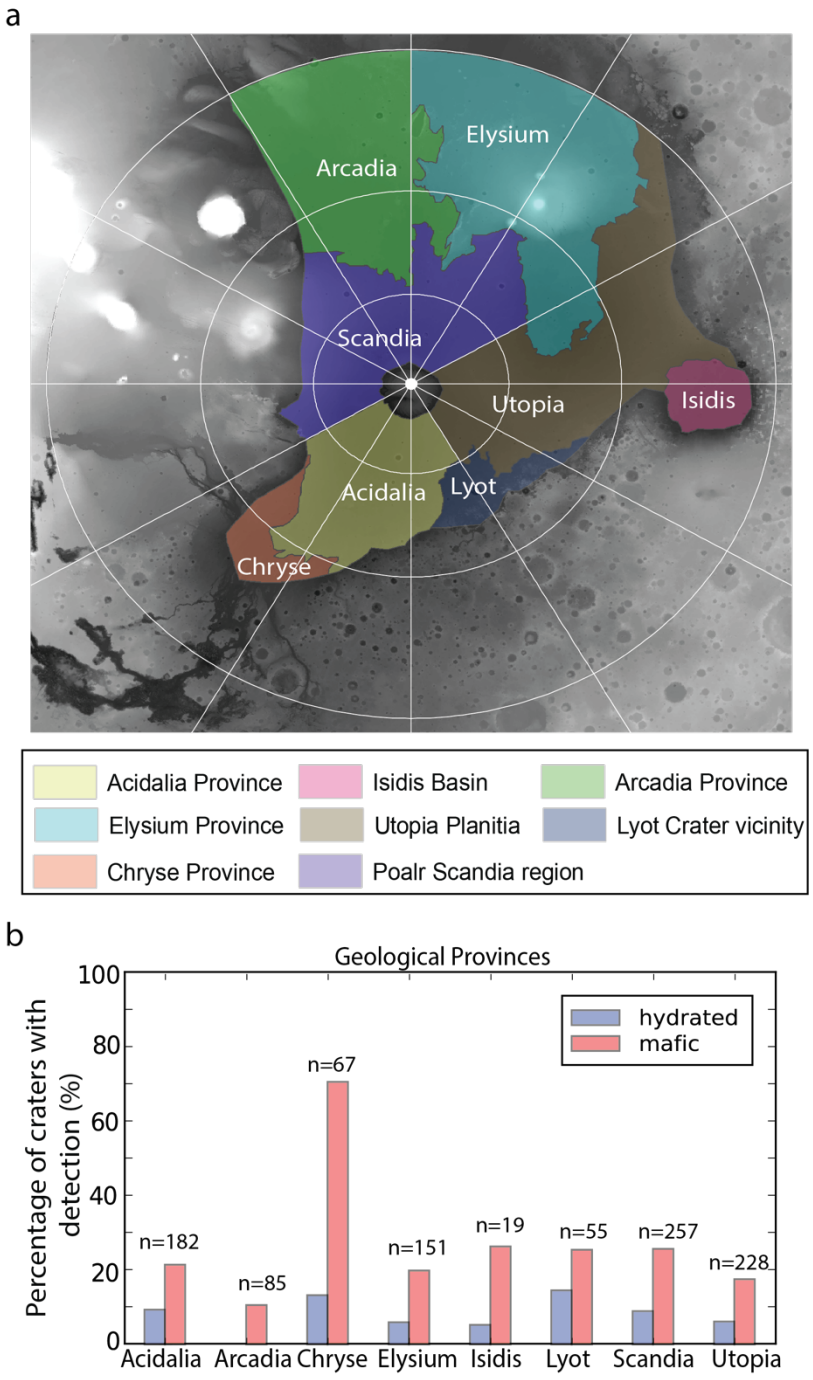

Figure 14. a) Geological provinces in the northern plains delineated according to Tanaka et al., [2005]. b) Comparison of different geological provinces on the percentage of craters with detection of mafic and hydrated minerals, with the total number of craters (n) in each geological province. The base maps are the MOLA topography data of the northern hemisphere in Mars North Polar Stereographic Projection.

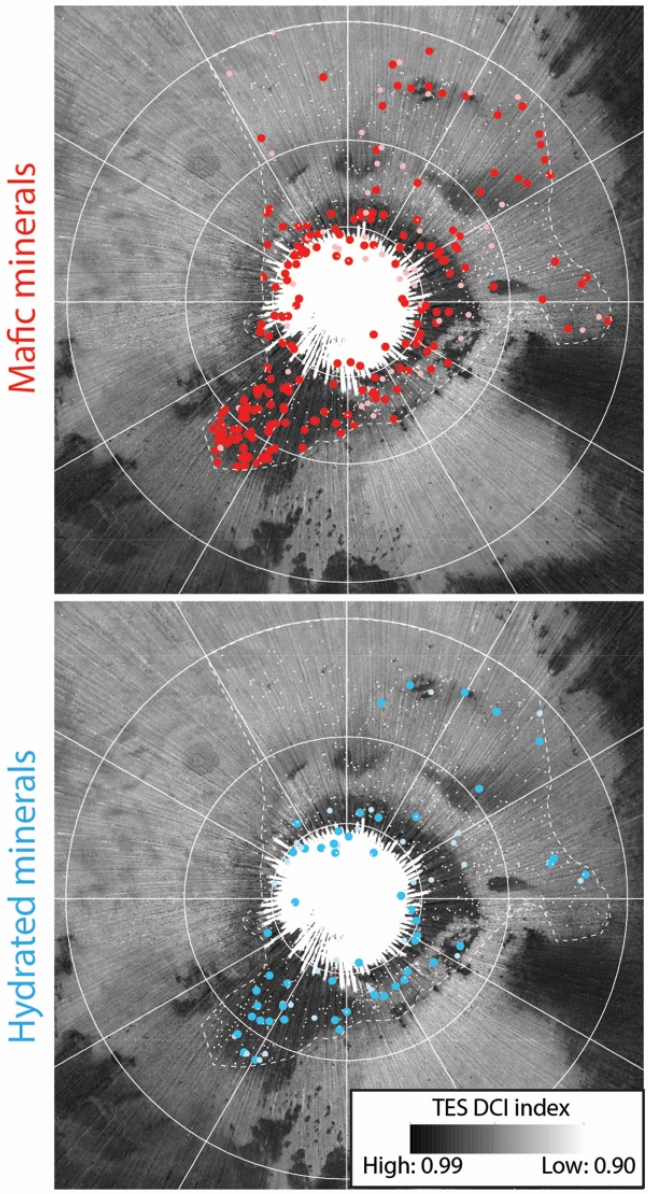

Figure 15. Mineral detections on a TES global dust index map with high dust cover in bright shades and low dust cover in dark shades. (Note that the formulation of dust cover index (DCI) is such that high DCI indicates less dusty and low DCI means dustier.) The base map is TES global dust cover index map of the northern hemisphere of Mars, in Mars North Polar Stereographic Projection.

differences in coverage can be accounted for, approximately, by ratioing the number of hydrated detections to mafic detections (Figure 12b). Though comparing the detection rate for mafic and hydrated minerals, the mafic detections are made in a more conservative way since mixture with mafic mineral is not counted. The increasing trend in the ratio of hydrated detections over mafic detections with increasing crater size implies that hydrated mineral detections are indeed more dependent on crater size.

The correlation between the percentage of craters with mineral occurrence and crater diameter (D) for both mafic and hydrated minerals can be fitted to a logistic function (see Section 3.4) at a 99% confidence level. In the best-fit logistic function (Figure 13), the fitted probability of detection is p=0.15 for mafic mineral detection and p=0.03 for hydrated mineral detection for the smallest crater size in the sample (D=1 km). The probability of making a hydrated mineral detection only reaches the same level (p=0.15) for a crater size of 29 km. Both mafic and hydrated minerals have higher probability of detection in larger craters; however, compared to hydrated minerals, mafic detections are less dependent on crater size. The fact that hydrated minerals are more likely to be found in large craters can be explained by a deeper origin for hydrated minerals, by a scenario in which alteration occurred due to impact-induced hydrothermal activity, or a combination of the two (see section 5.2).

4.3.2 Geographic distribution of mineralogy in the northern lowlands

To determine any region-specific processes and the related mineralogy, the northern lowlands were subdivided into 8 major geologic provinces: Acidalia, Chryse, Lyot vicinity, Isidis, Utopia, Elysium, Arcadia, and Scandia region (Figure 14a). The geological boundaries follow previous geological mapping of the northern lowlands [Tanaka et al., 2005] with the "Borealis Province" subdivided into Acidalia, Utopia, and Scandia regions at longitude 30°E and 270°E. The number of craters with detections of mafic and hydrated minerals is then compared to the total number of craters surveyed within that geological province (Figure 14b).

On average ~20-26% of craters show mafic detections and 5-10% show hydrated mineral detections in most of the geologic provinces. In Chryse Planitia, however, 71% of craters show mafic mineral detections, significantly higher than the rest of the northern

lowlands. For hydrated detections, both Chryse Planitia and the vicinity of Lyot show a slightly higher percentage of hydrated mineral detections than the average northern lowlands. On the contrary, Arcadia Planitia has a paucity of mineral detections for both mafic and hydrated minerals. Mafic mineral detections within Chryse Planitia (+), Arcadia Planitia (-), and Utopia Planitia (-) are statistically different from the detections in the rest of the northern lowlands at the 95% confidence level from a Mann-Whitney U test (Table 1) ("+/-" referring to more/less than average) (Figure 14). Hydrated mineral detections within Arcadia Planitia (-), Chryse Planitia (+) and Lyot vicinity (+) are statistically distinct at the 95% confidence level (Table 1). The differences in mineral occurrences associated with impact craters in these different regions are probably related to distinctive regional geologic histories since dichotomy formation and will be discussed in detail (see section 5.7).

4.3.3 Effect of dust cover on CRISM detections

To better understand how the mineralogy detected by shortwave infrared data correlates with dust cover, we show the mineralogy detections plotted on a dust cover index map (DCI) derived from Thermal Emission Spectrometer (TES) data (Figure 15) [Ruff et al., 2002] as well as the percentage of detections plotted against binned dust cover index (Figure 16). There is a strong negative correlation of mineral detections with the TES-determined dust cover, which confirms that our detections are concentrated in the more "dust-free" regions (Figure 15). Mineral detections are more prevalent where there is less dust cover relative to the sampled population of craters (Figure 16), except for the last few bins where sample size is small. This correlation implies obscuration of mineral signatures in high dust cover locations, which indicates the mafic and hydrated minerals associated with impact craters may be even more widespread than recognized from our analyses.

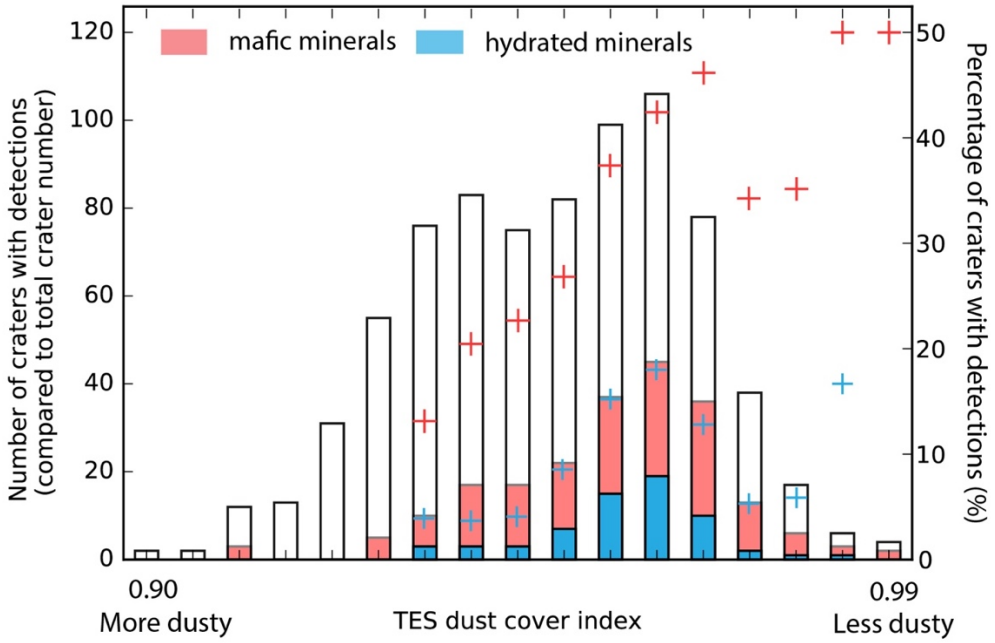

Figure 16. Correlation of mafic and hydrated mineral detections to the TES global dust index. The left axis is for the bar chart showing the number of craters with and without detections as a function of dust index. The right axis shows the percentage of mineral detections in all craters sampled, marked with the red and blue crosses for mafic and hydrated minerals.

4.3.4 Crater modification

Impact craters scattered throughout the northern lowlands have been modified due to erosion of crater rims and ejecta and infill of the crater floor, resulting in subdued crater forms with subtle rims, degraded or buried ejecta, and reduced depth to diameter ratios. Such processes mantle bedrock exposure and can prevent detection of the mineralogy of the impacted bedrock. Degradation state was assessed and recorded in a Mars crater database [Robbins et al., 2011] as a quantized measure from class 1 to 4 ("1" being most degraded), depending on the sharpness and relief of crater rim, ejecta preservation, floor infilling, and relative depth/diameter ratio. We find that the ratio of detections for both mafic and hydrated minerals increases with the preservation state, i.e., less degraded craters have a higher percentage of mineral detections (Figure 17).

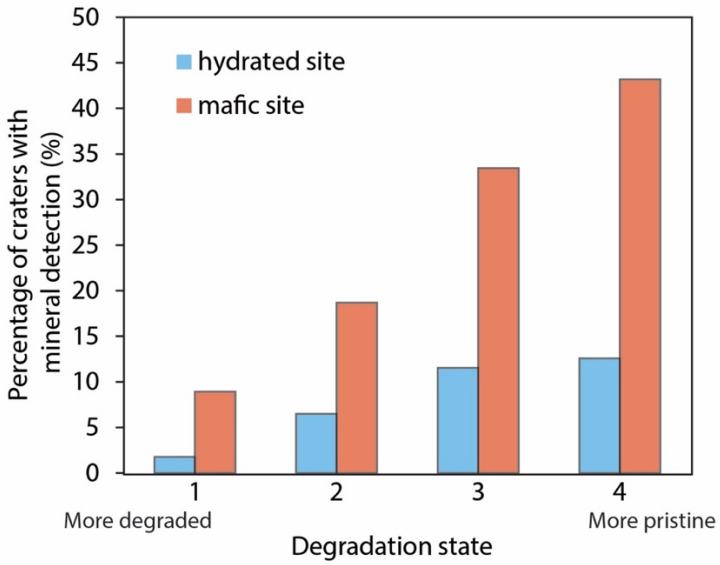

Figure 17. Percentage of craters with mineral detections as a function of the degradation state of craters.

4.3.5 Multivariate statistical significance of different factors

To understand the relative importance of the different factors that affect the mineral detections in the northern lowlands, we performed a multivariate statistical analysis on the mafic and hydrated detections as a function of crater size, dust index and modification using a logistic function fit to evaluate the relative influence of each factor on the probability of detection. We evaluated the data for 487 (out of 1045) observations, filtered to remove craters with missing dust cover index or degradation state. We find that for both mafic and hydrated minerals, all of these factors are important to the identification of a mineral detection with a confidence level of 95%, which confirms that the final detection of a mafic or hydrated mineral is sensitive to dust cover and post-impact modification as well as crater diameter (Table 2).

Table 2. Regression results from a multivariate binary logistic model with the z-stat and p-value of different factors in CRISM survey. Asterisks indicate influencing factors that are important to the number of detections with 95% confidence. (c is a constant needed to fit the regression; it does not have a statistical significance).

Mineralogy	**Mafic mineral detection**		**Hydrated mineral detection**	
Factors	**z-stat**	**p-value**	**z-stat**	**p-value**
Diameter	3.40	0.0007*	5.33	0.0000*
Dust index	5.84	0.0000*	3.84	0.0001*
Degradation state	4.06	0.0000*	1.98	0.0481*
c	-6.19	0.0000	-4.18	0.0000

5 Discussion

5.1 The nature and origin of mafic minerals

As discussed above, subject to factors including dust cover and crater modification, mafic minerals, including olivine and pyroxene, are found in all regions of the northern lowlands associated with impact craters of different sizes. Olivine is more commonly detected than pyroxene (Figure 5). This may be due to stronger olivine absorptions than pyroxenes as observed in southern highlands [Mustard et al., 2005] or the high-pyroxene image background resulting in enhancement of olivine signature in ratioed spectra. Though non-detections of mafic minerals do not mean absence, the commonly occurring olivine detections in the northern lowlands indicate olivine-bearing volcanic rocks are widespread in the subsurface of northern lowlands, confirming the previous identification of olivine-enriched deposits [Ody et al., 2013] and suggest the olivine-bearing volcanic materials in the northern lowlands may be associated with the Early Hesperian floor depostis in the southern highlands and in the vicinity of Valles Marineris. We do not observe impact melt sheets in the northern lowland craters, but they may exist under sediments from later infill. The lack of crystalline mafic minerals on the bulk surface of the northern lowlands [Bibring et al., 2005; Mustard et al., 2005] but widespread detections of mafic minerals associated with the crater settings indicates that the mafic minerals detected are most likely excavated from the subsurface, as suggested for olivine identified in small craters of Acidalia [Salvatore et al., 2010]. The mafic minerals we observe uplifted and exposed by impacts were emplaced before the surface plains with their ages ranging from late Hesperian to Amazonian. The areal extent and the possible age of the mafic units include, but are not limited to, the widespread Hesperian lava flows indicated by wrinkled ridges [Head et al., 2002]. The mafic detections may also be hosted in mafic sediments that were transported by aeolian or fluvial processes, though this is not possible to uniquely discern from orbit. Overall, the mafic mineralogy revealed in the northern lowlands impact craters is consistent with widespread volcanism in the northern hemisphere previously suggested [Head et al., 2002], and implies an extended spatial distribution of this volcanic unit to the polar region and beneath Amazonian-aged smooth terrains. The overall estimates of volume of this volcanic unit is great than that in prior works (see 5.7).

5.2 The nature and origin of hydrated minerals

The survey of the impact craters of the northern lowlands revealed Fe/Mg smectite or mixed-layer clays, chlorite/prehnite and hydrated silica as the most abundant identifiable hydrated phases in the northern plains, based on the number of occurrences (Figure 7), similar to the trends in the relative proportions of major hydrated minerals found in the southern highlands and other large-scale surveys [Ehlmann et al., 2011, Carter et al., 2013; Sun and Milliken, 2015]. In our survey, Fe/Mg smectite is found in 32% of all the 81 craters with hydrated minerals, followed by silica (17%) and chlorite/prehnite (11%). These observations are similar in relative prevalence to a prior global survey of central peaks where they identified Fe/Mg smectite (in ~ 81.9% of all 444 hydrated central peak regions globally), followed by chlorite (26.8%), and hydrated silica (22.6%) [Sun and Milliken, 2015].

Interestingly, unidentified hydrated minerals are found in the majority of craters (~74%) with any hydrated mineral detection, which have been recognized previously but in much smaller proportion of their dataset (found in only 6.8% of the southern highlands central peaks) [Sun and Milliken, 2015]. As discussed in Sun and Milliken [2015], the spectral signatures could be explained by zeolite, sulfate, or other hydrated salts. Poorly crystalline clays or quasi-amorphous materials with weaker metal-OH absorptions at 1.4 and 2.3 μm are other possibilities. H_2O can be added to or removed from many hydrated minerals, including the above, as a function of relative humidity. Thus, the particular spectral character in the north may be due to enhanced hydration (colder temperatures raising relative humidity, nearer ice table), resulting in a stronger 1.9 μm absorption with other weaker H_2O and metal-OH absorptions absent due to mixing, dust cover, or low signal to noise.

As with mafic minerals, the hydrated minerals found in large craters could be excavated from the subsurface. They could also form post-impact via hydrothermal systems, deposition in aqueous environments, or fluvial or aeolian transport from elsewhere. The strong correlation of hydrated minerals and large craters indicates that the formation or exposure mechanism for the majority of hydrated detections involves the energy of the impact directly. Among the 81 craters we identify here with possible hydrated/hydroxylated minerals, we find morphological evidences that indicate excavation

processes related to the mineralogy, including juxtaposed mafic and hydrated minerals in the central peak and ejecta blanket (e.g., Figure 18a,b and [Carter et al., 2010]), uplifted bedrock collocated with hydrated mineral detections (e.g., Figure 18c and [Gross et al., 2015]), or consistent mineralogy on the crater central peak, ejecta and crater wall (e.g., Figure 18b). Though crater ejecta is typically not preserved in the lowlands, we still observe ~15% of hydrated mineral detections in well-preserved crater ejecta (e.g., Figure 18d). In previous surveys, uplifted bedrocks in the central peak of large craters indicating excavation process are found to correlate with phyllosilicate detection [Caudill et al., 2012; Gross et al., 2015; Pan and Ehlmann, 2017]. Small craters that do not generate enough heat to produce a long-lived hydrothermal system, are found with hydrated mineral-bearing strata exposed on crater walls. These hydrated mineral detections clearly represent subsurface material excavated by these craters. We also find the spatial distributions of mafic and hydrated mineral-bearing craters to be quite similar (Figure 6 and Figure 15), largely controlled by dust cover and degradation, though hydrated minerals are found, on average, in larger craters. Together, the detections are consistent with excavation of the hydrated minerals from an ancient altered basement, as previously proposed [Carter et al., 2010].

It remains a possibility that some hydrated minerals may form during or post-impact for certain large, complex craters where geologic context of the mineral detections is less clear (as opposed to Figure 18), though at CRISM resolution we were not able to resolve veins in the central peak/ring region or morphology related to hydrothermal fluids during/post impact. With future orbital/in situ data acquired that resolve finer scale texture combined with mineralogy, we will be able to perform detailed mapping to establish the time-relationship of the geological units in each crater and further distinguish the post-impact formation of hydrated/hydroxylated minerals. Recognizing and confirming the post-impact formation mechanisms for these minerals would have great implications for the Martian environment in the Amazonian. In the following discussion, we discuss the constraints on the stratigraphy of the northern lowlands based on an excavation origin of the mafic and hydrated minerals.

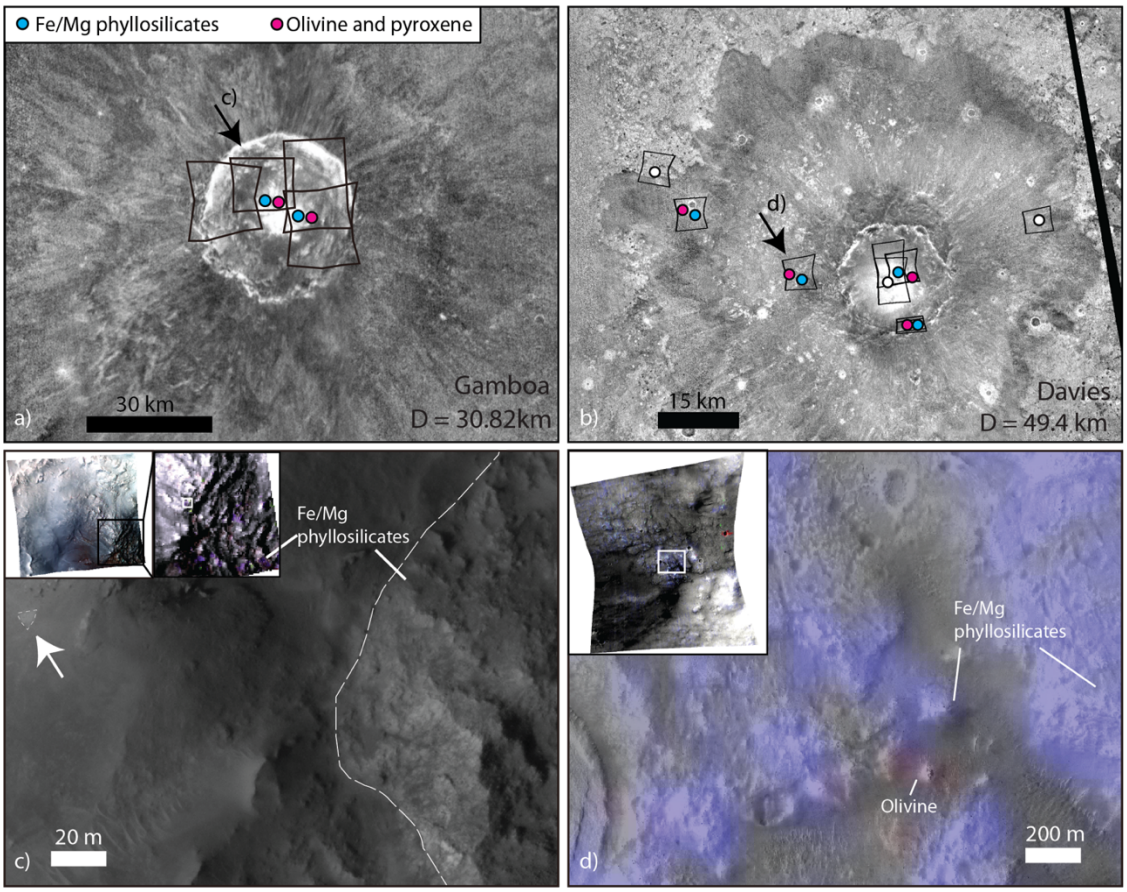

Figure 18. Examples of excavation of hydrated mineral bearing stratigraphy. a) CRISM target footprints with mineral detections of Gamboa crater on a THEMIS night-time infrared image mosaic as base map; b) CRISM target footprints with detections for Davies crater on a THEMIS night-time infrared image mosaic as base map. Notice that same mineralogy is found in crater central peak, crater walls, and ejecta blanket, consistent with an excavation origin. c) HiRISE image showing the phyllosilicate-bearing uplifted bedrock units in Gamboa crater central peak. In the upper left corner, CRISM false color image (HRS0000CA51) and a grey-scale zoom-in overlain by mineral parameter maps (R: Olivine, G: BD1900, B: BDMG) are shown, with the white outlined-box showing the context for HiRISE image (ESP_028724_2210). d) Zoom-in image of mineralogy overlain on the CTX mosaic of Davies crater, showing the rocky texture of Davies crater ejecta units with phyllosilicate detections. CRISM image (FRT00018AEF) with color overlay (R:

Olivine, G: BD1900, B: BDMG) in the upper left corner with white outlined-box showing the context for the zoom-in.

5.3 Mineralogy of the upper layer of the northern lowlands.

The surface units of the northern lowlands do not typically have the mafic absorption features of crystalline basaltic rock or the spectral features of hydrated/hydroxylated minerals. The upper layer encompasses a number of different geologic units: the Vastitas Borealis Formation covering Acidalia, Utopia and Polar Scandia regions, Amazonian smoothed terrains in Amazonis, and Arcadia Planitia and Isidis basin filling materials. The units probably consist of a variety of materials including loess-like deposits [Skinner et al., 2012], sediments, lavas, and/or volcaniclastic materials in the major basins, yet the signals of hydrated or mafic mineralogy are not observed using CRISM data. Puzzling as it is, we suggest the "bland" VSWIR spectral features of the upper layer may be due to either weathering products of basaltic glass with silica-enriched rinds [Kraft et al., 2003; Horgan and Bell, 2012] or alteration coatings of optically active Fe minerals in basalt, analogous to those observed at Gusev crater [McSween et al., 2005; Mustard et al., 2005; Salvatore et al., 2010]. Alternatively, these features may be due to poorly crystalline phases dominating the spectral feature, similar to the abundant amorphous material in sediments within Gale crater as explored by the Curiosity rover [e.g., Blake et al., 2013; Bish et al., 2014].

5.4 Inferred subsurface stratigraphy based on an impact excavation model

Assuming an excavation origin of the observed mineralogy associated with impact craters, we apply impact crater models to provide insights into subsurface stratigraphy by exposing materials in the ejecta, walls and central peaks. In the northern lowlands survey, 14 % of all mineral detections are found in crater ejecta. Materials ejected from within the crater nearer to the point of impact are sourced much deeper and travel further. Scaling relationships from lab experiments and computational simulations can be applied to estimate the maximum excavation depth from the rim-to-rim diameter of the craters and place a lower bound of the starting position in the stratigraphy for the ejected materials. Additionally, 41% of total mineral detections are found in the central peak region. Some

of the bedrock exposed in the central structure of a crater has an origin deeper than the maximum depth of melting, a calculable parameter [Cintala and Grieve, 1998]. A different empirical relationship predicts the origin of uplifted material from observation of 24 terrestrial complex structures [Grieve and Pilkington, 1996; Cintala and Grieve, 1998] to be $0.086*D^{1.03}$ (where D is the diameter of the crater), and has been applied to Mars [Quantin et al., 2012; Tornabene et al., 2013]. However, both of these parameters do not give a strong constraint because numerical models have found that at and near the center of the crater, elements of a subsurface stratigraphy are mixed [O'Keefe and Ahrens, 1999]. The mineralogy exposed in the central peak/ring region represents a mixture of lithologies from the shallow subsurface to the unmelted deeper stratigraphy with the possibility also of sampling a deeper layer than the mineralogy seen in the ejecta and crater wall regions [e.g., Ernst et al., 2010]. Here we use the maximum excavation depth to place constraint on the starting elevation of the materials in the central peak as well as ejecta, crater floor and detections in the terraced rim of large complex crater, which could be mixed with proximal ejecta. On the other hand, a small number of detections are found on the overturned flap on crater wall/rim of small, simple craters. These exposures represent deposits very close to the pre-impact surface and we use the elevation of the pre-existing surface as a constraint on the upper bound of the original elevation of these deposits.

A static Maxwell-Z model predicts the maximum excavation depth ($d_{max\ \_excavation}$) to be approximately 1/10 of the diameter of the transient crater ($D_{transient}$) [Eq. (3); Melosh, 1989].

$$d_{max\ \_excavation} = \frac{1}{10} D_{transient} \qquad (3)$$

The diameter of the transient cavity is related to the final crater diameter (D_{final}) by a scaling relationship as shown in Eq. (4)

$$D_{transient} \cong a\,(D_{final})^{b}(D_{*})^{c} \qquad (4)$$

Here D_{*} is the transition diameter from simple to complex crater on Mars, estimated to be ~8 km from observations [Garvin and Frawley, 1998], and a, b, and c are constants. Data from different workers support different parameters, and we examine three different parameterizations given in Table 3 [Melosh 1989; Hosapple, 1993; Croft, 1985]. From Eq.

(3) and (4), we calculate that the majority of the craters we investigated have excavated materials from a depth of ~0.1-5.0 km below the pre-impact surface. For the diameter range of craters examined in this survey, the different parameterizations result in a difference of less than 500 m for estimated maximum excavation depth for more than 99% of all the craters. We use the maximum excavation depth based on Holsapple [1993], which gives the intermediate estimate for observed crater diameter range to calculate maximum excavation depth for all craters. The excavation depth is then subtracted from the elevation of the pre-impact surface, which is calculated as the median MOLA elevation of 4-5 locations at 2.5 crater radii outside the crater ejecta blanket (except for pedestal craters with ejecta blanket above the surrounding plains, the elevation in the center of the crater is used). We simply record the MOLA elevation for small, simple craters where we observe materials in situ on the walls.

Assuming an excavation origin, the data show that the hydrated minerals may have originated from stratigraphic locations of -4 to -5.5 km or deeper relative to MOLA (Figure 19). In contrast, mafic mineral maximum excavation depths are found to range from ~100 m to several kilometers across the northern lowlands. In some locations, especially Chryse and Acidalia, mafic minerals exposed on the crater wall as part of the non-disrupted stratigraphy indicate very shallow (several meters) origin of these detections. The highest predicted stratigraphic location for hydrated mineral detections is consistently lower than that for mafic minerals (excluding the hydrated silica detections in small craters in Acidalia, which are not representative of the ancient basement, see 5.6.2). The elevation difference between the first appearing hydrated mineral detection and that of mafic detection in the same geological province gives a rough estimate of the thickness of this mafic mineral-bearing layer—likely made up of several discrete mafic units—is 1-2 km and varies across the plains, which is consistent with or somewhat deeper than the estimate from a prior lava filling model (820-1000 m on average) [Head et al., 2002]. This layer with mafic minerals seems to be thicker in Utopia and Elysium Planitia than in Acidalia, Chryse, Lyot or Scandia. Arcadia and Isidis have only a few mafic detections and no certain hydrated mineral detections so the existence and depth of the mafic layer(s) and hydrated basement cannot be well constrained (Figure 19).

The thickness of the upper layer with no mineral detection may be highly variable across the entire lowlands area. The layer is probably thinner (several meters to 100 m, consistent with previous estimates for VBF [Kreslavsky and Head, 2002, Salvatore and Christensen, 2014b]) in Acidalia and Chryse Planitia, but much thicker (up to several km) in Lyot, Elysium and Arcadia region, with different resurfacing processes than the Vastitas Borealis Formation.

Table 3. Scaling parameters from different scaling models for the diameter of the transient crater.

Parameters	**a**	**b**	**c**
Melosh, 1989	0.84 for simple crater 0.65 for complex	1	0
Holsapple, 1993	0.758	0.921	0.079
Croft, 1985	1	0.85	0.15

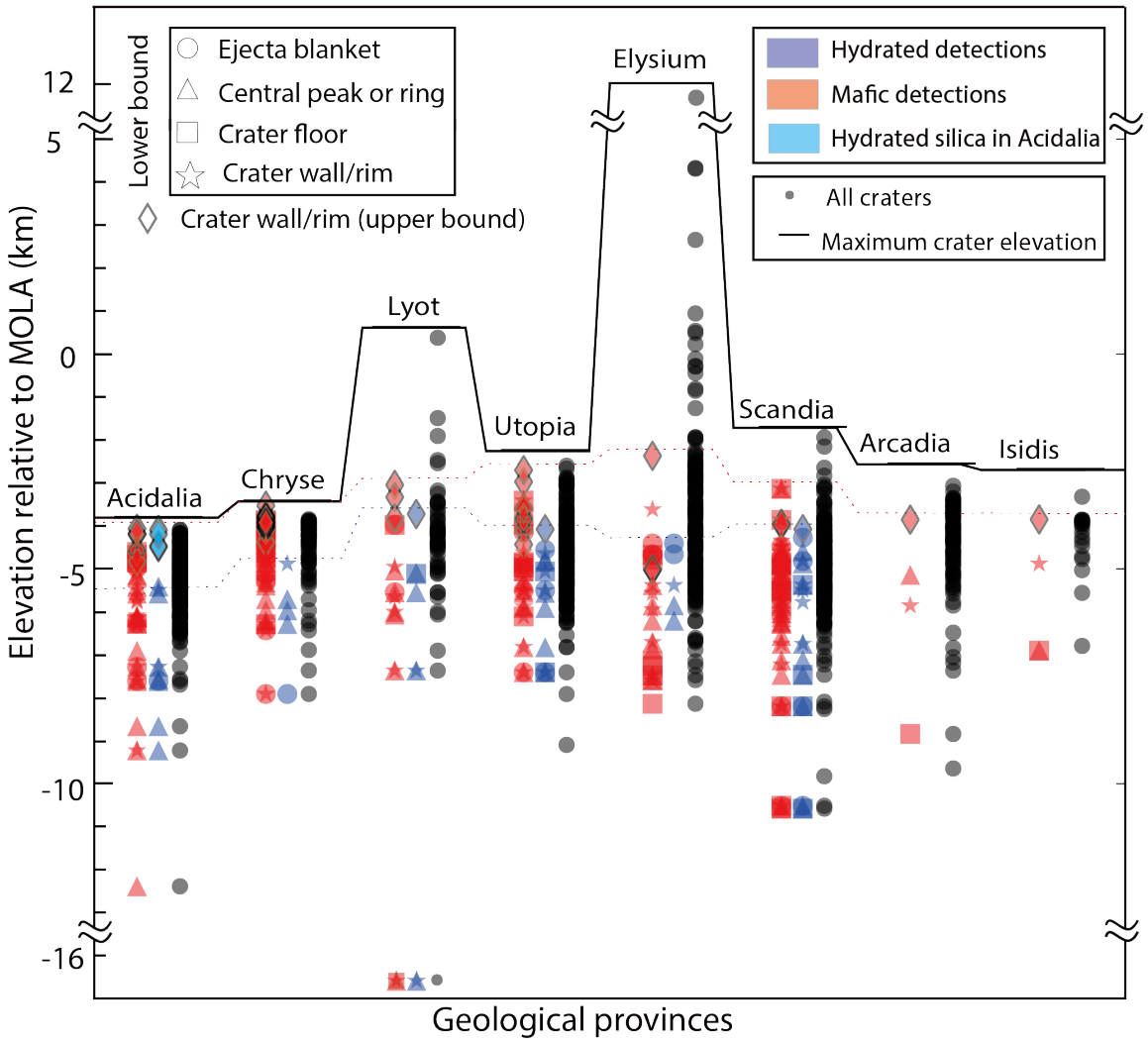

Figure 19. Origin depth of materials within different geological provinces in the northern plains assuming the excavation origin, as described in 5.4. Small black dots show the calculated elevation of origin for all the studied craters in each geological province. Mafic detections (red), hydrated mineral detections (blue), and Acidalia hydrated silica (cyan) are plotted with different symbols for occurrences in crater ejecta (circle), crater central peak/ring (triangle), crater floor (square) and crater walls (star). Detections on the crater wall/rim of small, simple craters are plotted the average elevation of the crater in diamonds, as an upper bound of the elevation in stratigraphy. The colored dashed lines indicate the uppermost crater showing mafic (red) or hydrated (blue) mineral in stratigraphic location. The solid black line shows the maximum surface elevation of all craters in each geological province.

5.5 A missing mineralogy record of a global northern ocean?

As summarized above, the stratigraphy we present in section 5.5 does not include a clear mineralogic record of a global northern ocean. There is no mineralogically distinct intermediate depth unit between the inferred basement and mafic units, nor between mafic units and surface units. We do not observe large-scale local concentrations for sulfate, hydrated salt, and carbonate, or obvious clustering for Fe/Mg clays. On Earth, oceanic sediments include constituents originated from Earth's lithosphere, e.g. transported crustal materials, organic and inorganic biomaterials (some carbonates, some silica, a small amount of organic matter), authigenic ferromanganesian minerals, and clays (montmorillonite, illite, chlorite, zeolites, and smectites) [Goldberg, 1961].

If a long-lived ocean existed within the northern lowlands of Mars, it could form extensive clay minerals like those on Earth through water-rock interaction. Also, as the ocean evaporated, dissolved chemical constituents could form salt deposits (including carbonate, sulfate, chloride salts) similar to salt sediments on Earth where ancient lakes dried out [Braitsch, 2012]. Although salt is not readily detectable in CRISM data, they often occur in hydrated form (gypsum, monohydrated sulfates, or hydrated chloride salts), which show the spectral signatures of water, are not found in the survey of the northern lowlands. It is possible that some phyllosilicates in the lowlands could have formed as detrital or authigenic minerals in the presence of an ocean, but no particular clustering in spatial distribution has been observed for the phyllosilicate detections, and they have been found to co-occur with other higher temperature phases (e.g. prehnite) unrelated to the secondary alteration of an ocean. The lack of associated mineralogy does not completely preclude a northern ocean(s) but suggests that if an ocean did exist: (a) that the spatial and temporal extent of the "ocean" may have been limited, resulting in insufficient water-rock interaction for mineralization; (b) the water-rock interactions may also have been kinetically inhibited due to lower temperature; (c) the liquid water may have low ionic strength resulting in limited salt formation as the ocean evaporates; or some combination. We considered whether the "hydrated unidentified" minerals might be a group of hydrated salts that represent remnants of a northern ocean. However, the distribution within the northern lowlands overlaps with other Fe/Mg phyllosilicate detections. No particular clusters have

been identified in spatial distribution or original stratigraphic position as inferred from stratigraphic position, which does not suggest a different origin from the phyllosilicates. The few sulfate and zeolite detections made do suggest there are locations in the lowlands region potentially with different forms of aqueous alteration from the hydrated basement. In any case, we did not discover widespread mineralogy in support of a long-lived global ocean, but if an ocean did exist in the northern lowlands, the formation of alteration minerals and salts could have been inhibited by the reasons above.

5.6 Regional geological and aqueous history revealed by impacts

Though mineralogical evidence of a northern ocean was not discovered, distinctive regional differences in mineralogy were revealed in a few select geologic provinces, described below.

5.6.1 Mafic minerals in Chryse Planitia

Chryse Planitia and Acidalia Planitia are adjacent to one another and are both regions of interest because of the immense outflow channels that debouch into them and the water-related sedimentation features on the surface. Geological mapping has revealed widespread possible water-lain sediments on the surface of Chryse and Acidalia [Tanaka et al., 1997; Salvatore and Christensen, 2014a]. In this study, we find that beneath a thin layer of spectrally-bland sediments, Chryse Planitia has a high occurrence of mafic detections compared to the rest of the northern lowlands. Specifically, the detection rate differs substantially for small craters (D<10km) in Chryse and Acidalia, but much less for large craters (Figure 6). There are at least 3 possible explanations for the mafic minerals in Chryse Planitia: a localized source of volcanic lava flows; mafic mineral-bearing outflow channel deposits; and better exposure due to less resurfacing and dust cover in the region. The relative depletion of mafic mineralogy in Acidalia compared to Chryse by more deposition of the Vastitas Borealis Formation at higher latitudes, seems consistent with larger depth/diameter ratio of craters in Chryse (~0.08) than Acidalia (~0.04). Yet, the mafics detection rate in Acidalia is consistent with the rest of the northern lowlands, including areas like Elysium Planitia and Isidis Basin that have not been covered by the Vastitas Borealis Formation. Moreover, detections of hydrated minerals in several small

craters in Acidalia confirm that exposures in smaller craters have not been completely obscured. Therefore, it is more likely the enhanced mafic detections represent a stratigraphic difference in Chryse Planitia rather than surface mantling effects, either from deposition of mafic mineral-bearing sediments from outflow channel deposits or from a source of volcanic materials that is not found in other parts of the lowlands. It is less likely that these are sedimentary deposits from outflow channels, since alteration and sorting during transport tends to deplete or weather pristine olivine and produce less pronounced spectral features in the sediments. If they are indeed sediments transported and deposited from outflow channel debouching, they represent a mafic mineral-bearing unit originated from highlands which has been transported in an environment where alteration is limited. If these represent deposits from volcanic activity directly, it is possible a previously unrecognized source exists in/around Chryse (e.g., fissure eruptions), since there is no obvious lava source in the vicinity of Chryse Planitia except for Tharsis. Although interestingly, olivine has been identified in Ganges and Eos Chasmain the neighboring southern highlands in patchy deposits which can be traced as a layer [Edwards et al., 2008], which could potentially provide a source layer for the outflow channel deposits or be related to the same episode of effusive volcanic flow.

5.6.2 Silica deposits in small craters in Acidalia

In Acidalia and Chryse Planitia, light-toned layers have been identified on walls of small craters that suggest widespread sedimentation in the shallow subsurface, possibly due to outflow channels [Salvatore and Christensen, 2014b]. In this study, we do not find evidence for any aqueous alteration related to these deposits, but there are four small craters (with diameters 1-2.5 km) at the boundary between Chryse and Acidalia, each of which shows hydrated silica detections (Figure 10, Figure 20). In CRISM image FRT000093DC, hydrated silica is exposed on the crater wall in a layer a few CRISM pixels thick (~10-100 m) close to the surface (Figure 20a,c). The silica-bearing layer appears to be shedding high-albedo blocks from the crater wall, as observed from HiRISE image (Figure 20d). The extent of the layer on the image spans for 80-100 m, with the lower boundary covered by dark sands. The size of the craters implies that the impact energy is insufficient to generate a long-lived hydrothermal system, and the morphology of detections over crater rims is

likely to be the result of excavation of a shallow, subsurface deposit.

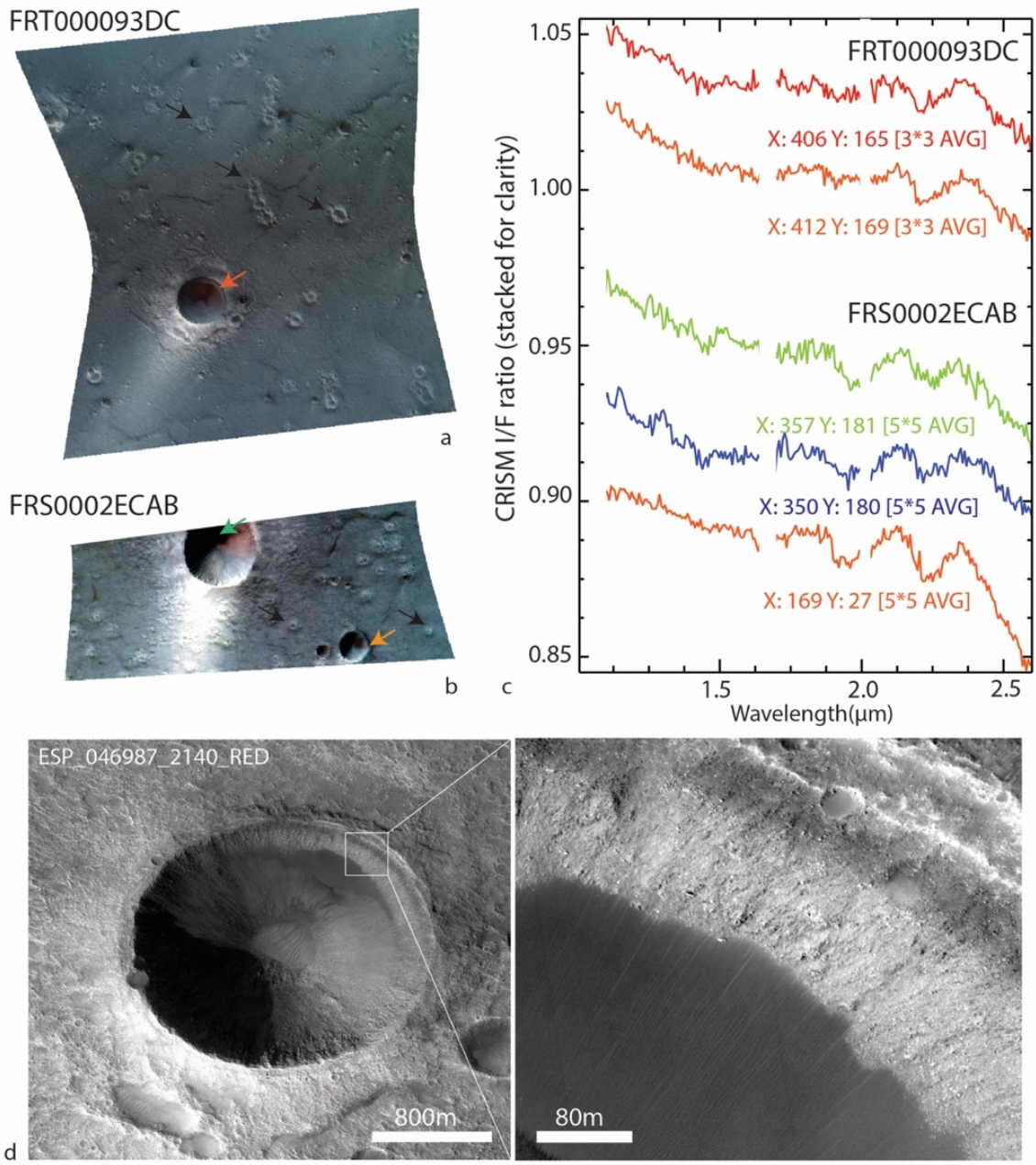

Figure 20. Hydrated silica detections in Acidalia Planitia, on Vastitas Borealis Formation boundary units with small degraded conical features (black arrows). a) CRISM image FRT000093DC where hydrated silica is found as exposed on crater walls, consistent with the interpretation of an excavated shallow subsurface deposit. Arrows point to the locations

where the spectra in Panel C are taken from. b) CRISM image FRS0002ECAB where silica is detected in 2 small craters (with diameters 1 km and 2.5 km). c) Hydrated silica spectra from the CRISM images in a) and b). Absorption features are sharper and 2.2 μm feature is wider for the smaller small crater (orange arrow) than the larger one (green arrow) in FRS0002ECAB. d) HiRISE coverage of crater in FRT000093DC with zoomed-in image showing the high albedo and rocky texture of the silica-bearing layer with a layer extent of 80-100 m.

Other than these four craters, most other hydrated mineral detections in Acidalia are phyllosilicates or unidentified hydrated minerals in craters with diameter larger than ~11 km. The small craters probably represent a distinct, shallow subsurface hydrated silica unit in southern Acidalia, likely post-dating the formation of most phyllosilicates found in larger craters. Hydrated silica has also been identified on the surface in non-crater related terrains [Pan and Ehlmann, 2014] within Acidalia Planitia, embaying and thus post-dating phyllosilicate-bearing knobs, which is consistent to the inferred stratigraphy from impact crater detections in this survey. The silica deposits in the knobby terrains have been suggested to form via localized aqueous alteration due to vapor weathering, thin film leaching, or silicate weathering with surface or subsurface water, and similar processes could have resulted in the formation of the hydrated silica deposits in southern Acidalia Planitia. The spatial proximity of these hydrated detections to conical features in Vastitas Borealis Formation (Figure 20) indicates they might have formed during the same episode of subsurface volatile mobility. It is also possible that the shallow hydrated silica is related to outflow channel sedimentation, since they are located at the termini of the large outflow channels.

5.6.3 Arcadia Province: few detections of mafic or hydrated mineralogy

The Arcadia Province encompasses both Arcadia and Amazonis Planitiae, west of the Elysium province and east of Acidalia Planitia. The topography of Amazonis Planitia is extremely flat with small surface slopes (1: 10,000 over a distance of 800 km) [Aharonson et al., 1998]. And wrinkle ridges that are widespread in other parts of the northern lowlands are obscured in this region [Head et al., 2002], possibly also due to

multiple mantling units of Amazonian-aged smooth terrain as mapped by Tanaka et al. [2014]. In this region, mafic and hydrated mineral detections are both atypically scarce, which cannot solely be explained by a moderately enhanced dust cover. The craters are more degraded in Arcadia and Amazonis Planitiae, and the depth to diameter ratios of these craters are small (average ~0.05). These data support a late resurfacing event in Arcadia and Amazonis. Thus, the lack of mafic and hydrated mineral detections for craters of all sizes in Arcadia and Amazonis Planitiae observed in this survey agrees with a complex resurfacing history in this region, and the depth of the first occurring mafic mineral in craters indicates this surface unit could have a thickness of 180-1340 m (Figure 19).

5.6.4 Scandia region north of Arcadia

The Scandia region north of Arcadia, part of the Vastitas Borealis Formation in the geological map by Tanaka et al. [2005], hosts 66 craters with mafic detections and 23 with hydrated detections. Due to the high latitude of this region, many images are affected by ice or dark sand dunes from the Olympia Undae field, so they were usually excluded from previous surveys. However, we were able to find hydrated and mafic minerals in relatively "clean" images. Mafic minerals are found in craters with a wide range of diameters and indicate widespread volcanic materials. The hydrated minerals found in this region include Fe/Mg phyllosilicates, chlorite/prehnite, and mostly unidentified hydrated minerals. The hydrated mineral detections in the Scandia region discovered in this study are the highest latitude phyllosilicate detections on Mars.

The region sits in between the north polar plateau and the immense Alba Patera volcanic shield, largely covering the Vastitas Borealis plains with various Scandia landforms, including Scandia Colles (knobs or mesas), Cavis (irregular depressions), and Tholis (low rounded plateaus) [Tanaka et al., 2011]. After the emplacement of Vastitas Borealis Formation, a variety of resurfacing processes reshaped the surface of the Scandia region, including emplacement of Alba Mons volcanic material. The knobs and mesas were first interpreted to be remnants of ancient materials projecting through younger units [Tanaka and Scott, 1987], but later were suggested to be related to the warming of the volatile-rich sediments proximal to Alba Mons resulting in collapse, erosion and mud volcanism [Tanaka et al., 2011], a process that could be related to the hydrated minerals

found in small craters in this survey. It has been proposed that the gypsum at Olympia Undae may be sourced directly from this unit [Tanaka et al., 2008], though we do not detect gypsum in crater-exposed bedrock in the region.

5.7 Insights into the geologic and aqueous history of the northern lowlands

The impact crater mineralogy detected in the northern lowlands provides new insights into its geologic and aqueous history. The widespread hydrated minerals found in the largest craters are consistent with the inferred presence of the ancient basement (likely Noachian or pre-Noachian) at an elevation of -4 to -5.5 km. The basement is continuous and widespread in the northern lowlands, consistent with early formation of the crustal dichotomy, Noachian lowlands, and subsequent burial by the plains materials. The most frequently found hydrated minerals are Fe/Mg phyllosilicate (smectite), chlorite/prehnite, hydrated silica, and numerous unidentified hydrated minerals, similar to the southern highlands with the lack of pervasive carbonate or salt deposits. Together this indicates that a northern ocean is not necessary to account for the hydrated mineralogy seen in the northern lowlands. If a northern ocean did exist, the ionic strength may be low, mineralization of ocean sediments is kinetically inhibited.

Meanwhile, clay minerals, especially Fe/Mg smectite, are expected to undergo transformation into more stable mineral forms like chlorite under burial over several hundred Ma on Earth [e.g. Boles and Franks, 1979; Weaver, 1989]. The temperature at a depth of 2 km could vary from 35-90°C for estimated geothermal gradients in the Noachian, depending on surface temperature [Borlina et al., 2015], encompassing the typical transition temperatures from Fe/Mg smectite to illite or chlorite on Earth [e.g. Velde, 1985]. The preservation of the juvenile mineralogy in the northern lowlands, similar to the southern highlands, indicates a weak geothermal gradient and/or low surface temperature since time of burial, or the lack of post-depositional water for diagenetic maturation, or both [Tosca and Knoll, 2009].

Mafic mineral detections in 251 impact craters are consistent with the previous suggestion of extensive volcanic materials in the northern lowlands subsurface. The extent of the mafic detections in craters cover an estimated surface area of ~$66.7 \cdot 10^6$ km^2, more than doubling the area covered by Hesperian lava plains in the lowlands indicated by

wrinkle ridges (~$24.2 \cdot 10^6$ km^2) [Head et al., 2002]. In particular, the widespread olivine detections indicate the Hesperian widespread lava plains in the lowlands may be related to the Early Hesperian aged olivine-bearing lava flows found in the southern highlands. Using the inferred thickness of the mafic-bearing layer for each geological province, the extent of the mafic-bearing layer yields an estimate of ~$1–4 \cdot 10^7$ km^3 for the volume of volcanic materials in the subsurface of the northern lowlands, as much as the previous estimates of Hesperian lava flows globally (~$3.3 \cdot 10^7$ km^3, including highlands) [Head et al., 2002]. Volatile release from volcanic activity has been suggested to be capable of increasing the atmospheric pressure to ~0.3 bar and may induce transient warming effects [Greeley, 1987; Craddock and Greeley, 2009; Halevy and Head, 2014]. Although the overall effect on climate is debated due to the complication of competing cooling effects from aerosol [Kerber et al., 2015], the voluminous deposits in the northern lowlands indicates increased volatile release throughout the history of Mars and may have played important role in the early climate on Mars.

During the late Hesperian and through the Amazonian ages, many regional resurfacing events, not plains-wide filling, were dominant in shaping the northern lowlands surface. Specifically, we have found localized aqueous alteration in Acidalia formed hydrated silica deposits in subsurface; regional volcanic activity resurfaced Chryse Planitia forming the mafic minerals. These hydrated silica and mafic minerals predate the sedimentation of a thin layer with no specific mineral detection, previous recognized as Vastitas Borealis Formation. Arcadia and Amazonis Planitiae however, were probably heavily resurfaced in mid-to-late Amazonian by loess, aeolian sediments, lavas or pyroclastic deposits, forming the smooth terrains unit that filled in the majority of craters in the region. The mineralogical evidence revealed surface aqueous and volcanic activity in the Amazonian. It is yet unclear how these events relate to the surface morphologic features observed (cones, polygons and VBF), but the active geologic processes observed in the northern lowlands request future studies to better understand Mars in the late Hesperian and Amazonian.

6 Conclusions

Here we summarize the main conclusions from the survey of impact crater mineralogy in the northern lowlands of Mars:

1. We observe mafic and hydrated minerals associated with impact craters in all of the major provinces in the northern lowlands.
2. Hydrated and mafic mineral detections are both positively correlated with crater size. Mafic minerals are more widespread in smaller craters (> ~1 km) while hydrated minerals are mostly detected in the larger craters (> ~29 km) with a much lower probability of detection in small craters. The relationship of crater size to hydrated minerals suggests that they may represent an underlying hydrated basement excavated by large impact craters. We have not positively identified formation of hydrated minerals via impact-induced hydrothermal alteration, but it remains a possibility to explain some of the data.
3. We have identified hydrated minerals in 81 out of 1045 craters in the northern lowlands, including Fe/Mg phyllosilicates, chlorite/prehnite and hydrated silica. The presence of hydrated minerals in the Scandia region north of Arcadia is a new discovery. The frequency statistics of hydrated mineral phases are similar to those determined for southern highlands observations and global statistics except for the significantly greater prevalence of unidentified hydrated phases, where the exact mineral phase responsible for a 1.9-μm H_2O absorption cannot be identified.
4. Mafic mineral detections are widespread in all northern lowlands basins and are consistent with a substantial depth and volume of volcanic materials. The observed thickness of mafic hosting materials implies volumes of volcanic materials in northern lowlands ($1\text{-}4\cdot10^7$ km^3) could reach more than previous global estimates including highlands ($\sim3.3\cdot10^7$ km^3).
5. No strong evidence for pervasive carbonate or other evaporative salts has been found to support the hypothesis of a global ocean. Instead the hydrated minerals (in particular Fe/Mg phyllosilicates) detected are probably mostly related to an ancient Noachian basement, excavated from a depth of -4 to -5.5 km relative to the MOLA datum.

6. Different regions of the northern lowlands show differences in the frequency of occurrences of mineral detections. Chryse Planitia has a significantly higher number of detections of mafic minerals, especially in small craters, which could be related to Tharsis volcanic products or other unrecognized volcanic sources. Small craters with hydrated silica detections are found in central Acidalia Planitia, representing younger and localized aqueous mineral formation. Amazonis and Arcadia Planitiae lack both mafic and hydrated detections, possibly due to later burial by the resurfacing events.
7. Further investigation of individual craters or regions will provide important insights into the local stratigraphy or aqueous activity specific to each crater or region in addition to the aqueous and geologic history of the northern lowlands.

Acknowledgement

The data supporting the analysis and conclusions have been included in the supporting materials and the processing details will be provided upon request. This work has been fully supported by NASA Mars Data Analysis Program grant NNX12AJ43G. We would also like to thank the CRISM team for targeting and providing the dataset, as well as internal reviews which helped shape the early stage of the manuscript. The author also appreciates help in data processing from Kelsey Logan, and discussion with Shasha Tong and Qiong Zhang. We also thank the constructive reviews from two reviewers.

References

Abramov, O., and D. A. Kring (2005), Impact-induced hydrothermal activity on early Mars, J. Geophys. Res., 110, E12S09, doi:10.1029/2005je002453.

Aharonson, O., M. T. Zuber, G. A. Neumann, and J. W. Head (1998), Mars: Northern hemisphere slopes and slope distributions, Geophys. Res. Lett., 25(24), 4413-4416, doi:10.1029/1998gl900057.

Anderson, J. H., and K. A. Wickersheim (1964), Near infrared characterization of water and hydroxyl groups on silica surfaces, Surf. Sci., 2, 252-260, doi:10.1016/0039-6028(64)90064-0.

Andrews-Hanna, J. C., M. T. Zuber, and W. B. Banerdt (2008), The Borealis basin and the origin of the martian crustal dichotomy, Nature, 453(7199), 1212-U1227, doi:10.1038/Nature07011.

Baker, V. R., R. G. Strom, V. C. Gulick, J. S. Kargel, G. Komatsu, and V. S. Kale (1991), Ancient oceans, ice sheets and the hydrological cycle on Mars, Nature, 352(6336), 589-594, doi:10.1038/352589a0.

Bandfield, J. L., V. E. Hamilton, and P. R. Christensen (2000), A global view of Martian surface compositions from MGS-TES, Science, 287(5458), 1626-1630, doi:10.1126/science.287.5458.1626.

Baratoux, D., P. Pinet, A. Gendrin, L. Kanner, J. Mustard, Y. Daydou, J. Vaucher, and J.-P. Bibring (2007), Mineralogical structure of the subsurface of Syrtis Major from OMEGA observations of lobate ejecta blankets, J. Geophys. Res., 112, E08S05, doi:10.1029/2007JE002890.

Barlow, N. G. (2004), Martian subsurface volatile concentrations as a function of time: Clues from layered ejecta craters, Geophys. Res. Lett., 31(5), L05703, doi:10.1029/2003gl019075.

Barnhart, C. J., and F. Nimmo (2011), Role of impact excavation in distributing clays over Noachian surfaces, J. Geophys. Res., 116, E01009, doi:10.1029/2010JE003629.

Bibring, J. P., et al. (2005), Mars surface diversity as revealed by the OMEGA/Mars Express observations, Science, 307(5715), 1576-1581, doi:10.1126/science.1108806.

Bish, D., D. Blake, D. Vaniman, P. Sarrazin, T. Bristow, C. Achilles, P. Dera, S. Chipera, J. Crisp, and R. T. Downs (2014), The first X-ray diffraction measurements on Mars, IUCrJ, 1(6), 514-522.

Bishop, J., J. Madejova, P. Komadel, and H. Froschl (2002), The influence of structural Fe, Al and Mg on the infrared OH bands in spectra of dioctahedral smectites, Clay Miner., 37(4), 607-616, doi:10.1180/0009855023740063.

Bishop, J. L., M. D. Lane, M. D. Dyar, and A. J. Brown (2008), Reflectance and emission spectroscopy study of four groups of phyllosilicates: smectites, kaolinite-serpentines, chlorites and micas, Clay Miner., 43(1), 35-54, doi:10.1180/claymin.2008.043.1.03.

Blake, D. F., et al. (2013), Curiosity at Gale Crater, Mars: Characterization and Analysis of the Rocknest Sand Shadow, Science, 341(6153), doi:123950510.1126/science.1239505.

Borlina C. S., B. L. Ehlmann, and E. S. Kite (2015), Modeling the thermal and physical evolution of Mount Sharp's sedimentary rocks, Gale crater, Mars: Implications for

diagenetic minerals on the MSL Curiosity Rover traverse. J Geophys Res, 120(8):1396–1414.

Boynton, W. V., et al. (2007), Concentration of H, Si, Cl, K, Fe, and Th in the low- and mid-latitude regions of Mars, J. Geophys. Res., 112, E12S99, doi: 10.1029/2007je002887.

Bramson, A. M., S. Byrne, N. E. Putzig, S. Sutton, J. J. Plaut, T. C. Brothers, and J. W. Holt (2015), Widespread excess ice in Arcadia Planitia, Mars, Geophys. Res. Lett., 42(16), 6566-6574, doi:10.1002/2015gl064844.

Budney, C. J., and P. G. Lucey (1998), Basalt thickness in Mare Humorum: The crater excavation method, J. Geophys. Res., 103(E7), 16855-16870, doi: 10.1029/98je01602.

Burns, R. G. (1970), Crystal Field Spectra and Evidence of Cation Ordering in Olivine Minerals, Am. Mineral., 55.9-10 (1970): 1608.

Carr, M. H., and J. W. Head (2003), Oceans on Mars: An assessment of the observational evidence and possible fate, J. Geophys. Res., 108(E5), 5042， doi:10.1029/2002je001963.

Carter, J., F. Poulet, J. P. Bibring, N. Mangold, and S. Murchie (2013), Hydrous minerals on Mars as seen by the CRISM and OMEGA imaging spectrometers: Updated global view J. Geophys. Res.,, 118(4), 831-858, doi:10.1029/2012je004145.

Carter, J., F. Poulet, J. P. Bibring, and S. Murchie (2010), Detection of Hydrated Silicates in Crustal Outcrops in the Northern Plains of Mars, Science, 328(5986), 1682-1686, doi:10.1126/science.1189013.

Carter, J., F. Poulet, S. Murchie, and J. P. Bibring (2013), Automated processing of planetary hyperspectral datasets for the extraction of weak mineral signatures and applications to CRISM observations of hydrated silicates on Mars, Planet Space Sci., 76, 53-67, doi:10.1016/j.pss.2012.11.007.

Caudill, C. M., L. L. Tornabene, A. S. McEwen, S. Byrne, L. Ojha, and S. Mattson (2012), Layered MegaBlocks in the central uplifts of impact craters, Icarus, 221(2), 710-720, doi:10.1016/j.icarus.2012.08.033.

Christensen, P. R., et al. (2001), Mars Global Surveyor Thermal Emission Spectrometer experiment: Investigation description and surface science results, J. Geophys. Res., 106(E10), 23823-23871, doi: 10.1029/2000je001370.

Cintala, M. J., and R. A. F. Grieve (1998), Scaling impact melting and crater dimensions: Implications for the lunar cratering record (vol 33, pg 889, 1998), Meteorit. Planet Sci., 33(6), 1343-1343.

Clark, R. N. (1999), Spectroscopy of rocks and minerals, and principles of spectroscopy, Manual of remote sensing, 3, 3-58.

Clark, R. N., and T. L. Roush (1984), Reflectance Spectroscopy - Quantitative-Analysis Techniques for Remote-Sensing Applications, J. Geophys. Res., 89(Nb7), 6329-6340, doi:10.1029/JB089iB07p06329.

Clark, R. N., G. A. Swayze, R. Wise, K. E. Livo, T. Hoefen, R. F. Kokaly, and S. J. Sutley (2007), USGS digital spectral library splib06a, US Geological Survey, Digital Data Series, 231.

Clifford, S. M., and T. J. Parker (2001), The evolution of the Martian hydrosphere: Implications for the fate of a primordial ocean and the current state of the northern plains, Icarus, 154(1), 40-79, doi:10.1006/icar.2001.6671.

Craddock, R. A., and R. Greeley (2009), Minimum estimates of the amount and timing of gases released into the martian atmosphere from volcanic eruptions, Icarus, 204(2), 512-526, doi:10.1016/j.icarus.2009.07.026.

Croft, S. K. (1985), The Scaling of Complex Craters, J. Geophys. Res., 90, C828-C842.

Di Achille, G., and B. M. Hynek (2010), Ancient ocean on Mars supported by global distribution of deltas and valleys, Nat. Geosci., 3(7), 459-463, doi:10.1038/Ngeo891.

Ehlmann, B. L., J. F. Mustard, S. L. Murchie, J. P. Bibring, A. Meunier, A. A. Fraeman, and Y. Langevin (2011), Subsurface water and clay mineral formation during the early history of Mars, Nature, 479(7371), 53-60, doi:10.1038/Nature10582.

Ehlmann, B. L., et al. (2009), Identification of hydrated silicate minerals on Mars using MRO-CRISM: Geologic context near Nili Fossae and implications for aqueous alteration, J. Geophys. Res., 114, E00D08, doi:10.1029/2009je003339.

Ernst, C. M., S. L. Murchie, O. S. Barnouin, M. S. Robinson, B. W. Denevi, D. T. Blewett, J. W. Head, N. R. Izenberg, S. C. Solomon, and J. H. Roberts (2010), Exposure of spectrally distinct material by impact craters on Mercury: Implications for global stratigraphy, Icarus, 209(1), 210-223, doi:10.1016/j.icarus.2010.05.022.

Farrand, W. H., L. R. Gaddis, and L. Keszthelyi (2005), Pitted cones and domes on Mars: Observations in Acidalia Planitia and Cydonia Mensae using MOC, THEMIS, and TES data, J. Geophy. Res., 110(E5), doi:10.1029/2004je002297.

Frey, H. (2008), Ages of very large impact basins on Mars: Implications for the late heavy bombardment in the inner solar system, Geophys. Res. Lett., 35, L13203, doi:10.1029/2008gl033515.

Frey, H., and M. Jarosewich (1982), Sub-Kilometer Martian Volcanos - Properties and Possible Terrestrial Analogs, J. Geophy. Res., 87(Nb12), 9867-9879, doi:10.1029/Jb087ib12p09867.

Frey, H. V., J. H. Roark, K. M. Shockey, E. L. Frey, and S. E. H. Sakimoto (2002), Ancient lowlands on Mars, Geophys. Res. Lett., 29(10), doi:10.1029/2001gl013832.

Frey, H. (2008), Ages of very large impact basins on Mars: Implications for the late heavy bombardment in the inner solar system, Geophys. Res. Lett., 35, L13203, doi:10.1029/2008GL033515.

Fuller, E. R., and J. W. Head (2002), Amazonis Planitia: The role of geologically recent volcanism and sedimentation in the formation of the smoothest plains on Mars, J. Geophy. Res., 107(E10), 5081，doi: 10.1029/2002je001842.

Garvin, J. B., and J. J. Frawley (1998), Geometric properties of Martian impact craters: Preliminary results from the Mars Orbiter Laser Altimeter, Geophys. Res. Lett., 25(24), 4405-4408, doi: 10.1029/1998gl900177.

Greeley, R. (1987), Release of Juvenile Water on Mars - Estimated Amounts and Timing Associated with Volcanism, Science, 236(4809), 1653-1654, doi: 10.1126/science.236.4809.1653.

Gross, C., J. Carter, L. L. Tornabeme, M. Sowe and J. L. Bishop. (2015) Stratified Phyllosilicate-bearing Deposits within Impact Craters in the Northern Plains of Mars. Lunar and Planetary Science Conference. Vol. 1817. 2015.

Hartmann, W. K., and D. C. Berman (2000), Elysium Planitia lava flows: Crater count chronology and geological implications, J. Geophys. Res., 105(E6), 15011–15025, doi:10.1029/1999JE001189.

Hazen, R. M., P. M. Bell, and H. K. Mao (1978), Effects of compositional variation on absorption spectra of lunar pyroxenes, Lunar and Planetary Science Conference. Vol. 9. 1978.

Head, J. W., and M. A. Kreslavsky (2002), Northern lowlands of Mars: Evidence for widespread volcanic flooding and tectonic deformation in the Hesperian Period, J. Geophy. Res., 107(E1), doi: 10.1029/2000je001445.

Hiesinger, H., and J. W. Head (2000), Characteristics and origin of polygonal terrain in southern Utopia Planitia, Mars: results from Mars Orbiter Laser Altimeter and Mars Orbiter Camera data, J. Geophy. Res., 105(E5), 11999-12022.

Holsapple, K. (1993), The scaling of impact processes in planetary sciences, Annu. Rev. Earth Planet. Sci., 21, 333-373.

Horgan, B., and J. F. Bell III (2012), Widespread weathered glass on the surface of Mars, Geology, 40(5), 391-394, doi:10.1130/g32755.1.

Karunatillake, S., et al. (2006), Composition of northern low-albedo regions of Mars: Insights from the Mars Odyssey Gamma Ray Spectrometer, J. Geophy. Res., 111(E3), doi:10.1029/2006je002675.

Kraft, M. D., J. R. Michalski, and T. G. Sharp (2003), Effects of pure silica coatings on thermal emission spectra of basaltic rocks: Considerations for Martian surface mineralogy, Geophys. Res. Lett., 30(24), 2288，doi:10.1029/2003gl018848.

Kreslavsky, M. A., and J. W. Head (2002), Fate of outflow channel effluents in the northern lowlands of Mars: The Vastitas Borealis Formation as a sublimation residue from frozen ponded bodies of water, J. Geophys. Res., 107(E12), 5121, doi:10.1029/2001JE001831.

Lucchitta, B. K., H. M. Ferguson, and C. Summers (1986), Sedimentary Deposits in the Northern Lowland Plains, Mars, J. Geophys. Res., 91(B13), E166-E174, doi:10.1029/JB091iB13p0E166.

Malin, M. C., and K. S. Edgett (1999), Oceans or seas in the Martian northern lowlands: High resolution imaging tests of proposed coastlines, Geophys. Res. Lett., 26(19), 3049-3052, doi:10.1029/1999gl002342.

Mangold, N., S. Maurice, W. C. Feldman, F. Costard, and F. Forget (2004), Spatial relationships between patterned ground and ground ice detected by the Neutron Spectrometer on Mars, J. Geophys. Res., 109, E08001, doi: 10.1029/2004je002235.

Marinova, M. M., O. Aharonson, and E. Asphaug (2008), Mega-impact formation of the Mars hemispheric dichotomy, Nature, 453(7199), 1216-1219, doi:10.1038/nature07070.

McGill, G. E., and L. S. Hills (1992), Origin of giant Martian polygons, J. Geophys. Res., 97(E2), 2633–2647, doi:10.1029/91JE02863.

McSween, H. Y., et al. (2006), Characterization and petrologic interpretation of olivine-rich basalts at Gusev Crater, Mars, J. Geophys. Res.,111, E02S10 doi: 10.1029/2005je002477.

Melosh, H. J. (1989), Impact cratering: A geologic process, Research supported by NASA. New York, Oxford University Press (Oxford Monographs on Geology and Geophysics, No. 11), 1989, 253 p., 1.

Michalski, J. R., M. D. Kraft, T. G. Sharp, L. B. Williams, and P. R. Christensen (2005), Mineralogical constraints on the high-silica martian surface component observed by TES, Icarus, 174(1), 161-177, doi:10.1016/j.icarus.2004.10.022.

Milliken, R. E. et al. (2008), Opaline silica in young deposits on Mars, Geology, 36(11), 847–850.

Murchie, S. L., et al. (2009), Compact Reconnaissance Imaging Spectrometer for Mars investigation and data set from the Mars Reconnaissance Orbiter's primary science phase, J. Geophys. Res., 114, E00D07, doi: 10.1029/2009je003344.

Mustard, J. F., F. Poulet, A. Gendrin, J. P. Bibring, Y. Langevin, B. Gondet, N. Mangold, G. Bellucci, and F. Altieri (2005), Olivine and pyroxene, diversity in the crust of Mars, Science, 307(5715), 1594-1597, doi:10.1126/science.1109098.

O'Keefe, J. D., and T. J. Ahrens (1999), Complex craters: Relationship of stratigraphy and rings to impact conditions, J. Geophys. Res., 104(E11), 27091-27104, doi:10.1029/1998je000596.

Ody, A., F. Poulet, Y. Langevin, J. P. Bibring, G. Bellucci, F. Altieri, B. Gondet, M. Vincendon, J. Carter, and N. Manaud (2012), Global maps of anhydrous minerals at the surface of Mars from OMEGA/MEx, J. Geophys. Res., 117, E00J14, doi: 10.1029/2012je004117.

Ody, A., F. Poulet, J.-P. Bibring, D. Loizeau, J. Carter, B. Gondet, and Y. Langevin (2013), Global investigation of olivine on Mars: Insights into crust and mantle compositions, J. Geophys. Res. Planets, 118, 234–262, doi:10.1029/2012JE004149.

Oehler, D. Z., and C. C. Allen (2010), Evidence for pervasive mud volcanism in Acidalia Planitia, Mars, Icarus, 208(2), 636-657, doi: 10.1016/J.Icarus.2010.03.031.

Oehler, D. Z., and C. C. Allen (2012), Giant polygons and mounds in the lowlands of Mars: signatures of an ancient ocean?, Astrobiology, 12(6), 601–15, doi:10.1089/ast.2011.0803.

Osinski G. R., Livio L. Tornabene, N. R. Banerjee, C. S. Cockell, R. Flemming, M. R.M. Izawa, J. McCutcheon, J. Parnell, L. J. Preston, A. E. Pickersgill, A. Pontefract, H. M. Sapers, and Go. Southam, (2013), Impact-generated hydrothermal systems on Earth and Mars, Icarus, 224(2), 347-363, doi:10.1016/j.icarus.2012.08.030.

Pan, L., and B. L. Ehlmann (2014), Phyllosilicate and hydrated silica detections in the knobby terrains of Acidalia Planitia, northern plains, Mars, Geophys. Res. Lett., 41(6), 1890-1898, doi:10.1002/2014gl059423.

Parker, T. J., D. S. Gorsline, R. S. Saunders, D. C. Pieri, and D. M. Schneeberger (1993), Coastal Geomorphology of the Martian Northern Plains, J. Geophys. Res., 98(E6), 11061-11078, doi:10.1029/93je00618.

Parker, T. J., R. S. Saunders, and D. M. Schneeberger (1989), Transitional Morphology in West Deuteronilus Mensae, Mars - Implications for Modification of the Lowland Upland Boundary, Icarus, 82(1), 111-145, doi:10.1016/0019-1035(89)90027-4.

Pelkey, S. M., et al. (2007), CRISM multispectral summary products: Parameterizing mineral diversity on Mars from reflectance, J. Geophys. Res., 112, E08S14, doi:10.1029/2006JE002831.

Perron, J. T., J. X. Mitrovica, M. Manga, I. Matsuyama, and M. A. Richards (2007), Evidence for an ancient martian ocean in the topography of deformed shorelines, Nature, 447(7146), 840-843, doi:10.1038/nature05873.

Platz T., G. Michael (2011), Eruption history of the Elysium Volcanic Province, Mars, Earth Planet. Sci. Lett., 312(1–2), 140-151, ISSN 0012-821X, http://dx.doi.org/10.1016/j.epsl.2011.10.001.

Rathbun, J. A., and S. W. Squyres (2002), Hydrothermal systems associated with martian impact craters, Icarus, 157(2), 362-372, doi:10.1006/icar.2002.6838.

Rice, M. S., E. A. Cloutis, J. F. Bell, D. L. Bish, B. H. Horgan, S. A. Mertzman, M. A. Craig, R. W. Renaut, B. Gautason, and B. Mountain (2013), Reflectance spectra diversity of silica-rich materials: Sensitivity to environment and implications for detections on Mars, Icarus, 223(1), 499-533, doi:10.1016/j.icarus.2012.09.021.

Roach, L. H., J. F. Mustard, G. Swayze, R. E. Milliken, J. L. Bishop, S. L. Murchie, and K. Lichtenberg (2010), Hydrated mineral stratigraphy of Ius Chasma, Valles Marineris, Icarus, 206(1), 253-268, doi:10.1016/j.icarus.2009.09.003.

Robbins, S. J., and B. M. Hynek (2012), A new global database of Mars impact craters >= 1 km: 1. Database creation, properties, and parameters, J. Geophys. Res., 117, E05004, doi:10.1029/2011je003966.

Ruff, S. W., and P. R. Christensen (2002), Bright and dark regions on Mars: Particle size and mineralogical characteristics based on Thermal Emission Spectrometer data, J. Geophys. Res., 107, 5127, doi:10.1029/2001je001580.

Salvatore, M. R., and P. R. Christensen (2014), On the origin of the Vastitas Borealis Formation in Chryse and Acidalia Planitiae, Mars, J. Geophys. Res. Planets, 119(12), 2437-2456, doi:10.1002/2014je004682.

Salvatore, M. R., and P. R. Christensen (2014), Evidence for widespread aqueous sedimentation in the northern plains of Mars, Geology, 42(5), 423-426, doi:10.1130/G35319.1.

Salvatore, M. R., J. F. Mustard, M. B. Wyatt, and S. L. Murchie (2010), Definitive evidence of Hesperian basalt in Acidalia and Chryse planitiae, J. Geophys. Res., 115, doi: 10.1029/2009je003519.

Skinner, J.A., Jr., Tanaka, K.L., and Platz, T. (2012), Widespread loess-like deposit in the Martian northern lowlands identifies middle Amazonian climate change, Geology, v. 40, pp. 1127-1130, doi:10.1130/G33513.1.

Smith, D. E. (1999), The global topography of Mars and Implications for surface evolution, Science, 284 (5419), pp. 1495-1503. doi: 10.1126/science.284.5419.1495

Smith, M. R., J. L. Bandfield, E. A. Cloutis, and M. S. Rice (2013), Hydrated silica on Mars: Combined analysis with near-infrared and thermal-i¬nfrared spectroscopy, Icarus, 223(2), 633-648, doi:10.1016/j.icarus.2013.01.024.

Stoffler, D., D. E. Gault, J. Wedekind, and G. Polkowski (1975), Experimental Hypervelocity Impact into Quartz Sand - Distribution and Shock Metamorphism of Ejecta, J. Geophys. Res., 80(29), 4062-4077, doi:10.1029/JB080i029p04062.

Sun, V. Z., and R. E. Milliken (2015), Ancient and recent clay formation on Mars as revealed from a global survey of hydrous minerals in crater central peaks, J. Geophys. Res., 120(12), 2293-2332, doi:10.1002/2015je004918.

Tanaka, K. L., and D. H. Scott (1987), Geologic map of the polar regions of Mars, U.S. Geol. Surv. MiSci. Invest. Ser., Map I-1802-C, scale 1:15,000,000, 1987.

Tanaka, K. L. (1997), Sedimentary history and mass flow structures of Chryse and Acidalia Planitiae, Mars, J. Geophys. Res., 102(E2), 4131-4149, doi: 10.1029/96je02862.

Tanaka, K. L., W. B. Banerdt, J. S. Kargel, and N. Hoffman (2001), Huge, CO2-charged debris-flow deposit and tectonic sagging in the northern plains of Mars, Geology, 29(5), 427-430. doi: 10.1130/0091-7613(2001)029<0427:HCCDFD>2.0.CO;2

Tanaka, K. L., C. M. Fortezzo, R. K. Hayward, J. A. P. Rodriguez, and J. A. Skinner (2011), History of plains resurfacing in the Scandia region of Mars, Planet Space Sci., 59(11-12), 1128-1142, doi:10.1016/j.pss.2010.11.004.

Tanaka, K. L., J. A. P. Rodriguez, J. A. Skinner, M. C. Bourke, C. M. Fortezzo, K. E. Herkenhoff, E. J. Kolb, and C. H. Okubo (2008), North polar region of Mars: Advances in stratigraphy, structure, and erosional modification, Icarus, 196(2), 318-358, doi:10.1016/j.icarus.2008.01.021.

Tanaka, K. L., et al. (2005), Geologic map of the northern plains of Mars, U.S. Geol. Surv. Sci. Invest. Map, 2888.

Tompkins, S., and C. M. Pieters (1999), Mineralogy of the lunar crust: Results from Clementine, Meteorit. Planet. Sci., 34(1), 25-41.

Tosca, N. J., and A. H. Knoll (2009), Juvenile chemical sediments and the long term persistence of water at the surface of Mars, Earth Planet. Sci. Lett., 286(3-4), 379-386, doi:10.1016/j.epsl.2009.07.004.

Velde, B. (1985), Clay Minerals: A Physico-Chemical Explanation of Their Occurrence, Dev. Sedimentol., vol. 40, 427 pp., Elsevier, New York.

Weaver, C. Edward (1989), Clays, muds, and shales. Vol. 44. Elsevier, 1989.

Weiss, D. K., and J. W. Head (2013), Formation of double-layered ejecta craters on Mars: A glacial substrate model, Geophys. Res. Lett., 40(15), 3819-3824, doi:10.1002/grl.50778.

Wyatt, M. B., and H. Y. McSween (2002), Spectral evidence for weathered basalt as an alternative to andesite in the northern lowlands of Mars, Nature, 417(6886), 263-266, doi:10.1038/417263a.

Yoshikawa, K. (2003), Origin of the polygons and the thickness of Vastitas Borealis Formation in Western Utopia Planitia on Mars, Geophys. Res. Lett., 30(12), 1603, doi:160310.1029/2003gl017165.

Zhong, S. J., and M. T. Zuber (2001), Degree-1 mantle convection and the crustal dichotomy on Mars, Earth Planet. Sci. Lett., 189(1-2), 75-84, doi:10.1016/S0012-821x(01)00345-4.

Zuber, M. T., et al. (2000), Internal structure and early thermal evolution of Mars from Mars Global Surveyor topography and gravity, Science, 287(5459), 1788-1793, doi:10.1126/science.287.5459.1788.

Chapter 3

PHYLLOSILICATE AND HYDRATED SILICA DETECTIONS IN THE KNOBBY TERRAINS OF ACIDALIA PLANITIA, NORTHERN PLAINS, MARS

L. Pan[1] and B. L. Ehlmann[1,2]

1 Division of Geological and Planetary Science, California Institute of Technology, Pasadena, California, USA.

2 Jet Propulsion Laboratory, California Institute of Technology, Pasadena, California, USA.

Corresponding author: L. Pan. Division of Geological and Planetary Science, California Institute of Technology, Pasadena, California, 91125, USA. (lpan@caltech.edu)

Pan, L., and B. L. Ehlmann. "Phyllosilicate and hydrated silica detections in the knobby terrains of Acidalia Planitia, northern plains, Mars." Geophysical Research Letters 41.6 (2014): 1890-1898.

Abstract:

Here we report detections of Fe/Mg phyllosilicates and hydrated silica in discrete stratigraphic units within the knobby terrains of Acidalia Planitia made using data acquired by Compact Reconnaissance Imaging Spectrometer for Mars (CRISM). Fe/Mg phyllosilicates are detected in knobs that were eroded during southward retreat of the dichotomy boundary. A second later unit, now eroded to steep-sided platforms embaying the knobs, contains hydrated silica, which may have formed via localized vapor weathering, thin film leaching, or transient water that resulted in surface alteration. These are then overlain by smooth plains with small cones, hypothesized to be mud volcanoes which previous studies have shown have no hydrated minerals. In spite of Acidalia's location within the putative northern ocean, collectively, the data record a history of aqueous processes much like that in the southern highlands with progressively less intensive aqueous chemical alteration from the Noachian to Amazonian.

1. Introduction

In contrast to the southern highlands, the northern plains have been topographically low throughout most of the history of Mars and have served as a depositional center that preserves a geologic record from the Noachian to present. The dichotomy between the southern highlands and northern plains formed in the pre-Noachian [Frey et al., 2002], and the heavily cratered Noachian basement was subsequently overlain by Hesperian and Amazonian lavas [Head et al., 2002] and sediments [Tanaka, 1997]. Presently, the northern plains are largely covered by the Vastitas Borealis Formation generally thought to be sediments derived from highland rocks [Tanaka et al., 2003; Kreslavsky and Head, 2002]. An outstanding question is the prevalence of water in the lowlands, i.e., whether they hosted an ancient ocean for long periods of Mars history [Parker et al., 1993; Head et al., 1999] or were only intermittently flooded by discharge from outflow channels [Tanaka et al., 2001; Carr and Head, 2003]. Inspection of hydrated minerals in the northern plains may help resolve the nature of aqueous processes experienced and improve our understanding of the timing and prevalence of liquid water throughout Mars history.

Previous missions have characterized northern plains composition. Data from the Thermal Emission Spectrometer on board Mars Global Surveyor showed a relatively silica-rich

surface compared to basalts found in the southern highlands [Bandfield et al., 2000; Christensen et al., 2001], which was first proposed to originate from andesitic volcanism [Bandfield et al., 2000] but later suggested to result from aqueous alteration of basalt, ranging from intensive alteration to form phyllosilicates [Wyatt & McSween, 2002] to high-silica coatings on basalt [Kraft et al., 2003; Michalski et al., 2005] or basaltic glass [Horgan and Bell, 2012]. In contrast to the southern highlands, later visible/shortwave-infrared OMEGA data showed no evidence for widespread hydrated silicates in the north. Instead the plains were characterized by a spectral signature typical of coated materials, which is downward sloping to longer wavelengths [Mustard et al., 2005]. Higher spatial resolution data from the Compact Reconnaissance Imaging Spectrometer for Mars (CRISM) onboard Mars Reconnaissance Orbiter enabled recent discoveries of mafic minerals (olivine and pyroxene) associated with crater walls and ejecta [Salvatore et al., 2010] and hydrated silicate detections in large craters [Carter et al., 2010]. These observations collectively suggested a stratigraphy of altered Noachian basement, covered by unaltered Hesperian lavas, covered by later mantling materials; however, the association of all these materials with craters led to some ambiguity in formation history, e.g., with regard to the timing of aqueous alteration. Here we examine the composition and morphology of in-place stratigraphy in the Acidalia Planitia region to better understand the history of geologic processes and aqueous alteration in Mars' northern plains.

2. Geologic context and study area

Acidalia Planitia terrains include small conical and mound-shaped knobs with intriguing origins. The knobs and cones (Figure 1) of Acidalia/Chryse Planitia were first recognized in Viking imagery [Frey et al., 1979] and show diverse sizes and morphology. Here we refer to "knobs" as mound-like features that are 1-5 kilometers across, while "cones" are sub-kilometer features usually with a summit pit (annotated in Figure 1). At least five hypotheses have been proposed for the origin of the cones found within Amazonian terrains, including cinder cones of volcanic origin [Frey and Jarosewich, 1982], rootless cones (or pseudocraters) formed by lava flows interacting with groundwater [Frey et al., 1979; Frey and Jarosewich, 1981], pingos, which are ice-cored mounds formed due to freeze-thaw changes [Lucchitta, 1981], mud volcanoes formed by pressurized release of a liquid slurry of fine-grained materials [Farrand et al., 2005; Oehler and Allen, 2010], or geysers and springs [Farrand et

al., 2005]. Possibly more than one process is involved in the formation of these features [McGill, 2005]. Larger mounds were previously suggested to be eroded remnants from the southern highlands [Tanaka et al., 1997; Nimmo & Tanaka, 2005; McGill, 2005], but recent studies using HiRISE images gave rise to the hypothesis that they form as tuyas in close relationship to chains of small cones within the plains, during volcano-ice interaction [Martinez-Alonso et al., 2011].

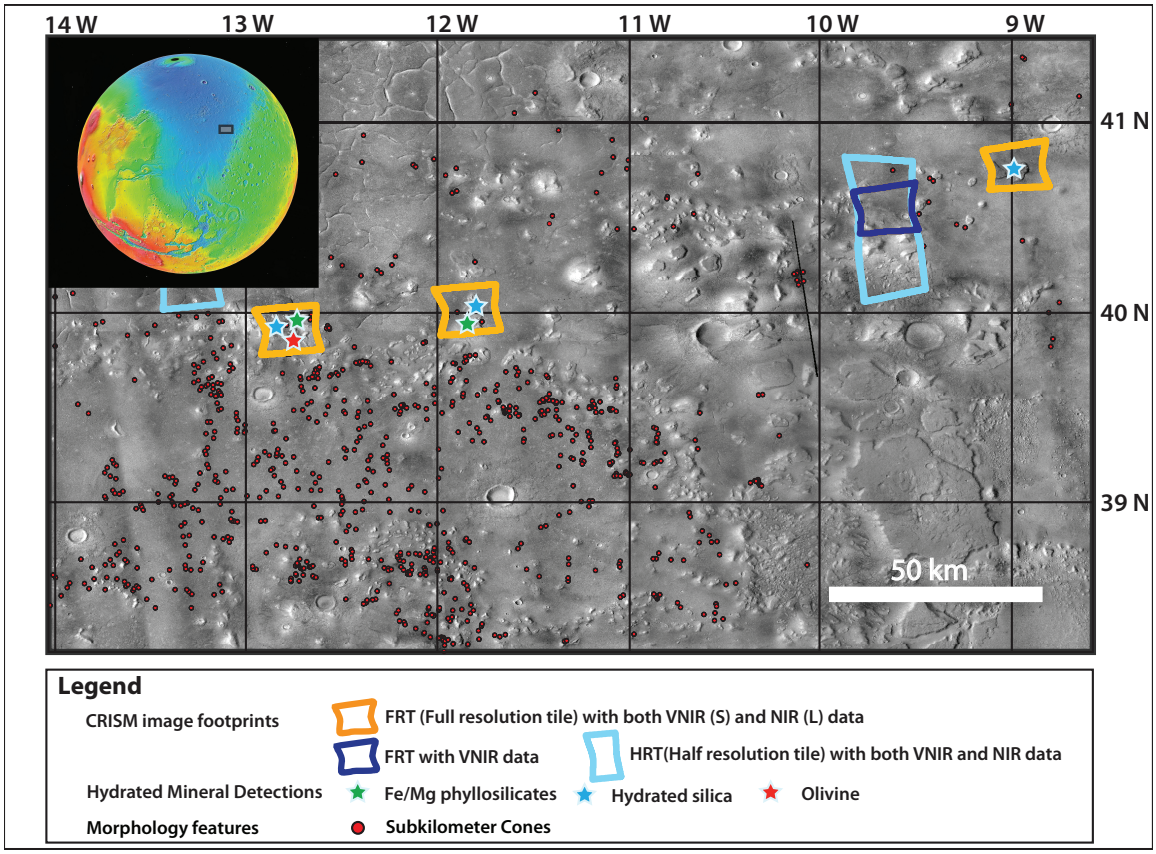

Figure 1. Geological context of the knobby terrains in Acidalia. Background image is a 38 image mosaic with data from Mars Context Camera (CTX); colored boxes show the CRISM image footprints with stars representing hydrated mineral detections. Red dots show the geographical distribution of cones with respect to the knobby terrains.

Previous works that looked at conical features using CRISM data showed ferrous and ferric variations and hints of olivine and augite features but did not find hydrated minerals [Oehler and Allen, 2010; Farrand et al., 2011]. Here we report hydrated mineral detections, including

Fe/Mg phyllosilicates and hydrated silica that are related to the knobby terrains near the eastern margin of the Acidalia Planitia. We also discuss the formation mechanisms for these hydrated minerals and their implications for the geological processes the northern plains have undergone.

3. Methods

Mineral detections are made using near-infrared spectra of wavelengths 1 μm to 2.6 μm from data (Figure 1) acquired by the CRISM imaging spectrometer. Image cubes, converted to I/F [Murchie et al. 2009], were processed using atmospheric correction and noise removal procedures described in Ehlmann et al., [2009]. Spectra derived from pixels in processed CRISM images were averaged over a small area and ratioed to the average spectra of a spectrally "bland" region to highlight the different mineral phases within the target region. High-resolution images taken by the Context Camera (CTX) [Malin et al., 2007], the High Resolution Imaging Science Experiment (HiRISE) [McEwen et al., 2007], and digital elevation models derived from these using NASA Ames Stereo Pipeline [Moratto et al., 2010] were coregistered and overlain with CRISM detections to better understand the geological settings.

4. Minerals identified

Using the ratioed spectra, mafic minerals and hydrated silicates were identified by electronic transition absorptions caused by Fe in octahedral sites and vibrational absorptions caused by overtones and combinations related to H2O and OH in the mineral structure. Three distinct spectral classes were initially identified using parameter maps [Pelkey et al., 2007] in the region near Acidalia/Chryse dichotomy: olivine with a ~1 μm broad band, Fe/Mg phyllosilicates with a ~2.3 μm absorption band, and hydrated silica with a broad 2.2 μm absorption (Figure 2).

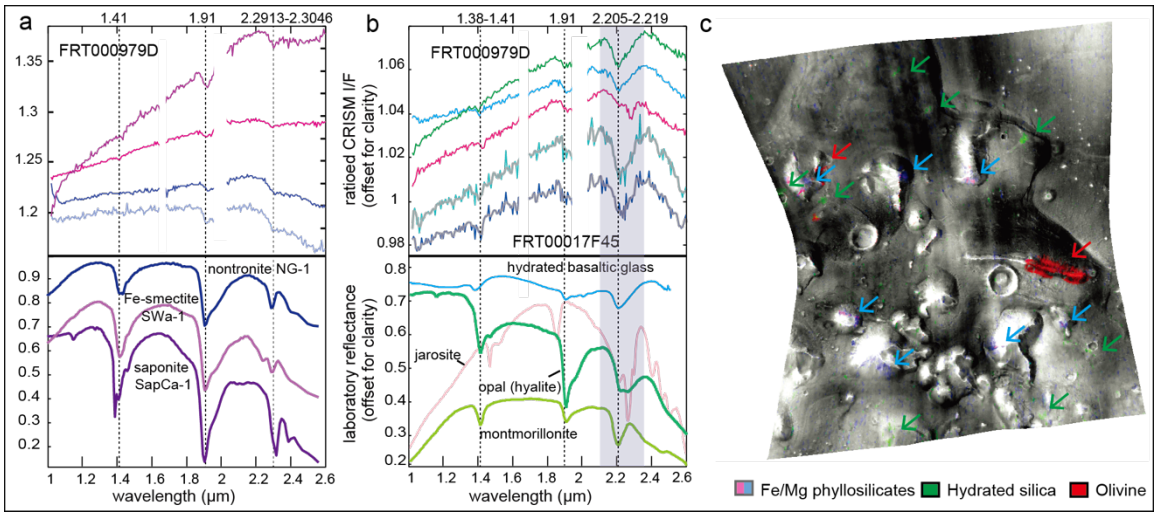

Figure 2. Representative spectra of the hydrated mineral detections in Acidalia knobby terrains. (A) Upper panel: representative Fe/Mg phyllosilicate spectra in the scene. Lower panel: Fe and Mg smectite laboratory spectra. (B) Upper panel: 2 hydrated silica for each image. Pink one is the "doublet" material. Lower panel: laboratory spectra of minerals with 2.2 μm absorption band. Light grey band shows the width of the 2.2 μm band in the detections. (C) CRISM image FRT0000979D with colored parameter [R: OLINDEX2, G: BD2200, B: D2300] showing composition overlain on a grey-scale background. Note the different occurrences of the Fe/Mg phyllosilicates and the hydrated silica.

Olivine is identified by the broad absorption around 1 μm due to electronic transitions. There are three distinctive occurrences of olivine in the study area, and they are confined to local topographically high units with a close relationship to Fe/Mg phyllosilicates.

Fe/Mg phyllosilicates are detected by the 2.3 μm absorption, caused by Fe-OH or Mg-OH vibrations, along with absorption features at 1.4 μm due to the first overtone of OH vibration and 1.9 μm due to H2O combination modes. They most likely fall into the smectite group, where the Fe end-member of the smectite group (nontronite) has a band centered at 2.29 μm while the Mg end-member (saponite) is centered at 2.31-2.32 μm (Figure 2a) [Hunt, 1977; Bishop et al., 2002; Clark et al., 1990; Frost et al., 2002]. The CRISM data reported here fall in between those two end-members. Materials with similar spectral properties are widespread in the southern highlands [Ehlmann et al., 2009; 2011; Poulet et al., 2007; Carter et al., 2013], including elsewhere in Arabia Terra near the dichotomy boundary [Noe Dobrea et al., 2010].

There are also strong variations in the depth of 1.9 μm absorption band, indicating variability in H2O content. Differences in the slope of the spectra shortward of 1.9 μm are possibly due to mixture with a ferrous component, e.g. ferrous olivine that is found in the vicinity, or another Fe-bearing alteration mineral [Bishop et al., 2008; McKeown et al., 2009].

Hydrated silica is detected in three images in the Acidalia region (Figure 1) identified by a characteristic vibrational absorption band at ~2.21 μm (Figure 2b), caused by overlapping bands at 2.21 and 2.26 μm from Si-OH and H-bound Si-OH respectively [Anderson and Wickersheim, 1964; Milliken et al., 2008; Skok et al., 2010; Ehlmann et al., 2009]. Absorptions at 1.4 and 1.9 μm due to H2O are also present. The CRISM data all show a characteristic wide 2.2 μm absorption extending from 2.16 and 2.41 μm, distinct from Al-OH vibrational absorptions (e.g. in montmorillonite), which are much narrower (Figure 2b). Studies of laboratory reflectance spectra [Anderson and Wickersheim, 1964; Rice et al., 2013] of silica-rich materials show that the H2O content and form of H2O/OH present in silica-rich materials can significantly affect the band center (e.g. 1.41 to 1.38 μm) and band ratios (e.g. 2.21/2.26 μm) of major absorption features, for example, allowing hydrated glass to be distinguished from opal. For example, we observe shifts in the absorption near 1.4 μm in the CRISM spectra, possibly related to differences in water content (Figure 2b). However, in Acidalia, CO2 atmospheric bands obscure the details of the 1.9 μm absorptions, and the 1.4 and 2.2 μm band centers occur at wavelengths found in multiple types of high-silica phases, so we are not able to make unique interpretation of hydrated silica phase from the spectral analysis.

In one location, among the hydrated minerals mapped with the band depth at 2.2 μm (Figure 2b), is a spectrum similar to "doublet material" found in Valles Marineris [Roach et al., 2010] with absorption features at ~1.42 μm, ~1.92 μm, and a sharp doublet at 2.205–2.218μm and 2.265–2.278 μm. Mixtures of Fe/Mg smectite and hydrated silica were considered, as both are endmembers present in our scene, but the Fe/Mg-OH wavelength center is at longer wavelengths. Sulfates like jarosite seem to be a close match, but the doublet is shifted to longer wavelengths in CRISM data vs. terrestrial laboratory data. A plausible model would be poorly crystalline Fe–SiO2 phase due to either acid leaching or neoformation of a smectite as proposed in Roach et al. [2010].

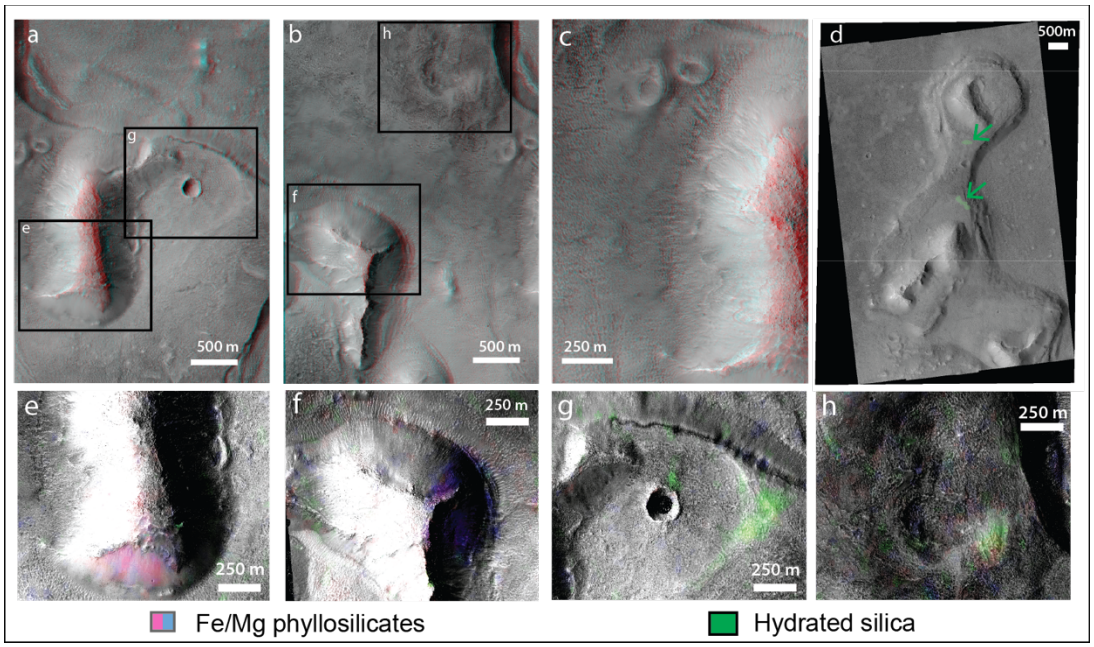

Figure 3. Unit relationship shown on HiRISE imagery. (A, B) Stereo anaglyph images from HiRISE PSP_009985_2205 and PSP_009708_2205 in the scene of CRISM image FRT0000979D. (C, D) The occurrences of Fe/Mg phyllosilicates on the slope of knobs. (E-G) Hydrated silica detections on the surrounding plains unit, occurring near impact crater (E), on local topographical high (F), and on the kinks of slopes in the plain unit (G).

5. Geomorphic setting

In the survey of Acidalia Planitia, of special interest are the three images with hydrated mineral detections. Within the knobby terrains, three morphologically different units can be discerned on the basis of distinct morphology and mineralogy (Figure 2c, 3a-b). The first unit consists of the knobs where Fe/Mg phyllosilicates and olivine are detected in discontinuous patches on the slope and ridges (Figure 3e-f, see Figure 3a-b for context) with no detections on the surrounding units. Olivine is also found within a 2.5-km east-west linear feature (~100m higher than surrounding unit according to MOLA and the HiRISE DEM). Detections of both Fe/Mg phyllosilicates and olivine are patchily distributed in the knobs, rather than pervasive. There is no preferred direction on the knob for Fe/Mg phyllosilicates

or olivines to occur and no obvious cover is being removed to reveal smectite or olivine-bearing materials, which indicate the patchiness may be a characteristic of the bedrock itself.

The knobs are embayed by a surrounding steep-sided plains unit (Figure 3c), which forms a platform around the knobs and within which the hydrated silica is detected (Figure 3a-b). There is no silica detection related to the knobs themselves. Instead, silica is restricted to local topographic highs or inflections in slope in the lower unit that embays the knobs. The detections themselves are discontinuous and patchy (Figure 3d, g-h), but the overall distribution extends to three CRISM images ~160 km apart. The occurrence of the "doublet" material coexists with hydrated silica in the unit embaying the knobs.

In total there are 9 discrete detections of Fe/Mg phyllosilicates and 11 detections of hydrated silica in the high-resolution data from the 300 km2 study area. The total area of Fe/Mg phyllosilicates covers about 1.041 km2 and hydrated silica ~ 0.71 km2. The third unit is the overlying smooth plains unit with subkilometer cones, which is the youngest terrain in this region and has with no hydrated mineral detections.

6. Discussion

Two hypotheses for the formation of the knobs have been proposed: terrestrial tuyas (emergent sub-ice volcanoes) or eroded remnants of the southern highlands-northern lowlands topographic dichotomy. Tuya formation was recently proposed because some of the bigger mesas form in chains with small conical features and might have been formed in a volcanic setting with glacier on top of the surface [Martinez-Alonso et al., 2011]. Extensive alteration to hydrated minerals and pillow lavas would be expected in such a scenario with melting of the ice sheet during eruption, as is typical for terrestrial tuyas [Bishop et al., 2002]. The observed patchiness of hydrated minerals and existence of apparently unaltered olivine are not consistent with large-scale volcano-ice interaction. On the other hand, Fe/Mg phyllosilicates are the most common hydrated mineral of Noachian southern highland materials, and patchiness of alteration is a characteristic of the highland phyllosilicates [Mustard et al., 2008], perhaps caused by preferential alteration along fractures during hydrothermalism or diagenesis. Consequently, the mineralogical composition is consistent with Acidalia's knobs being eroded Noachian highlands material, in agreement with Tanaka's

[2005] geologic mapping. The olivine-rich linear feature might be an eroded remnant of a dike.

The overlying and embaying units are more enigmatic. These units bearing hydrated silica are disconnected with the phyllosilicate-bearing knobs and likely formed in a different aqueous geochemical environment. The observed patchiness of the silica detections might result from the process that generated the hydrated mineral, i.e. concentration in localized areas, or might be the result of detection bias due to mantling or dissimilar rock textures. Here we favor that the detections are revealing the uneven distribution of hydrated silica within the surrounding plains unit, for in HiRISE images no mantling materials are observed, and the surfaces next to the hydrated silica detections with spectrally neutral signatures have similar textures at the resolution of HiRISE images.

Due to the highly mobile nature of silica [McLennan, 2003], the detected hydrated silica could form in multiple types of environments with varying amounts of water (Table 1). These include forming as hydrated silicate glass in volcanic ash/glass deposit [e.g. Stolper, 1982], vapor weathering from acid gases [e.g. Golden et al., 2005; Schiffman et al., 2006; Seelos et al., 2010], thin film leaching and coating formation [e.g. Chemtob et al., 2010; Golden et al., 2005,], in-situ silicate weathering with liquid water [e.g. McLennan, 2003; Squyres et al., 2008], and direct precipitation from a silica-saturated water body [e.g. Rodgers et al., 2004; Preston et al., 2008]. For each of these five scenarios, deposit characteristics would differ, in terms of type of silica, thickness, distribution and relation to topography (Table 1). The observed patchiness and discontinuous nature of silica detections in Acidalia make it unlikely the materials formed as a volcanic ash deposit, or from igneous melts, in which case the silica would be more widely distributed and definitively associated with a particular unit. The occurrence at local topographic highs is not consistent with the hypothesis of direct precipitation in a standing body of water. Therefore, the plausible conditions for hydrated silica to form are intermediate with regard to implications for the prevalence of water: vapor weathering, thin film leaching, or silicate weathering by surface or subsurface water. The presence of the “doublet” material in the same unit as the hydrated silica may indicate an acidic environment [Roach et al., 2010].

Table 1 Formation scenarios of hydrated silica

Formation Scenarios	Amount of water	Type of Silica	Continuity	Distribution	Thick-ness	Topography
Ash/Igneous melt	Low	Hydrated silicate glass	Continuous	Regional, related to volcanism	m~km	Fills topography
Vapor weathering		Opal A Opal C/CT	Discontinuous	Local, related to vapor fissures	μm~mm	Independent of topography
Thin film leaching		Hydrated silicate glass Opal A Opal C/CT	Discontinuous	Regional — local	μm~mm	Independent of topography
Silicate weathering		Opal A Opal C/CT	Patchy to Continuous	Regional — local	mm~m	Follows topographic surface
Direct precipitation	High	Opal A Opal C/CT Chalcedony	Continuous	Patchy, Depending on water body size	m~km	Concentrated in topographical low

These hydrated minerals have put further constraints on the origin of the knobs and surrounding unit and erosional and depositional processes within the northern plains. The integrated compositional stratigraphy of the knobby terrains of Acidalia implies a geological history that starts from ancient Noachian crustal materials (Figure 4):

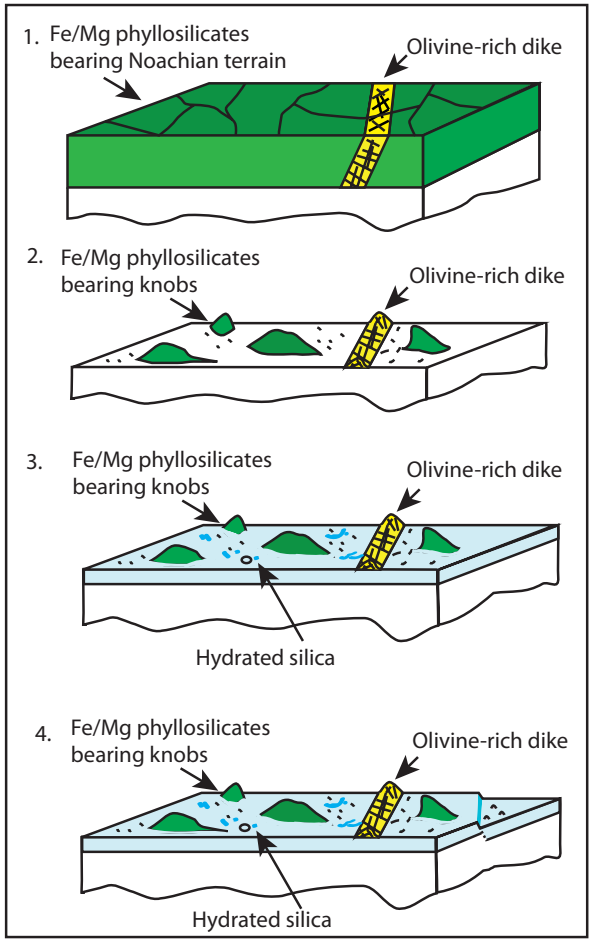

Figure 4. Schematic picture for geological history of the knobby terrains in Acidalia.

First, ancient Noachian (or pre-Noachian) crust was altered into patchily distributed phyllosilicates. As the dichotomy boundary was modified by mass wasting, impacts, outflow channels and aeolian processes, the Noachian crust was fractured, eroded into discrete but spatially aggregated knobs, and the overall dichotomy boundary retreated southward. For similar knobby morphology elsewhere, the "fretting" process can be initiated by fractures, subsurface piping, void collapse or significant aeolian deflation carving into friable sediments [Irwin et al., 2004]. In Acidalia, however, the knobs are likely more competent than friable sediments and have a higher dielectric constant than the rest of the lowland materials [Mouginot et al., 2012].

Resurfacing processes including mass wasting and volcanic activity then created sediment and lavas that fill in the northern plains. High resolution HiRISE stereo images show that the

steep-sided platform unit that surrounds the knobs has diverse texture and undulating topography, consistent with a complex sedimentary or volcanic history. Localized aqueous activity resulted in the formation of hydrated silica and the hydrated "doublet" material in the platform unit that surrounds the knobs. Thin film leaching, vapor weathering or in situ weathering of silicates in acidic environment may be responsible for the localized aqueous events. The geographic restriction of silica disfavors extensive water bodies (e.g. from interaction with an ocean or an ice sheet), instead favoring environments like springs or steam vents.

Then, sediments undergo collapse and create scarps that define the platform unit that surrounds the knobs. This boundary creates a bench-like morphology and is found to be spatially correlated with local depressions, which are proposed to be formed by volatile-driven collapse and/or basal sapping [Tanaka et al., 2003] rather than wave-cut erosion [Parker et al., 1993]. In this analysis and in previous studies [Farrand et al., 2011; Oehler et al., 2010], the topographically lower unit with pitted cones and polygonal troughs lacks hydrated silicate mineral detections, which suggests that the lower unit formed after a decrease in the prevalence or longevity of near-surface liquid water. Collectively, this succession of Noachian, Fe/Mg phyllosilicate-bearing materials, younger hydrated silica-bearing materials, and still younger terrains with no hydrated silicate detections is similar to time-succession of minerals found in the southern highlands, in spite of evidence for more volcano-ice interaction and location of the study area within the basin of the proposed northern ocean.

7. Conclusions

Fe/Mg phyllosilicates and hydrated silica have been detected within discrete strata in the knobby terrains in Acidalia and related to units where different morphologic features are present. Fe/Mg phyllosilicates and olivine occur in knobs that are inferred to be eroded remnants from the southern highlands. They are embayed by a platform of surrounding plains with hydrated silica detections, which formed later in a different, possibly more acidic aqueous environment where the availability of water was geographically localized. The hydrated silica detected may have formed via vapor weathering, thin film leaching, or silicate weathering by liquid water, while the scenarios of volcanic ash/igneous melt deposit and

direct precipitation from water bodies are excluded based on the topography and distribution. This study of Acidalia's compositional stratigraphy refines our understanding of the geologic history of Mars' northern plains, and together indicates a declining prevalence of aqueous alteration within the northern lowlands through time.

Acknowledgments: Thanks to Jim Skinner for early discussions about northern plains evolution, Ara Oshagan for CTX mosaic and DEM processing, the MRO science operation teams for collecting the dataset and the constructive comments of Nancy McKeown and one anonymous reviewer, which improved this manuscript. This work was supported by NASA Mars Data Analysis Program award NNX12AJ43G.

References:

Anderson, J. H., and K. A. Wickersheim (1964), Near Infrared Characterization of Water and Hydroxyl Groups on Silica Surfaces, Surf Sci., 2, 252-260, doi: 10.1016/0039-6028(64)90064-0.

Bandfield, J. L., V. E. Hamilton, and P. R. Christensen (2000), A global view of Martian surface compositions from MGS-TES, Science, 287(5458), 1626-1630, doi: 10.1126/science.287.5458.1626.

Bishop, J., J. Madejova, P. Komadel, and H. Froschl (2002), The influence of structural Fe, Al and Mg on the infrared OH bands in spectra of dioctahedral smectites, Clay Miner, 37(4), 607-616, doi: 10.1180/0009855023740063.

Bishop, J. L., P. Schiffman, and R. Southard (2002), Geochemical and mineralogical analyses of palagonitic tuffs and altered rinds of pillow basalts in Iceland and applications to Mars, Geological Society, London, Special Publications, 202(1), 371-392, doi:10.1144/gsl.sp.2002.202.01.19.

Bishop, J. L., et al. (2008), Phyllosilicate diversity and past aqueous activity revealed at Mawrth Vallis, Mars, Science, 321(5890), 830-833.

Carter, J., F. Poulet, J. P. Bibring, and S. Murchie (2010), Detection of Hydrated Silicates in Crustal Outcrops in the Northern Plains of Mars, Science, 328(5986), 1682-1686, doi: 10.1126/science.1189013.

Carter, J., F. Poulet, J. P. Bibring, N. Mangold, and S. Murchie (2013), Hydrous minerals on Mars as seen by the CRISM and OMEGA imaging spectrometers: Updated global view, Journal of Geophysical Research: Planets, 118(4), 831-858, doi:10.1029/2012je004145.

Carr, M. H., and J. W. Head (2003), Oceans on Mars: An assessment of the observational evidence and possible fate, J Geophys Res-Planet, 108(E5), doi: 10.1029/2002je001963.

Chemtob, S. M., B. L. Jolliff, G. R. Rossman, J. M. Eiler, and R. E. Arvidson (2010), Silica coatings in the Ka'u Desert, Hawaii, a Mars analog terrain: A micromorphological, spectral, chemical, and isotopic study, J Geophys Res-Planet, 115, E04001. doi: 10.1029/2009je003473.

Christensen, P., R. Morris, M. Lane, J. Bandfield, and M. Malin (2001), Global mapping of Martian hematite mineral deposits: Remnants of water-driven processes on early Mars, Journal of Geophysical Research: Planets (1991–2012), 106(E10), 23873-23885.

Clark R. N., King, T. V. V., Klejwa, M., Swayze, G. A. (1990), High Spectral Resolution Reflectance Spectroscopy of Minerals, J. Geophys. Res., 95, B8, 12,653–12,680

Ehlmann, B. L., et al. (2009), Identification of hydrated silicate minerals on Mars using MRO-CRISM: Geologic context near Nili Fossae and implications for aqueous alteration, Journal of Geophysical Research: Planets, 114, E00d08, doi: 10.1029/2009je003339.

Ehlmann, B. L., J. F. Mustard, S. L. Murchie, J. P. Bibring, A. Meunier, A. A. Fraeman, and Y. Langevin (2011), Subsurface water and clay mineral formation during the early history of Mars, Nature, 479(7371), 53-60, doi: 10.1038/Nature10582.

Farrand, W. H., L. R. Gaddis, and L. Keszthelyi (2005), Pitted cones and domes on Mars: Observations in Acidalia Planitia and Cydonia Mensae using MOC, THEMIS, and TES data, Journal of Geophysical Research (Planets), 110, 5005. doi:10.1029/2004JE002297.

Farrand, W. H., M. D. Lane, B. R. Edwards, and R. A. Yingst (2011), Spectral evidence of volcanic cryptodomes on the northern plains of Mars, Icarus, 211(1), 139-156, doi: 10.1016/J.Icarus.2010.09.006.

Frey, H., B. L. Lowry, and S. A. Chase (1979), Pseudo-Craters on Mars, Journal of Geophysical Research, 84, 8075-8086, doi: 10.1029/Jb084ib14p08075.

Frey, H., and M. Jarosewich (1982), Sub-Kilometer Martian Volcanos - Properties and Possible Terrestrial Analogs, Journal of Geophysical Research, 87(Nb12), 9867-9879, doi: 10.1029/Jb087ib12p09867.

Frey, H. V., J. H. Roark, K. M. Shockey, E. L. Frey, and S. E. H. Sakimoto (2002), Ancient lowlands on Mars, Geophys Res Lett, 29(10), doi: 1384. 10.1029/2001gl013832.

Frost, R. L., J. T. Kloprogge, and Z. Ding (2002), Near-infrared spectroscopic study of nontronites and ferruginous smectite, Spectrochim Acta A, 58(8), 1657-1668, doi: 10.1016/S1386-1425(01)00637-0.

Golden, D. C., D. W. Ming, R. V. Morris, and S. A. Mertzman (2005), Laboratory-simulated acid-sulfate weathering of basaltic materials: Implications for formation of sulfates at Meridiani Planum and Gusev crater, Mars, J Geophys Res-Planet, 110(E12), E12s07. doi: 10.1029/2005je002451.

Head, J. W., M. A. Kreslavsky, and S. Pratt (2002), Northern lowlands of Mars: Evidence for widespread volcanic flooding and tectonic deformation in the Hesperian Period, Journal of Geophysical Research: Planets, 107(E1), 3-1-3-29, doi:10.1029/2000JE001445.

Horgan, B., and J. F. Bell III (2012), Widespread weathered glass on the surface of Mars, Geology, 40(5), 391-394, doi:10.1130/g32755.1.

Hunt, G. R. (1977), Spectral Signatures of Particulate Minerals in Visible and Near Infrared, Geophysics, 42(3), 501-513, doi: 10.1190/1.1440721.

Irwin, R.P., T. R. Watters, A. D. Howard, J. R. Zimbelman, (2004), Sedimentary resurfacing and fretted terrain development along the crustal dichotomy boundary, Aeolis Mensae, Mars. J. Geophys. Res., 109, E09011, doi:10.1029/2004JE002248

Kraft, M. D., J. R. Michalski, and T. G. Sharp (2003), Effects of pure silica coatings on thermal emission spectra of basaltic rocks: Considerations for Martian surface mineralogy, Geophys Res Lett, 30(24).

Kreslavsky, M. A., and J. W. Head (2002), Fate of outflow channel effluents in the northern lowlands of Mars: The Vastitas Borealis Formation as a sublimation residue from frozen ponded bodies of water, J Geophys Res-Planet, 107(E12), 5121, doi: 10.1029/2001je001831.

Lucchitta, B. K. (1981), Mars and Earth - Comparison of Cold-Climate Features, Icarus, 45(2), 264-303, doi: 10.1016/0019-1035(81)90035-X.

Malin, M. C., et al. (2007), Context Camera Investigation on board the Mars Reconnaissance Orbiter, J Geophys Res-Planet, 112(E5), E05s04, doi: 10.1029/2006je002808.

McEwen, A. S., et al. (2007), Mars Reconnaissance Orbiter's High Resolution Imaging Science Experiment (HiRISE), J Geophys Res-Planet, 112(E5), E05s02, doi: 10.1029/2005je002605.

McKeown, N. K., J. L. Bishop, E. Z. N. Dobrea, B. L. Ehlmann, M. Parente, J. F. Mustard, S. L. Murchie, G. A. Swayze, J. P. Bibring, and E. A. Silver (2009), Characterization of phyllosilicates observed in the central Mawrth Vallis region, Mars, their potential formational processes, and implications for past climate, J Geophys Res-Planet, 114, doi 10.1029/2008je003301.

McGill, G.E. (2005), Geologic map of Cydonia Mensae-southern Acidalia Planitia, Mars: Quadrangles 40007, 40012, 40017, 45007, 45012, and 45017, U.S. Geol. Survey, Geol. Invest. Map I-2811.

McLennan, S. M. (2003), Sedimentary silica on Mars, Geology, 31(4), 315-318, doi: 10.1130/0091-7613(2003)031<0315:Ssom>2.0.Co;2.

Martinez-Alonso, S., M. T. Mellon, M. E. Banks, L. P. Keszthelyi, A. S. McEwen, and H. Team (2011), Evidence of volcanic and glacial activity in Chryse and Acidalia Planitiae, Mars, Icarus, 212(2), 597-621, doi: 10.1016/J.Icarus.2011.01.004.

Michalski, J. R., M. D. Kraft, T. G. Sharp, L. B. Williams, and P. R. Christensen (2005), Mineralogical constraints on the high-silica martian surface component observed by TES, Icarus, 174(1), 161-177, doi: 10.1016/J.Icarus.2004.10.022.

Milliken, R. E., et al. (2008), Opaline silica in young deposits on Mars, Geology, 36(11), 847-850, doi: 10.1130/G24967a.1.

Moratto, Z. M., Broxton, M. J., Beyer, R. A., Lundy, M. and K. Husmann (2010), Ames Stereo Pipeline, NASA's Open Source Automated Stereogrammetry Software, 41st LPSC, 2364.

Mouginot, J., A. Pommerol, P. Beck, W. Kofman, and S. M. Clifford (2012), Dielectric map of the Martian northern hemisphere and the nature of plain filling materials, Geophys Res Lett, 39, L02202. doi 10.1029/2011gl050286.

Murchie, S. L., et al. (2009), Compact Reconnaissance Imaging Spectrometer for Mars investigation and data set from the Mars Reconnaissance Orbiter's primary science phase, Journal of Geophysical Research: Planets, 114, E00d07. doi: 10.1029/2009je003344.

Mustard, J. F., F. Poulet, A. Gendrin, J. P. Bibring, Y. Langevin, B. Gondet, N. Mangold, G. Bellucci, and F. Altieri (2005), Olivine and pyroxene, diversity in the crust of Mars, Science, 307(5715), 1594-1597, doi: 10.1126/science.1109098.

Mustard, J. F., et al. (2008), Hydrated silicate minerals on mars observed by the Mars reconnaissance orbiter CRISM instrument, Nature, 454(7202), 305-309, doi: 10.1038/Nature07097.

Nimmo, F., and K. Tanaka (2005), Early crustal evolution of mars, Annual Review of Earth and Planetary Sciences, 33, 133-161, doi: 10.1146/Annurev.Earth.33.092203.122637.

Noe Dobrea, E. Z., et al. (2010), Mineralogy and stratigraphy of phyllosilicate-bearing and dark mantling units in the greater Mawrth Vallis/west Arabia Terra area: Constraints on geological origin, J. Geophys. Res., 115, E00D19, doi:10.1029/2009JE003351.

Oehler, D. Z., and C. C. Allen (2010), Evidence for pervasive mud volcanism in Acidalia Planitia, Mars, Icarus, 208(2), 636-657, doi: 10.1016/J.Icarus.2010.03.031.

Parker, T. J., D. S. Gorsline, R. S. Saunders, D. C. Pieri, and D. M. Schneeberger (1993), Coastal Geomorphology of the Martian Northern Plains, J Geophys Res-Planet, 98(E6), 11061-11078, doi: 10.1029/93je00618.

Pelkey, S. M., et al. (2007), CRISM multispectral summary products: Parameterizing mineral diversity on Mars from reflectance, J Geophys Res-Planet, 112(E8), E08s14. doi: 10.1029/2006je002831.

Poulet, F., C. Gomez, J.-P. Bibring, Y. Langevin, B. Gondet, P. Pinet, G. Belluci, and J. Mustard (2007), Martian surface mineralogy from Observatoire pour la Mine´ralogie, l'Eau, les Glaces et l'Activite´ on board the Mars Express spacecraft (OMEGA/MEx): Global mineral maps, J. Geophys. Res., 112, E08S02, doi:10.1029/2006JE002840.

Preston, L. J., G. K. Benedix, M. J. Genge, and M. A. Sephton (2008), A multidisciplinary study of silica sinter deposits with applications to silica identification and detection of fossil life on Mars, Icarus, 198(2), 331-350, doi: 10.1016/J.Icarus.2008.08.006.

Rice, M. S., E. A. Cloutis, J. F. Bell, D. L. Bish, B. H. Horgan, S. A. Mertzman, M. A. Craig, R. W. Renaut, B. Gautason, and B. Mountain (2013), Reflectance spectra diversity of silica-rich materials: Sensitivity to environment and implications for detections on Mars, Icarus, 223(1), 499-533, doi: 10.1016/J.Icarus.2012.09.021.

Roach, L. H., J. F. Mustard, G. Swayze, R. E. Milliken, J. L. Bishop, S. L. Murchie, and K. Lichtenberg (2010), Hydrated mineral stratigraphy of Ius Chasma, Valles Marineris, Icarus, 206(1), 253-268, doi: 10.1016/J.Icarus.2009.09.003.

Rodgers, K. A., et al. (2004), Silica phases in sinters and residues from geothermal fields of New Zealand, Earth-Science Reviews, 66(1–2), 1-61, doi:10.1016/j.earscirev.2003.10.001.

Salvatore, M. R., J. F. Mustard, M. B. Wyatt, and S. L. Murchie (2010), Definitive evidence of Hesperian basalt in Acidalia and Chryse planitiae, J. Geophys. Res., 115, E07005, doi:10.1029/2009JE003519

Seelos, K. D., R. E. Arvidson, B. L. Jolliff, S. M. Chemtob, R. V. Morris, D. W. Ming, and G. A. Swayze (2010), Silica in a Mars analog environment: Ka'u Desert, Kilauea Volcano, Hawaii, J Geophys Res-Planet, 115, E00d15. doi: 10.1029/2009je003347.

Schiffman, P., R. Zierenberg, N. Marks, J. L. Bishop, and M. D. Dyar (2006), Acid-fog deposition at Kilauea volcano: A possible mechanism for the formation of siliceous-sulfate rock coatings on Mars, Geology, 34(11), 921-924, doi: 10.1130/G22620a.1.

Skok, J. R., J. F. Mustard, S. L. Murchie, M. B. Wyatt, and B. L. Ehlmann (2010), Spectrally distinct ejecta in Syrtis Major, Mars: Evidence for environmental change at the Hesperian-Amazonian boundary, J. Geophys. Res., 115, E00D14, doi:10.1029/2009JE003338.

Squyres, S. W., et al. (2008), Detection of silica-rich deposits on Mars, Science, 320(5879), 1063-1067, doi: 10.1126/Science.1155429.

Stolper, E. (1982), Water in silicate glasses: An infrared spectroscopic study: Contributions to Mineralogy and Petrology, v. 81, p. 1–17, doi: 10.1007/BF00371154.

Tanaka, K. L. (1997), Sedimentary history and mass flow structures of Chryse and Acidalia Planitiae, Mars, J Geophys Res-Planet, 102(E2), 4131-4149, doi: 10.1029/96je02862.

Tanaka, K. L., W. B. Banerdt, J. S. Kargel, and N. Hoffman (2001), Huge, CO2-charged debris-flow deposit and tectonic sagging in the northern plains of Mars, Geology, 29(5), 427-430.

Tanaka, K. L., J. A. Skinner, T. M. Hare, T. Joyal, and A. Wenker (2003), Resurfacing history of the northern plains of Mars based on geologic mapping of Mars Global Surveyor data, J Geophys Res-Planet, 108(E4), 8043, doi: 10.1029/2002je001908.

Wyatt, M. B., and H. Y. McSween (2002), Spectral evidence for weathered basalt as an alternative to andesite in the northern lowlands of Mars, Nature, 417, 263–266.

Chapter 4

AQUEOUS PROCESSES FROM DIVERSE HYDRATED MINERALS IN THE VICINITY OF AMAZONIAN-AGED LYOT CRATER

L. Pan and B. L. Ehlmann

Abstract

Lyot crater is the largest and deepest impact crater in the northern lowlands of Mars, and the impact event may have had significant influence on the Amazonian climate. Previous works documented the morphological features in and surrounding Lyot crater to understand the hydrological activity associated with the impact, including channels emanating from near the ejecta blanket. Here, we use images acquired predominantly by the Compact Reconnaissance Imaging Spectrometer for Mars (CRISM) on board the Mars Reconnaissance Orbiter (MRO) to investigate the mineralogical record in Lyot and its surroundings. We combine with high resolution imagery data from Context Camera (CTX) and High Resolution Imaging Science Experiment (HiRISE) to understand the aqueous processes and their timing. We find diverse hydrated minerals, including Fe/Mg phyllosilicate, chlorite, illite/muscovite, prehnite in the central ring, crater floor, crater rim, and ejecta of Lyot crater. In small craters next to Lyot, we find similar mineralogy in two craters to the west of Lyot, and chlorite in two craters to the east. The diverse mineralogy specifically of the exposure and distribution of the minerals in Lyot crater suggests pre-existing subsurface alteration. The occurrences of prehnite with chlorite and illite/muscovite probably formed in a pre-impact hydrothermal system with burial diagenesis in the Noachian-Hesperian. These hydrated minerals are then exposed by the Lyot impact event and the other small craters in the early Amazonian. The Lyot impact may have induced the channels to the north of Lyot, but no direct evidence of aqueous alteration has been observed associated with the channels. In two small, infilled craters, chlorite detections indicate an episode of sediment transport post-impact. The sinuous channels

within Lyot, diverted by bedrock units with hydrated mineral detections, likely represent the last stage of water activity in Lyot crater, not associated with mineralization.

1. Introduction

Mars throughout the Amazonian period is thought to be relatively cold and dry like the present day Mars with few indication of surface water activity, as opposed to the widespread valley networks and large outflow channels which formed in Noachian and early Hesperian periods. The widespread hydrated mineral detections made possible by instruments like the Observatoire pour la Minéralogie, l'Eau, les Glaces et l'Activité (OMEGA) on board Mars Express and the Compact Reconnaissance Imaging Spectrometer for Mars (CRISM) on board Mars Reconnaissance Orbiter (MRO) also found that the youngest surfaces on Mars lack hydrated mineral detections at orbital scale [Bibring et al., 2006; Mustard et al., 2008; Carter et al., 2013; Ehlmann and Edwards, 2014]. Together, this indicates that by the start of Amazonian period, the widespread, global hydrological activity has been taken over by a cold and arid environment. However, emerging evidence from orbital observations suggests that Mars is more active than previously thought in the Amazonian period with a variety of geologic processes, including the widespread mantling of units in the mid-latitudes of Mars [Mustard et al., 2001; Head et al., 2003]; formation of gullies on crater central peaks and walls [Malin and Edgett, 2000; Mellon and Phillips, 2001], and the activity of recurring slope lineae [Ojha et al., 2015]. Understanding the forms of water-related activity in the Amazonian is crucial to our understanding of the changing hydrological cycle and climate on Mars.

One possible form of aqueous activity in the Amazonian age is the melting and circulation of ground water in the subsurface by impacts with enough energy [Abramov and Kring, 2005; Barnhart et al., 2010]. A global cryosphere with ice stable in the subsurface in the mid- to high- latitudes has been predicted in the Amazonian and is supported by features that are likely glacial in origin, such as lobate debris apron, linear valley fill and concentric crater fill [Squyres, 1978; Lucchitta and Earth, 1981; Head et al., 2006; Dickson et al., 2008, Levy et al., 2007, 2010]. During this period, impact cratering and volcanism may have been the most important events in dramatically shaping the global climate and may have created localized habitable environments on the surface of Mars.

Lyot crater is the largest (diameter ~220 km) and deepest impact crater in the northern lowlands of Mars. The impact event is dated to be Early Amazonian, after the cessation of ancient valley network activity [Dickson et al., 2009]. As the youngest large impact in the northern lowlands located near dichotomy boundary, close to Deuteronilus Mensae where subsurface ice has been detected [Plaut et al., 2009; 2010, Baker and Carter, 2017], the impact event could have interacted with the local cryosphere and induced significant effect on the global climate in the Amazonian [Russel and Head, 2002]. Similar sized terrestrial craters include Chicxulub crater impacted at the K-T boundary. Such energetic impact could have caused a series of effects on climate, including the generation of a localized hydrothermal system, dust loading, release of subsurface CO_2 and H_2O into atmosphere, and release of SO_2, causing tsunami, and triggering flood basalt emplacement [Pope et al., 1997; Toon et al., 1997; Kring et al., 2007; Schulte et al., 2010].

In the recent mineralogy survey of the northern lowlands' impact craters [Pan et al., *in revision*], the vicinity of Lyot crater was found to have spatially-concentrated exposures of diverse hydrated minerals relative to the entire northern lowlands, including phases in addition to chlorite-prehnite detections mapped by Carter et al., [2010]. The origin of the hydrated minerals near Lyot crater is intriguing and may result from disrupted stratigraphy that was altered locally pre-impact, impact-induced hydrothermal alteration, or post-impact modification from fluvial/glacial activity. In this work, we utilize combined analysis of multiple Mars datasets to better understand the origin of hydrated minerals in this region and the timing of their formation relative to Lyot's geologic history. The inferred aqueous processes associated with the hydrated minerals provide new constraints on Mars' climate in the Amazonian-age.

2. Geological context of Lyot and previous work

Lyot crater (50.46^{o}N, 29.31^{o}E) is located close to the dichotomy boundary in the northern lowlands of Mars. To the south of Lyot is the chaos terrain of Deuteronilus Mensae, a region of dissected valleys, mesas, knobs and craters of various origin and age [Lucchitta, 1984; Parker et al., 1989]. Linear valley fills and lobate apron deposits have been found to be widespread in this region and hypothesized to be related to Amazonian glacial deposits [Head et al., 2006; Dickson et al., 2008; Morgan et al., 2009; Baker et al., 2010]. Data from

the Mars SHAllow RADar sounder (SHARAD) data indicate the existence of subsurface ice in lobate debris aprons [Plaut et al., 2009; 2010]).

Lyot is also located in the transition region between Acidalia Planitia and Utopia Planitia in the northern lowlands. The crustal structure near Lyot is likely similar to that of the rest of the northern lowlands [Russell and Head, 2002] with older Noachian terrains, ~1km thick overlying lava flows of Hesperian age, and Amazonian surface materials. Based on the relationship with adjacent units (including crater ejecta overlying Hesperian ridged plains and the mantling materials inside crater) [Russell and Head, 2002] and crater count statistics [Dickson et al., 2009], the Lyot impact is inferred to have formed in Early Amazonian epoch (Figure 1b). Four small craters in the vicinity of Lyot are also found with hydrated mineral detections (Table 1). Among the four craters, *Micoud*, *c308* and *c375* may have formed coeval as or later than Lyot impact, while c194 (mapped in the Hesperian-Noachian transitional unit [Tanaka et al., 2014]) probably formed earlier in the Hesperian and is later covered by mid-late Amazonian crater fill. The age constraints and morphology description will be further discussed in Section 4.2.

Previous studies focused on the morphological features near Lyot crater and the indications of water activity at different points in time. Initial attempts to identify features related to surface waters [Russel and Head, 2002] in Viking, Mars Orbiter Laser Altimeter (MOLA), and Mars Orbiter Camera (MOC) data, did not find channels, valleys, crater wall gullies, crater floor sedimentation, or layered deposits. Later investigations of higher resolution imagery from Mars Reconnaissance Orbiter (MRO) Context Camera (CTX) and The Thermal Emission Imaging System (THEMIS) have been successful in observing water-related features within and outside of Lyot. These include overland scouring channels to the north of Lyot, proposed to be due to the release of a substantial amount of volatiles by the impact itself [Harrison et al., 2009], and km-long fluvial channels within the crater, possibly due to the low elevation of Lyot and relatively higher surface atmospheric pressures that promoted localized melting [Dickson et al., 2009]. In a recent CRISM survey of the impact craters in the northern lowlands, the region in the vicinity of Lyot has been found with significantly higher spatial-density of hydrated minerals than the rest of the lowlands [Pan et al., *in rev*]. The detection of hydrated minerals in Lyot could in part relate to the aqueous processes indicated by geomorphic features and previous

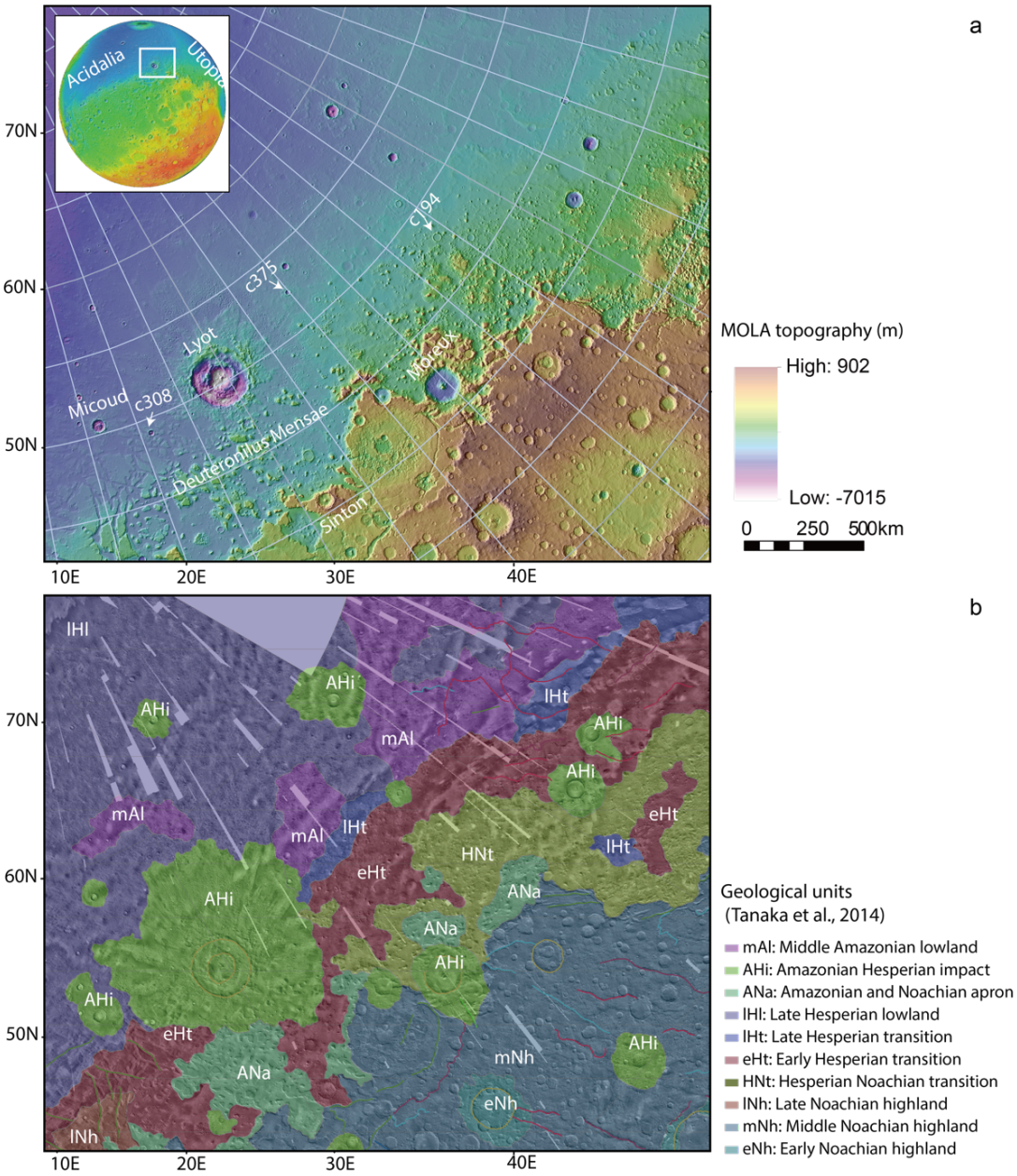

Figure 1: The geologic context of the study region of Lyot crater and its vicinity at the dichotomy boundary: a) Lyot crater at 55°N, 30°E on Mars topographic map (data from Mars Orbital Laser Altimeter in Mars Polar Stereographic Projection) and four small craters investigated in this study (Micoud, c308, c375, c194); b) Geological units mapping of the same region [Tanaka et al., 2014]. Here Amazonian units are in green, and Hesperian units are in red and purple. Except for c194, which is situated in the Hesperian Noachian transitional unit, all the other craters investigated in this study are mapped as Amazonian Hesperian impact (Ahi) unit, overlying the late Hesperian terrains of the northern lowlands.

Table 1: Summary of hydrated mineral detections in Lyot crater and small craters in the vicinity of Lyot. (n.d. = not detected).

crater ID	crater name	latitude	longitude	diameter	central peak detections	crater wall detections	ejecta detections	crater floor	age
05-000000	Lyot	50.457	29.31	220.3	Phyll, chl, pre, ill/mus, hyd	n.d*.	Phyll, chl, ill/mus, hyd	n.d.	Early Amazonian
05-000053	Micoud	50.56	16.345	50.25	ch/pre, phy, ill/mus	n.d.	no coverage	n.d.	Early Amazonian
05-000308	(c308)	49.086	20.993	22.38	silica, hyd, phy	no coverage	n.d.	n.d.	Amazonian , probably younger than Lyot
05-000375	(c375)	52.415	39.861	20.01	chl	n.d.	n.d.	n.d.	Amazonian , probably younger than Lyot
05-000194	(c194)	47.913	53.778	28.38	-	n.d.	n.d.	chl	Hesperian-Amazonian

modeling. The nature of these hydrated mineral-bearing units and related geological processes still need to be better understood through detailed analysis. Here we present our investigation of the relationship between the formation of these hydrated minerals and previously identified water-related surface processes in the vicinity of Lyot.

3. Method

3.1 *Impact craters investigated in this study*

Among all the craters >1km with required CRISM coverage, five craters (Lyot, Micoud, c308, c375, c194) in the Lyot vicinity were identified with one or more classes of hydrated minerals in previous work [Pan et al., *in revision*]. We extracted the geometric data for each of these 5 craters from the Mars Global Crater Database [Robbins et al., 2011a] (Table 1), and the unnamed craters are referred to as the ID in the crater database (i.e. c308, c375, and c194) (Figure 1). Except for the case of c194, which is located in the Hesperian-Noachian transition unit mapped by Tanaka et al [2014], all the craters formed coeval with or post-date Lyot in the Amazonian. The craters have diameters ranging from 20 km to 220 km, with hydrated minerals located in crater central structures, crater walls, ejecta blankets and crater floors (Table 1). In this study, we present a comprehensive analysis of the geological context of hydrated minerals for all five craters in the Lyot vicinity in order to better understand related timing and processes. Using the combination of multiple Mars datasets covering five craters, we construct the geologic history of the region with a focus on water-related processes.

3.2 *Mineralogy identification and mapping*

To identify and map the different hydrated minerals in the Lyot vicinity, we studied the full and half resolution targeted images from CRISM on board MRO. CRISM is a push-broom imaging spectrometer, which acquires visible/shortwave-infrared wavelength reflectance data over two detectors between 0.36-3.92 μm with the highest spatial resolution of 15-19 m/pixel [Murchie et al., 2007]. Data processing follows standard routines, including converting radiance to I/F data, photometric, and atmospheric correction [e.g., Ehlmann et al., 2009]. A new denoise algorithm has been applied after the routine corrections [Pan et al., *in revision*], from which a ratioed image cube, where original

spectra are ratioed to spetrally bland data, is computed and used for identifying mineralogy in quick surveys. The spectra are then compared to original spectra from standard processing steps and standard parameter maps that calculate absorption band depths [Pelkey et al., 2007]. In total, we analyzed 73 CRISM targeted images with L-detector data (FRT, HRL, FRS, and HRS, with resolution 18-36 m/pixel), covering any part of the impact structure of the five craters with previously identified mafic and/or hydrated minerals; and 32 images covering the overland channels to the north of Lyot. A spectral library of different spectral classes in CRISM images was used to compare spectral features among different craters, and the mineralogy of the units with hydrated spectral features are discussed in 4.1.1. We also map all the units with one or more hydrated mineral detections in a Geographic Information System (GIS) project, based on the parameter maps calculated from the denoise algorithm, to better understand their distribution and correlation to morphology.

3.3 Correlation with geomorphology using CTX and HiRISE

To further our understanding of the formation processes for the hydrated mineral bearing units in Lyot and its vicinity, we investigated data from Mars Context Camera (CTX) [Malin et al., 2007] and High Resolution Imaging Science Experiment (HIRISE) [McEwen et al., 2007] instruments, both on board MRO. We constructed a full coverage CTX mosaic over the Lyot crater, using images acquired in greyscale visible at a resolution of ~6 m/pixel and in swaths of ~30 km. The HiRISE instrument, which has a resolution ~30 cm/pixel, also acquired imagery covering part of the five impact craters. HiRISE acquires both greyscale and 3-band color with the greyscale captured in ~6 km wide swaths and the color acquired in ~1.2 km wide swaths in the center of the greyscale image. High spatial resolution of CTX and HiRISE images provide information about the geologic context of the hydrated mineral bearing units. We co-resgister overlapping CTX or HiRISE images with CRISM targets where hydrated mineral detections are made to investigate the correlation of mineralogy to morphological units and better understand the geologic context of these minerals.

3.4 *Investigation of Deuteronilus Mensae*

SHARAD detects subsurface reflectors, including ice deposits in the shallow crust of Mars. Detection of subsurface ice deposits in Deuteronilus Mensae was first reported in one radargram by Plaut et al., [2009]. Potential reflectors have been identified to be extensive in this region in the subsurface through the analysis of SHARAD radargrams compared to clutter simulation. In this study, the morphology of subsurface ice deposits identified in SHARAD data are compared to the hydrated mineral bearing units in CRISM to understand if there is a relationship between the ice and the hydrated minerals. We surveyed 93 CRISM images in the Deuteronilus Mensae region south of Lyot Crater. The mineral detections are overlain on the SHARAD subsurface ice deposit [Plaut et al., 2010]. CTX and HiRISE covering the mineral bearing units are investigated to understand the origin of the hydrated minerals.

4. Results:

4.1 Geological investigation of Lyot Crater

With the analysis of CRISM, CTX, and HiRISE data, we have identified and mapped out associations with rocks and sediments for at least five distinguishable spectral classes associated with Lyot crater to better understand the hydrated mineralogy, distribution, and origin of the hydrated minerals.

4.1.1 Spectral properties and distribution of hydrated minerals

Fe/Mg phyllosilicate detections, likely smectite or mixed-layer smectite-chlorite, are found with weak 2.3-μm absorptions coexisting with 1.9-μm absorptions (Figure 2). The detections of Fe/Mg phyllosilicate in Lyot have weak (~0.5% lower reflectance than continuum in channels between 2.29-2.31 μm) and narrow absorptions in the 2.3-μm region, but the co-existence with weak 1.9-μm bands and the correlation with surface morphology features leads to the inference that these spectra are associated with distinct mineralogical compositions of discreet geologic units.

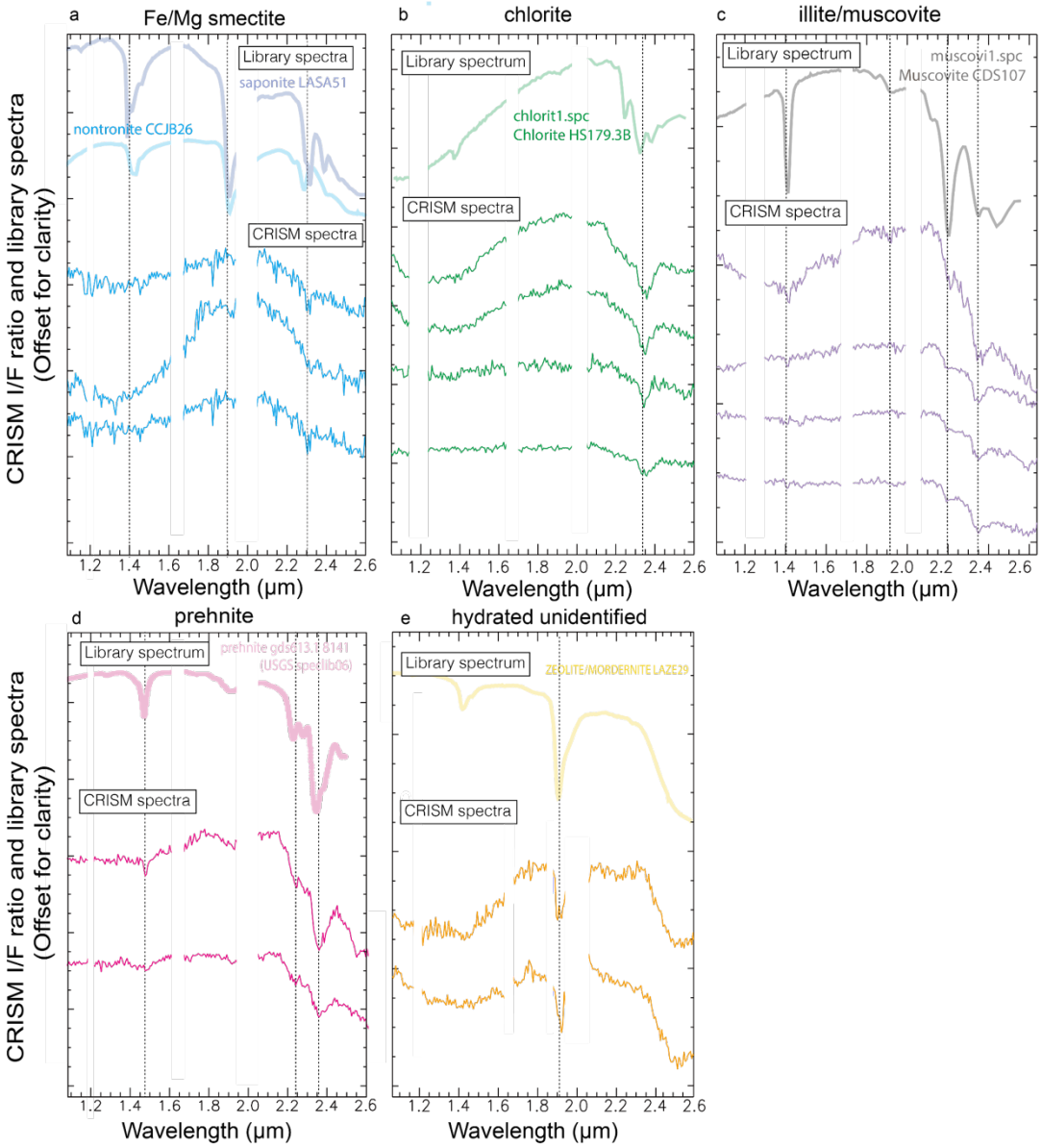

Figure 2: CRISM spectra and associated library spectra of hydrated minerals identified in Lyot crater. a) Fe/Mg phyllosilicate detections, likely smectite or mixed-layer smectite-chlorite, are found with weak 2.3 μm absorptions. b) Chlorite is detected with a strong 2.35 μm absorption band, in most cases lacking 1.9 μm. c) Illite/muscovite is identified with a 2.21 μm coexisting with a 2.35 μm absorption. d) Prehnite detection is found with distinctive 1.47-1.48 μm absorption coexisting with a 2.2 μm and 2.35 μm bands; e) Unidentified hydrated minerals with only distinctive 1.9 μm absorption. Here we show the library spectra of zeolite, which is one of the potential minerals with matching spectral features.

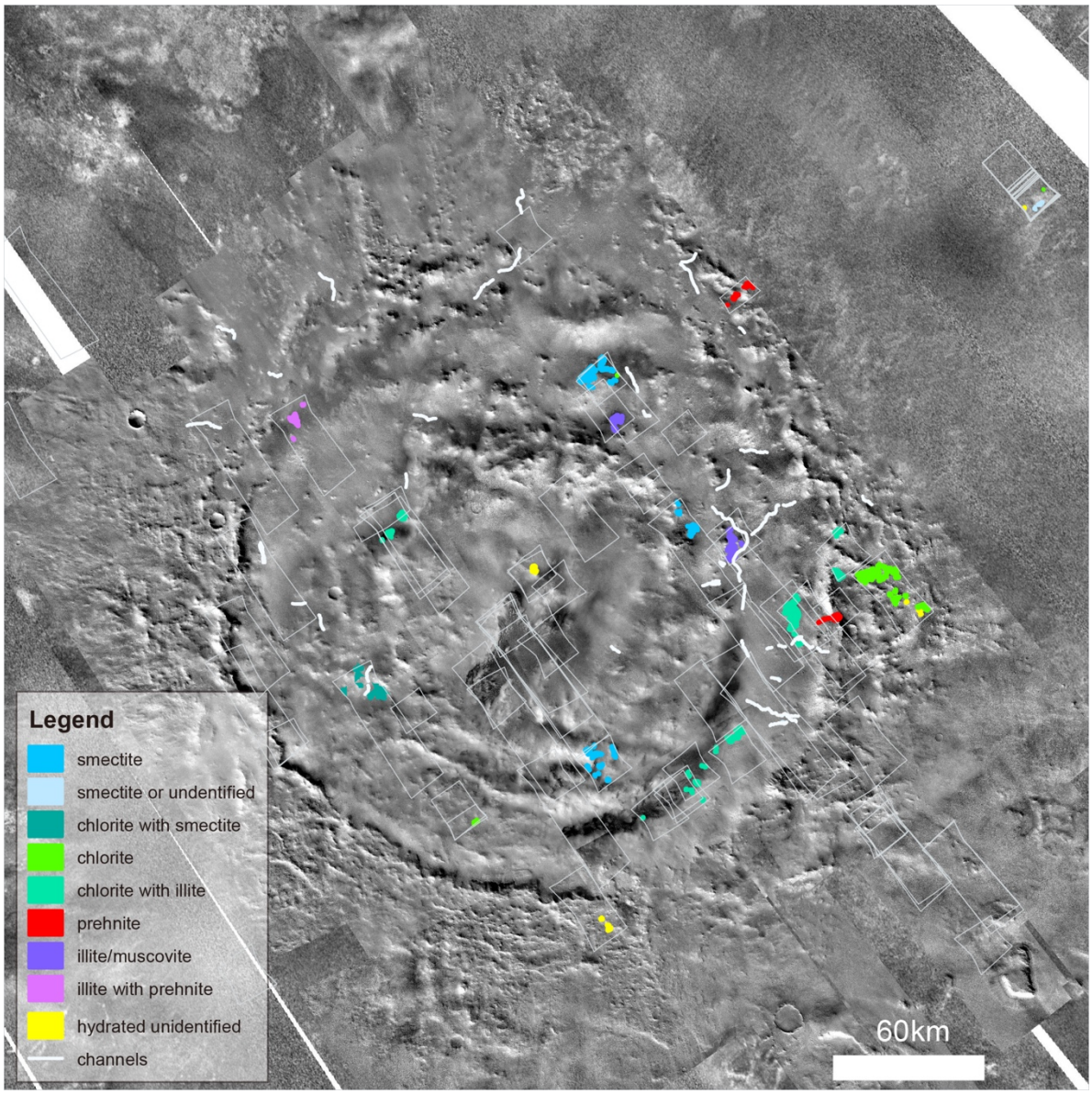

Figure 3: Distribution of the detections of different spectral classes from CRISM data on a CTX mosaic of Lyot crater, with fluvial channels mapped inside the crater.

Fe/Mg phyllosilicates are quite widespread in the crater and mostly concentrated in the kilometer-sized knobs in the central ring of Lyot (Figure 3).

A different spectral class is identified as chlorite with a strong (and broad) 2.35-μm absorption band (Figure 2), consistent with the library spectra of chlorite with a strong 2.35-μm band and absence of or presence of weak 1.9-μm H_2O absorption. In Lyot crater, chlorite detections often appear in spatial mixture with other phases, including Fe/Mg phyllosilicate, illite/muscovite, prehnite, which causes variations in band position and width. For example, in a few cases, the 2.35-μm band can shift to shorter wavelength, resulting in a broader band at 2.33-2.35-μm, which may be due to mixing with a Fe/Mg phyllosilicate phase. Chlorite detections are widely distributed in Lyot crater (Figure 3). They are mostly found in megablocks in the central ring and terraced rim of the crater, but they also occur as the most common spectral type on Lyot proximal ejecta.

A distinct class of spectra is found with a 2.21-μm absorption coexisting with a 2.35 μm absorption (Figure 2), sometimes associated with 1.4 μm and 1.9 μm bands. This is identified as illite or muscovite, matching the spectral features of K mica library with both a sharp 2.21-μm and a 2.35-μm absorption. The width of the 2.21-um feature is inconsistent with that of hydrated silica, which has a broader absorption. In Lyot, illite/muscovite always occurs in close proximity to chlorite/prehnite features (Figure 3). In many cases, the strong 2.35-μm feature is equivalent or stronger than the 2.21-μm feature, for which a possible explanation is due to mixing with chlorite in the vicinity. Illite/muscovite has been identified previously in the southern highlands, and often co-occur with chlorite minerals [Ehlmann et al., 2009] but is only found to occur in the Lyot vicinity in the northern lowlands [Carter et al., 2013; Pan et al., *in rev*].

Prehnite is identified with a distinctive 1.47-1.48 μm absorption coexisting with 2.23-4 μm and 2.35 μm absorption (Figure 2). The spectra are distinctive from illite/muscovite since the 1.48-μm absorption is strong and the 2.2-μm feature is shifted to longer wavelength. Prehnite is a Ca- and Al-rich inosilicate mineral which forms in hydrothermal environments on Earth. The occurrence of prehnite usually indicates an elevated temperature of ~200^{o}C and is a typical product in low-grade metamorphism [Robinson, 1987]. The prehnite detection is confined to three occurrences in small regions on the crater

rim of Lyot and is not found within the crater or on the ejecta blanket (Figure 3). Prehnite detections in Lyot sometimes occur in close proximity to illite/muscovite and chlorite deposits. In several pixels on the northwest rim, both 1.41-μm and 1.48-μm features are present in addition to the ~2.2 μm and 2.35 μm features, which is likely due to mixing with illite/muscovite.

There is an additional spectral class which has a distinctive 1.9 μm absorption but lacks other diagnostic well-defined absorption bands in the 2.1-2.5 μm region (Figure 2). This type of spectra could be explained by a hydrated chloride salt, a zeolite with absorptions only at 1.9 μm and 2.5 μm, or poly-hydrated sulfates with drop off at 2.4 μm. Alternatively, these could be other kinds of hydrated silicate minerals with enhanced water absorptions relative to metal-OH absorptions due to high relative humidity, while the absorptions in the 2.1-2.5 μm region are weak and cannot be distinguished from noise in the CRISM spectra. In Lyot crater the unidentified hydrated mineral occurs in the central peak as well as on the ejecta blanket (Figure 3).

4.1.2 Morphology of hydrated mineral units

As the previous mapping in Lyot based on CTX data showed, several different surface morphology units are present in Lyot crater [Dickson et al., 2009]. Based on observations of unit relationships, the identified units from older to younger ages are 1) the bedrock unit with knobs and mesas in the central ring, the crater floor and the terraced crater rim, 2) the stippled mantling unit that embay the knobs and mesas, 3) the sinuous channels and fans in the fluvial valley system, and 4) smooth mantling unit which often occurs on sloping surfaces near the central ring and crater rim in features that resemble lobate debris apron mapped in Deuteronilus Mensae. Previous work on the chronology indicates that the Lyot impact formed in Early Amazonian, followed by the emplacement of the stippled mantling unit (dated to be mid-late Amazonian). Afterwards, the channels and fans formed cross-cutting or overlying the mantling unit in the late Amazonian [Dickson et al., 2009]. The geologic context of subsequent figures is shown in Figure 4.

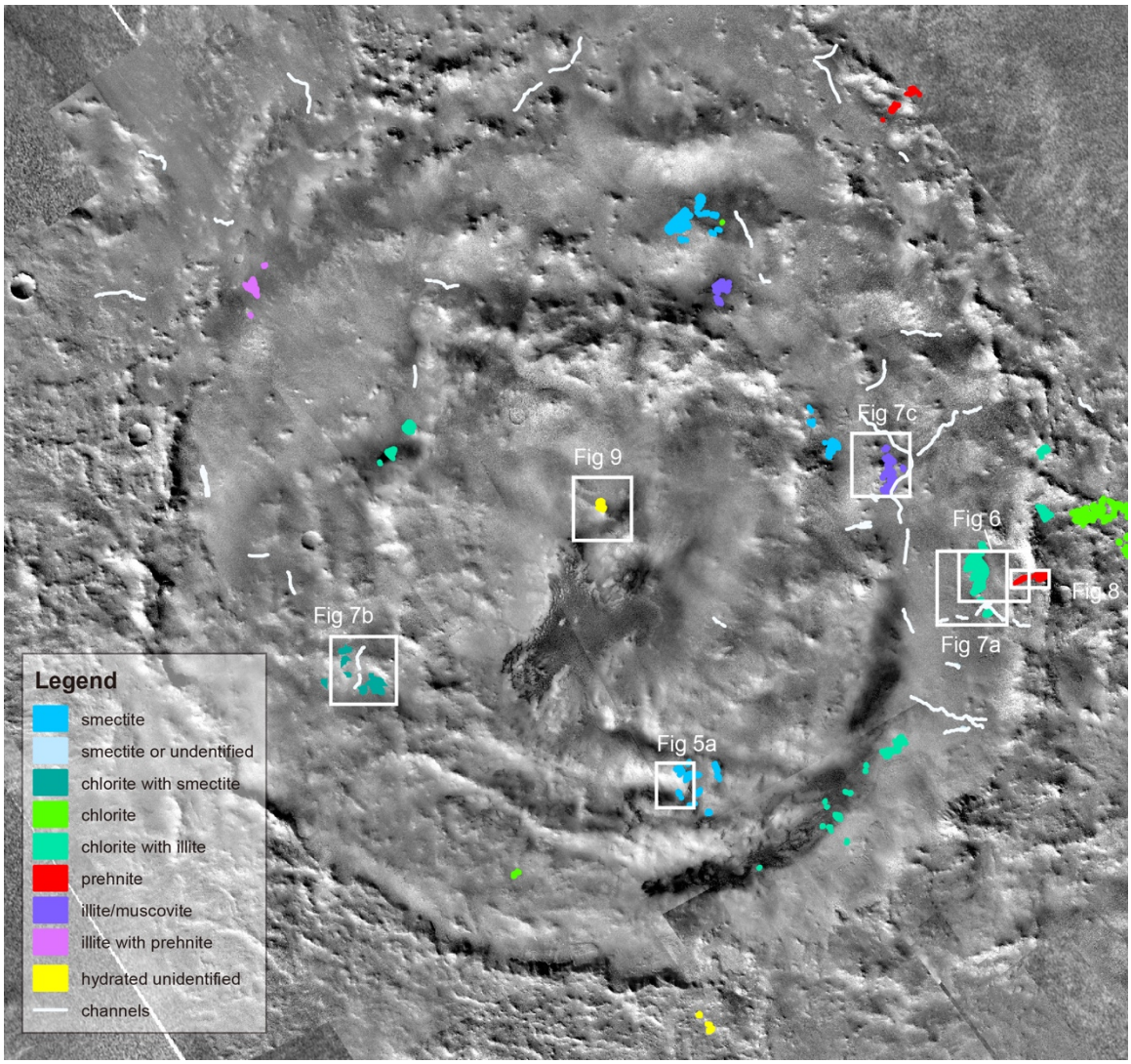

Figure 4: Lyot crater mineral map, with geological context highlighted for Figure 5-9.

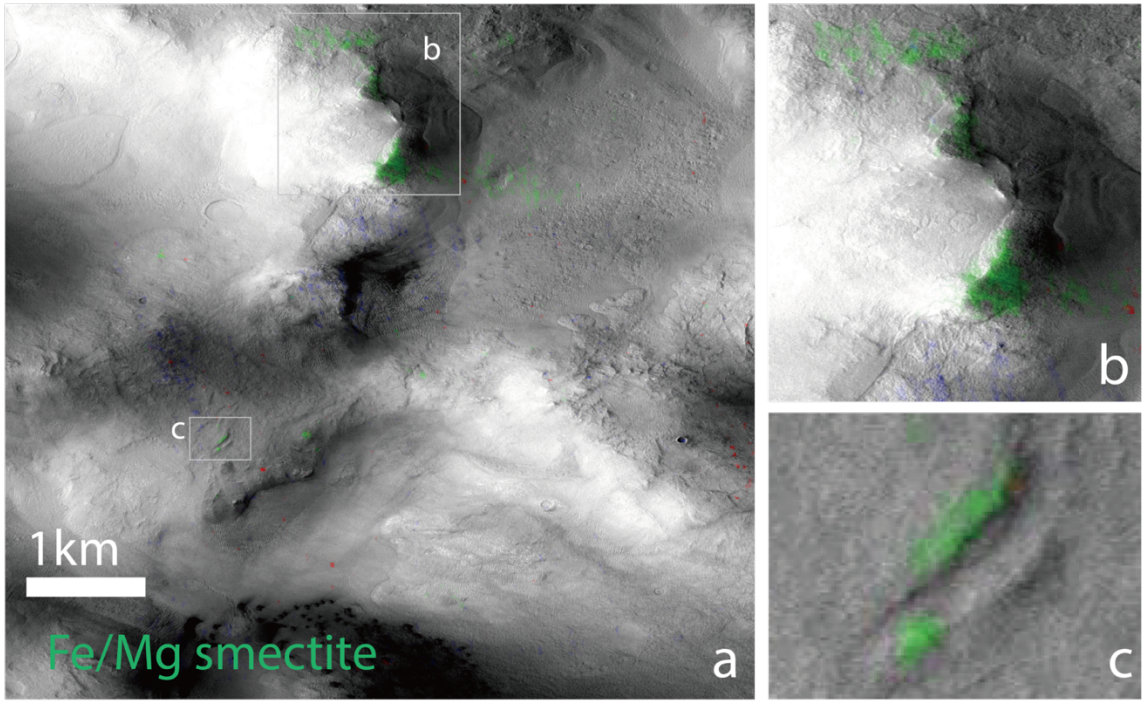

Figure 5: Morphology of Fe/Mg phyllosilicate bearing units in the central ring of Lyot crater. Note the mineral detection on carved ridges in the bedrock units

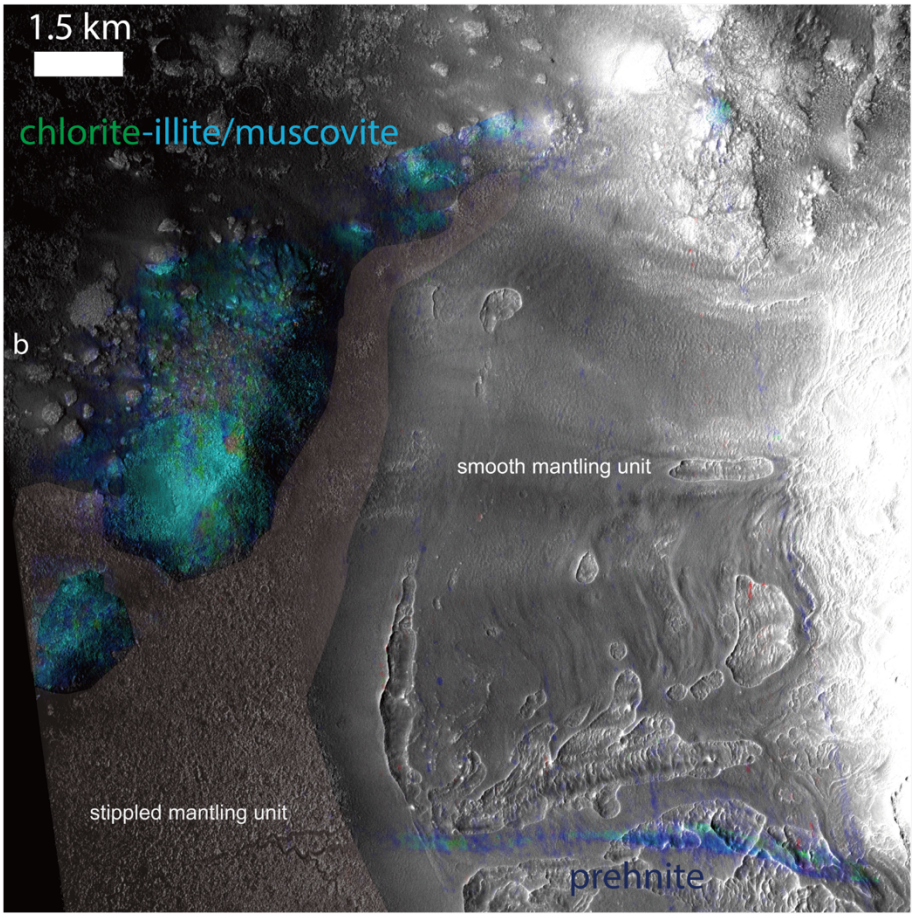

Figure 6: Morphology of chlorite and illite/muscovite detections in the terraced crater wall of Lyot. The detections correlate with degraded knobby features that are covered by stippled mantling unit, which are carved by sinuous channels. Prehnite detection is located near the crater rim on the smooth mantling units.

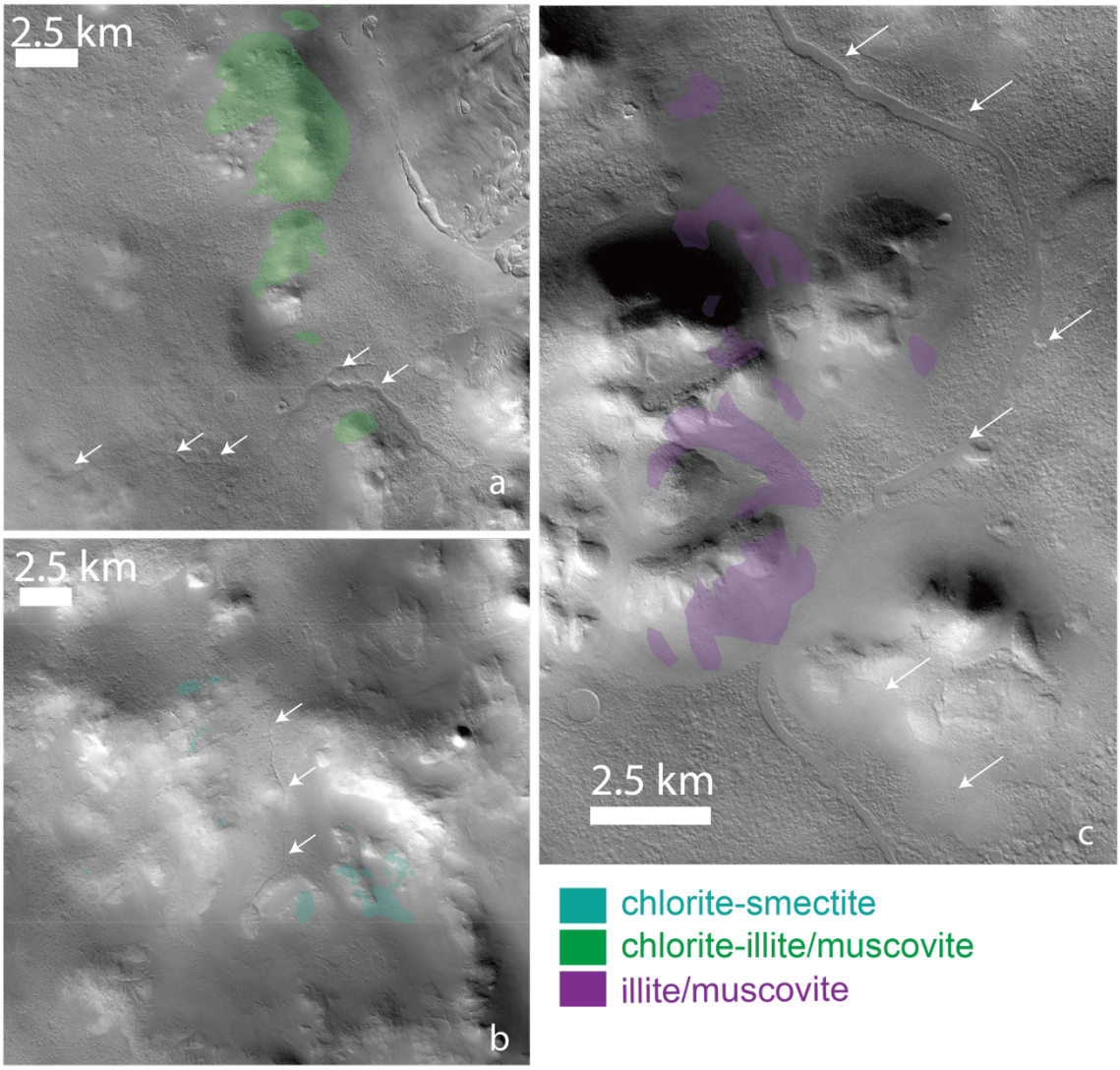

Figure 7: Representative sinuous channels that transect knobby regions in Lyot crater with hydrated mineral detections. Channels are diverted by units with hydrated mineral detections: a. chlorite and illite/muscovite; b. chlorite and Fe/Mg phyllosilicate; c. illite/muscovite.

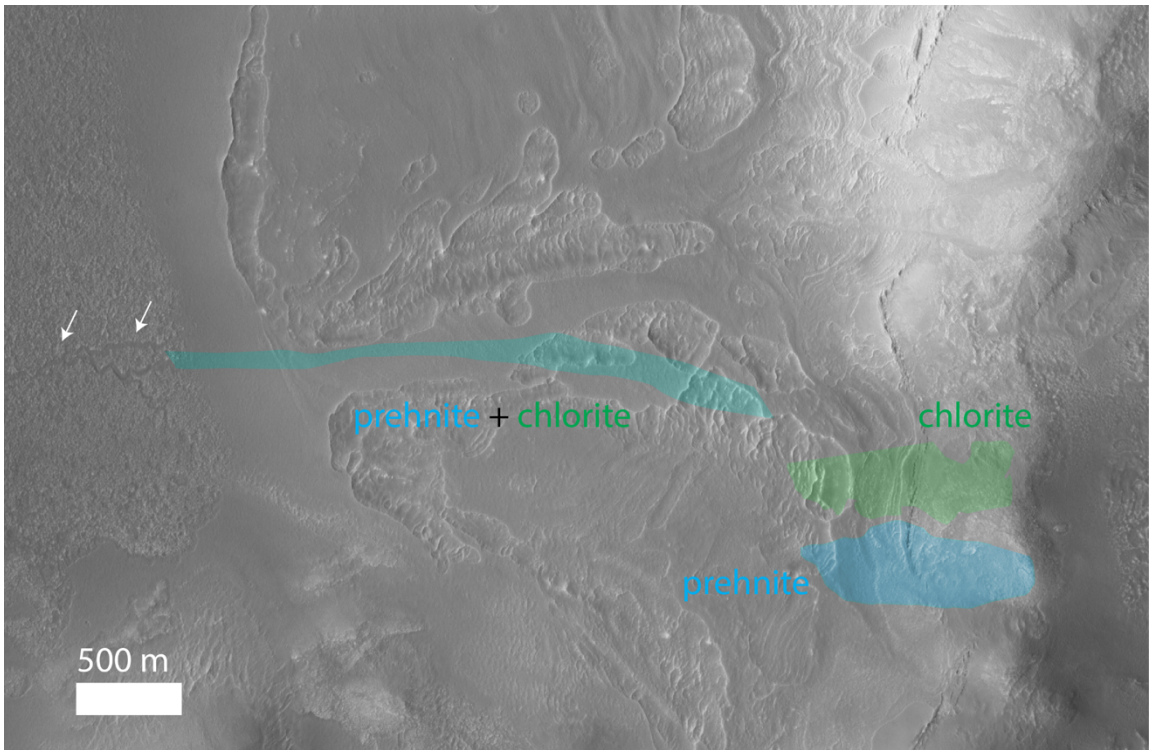

Figure 8: Detailed morphology of the prehnite and chlorite bearing units on the crater rim and the linear feature with prehnite and chlorite spectral signature near the crater rim. Two CRISM images have been both corregistered to the same CTX image, and the regions highlighted by spectral parameters are outlined in an ArcGIS project.

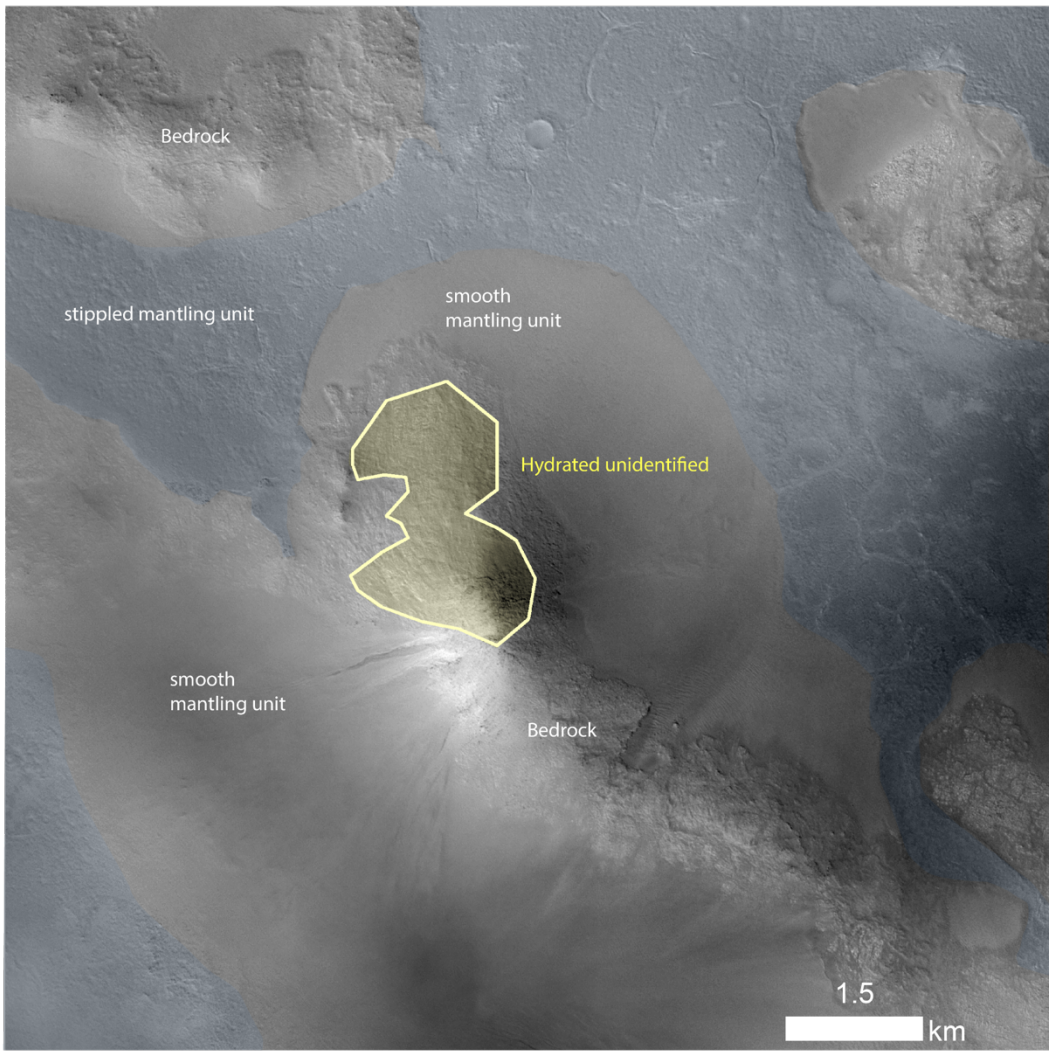

Figure 9: Lyot crater central peak region with detection of unidentified hydrated mineral on the bedrock unit.

To compare the morphology of the hydrated mineral-bearing units and their relationships with the previously mentioned geomorphologic units, we analyze co-registered images of CRISM parameter maps and CTX or HiRISE data. Fe/Mg phyllosilicate detections are found on the ridges of the megablocks (Figure 3, 5) in the central ring, sometimes exposed as channels cut through (Figure 3). These detections, though weak, are clearly associated with the bedrock morphology. Relatively pure chlorite

detections are located on the degraded knobs in the central ring, near the crater rim, and on the ejecta blanket (Figure 3). Some of the chlorite detections near the central ring have a broader absorption band at 2.3 μm indicative of mixing with Fe/Mg smectite. Near the crater rim, however, the chlorite detections tend to co-occur with illite/muscovite and sometimes these chlorite detections with illite/muscovite features are found mostly in degraded bedrock units (Figure 6, Figure 7b). Illite/muscovite deposits tend to occur on the central ring, terraced rim, and the slopes of megablocks in between. They are found largely in the vicinity of bedrock units but sometimes correlated with the smooth mantling units at a finer scale (Figure 7c). They often co-occur with chlorite and sometimes with prehnite. Prehnite has the most distinct distribution that all 4 locations of prehnite detection are found close to the crater rim (Figure 3) rather than the central regions. The northwest crater rim location shows mixture of prehnite and illite/muscovite but the eastern part of the crater has prehnite as the major phase. These units all occur on the crater wall except one that can be traced from the crater rim to within the crater, following topographical lows, in the form of a 3-4 km long "stream" of sediments (Figure 6; Figure 8). The trace of sediments seems to be on the surface of the mantling units near crater rim but cannot be correlated with the surface morphology in the overlapping HiRISE image (Figure 8). The hydrated unidentified mineral found in the central peak image is correlated with a bedrock unit in the central peak (Figure 9), while the hydrated unidentified minerals on the ejecta are in diffuse sediments and are not correlated with a certain morphology.

Sinuous, km-long channels have been mapped in Lyot cutting across the smooth mantling unit with a mid-late Amazonian age using crater count statistics [Dickson et al., 2009]. The positions of these channels are clearly influenced by bedrock units with Fe/Mg phyllosilicate and chlorite detections within the crater and on the crater rim (Figure 7 a-c). The channels divert around the bedrock knobs. This relationship demonstrates that the fluvial activity forming sinuous channels started later than the emplacement of mantling units, which embay the phyllosilicate/chlorite-bearing bedrock units. Thus, the sinuous channels did not contribute to the formation of these hydrated minerals but rather play a role in exposing them. The channels are likely the latest aqueous event within Lyot crater.

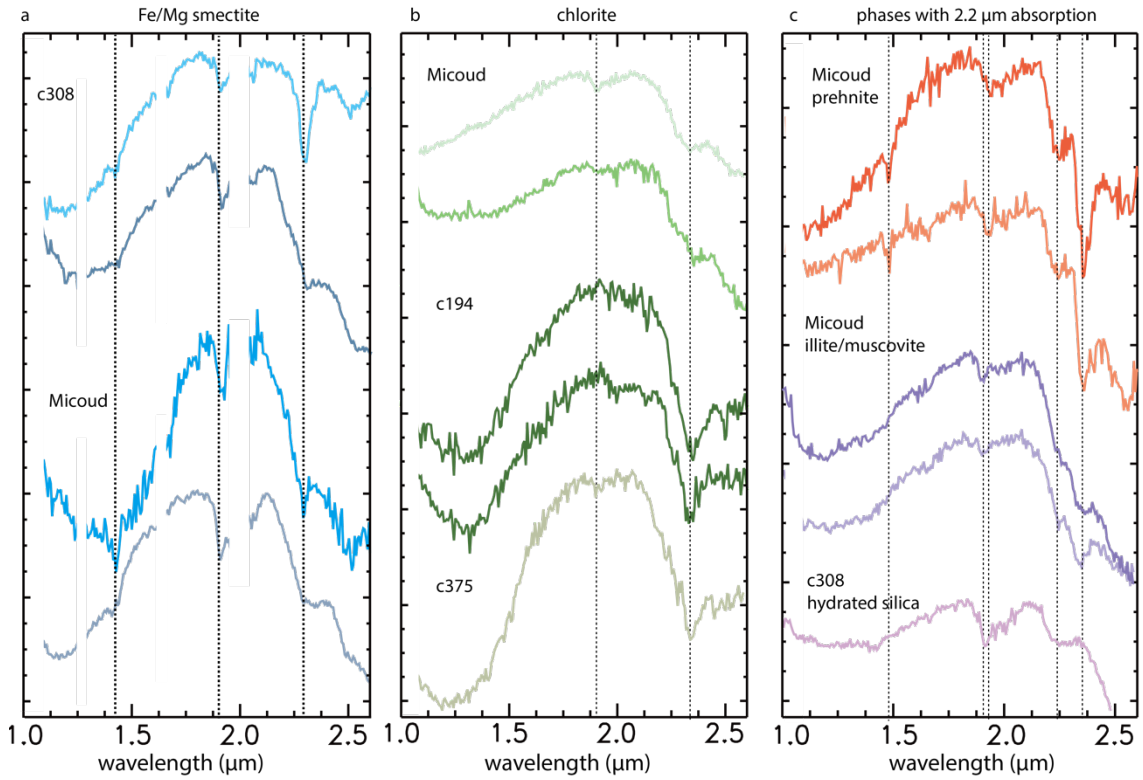

Figure 10: CRISM spectra of hydrated minerals identified in small craters around Lyot. a) Fe/Mg phyllosilicate detection in Micoud and c308. b) Chlorite detection in Micoud, c194 and c375 with a strong 2.35 µm absorption. The chlorite detections in c194 and c375 lack 1.9µm which is typical of chlorite, but the chlorite detection in Micoud has the additional 1.9µm feature. c) Less frequently appearing phases with 2.2 µm absorptions are shown in this panel. In the central peak of Micoud crater, prehnite detection is found with 1.48 µm in 2 locations; illite/muscovite is identified with a 2.21 µm coexisting with a 2.35 µm absorption, with a weak 1.41 µm band. In c308, we also detect the presence of hydrated silica, with a broad band at 2.2 µm as well as additional 1.4 µm band, distinct from the previous detections.

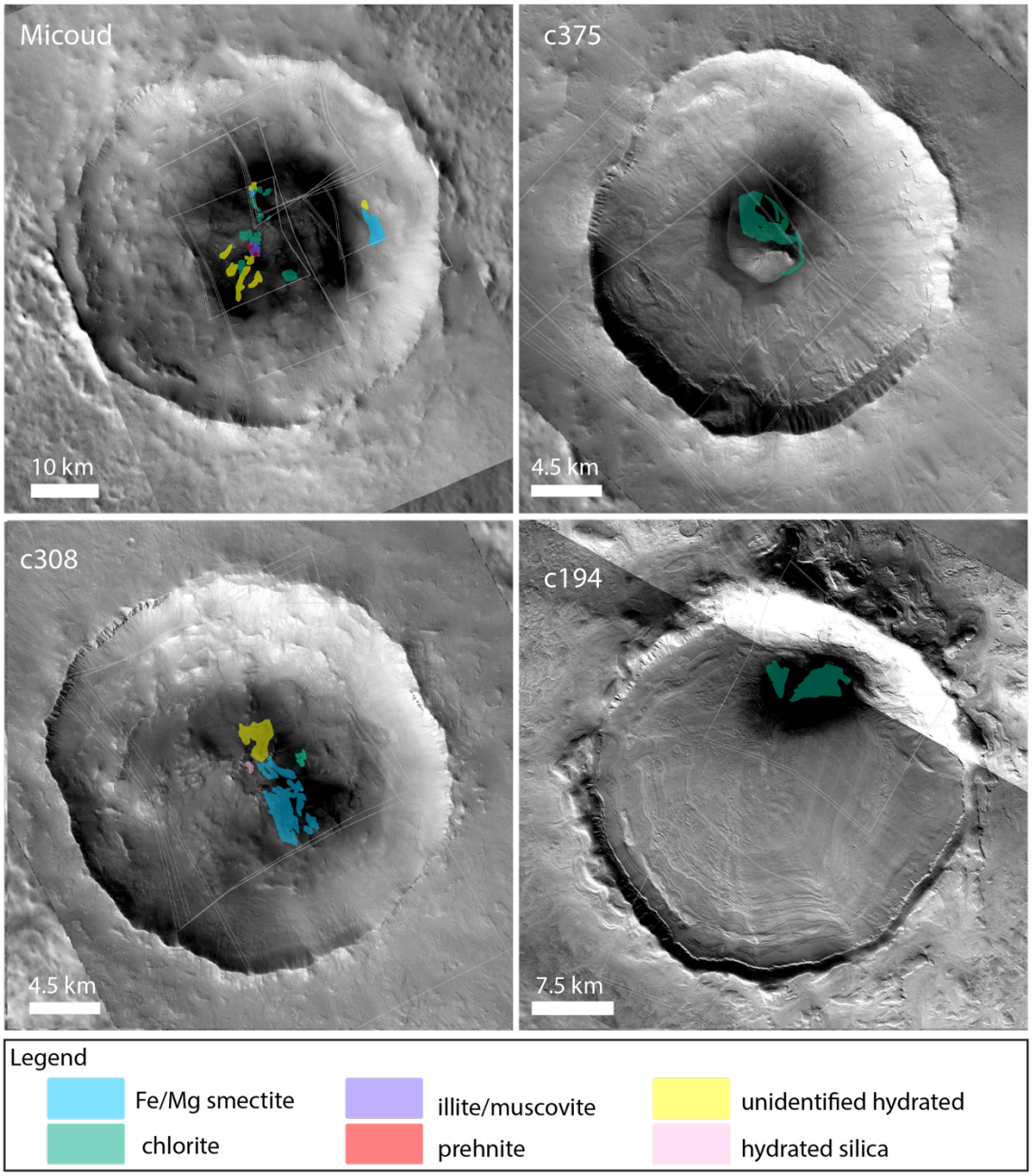

Figure 11: Distribution of hydrated minerals in small craters in the vicinity of Lyot: a. Micoud; b. c375; c. c308; d. c194. Multiple hydrated minerals have been found in Micoud and c308, distributed in the central peak region. Only chlorite has been identified in c375 and c194, associated with distinct morphologic features, respectively.

4.2 Mineralogy of small craters in the vicinity

4.2.1 Micoud crater

Micoud crater, with diameter of 50 km, is situated to the west of Lyot. Micoud, like Lyot, has a terraced rim and has been partially filled, evident by the remnant rim of a small crater in the central peak region. Micoud crater has partial impact ejecta on the Hesperian-Amazonian plains material, same as Lyot crater. The interior of Micoud is covered by a mantling unit that has been eroded. The stratigraphic relationship and degradation state are both similar to Lyot crater, which indicates a close formation age in Early Amazonian. The similar degradation state also indicates its formation coeval as Lyot.

Micoud crater is found with the same set of diverse hydrated minerals as Lyot, including Fe/Mg phyllosilicate (with possible carbonate detection, in this case), chlorite, illite/muscovite, prehnite, and unidentified hydrated mineral. The hydrated minerals are in discreet units within the central peak region. Two different kinds of Fe/Mg phyllosilicate features are found in Micoud (Figure 10). One has a sharper and narrower 2.3 μm and a possible 2.5 μm band, which matches the band positions in calcium carbonate spectra with C-O overtones at ~2.3 and ~2.5 μm. The width of the 2.3 μm band is narrower than that of carbonate spectra, which matches better with nontronite, though the 2.4 μm band often present in nontronite is not observed. The detections are limited to small regions of interest so it is unclear if the band depth of 2.3 and 2.5 μm bands are correlated. A second type of Fe/Mg phyllosilicate has a much broader, asymmetric 2.3-μm absorption and similar feature in the 2.5 μm region, which may be explained as Fe/Mg phyllosilicate and/or carbonate phases mixing with phases with a longer 2.35-μm feature such as chlorite or Fe-serpentines. Regardless of the phase(s) responsible, the 2.3 μm absorptions in these Micoud spectra are stronger and broader than what we see in Lyot. Since we do not observe a strong 2.5-μm absorption (comparable to or stronger than 2.3 μm) typical of spectra of pure carbonate, the hydrated mineral present in Micoud with 2.3 μm and 2.5 μm is mapped as Fe/Mg phyllosilicate, though co-existence of intermixed carbonate is possible.

Chlorite detected in Micoud also has distinct spectral features. The 2.35 μm absorption is broad and associated with a weak 1.9-μm absorption, similar to the second type of Fe/Mg phyllosilicate described above (Figure 10). These chlorite detections are

likely in mixture with Fe/Mg phyllosilicates. Illite/muscovite and prehnite detections occur in the same region within the central peak. Several pixels close to the illite/muscovite deposit have 1.48 µm absorption band that matches prehnite (Figure 11, Figure 12). These spectra match well with the spectral features of illite/muscovite and prehnite in Lyot. The close appearance with illite/muscovite feature of the prehnite detection is intriguing and probably represents alteration units of same origin. Hydrated unidentified mineral is also found in Micoud within the central peak.

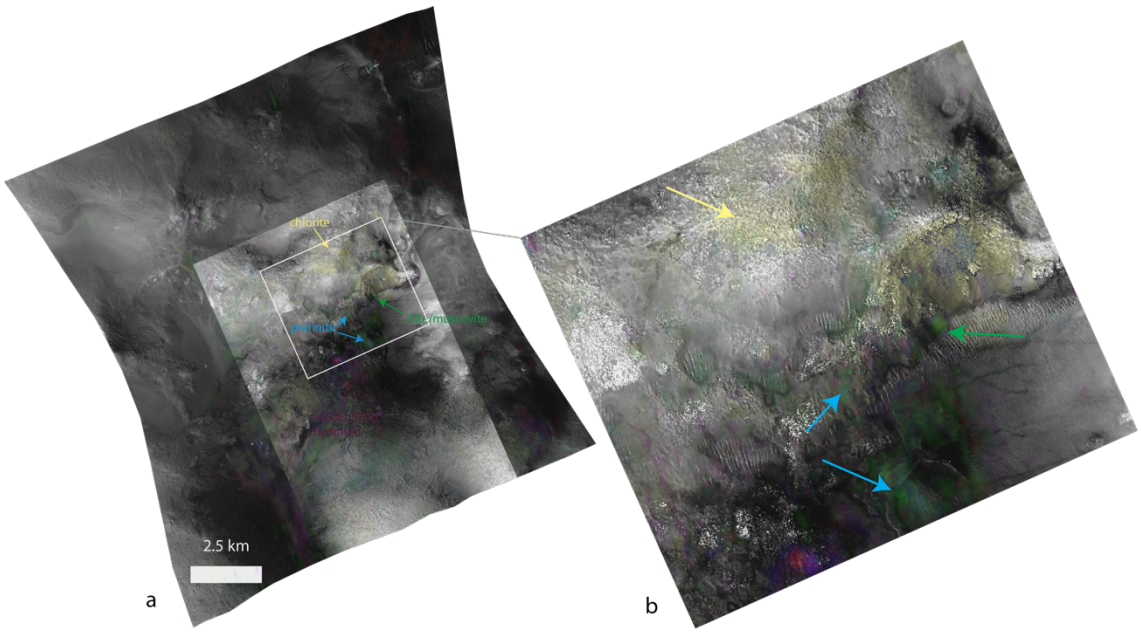

Figure 12: CRISM detection of the central peak region of Micoud crater overlain on HiRISE and CTX data. Imagery data in this image include: HiRISE image PSP_009997_2310; CRISM image FRT00019658 and CTX image J02_045561_2309_XB_50N34W. The CRISM imagery overlay uses a color combination of spectral parameters (R: Band depth at 1.9 µm; G: Band depth at 2.21 µm; B: Band depth at 2.33-2.35 µm) with different colors representing different hydrated mineralogy (Yellow: chlorite; Green: illite/muscovite; Greenish blue: prehnite; Red-purple: hydrated unidentified).

4.2.2 Crater c308

c308 is a small crater (diameter, 22 km) right next to Lyot in the western region. The impact crater ejecta overlies the distal ejecta blanket of Lyot and there is no sign of disruption by Lyot crater. This crater likely formed after Lyot formation. The hydrated minerals present comprise a different assemblage than that of Lyot or Micoud. Two kinds of spectra with a strong 2.3-μm band coexisting with 1.9 μm and 1.4 μm bands have been identified and recognized as Fe/Mg phyllosilicate (Figure 10). The one with narrower and deeper 2.3-μm also has a distinctive 2.5 μm band, though the 2.5-μm band is much weaker. In c308, we also detect the presence of hydrated silica, with a broad band at 2.2 μm as well as an additional 1.4-μm band, distinct from the previous detections. Hydrated unidentified mineral is also present. These detections are concentrated in the central peak region, not associated with a specific morphologic feature.

4.2.3 Crater c375

c375 is a 20-km diameter small crater on the distal ejecta blanket of Lyot. This crater also likely postdate Lyot impact. The crater is partially filled with later mantling units with a central mound of ~4.2 km in diameter, ~500 m in height in the center of the crater (Figure 13). Unlike Lyot, Micoud, and c308, chlorite is the only hydrated mineral detected here in the central mound, confirming detections made in a previous study [Turner et al., 2016]. Active gully formation creates new fan deposits in the central mound, and the chlorite detections are found on the dust-free surface in the central mound as well as in the fine-grained sediments at the base of the mound (Figure 11c). In addition, there is a linear, high-albedo feature ~1 km in length and 0-200 m in width that stems from the eastern slope of the mound, which is spatially correlated with the chlorite detection (Figure 11c, Figure 13). The linear, high-albedo feature has a sharp, abrupt boundary at the interface with the surrounding materials, indicating an injection or fluid-related process which confines the concentration/exposure of chlorite-bearing material in the linear zone.

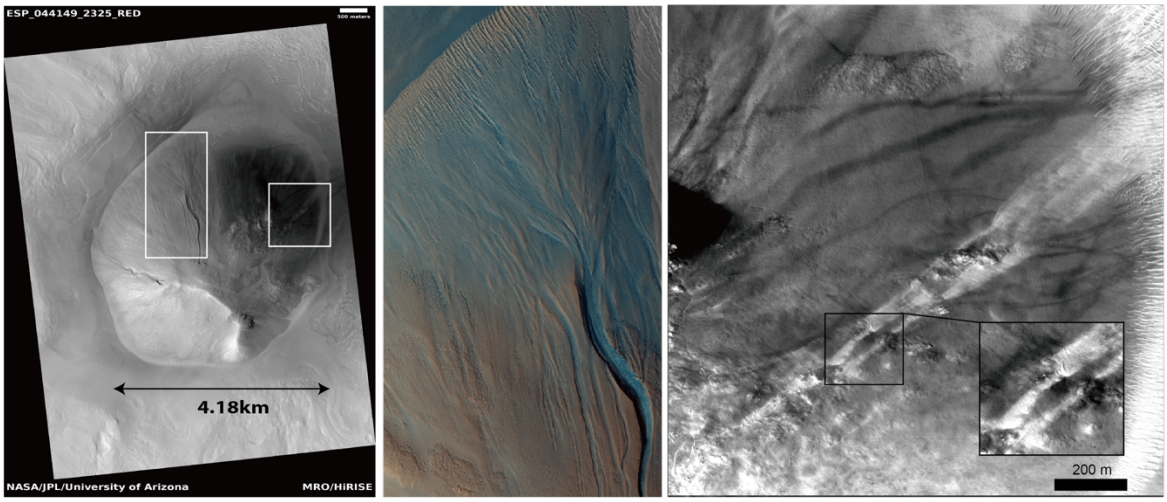

Figure 13: HiRISE image of the central mound of crater c375. a. The central mound of crater c375 and context for insert b and c. b. Inset showing the active gully and fan forming on the northern flank of the mound. From HiRISE color image, the fan has a bluish hue compared to the other parts of the mound, indicating fresh, dust-free surface. c. A linear, high-albedo feature in the mound ~1 km in length. Insert showing the high-albedo feature across the bedrock exposures on the central mound.

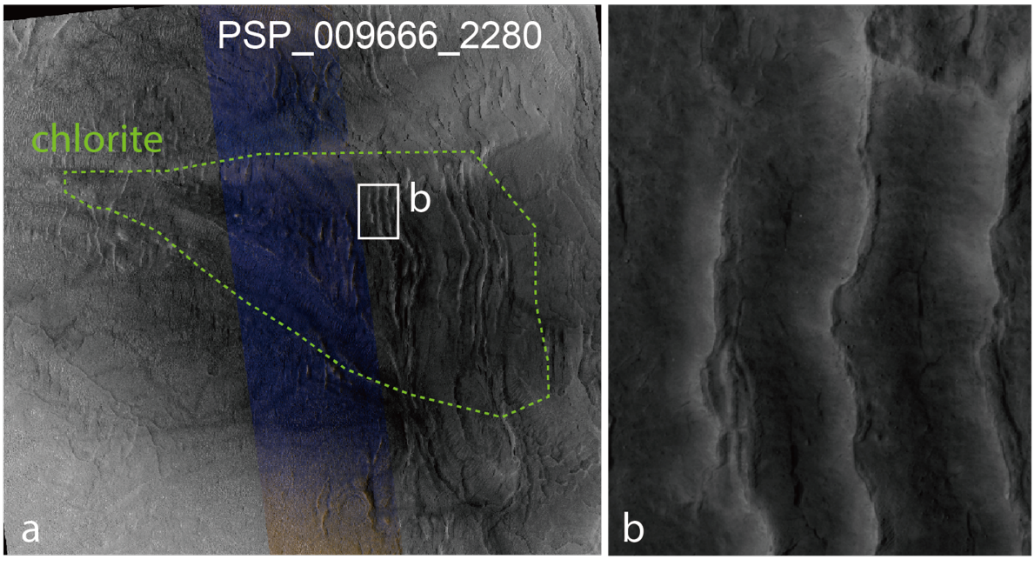

Figure 14: HiRISE image of the ridged crater floor units of crater c194, with inset (b) showing the ridged dark floor unit with chlorite detection.

4.2.4 Crater c194

c194, diameter of 28 km, is the only crater studied situated in a Hesperian-Noachian unit and has been partially filled with later stage mantling unit (Figure 11). The crater rim elevation varies from -2750 m (relative to MOLA datum) on the northwest side to -2350 m on the southeast side, but the crater fill is relatively homogeneous in elevation with the minimum at around -3100 m. The crater rim height is around 350 m to 750 m as compared to the ~1.47 km [Robbins et al., 2011] to ~1.85 km [Garvin et al., 2003] of crater rim height predicted based on the scaling relationship of depth/diameter for complex craters on Mars. Thus, the crater is heavily degraded by erosion and infill. These infilled sediments form a concentric ridged surface inside crater (Figure 11d). The feature is consistent with typical concentric crater fill (CCF) found in a large number of craters in the same region [Levy et al., 2010], proposed to be the same integrated glacier processes as LVF and LDA. That is, the fill is likely to have formed by successive episodes of sublimation of near-surface ice. The dark region located in the northeast part of the crater in the transition between the steep crater wall with ~300 m relief and the flat crater floor with infilled sediments. The dark region is located in the local topographic low and is relatively dust-free (Figure 14). Though dark in the visible-near-infrared, the area is brighter in the THEMIS night-time infrared image compared to surrounding units, indicating a higher temperature and thus higher thermal inertia compared to the surrounding surface. Chlorite features are detected in the dark regions with typical concave continuum and strong 2.35 μm band.

4.3 Subsurface ice deposit and hydrated minerals in Deuteronilus Mensae

Subsurface ice deposits can be identified using SHARAD data by a series of criteria, which include: comparison of with clutter simulations to exclude false positive detection from surface reflector; verification that the basal reflector comes from a reasonable depth; and correlation with morphology [Holt et al., 2008; Plaut et al., 2009; 2010]. Previous study in the Deuteronilus Mensae region has found that the subsurface ice deposit is extensive in this region within the lobate apron around mesas, linear valley fills as well as concentric crater fill [Plaut et al., 2010; Figure 15]. To the east of the region, a recent survey using SHARAD data showed that the regional-extensive, younger mantling units are also subsurface ice-rich deposits [Baker et al., 2017].

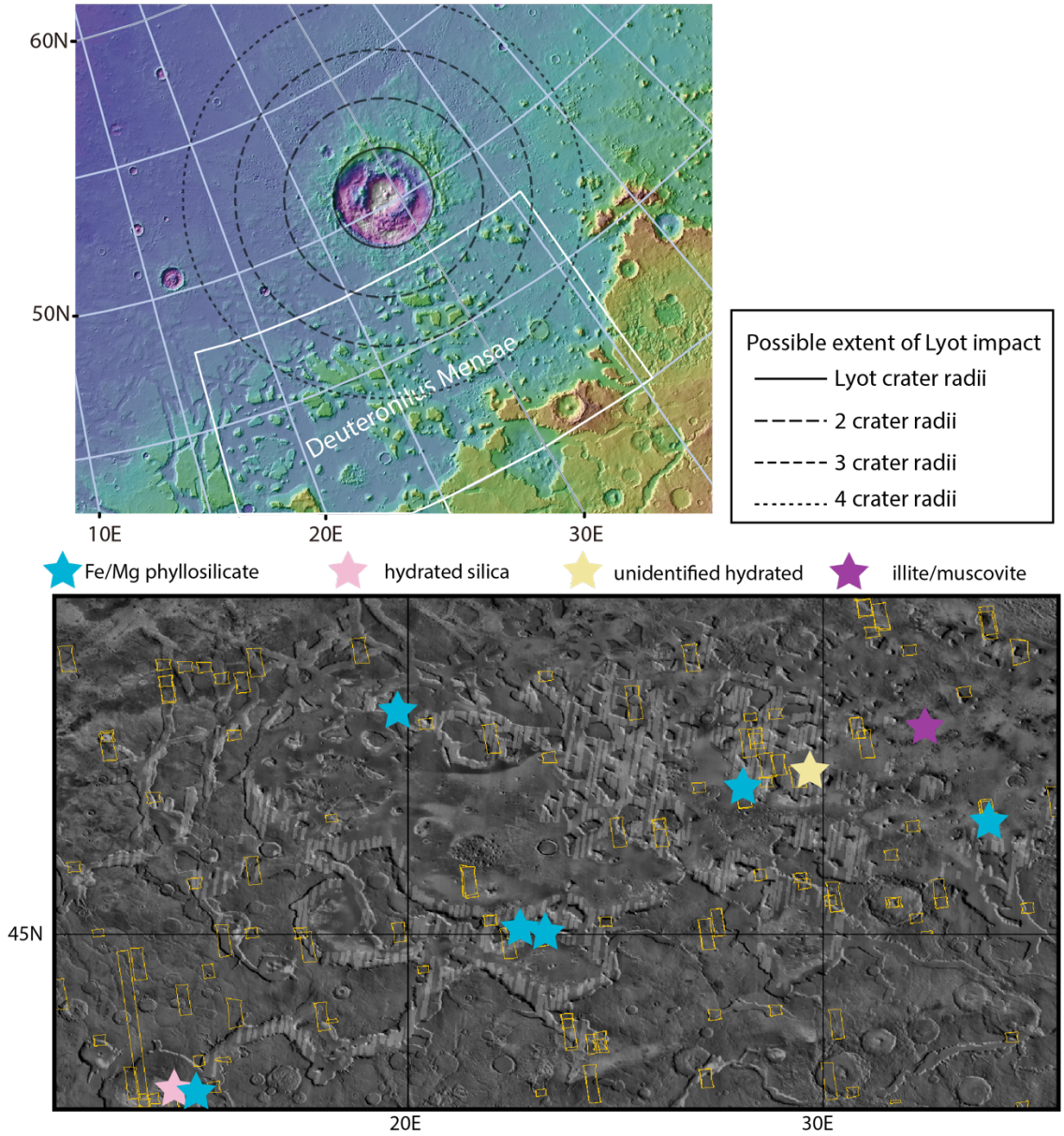

Figure 15: SHARAD detection of subsurface ice (white stripes in the zoom image, personal correspondence from J. Plaut) in Deuteronilus Mensae south of Lyot with THEMIS day IR mosaic in the background. Also shown here are the CRISM footprints in this region and associated hydrated mineral detections. In relatively dust-free regions, small outcrops of Fe/Mg phyllosilicate, illite/muscovite, and unidentified hydrated minerals have been identified.

A thorough survey of CRISM images has been conducted in this study to compare with the distribution of subsurface ice deposits (with results shown in Figure 15). All of the lobate debris aprons with subsurface ice detections in the study region have dusty surfaces and do not show different spectral properties from the surrounding units. One exposure of illite/muscovite is found ~250 km to the south of Lyot at -3510 m relative to MOLA datum, around the same elevation of the pre-impact surface. This lies around 1.5 crater radii to the center fo Lyot and could be either the buried strata of the highlands or the distal ejecta of Lyot. Seven other images are found with detections of Fe/Mg phyllosilicate in small knobs and on the wall of channels and mesas further south. These are located at a higher elevation of ~-2000 m to ~-3000 m relative to MOLA. Two images covering a steep-walled impact crater have both Fe/Mg phyllosilicate and hydrated silica detections on the crater floor. This crater is further away from Lyot at the elevation of -3600 m, probably unrelated to the Lyot impact. All of the above hydrated detections occur on small knobs or slopes of mesas and are not found to occur on the surface of or in association with any of the ice-bearing units.

4.4 Scouring channels to the north of Lyot.

Channelized scablands are found to the north of Lyot outside the ejecta blanket [Harrison et al., 2010] with the absence of channels on the ejecta of Lyot. 32 CRISM images in the north of Lyot have been examined, and we have not identified any hydrated minerals to the north of Lyot ejecta blanket.

5. Discussion

A wide variety of hydrated minerals are found in Lyot and in small craters in the vicinity of Lyot, including Fe/Mg phyllosilicate, hydrated silica, chlorite, illite/muscovite, and a higher-temperature phase-prehnite. Multiple formation scenarios are applicable to explain the diverse hydrous mineralogy and their distribution. Here we assess the constraints and possibilities for the formation of hydrated minerals in three time periods. First, hydrated minerals could form in pre-impact strata that are later disrupted and excavated by the impact process as uplifted bedrock unit. In such a scenario, hydrated minerals may form before the impact event in various environments (e.g. burial diagenesis, hydrothermal alteration, groundwater interaction, and top-down weathering) in Noachian to Hesperian

ages. Second, an impact-induced hydrothermal system may cause the circulation of groundwater and enhanced alteration of bedrock in the early Amazonian. In such a system, high-temperature, homogeneous distribution of alteration mineralogy would be expected in the central part of the crater, with probably different alteration products on the ejecta blanket. Third, hydrated alteration may occur in local environments due to the presence of surface liquid water after the formation of the crater, associated with the localized fluvial morphology within the crater. Here we discuss a detailed assessment of all three scenarios and their implications for the aqueous and geologic history of the region.

5.1 Hydrated mineral formation in post-impact aqueous activity

We first discuss the relationship of hydrated mineral formation to the post-impact aqueous activity associated with Lyot crater identified in previous work [Dickson et al., 2009; Harrison et al., 2010].

Fluvial channels were found to the north of Lyot, which have been hypothesized to be due to the dewatering of Lyot's ejecta blanket [Harrison et al., 2010]. However, due to the high degree of erosion of Lyot's ejecta blanket in the norther lowlands, it remains unclear if the channeled scabland is directly related to the impact event. In this study, we find no hydrated mineral detections in this region in the CRISM survey, in contrast to the diverse hydrated mineralogy found within Lyot crater. This implies the formation of the hydrated minerals inside crater is likely a distinct event from channel formation to the north of Lyot.

Several lines of geomorphologic evidence indicate post-impact modification to the morphology of the Lyot crater, including the stippled mantling units embaying the knobby features in the crater rim and central ring; sinuous channels and gullies and fan formation in the crater rim; as well as the smooth mantling units on the slopes of central ring and crater rim. No hydrated minerals are found in association with the stippled mantling unit, but some of the smooth mantling units in Lyot have chlorite/illite/muscovite features, but these usually occur next to bedrock units with the same mineralogy. This implies that the hydrated minerals in the mantling units may be sourced locally and deposited in the mantling units after the emplacement of the bedrock unit by impact excavation.

Within Lyot, sinuous channels on the crater wall are observed to be clearly diverted by the hydrated mineral bearing knobs and mesas, and thus fluvial activity postdates the

hydrated mineral forming units, mostly chlorite and Fe/Mg phyllosilicate. Thus, the sinuous channels and fans in Lyot represent a separate, later stage of aqueous activity in Lyot crater. This episode of water activity is unlikely related to the formation of the hydrated mineral units detected from orbit within Lyot.

5.2 Impact-induced hydrothermal system.

Both numerical models [Abramov and Kring, 2005; Barnhart et al., 2010] and terrestrial craters show that if water supply is not a limiting factor, large impacts can tap into the subsurface water reservoir and produce long-lived groundwater circulation and subsequent water-rock interaction in a hydrothermal system. In such cases, upon the impact, the large kinetic energy results in elevated temperature in the crater and the possible formation of higher temperature alteration phases, including chlorite, K mica, and prehnite.

However, the crater floor and crater center are not found with hydrated mineralogy indicative of elevated temperature, while the crater rim preserves such phases. This is contradictory to the theoretical model in which the temperature of the target materials decreases asymptotically as a function of the distance from the impact center. Models of impact-induced hydrothermal system in a crater of 180 km in diameter found hydrothermal fluids circulating through the rim can only reach temperature as high as 50 ^{0}C regardless of the presence of a crater lake [Abramov and Kring, 2005], which is not enough to explain the presence of prehnite.

Therefore, though the Lyot impact event had enough energy to mobilize the subsurface cryosphere and sustain a hydrothermal system based on numerical models, the predicted temperature is not sufficient to explain the prehnite detections on the crater rim. This does not preclude the possibility that some of the hydrated minerals, including Fe/Mg phyllosilicate in the central ring, chlorite, and illite/muscovite on the crater floor, may form during the impact. In such scenario, the secondary minerals may have distinct texture due to formation as cements or alteration coatings via groundwater flow, which would not be readily observable from orbit. Future missions with the capability of resolving the micro-scale texture of the mineralogy may shed new lights on the existence/absence of such systems on Mars.

5.3 Excavation from the Lyot impact

Impact craters excavate materials up to several km in depth and expose them on the surface of the planet [Melosh, 1989]. Lyot crater, with its 220 km, underwent gravity-induced collapse which results in the formation of a central-peak and a central ring. The transition diameter between central peak to peak-ring crater is found to be ~30 km on Earth and Venus [Melosh, 1989], and scales to ~100 km on Mars. Direct analogy can be made to Chixculub crater on Earth, a multi-ring impact structure with ~200 km in diameter. The structure of the Chixculub crater indicates the peak ring originates from the mid-crustal basement (~8-10 km in depth) and the sedimentary layer above forms terraced zone between the central ring and the crater rim [Morgan et al., 2016]. This is consistent with the prediction from the dynamical collapse model. If the same model applies to the Lyot crater, we would expect the central ring to be made up of deeper crustal materials and the intermediate layers to be scattered in between the central ring and crater rim. We also expect to observe similar mineralogy on the ejecta blanket, and in nearby outcrop of crustal rocks.

We have found weak Fe/Mg phyllosilicate detections on the central ring of the crater. Between the central ring and the crater rim we observe blocks of chlorite illite/muscovite, and prehnite detections. According to a Chixculub-based model, the distribution at Lyot implies Fe/Mg phyllosilicate may be buried deeper than the other mineral phases, equivalent to the "deeper crystalline basement". The chlorite, illite/muscovite, and prehnite detections close to the edge of the crater rim may be locally displaced and exposed near the crater rim. We also found illite/muscovite detections ~1.5 crater radii away from Lyot crater center in Deuteronilus Mensae, consistent with the location and elevation expected for Lyot distal ejecta. Either as part of the ejecta blanket or as the locally-derived crustal material, the presence of illite/muscovite feature in nearby terrains is suggestive for the excavation origin of illite/muscovite detected within Lyot. The detection of Fe/Mg phyllosilicate associated with mesas and channels in the southern highlands also supports the excavation origin of Fe/Mg phyllosilicates within the crater.

There can be a variety of environments in which the hydrated minerals in Lyot formed pre-impact. The diagenetic formation of chlorite and illite/muscovite on Earth usually

occurs at temperature of 50-90 ^{o}C, but can form in variable conditions depending on the coexisting assemblages, CO_2 partial pressure, and chemistry of the bulk rock [Hurst et al., 1985; Caritat, 1993]. On Earth, prehnite forms under conditions of <3 kbar, 200–350°C, and $XCO_2 < 0.004$ [Robinson et al., 1999; Schiffman and Day, 1999], typically in association with chlorite and pumpellyite. In the Noachian, the geotherm of Mars requires at least 1-2.5 km of depth to reach the minimum temperature of typical chlorite/illite formation temperature [Borlina et al., 2015]. For prehnite formation, depths of > 5.5 km must be achieved or there has to be a local source of elevated temperature. Chlorite and illite/muscovite found in Lyot could have formed in pre-impact strata via burial diagenesis. However, if prehnite formed via burial in a stratigraphy deeper than 5.5 km, it is unlikely that the occurrences of prehnite are solely found on the crater rim and not in the central part of the crater. Thus, burial diagenesis alone may not account for the formation of chlorite, illite, and prehnite under the excavation scenario.

An alternative scenario for the formation of these minerals pre-impact is a hydrothermal system in the shallow subsurface before impact event with additional heat source from or near the surface of Mars. An ancient impact-induced hydrothermal system is a plausible explanation for elevated temperature at the surficial environment of Mars. Volcanic activity which mobilized water in the cryosphere is also a plausible explanation, but no known volcanic center has been reported in the vicinity of Lyot crater. The chlorite-prehnite series in the subsurface could have formed through an impact or volcanic-driven hydrothermal system are later disrupted and excavated by Lyot.

In the framework of excavation, the pre-impact stratigraphy corresponds to a Fe/Mg phyllosilicate-bearing basement with the shallow subsurface altered into higher temperature clay from an early hydrothermal system due to impact or volcanic activity with possible burial diagenesis. The stratigraphy is then excavated by Lyot impact, and due to the collapse of the steep central peak during transient crater phase, the basement phyllosilicate is overturned and forms the central ring of the crater, while the chlorite, illite/muscovite, and prehnite bearing strata in the subsurface collapsed into the terraced crater rim.

5.4 Synthesis of the timeline of aqueous activity in Lyot vicinity

Considering the origin of hydrated mineralogy and geomorphic features inside and surrounding Lyot crater, we identify at least four stages of aqueous activity in the vicinity of Lyot (Figure 16).

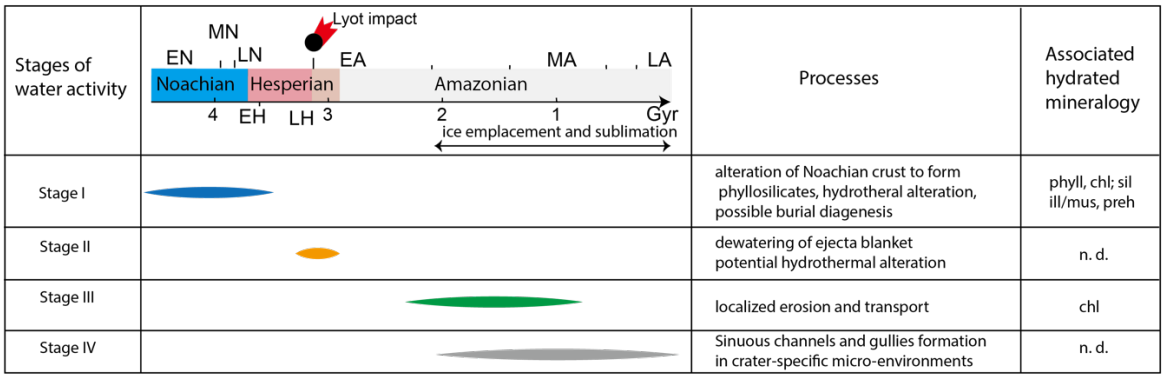

Figure 16: Timeline of different stages of aqueous activity in the Lyot vicinity. Mars epoch boundary is after the chronology by Hartmann and Neukum [2001].

In the Noachian period post dichotomy formation, Fe/Mg phyllosilicate is likely widespread in the basement of the northern lowlands, including the Lyot vicinity region. In the Noachian or Hesperian, a near-surface hydrothermal system formed in the region near Lyot crater close to the dichotomy in addition to burial diagenesis. The energy from an impact event or volcanic activity interacting with local hydrologic cycle resulted in the formation of hydrated/hydroxylated minerals like prehnite, and perhaps chlorite and illite/muscovite in the subsurface. Immediately after the impact of Lyot in the Early Amazonian, impact-induced overland flow may have formed the channeled scablands to the north of Lyot [Harrison et al., 2010]. This impact-induced groundwater generation could have created more hydrated alteration, but no hydrated mineral has been detected associated with channels to the north of Lyot crater. In the mid-late Amazonian, linear valley fills, lobate apron units, and mantling units are emplaced in the general region of Deuteronilus Mensae, extending to partially fill the craters in the vicinity of Lyot. During this period, chlorite-bearing sediments have been transported and deposited within craters to the East of Lyot. They are then exposed in relatively dust-free regions in small craters. In the same period, after the emplacement of the stippled mantling units in the Amazonian, localized channels are formed in Lyot crater that cut across the stippled mantling units and

are diverted by pre-existing topography with hydrated minerals bearing units. The lack of hydrated mineralization associated with the channeled scablands to the north of Lyot and the fluvial channels inside Lyot crater which post-date the mantling units indicates that during the period of formation of these geomorphic features related to liquid water activity, the surface water flow may be transient in nature and the water-rock interaction is kinetically inhibited, probably due to the low temperature of Mars surface.

6. Conclusions

From our investigation of the mineralogical record of aqueous processes in Lyot and its surroundings, we find diverse mineralogy including Fe/Mg phyllosilicate, chlorite, prehnite, illite/muscovite, and silica. The phyllosilicate, chlorite, and illite/muscovite detections mostly occur within the crater central ring and terraced crater rim, while prehnite units, indicative of formation temperature >200 ^{o}C, are found on the crater rim of Lyot. From analysis of the distribution and morphology of hydrated mineral bearing units, we find the hydrated minerals in Lyot can be best explained by excavation of a pre-impact stratigraphy with hydrothermal alteration or burial diagenesis in the Noachian or Hesperian. The occurrences of prehnite with chlorite and illite/muscovite support the existence of a pre-impact hydrothermal system, due to an earlier impact or volcanic activity providing external heat source.

No evidence of hydrated mineral is found in association with the channeled scablands to the north of Lyot. The sinuous, fluvial channels within Lyot forms in a later stage of aqueous activity which clearly post-dates the emplacement of the hydrated-mineral bearing knobs. The lack of hydrated mineralization in association with the geomorphic features of liquid water flow indicates that localized liquid water activity is present in the Amazonian but likely for a limited time in an environment where water-rock interaction is inhibited, possibly similar to the present Mars.

References:

Abramov, O., and D. A. Kring (2005), Impact-induced hydrothermal activity on early Mars, J. Geophys. Res. E Planets, 110(12), 1–19, doi:10.1029/2005JE002453.

Baker, D. M. H., and L. M. Carter (2017), Radar reflectors associated with an ice-rich mantle unit in Deuteronilus Mensae, Mars, in Lunar and Planetary Science Conference XLVII, vol. 1575.

Baker, D. M. H., J. W. Head, and D. R. Marchant (2010), Flow patterns of lobate debris aprons and lineated valley fill north of Ismeniae Fossae, Mars: Evidence for extensive mid-latitude glaciation in the Late Amazonian, Icarus, 207(1), 186–209, doi:10.1016/j.icarus.2009.11.017.

Barnhart, C. J., F. Nimmo, and B. J. Travis (2010), Martian post-impact hydrothermal systems incorporating freezing, Icarus, 208(1), 101–117, doi:10.1016/j.icarus.2010.01.013.

Bibring, J.-P. et al. (2006), Global Mineralogical and Aqueous Mars History Derived from OMEGA/Mars Express Data, Science (80-.)., 312(5772), 400–404, doi:10.1126/science.1122659.

Borlina, C. S., B. L. Ehlmann, and E. S. Kite (2015), Modeling the thermal and physical evolution of Mount Sharp's sedimentary rocks, Gale Crater, Mars: Implications for diagenesis on the MSL Curiosity rover traverse, J. Geophys. Res. E Planets, 120(8), 1396–1414, doi:10.1002/2015JE004799.

de Caritat, P., I. Hutcheon, and J. L. Walshe (1993), Chlorite geothermometry: A review, Clays Clay Miner., 41(2), 219–239, doi:10.1346/CCMN.1993.0410210.

Carter, J., F. Poulet, J.-P. Bibring, and S. Murchie (2010), Detection of hydrated silicates in crustal outcrops in the northern plains of Mars., Science, 328(5986), 1682–6, doi:10.1126/science.1189013.

Carter, J., F. Poulet, J. P. Bibring, N. Mangold, and S. Murchie (2013), Hydrous minerals on Mars as seen by the CRISM and OMEGA imaging spectrometers: Updated global view, J. Geophys. Res. E Planets, 118(4), 831–858, doi:10.1029/2012JE004145.

Dickson, J. L., J. W. Head, and D. R. Marchant (2008), Late Amazonian glaciation at the dichotomy boundary on Mars: Evidence for glacial thickness maxima and multiple glacial phases, Geology, 36(5), 411–414, doi:10.1130/G24382A.1.

Dickson, J. L., C. I. Fassett, and J. W. Head (2009), Amazonian-aged fluvial valley systems in a climatic microenvironment on Mars: Melting of ice deposits on the interior of Lyot crater, Geophys. Res. Lett., 36(8), 2–6, doi:10.1029/2009GL037472.

Ehlmann, B. L. et al. (2009), Identification of hydrated silicate minerals on Mars using MRO-CRISM: Geologic context near Nili Fossae and implications for aqueous alteration, J. Geophys. Res. E Planets, 114(10), 1–33, doi:10.1029/2009JE003339.

Ehlmann, B. L., and C. S. Edwards (2014), Mineralogy of the Martian Surface, Annu. Rev. Earth Planet. Sci, 42(February), 291–315, doi:10.1146/annurev-earth-060313-055024.

Garvin, J. B., S. E. H. Sakimoto, and J. J. Frawley (2003), Craters on Mars: Global Geometric Properties from Gridded MOLA Topography, Sxith Int. Conf. Mars, 7–9.

Harrison, T. N., M. C. Malin, K. S. Edgett, D. E. Shean, M. R. Kennedy, L. J. Lipkaman, B. A. Cantor, and L. V. Posiolova (2010), Impact-induced overland fluid flow and channelized erosion at Lyot Crater, Mars, Geophys. Res. Lett., 37(21), 1–6, doi:10.1029/2010GL045074.

Hartmann, W. K., and G. Neukum (2001), Cratering chronology and the evolution of Mars, Space Sci. Rev., 96, 165–194.

Head, J., J. Mustard, M. Kreslavsky, R. Milliken, and D. Marchant (2003), Recent ice ages on Mars., Nature, 426(6968), 797–802, doi:10.1038/nature02114.

Head, J. W., A. L. Nahm, D. R. Marchant, and G. Neukum (2006), Modification of the dichotomy boundary on Mars by Amazonian mid-latitude regional glaciation, Geophys. Res. Lett., 33(8), 2–4, doi:10.1029/2005GL024360.

Hurst, A. (1985), Diagenetic chlorite formation in some Mesozoic shales from the Sleipner Area of the North Sea, Clay Miner., 20, 69–79.

Kring, D. A. (2007), The Chicxulub impact event and its environmental consequences at the Cretaceous-Tertiary boundary, Palaeogeogr. Palaeoclimatol. Palaeoecol., 255(1–2), 4–21, doi:10.1016/j.palaeo.2007.02.037.

Levy, J. S., J. W. Head, and D. R. Marchant (2007), Lineated valley fill and lobate debris apron stratigraphy in Nilosyrtis Mensae, Mars: Evidence for phases of glacial modification of the dichotomy boundary, J. Geophys. Res. E Planets, 112(8), doi:10.1029/2006JE002852.

Levy, J., J. W. Head, and D. R. Marchant (2010), Concentric crater fill in the northern mid-latitudes of Mars: Formation processes and relationships to similar landforms of glacial origin, Icarus, 209(2), 390–404, doi:10.1016/j.icarus.2010.03.036.

Lucchitta, K., and O. Earth (1981), Mars and Earth : Comparison of Cold-Climate Features, 303, 264–303.

Lucchitta, B. K. (1984), Ice and debris in the fretted terrain, Mars, J. Geophys. Res. Suppl., 89, 409-, doi:10.1029/JB089iS02p0B409.

Malin, M. C. et al. (2007), Context Camera Investigation on board the Mars Reconnaissance Orbiter, J. Geophys. Res., 112, 1–25, doi:10.1029/2006JE002808.

Malin, M. C., and K. S. Edgett (2000), Evidence for recent groundwater seepage and surface runoff on Mars., Science, 288(5475), 2330–2335, doi:10.1126/science.288.5475.2330.

McEwen, A. S. et al. (2007), Mars Reconnaissance Orbiter's High Resolution Imaging Science Experiment (HiRISE), J. Geophys. Res., 112, 1–40, doi:10.1029/2005JE002605.

Mellon, M. T., and R. J. Phillips (2001), Recent gullies on Mars and the source of liquid water, J. Geophys. Res., 106(E10), 23165, doi:10.1029/2000JE001424.

Melosh, H. J. (1989), Impact cratering: A geologic process, Res. Support. by NASANew York Oxford Univ. Press Oxford Monogr. Geol. Geophys. No11 1989 253 p, 49(14–15), 245, doi:10.1103/PhysRevB.46.10411.

Morgan, G. A., J. W. Head, and D. R. Marchant (2009), Lineated valley fill (LVF) and lobate debris aprons (LDA) in the Deuteronilus Mensae northern dichotomy boundary region, Mars: Constraints on the extent, age and episodicity of Amazonian glacial events, Icarus, 202(1), 22–38, doi:10.1016/j.icarus.2009.02.017.

Morgan, J. V et al. (2016), The formation of peak rings in large impact craters, Science (80-)., 354(6314), 878–882.

Mustard, J. F., C. D. Cooper, and M. K. Rifkin (2001), Evidence for recent climate change on Mars from the identification of youthful near-surface ground ice., Nature, 412(1971), 411–414, doi:10.1038/35086515.

Mustard, J. F. et al. (2008), Hydrated silicate minerals on Mars observed by the Mars Reconnaissance Orbiter CRISM instrument., Nature, 454(7202), 305–309, doi:10.1038/nature07097.

Ojha, L., M. B. Wilhelm, S. L. Murchie, A. S. Mcewen, J. J. Wray, J. Hanley, M. Massé, and M. Chojnacki (2015), Spectral evidence for hydrated salts in recurring slope lineae on Mars, Nat. Geosci., (September), 1–5, doi:10.1038/NGEO2546.

Pan L. et al. (2017), "The Stratigraphy and History of Mars' Northern Lowlands Through Mineralogy of Impact Craters: A Comprehensive Survey." Journal of Geophysical Research: Planets. in revision.

Parker, T. J., R. Stephen Saunders, and D. M. Schneeberger (1989), Transitional morphology in West Deuteronilus Mensae, Mars: Implications for modification of the lowland/upland boundary, Icarus, 82(1), 111–145, doi:10.1016/0019-1035(89)90027-4.

Pelkey, S. M. et al. (2007), CRISM multispectral summary products: Parameterizing mineral diversity on Mars from reflectance, J. Geophys. Res. E Planets, 112(8), 1–18, doi:10.1029/2006JE002831.

Plaut, J. J., A. Safaeinili, J. W. Holt, R. J. Phillips, J. W. Head, R. Seu, N. E. Putzig, and A. Frigeri (2009), Radar evidence for ice in lobate debris aprons in the mid-northern latitudes of Mars, Geophys. Res. Lett., 36(2), doi:10.1029/2008GL036379.

Plaut, J. J., J. W. Holt, J. W. Head, Y. Gim, P. Choudhary, D. M. Baker, A. Kress, and the SHARAD Team. (2010), Thick ice deposits in Deuteronilus Mensae, Mars: regional distribution from radar sounding, pp. 26–27.

Pope, K. O., K. H. Baines, A. C. Ocampo, and B. A. Ivanov (1997), of the Chicxulub Cretaceous / Tertiary impact, J. Geophys. Res., 102.

Robbins, S. J., and B. M. Hynek (2011a), A new global database of Mars impact craters ≥ 1 km: 1. Database creation, properties, and parameters, 117(May), 1–18, doi:10.1029/2011JE003966.

Robbins, S. J., and B. M. Hynek (2011b), A new global database of Mars impact craters ≥1 km: 2. Global crater properties and regional variations of the simple-to-complex transition diameter, J. Geophys. Res. E Planets, 117(6), 1–21, doi:10.1029/2011JE003967.

Robinson, D., V. V Reverdatto, R. E. Bevins, O. P. Polyansky, and V. S. Sheplev (1999), Thermal modeling of convergent and extensional tectonic settings for the development of low-grade metamorphism in the Welsh Basin, J. Geophys. Res. B, Solid Earth Planets, 104(10), 23,23-69,79.

Robinson, D. (1987), Transition from diagenesis to metamorphism in extensional and collision settings, Geology, 15(9), 866–869, doi:10.1130/0091-7613(1987)15

Russell, P. S., and J. W. Head (2002), The martian hydrosphere/cryosphere system: Implications of the absence of hydrologic activity at Lyot crater, Geophys. Res. Lett., 29(17), 1–8, doi:10.1029/2002GL015178.

Schiffman, P., and H. W. Day. (1999) Petrological methods for the study of very low-grade metabasites." Low-Grade Metamorphism: 108-142.

Schulte, P., Alegret, L., Arenillas, I., Arz, J. A., Barton, P. J. et al. (2010). The Chicxulub asteroid impact and mass extinction at the Cretaceous-Paleogene boundary. Science, 327(5970), 1214-1218.

Squyres, S.W., (1978). Martian fretted terrain: Flow of erosional debris. Icarus, 34(3), pp.600-613.

Tanaka, K. L., J. a. Skinner, J. M. Dohm, R. P. Irwin, E. J. Kolb, C. M. Fortezzo, T. Platz, G. G. Michael, and T. M. Hare (2014), Geologic Map of Mars, U.S. Geol. Surv. Geol. Investig., 3292, doi:10.3133/sim3292.

Toon, O. B., K. Zahnle, D. Morrison, R. P. Turco, and C. Covey (1997), Environmental perturbations caused by the impacts of asteroids and comets, Rev. Geophys., 35(1), 41–78, doi:10.1029/96RG03038.

Turner, S. M. R., J. C. Bridges, S. Grebby, and B. L. Ehlmann (2016), Hydrothermal activity recorded in post Noachian-aged impact craters on Mars, J. Geophys. Res. Planets, 121, 608–625, doi:10.1002/2015JE004989.

Chapter 5

NEAR-INFRARED SPECTROSCOPY OF SHOCKED AND UNSHOCKED CARBONATES ON EARTH: ORIGINS OF A VISIBLE-NEAR-INFRARED SPECTRAL SLOPE AND ITS IMPLICATIONS FOR MARS

L. Pan and B. L. Ehlmann

Abstract

Carbonates are detected on Mars using near-infrared spectroscopy data. Understanding the true distribution of carbonates in the Martian crust relies on better characterization of their spectral variability. Here we present a survey of spectral properties of carbonates on Earth and analyze the variability and possible causes of different spectral features and their implications for Mars. We particularly focus on carbonates from impact craters because examination, using orbit-based spectroscopy, of the composition of materials excavated by Martian impact craters is the major means of surveying the composition of Noachian crust. We report the identification of a positive slope in the wavelength region of 1-1.7 μm in both Mars spectra and terrestrial samples. For the terrestrial samples, we determine via spectral and chemical analysis that the spectral slope is probably due to a small amount of organics dispersed in the carbonate rock, e.g. in shocked carbonates at the Haughton impact structure. Shock recovery experiments are performed on a terrestrial magnesite sample and it is found that carbonate absorptions remain mostly unchanged at peak pressure of ~5 and ~10 GPa. These results indicate that impact shock probably did not alter the spectral property of carbonates significantly, and different minor components in terrestrial carbonate samples likely resulted in most of the spectral variability in visible and near infrared wavelength. Similar processes may affect carbonate detections on Mars, and will be further analyzed in future work to more systematically compare the spectral features of Martian carbonate detections.

1. Introduction

Carbonate is an important reservoir and sink in the carbon cycle of Earth. On Mars, climate models [e.g. Pollack et al., 1987; Forget et al., 2013] require a dense CO_2 atmosphere of several bars to reproduce a long-term warm climate in the early stage of Mars history when liquid water flowed on the surface of Mars. Carbonate in Mars' crust is a potential reservoir for CO_2 in the atmosphere of early Mars, and its formation is anticipated with a basaltic upper crust interacting with a CO_2 rich atmosphere [Booth and Kieffer, 1978; Pollack et al., 1987].

Carbonates on Mars are found with low abundance (~1wt%) globally in the dust layer from observations by Thermal Emission Spectrometer on board Mars Global Surveyor [Bandfield et al., 2003]; in carbonate-rich accretions and veins in Martian meteorites [Lapen et al., 2010; Borg et al., 1999]; in situ as minor component of northern plains soil at phoenix landing sites [Boynton et al., 2009]; and in Columbia Hills at Gusev crater using Mini-TES on Spirit Rover [Morris et al., 2010]. Recent discovery of carbonate at orbital scale was made possible by high spatial resolution near-infrared spectroscopy data acquired by the Compact Reconnaissance Imaging Spectrometer for Mars (CRISM) on board Mars Reconnaissance Orbiter (MRO) [e.g. Ehlmann et al., 2008; Michalski and Niles, 2010; Wray et al., 2016], through identification of characteristic stretching and bending combinations in the 1-4 μm region. The carbonate-bearing stratigraphy in the Nili Fossae region is associated with olivine-rich bedrock and is found to contain no more than ~5-15 weight percent carbonate [Edwards and Ehlmann, 2015], which is equivalent to ~0.25-12 mbar of CO_2 in the atmosphere. Detections of carbonates in small outcrops in impact crater settings imply that there may exist early or pre-Noachian deeply buried a carbonate reservoir in the crust [Michalski and Niles, 2010; Michalski et al., 2013; Wray et al., 2016]. These uncertainties in the abundance of carbonate in the Martian crust are closely tied to the understanding and interpretation of the near-infrared spectroscopy of carbonate rocks and their variation in different environments.

Although the spectral properties of carbonate minerals have been well characterized [Gaffey, 1986; 1987], the spectral variability of carbonate rocks is more diverse. Fe-substitution, organics, clay, and aqueous inclusions all have significant influence on the

final spectral shape as well as the presence/absence of specific absorptions [Gaffey, 1986]. On the other hand, carbonates may undergo shock-induced melting, textural change, and molecular structural change in impact structures [Langenhorst and Deutsch, 2012], which may also produce effects on the near-infrared spectra of carbonate. These factors on the near-infrared spectroscopy of carbonate minerals, which can be highly relevant to Mars data, have not been well-characterized. Here in this study, we aim to better understand the spectral properties and variability of carbonate rocks, specifically related to impact environments, with implications for Mars. Here we first discuss carbonate detections based on near-infrared spectroscopy on Mars and previous work that conducted shock experiments on carbonate minerals and rocks. We then present the analysis of samples acquired from six terrestrial impact craters and several other sites to explore the spectral properties and variability of carbonate in shocked environments in the field. We also show the first results of a shock recovery experiment on a terrestrial magnesite sample to assess the effect of relevant shock pressure on spectral features of carbonates. With these datasets, we will discuss key factors in spectral variability of carbonate and the effects of shock, and compare the terrestrial dataset with carbonate spectra in CRISM data and discuss the implications for the carbonate reservoir on Mars.

2. Spectral characteristics of carbonate detections on Mars

Carbonates have identifiable absorption bands in the visible and near infrared due to vibrational absorptions of CO_3^{2-}. In the near-infrared region, strong overtone and combination bands appear at 3.4-3.5 μm and 3.9 μm. Higher-order and weaker overtones and combination bands occur most notably at 2.3-2.35 and 2.5-2.55 μm [Hunt and Salisbury, 1971] along with even weaker combination tones at 2.16-2.18 μm; 2.00 and 1.90 μm (Figure 1). The band center and shapes of these absorption features, in addition to absorptions due to metal transition ions and water molecules, can be diagnostic of carbonate chemistry and hydration state [Gaffey, 1986; 1987].

The recent discovery of carbonate on Mars is made possible by the high spectral and spatial resolution data in the near-infrared wavelength acquired by CRISM instrument. Since the first identification of Mg-carbonate in Nili Fossae [Ehlmann et al., 2008],

detections of carbonate materials have been reported via observation from orbit throughout Mars (Figure 2), mostly in the southern highlands near Isidis and Huygens impact basins.

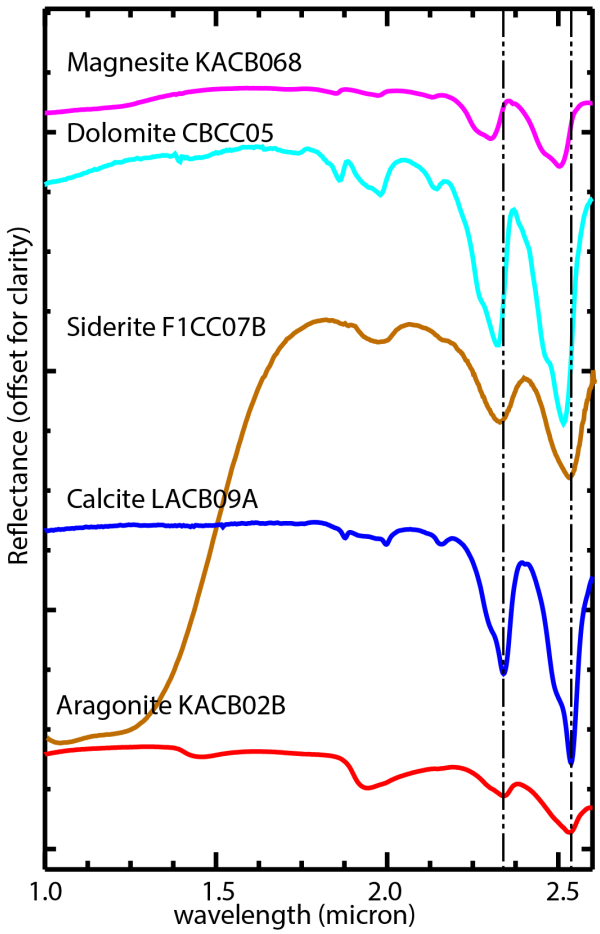

Figure 1: Near infrared spectra of carbonate minerals with different cations. Data are from the United States Geological Survey (USGS) spectral library (splib06a).

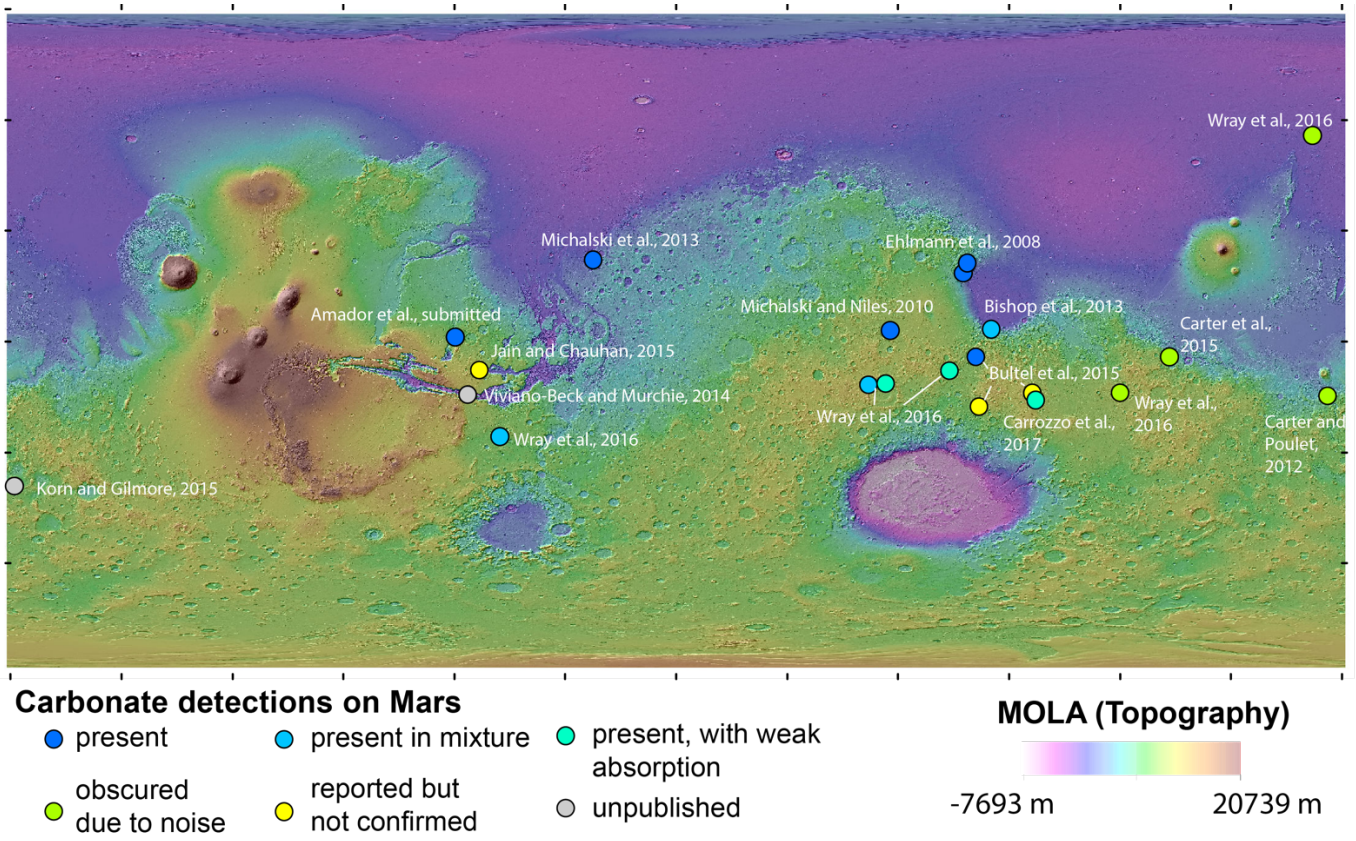

Figure 2: Carbonate detections on Mars reported till Jan 2017 based on CRISM observations. The detections are categorized according to the spectral features in CRISM data. Here "Reported but not confirmed" indicates the same spectral features were not reproduced given the information in the paper. "Obscured due to noise" indicates the detection is based on a few pixels with high noise. "Present with weak absorption" indicates that the 2.5-µm bands are weaker than expected for carbonate.

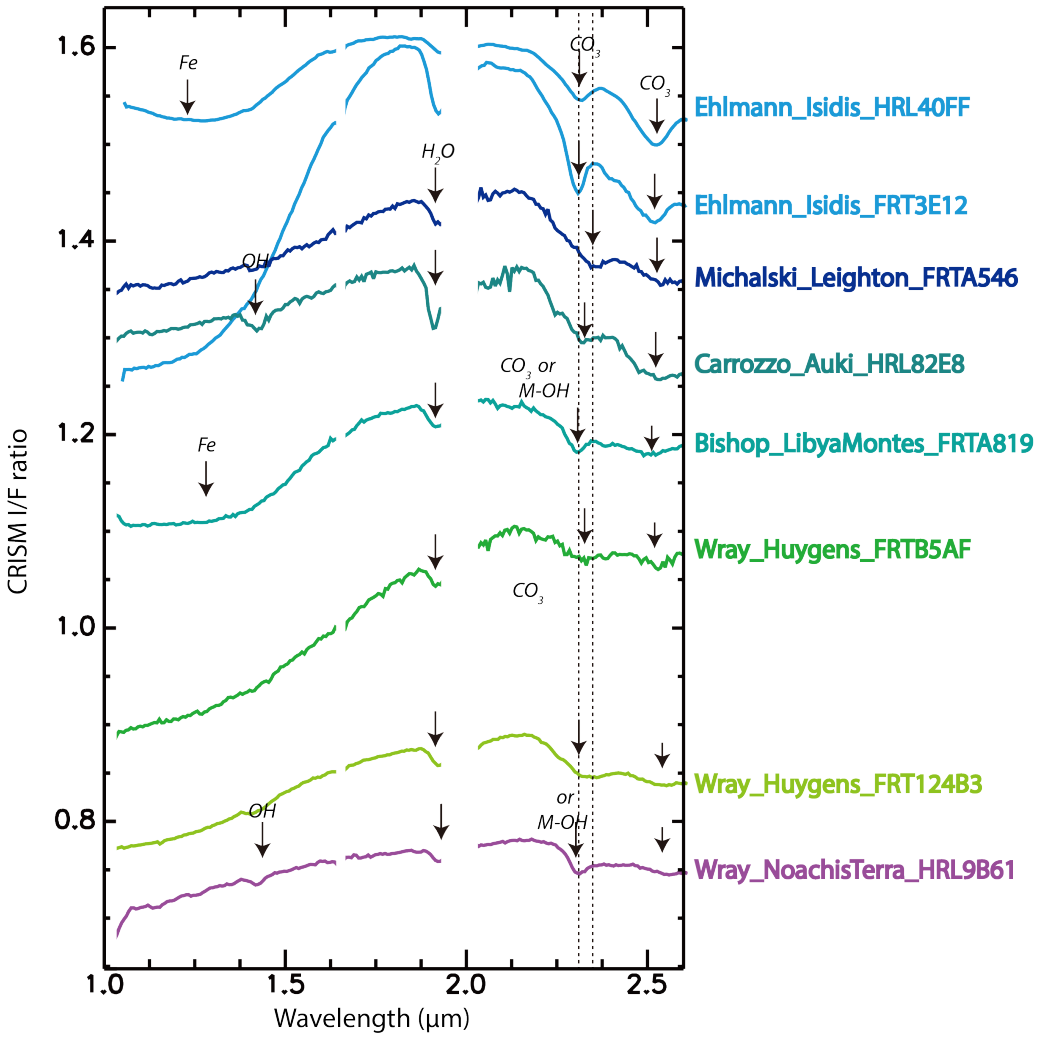

Figure 3: Typical carbonate spectra from CRISM data taken from locations with blue and cyan dots (present, present in mixture, and present with weak absorption) from Figure 2.

The strength and shape of specific spectral features are variable (Figure 3) across different images.

Carbonate is first identified in layered bedrock overlying olivine-rich units in the Isidis Basin region, where magnesium carbonate detections are made through identification of the paired absorptions at 2.3 μm and 2.5 μm due to overtones and combination of C-O stretch as well as co-existing 3.45 and 3.9 μm bands in several CRISM images [Ehlmann et al., 2008]. Here the spectra have a 1.1 μm broad absorption feature, which was assigned to the Fe transitional absorption due to the presence of small amount of Fe in carbonate or

intermixed olivine (Figure 3). In Libya Montes nearby, a carbonate detection is made which has a more symmetric 2.3 μm absorption and a weaker 2.5 μm absorption compared to lab spectra, and is suggested to be in intimate mixture with phyllosilicate [Bishop et al., 2013]. Mg-carbonate is also found in McLaughlin Crater with 2.30 μm and 2.50-2.52 μm bands, possibly in mixture with clay minerals [Michalski et al., 2013]. Fe- or Ca-carbonate is found in Leighton crater with co-occurrence of spectral absorptions at 2.35, 2.53, 3.4 and 3.9 μm [Michalski and Niles, 2010], made possible via endmember extraction in the CRISM scene. Detections of Fe/Ca-carbonates in the Huygens basin vicinity [Bultel et al. 2015, Wray et al., 2016; Carrozzo et al., 2017] have relatively weaker 2.5 μm features, and the detections in the 3.4-3.9 μm region are hardly above noise level. In the northern lowlands, one detection in the Stokes crater has been identified as carbonate, but the 2.5, 3.4 and 3.9 μm absorptions have been obscured by noise or dust cover [Wray et al., 2016; Pan et al., in revision]. Spectral features from Lyot and Micoud craters are also found have 2.3 and 2.5 μm absorption bands probably due to carbonate in mixture [Pan and Ehlmann, *in prep*]. An orbital carbonate detection [Carter and Poulet, 2012] in Gusev crater confirms the prior identification of carbonate by Spirit Rover [Morris et al., 2010], but the detection is only found in one CRISM pixel at high noise, and the spectral features are not as well defined. In several other works [Jain and Chauhan, 2015; Viviano-Beck and Murchie, 2014; Korn and Gilmore, 2015], carbonate detections are reported in the literature but have not been confirmed by us in this work due to lack of information on the location of extracted spectra.

Most of the carbonate detections are found with a 1.9-μm hydration band and sometimes with 1.4-μm band due to a combination and overtone of H_2O and OH. Except for the detections in the Isidis Basin vicinity [Ehlmann et al., 2008; Bishop et al., 2013], all of these carbonate spectra have a positive slope in the 1-1.7 μm region which cannot be solely due to a siderite- or olivine-related Fe absorption around 1 μm. The effect of mixing carbonates with a different endmember is indicated by a mixing trend on a plot of the positions of the 2.3 and 2.5 μm band (Figure 4).

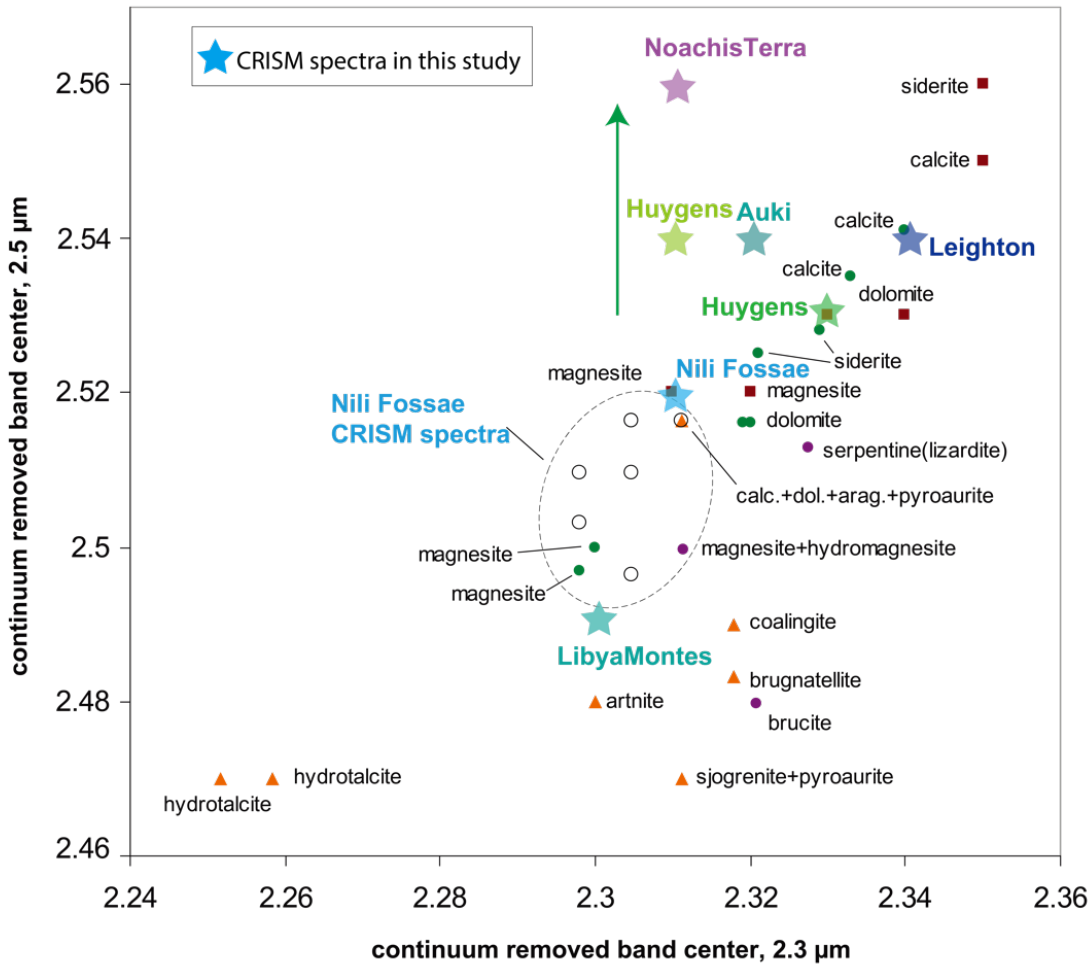

Figure 4: Comparison of the 2.3 µm and 2.5 µm band center in Mars spectra to Earth carbonate minerals (Adapted from Ehlmann et al., [2008]). Green arrow indicates mixing trend with clay minerals.

As discussed above, the spectral features of carbonate detections on Mars show a range of spectral features that are different from laboratory measurements of pure carbonate minerals. Thus, the effects of varying chemical composition, crystallinity, and/or physical texture in carbonate rocks on the near-infrared spectra needs to be further examined to understand the carbonate detections on Mars.

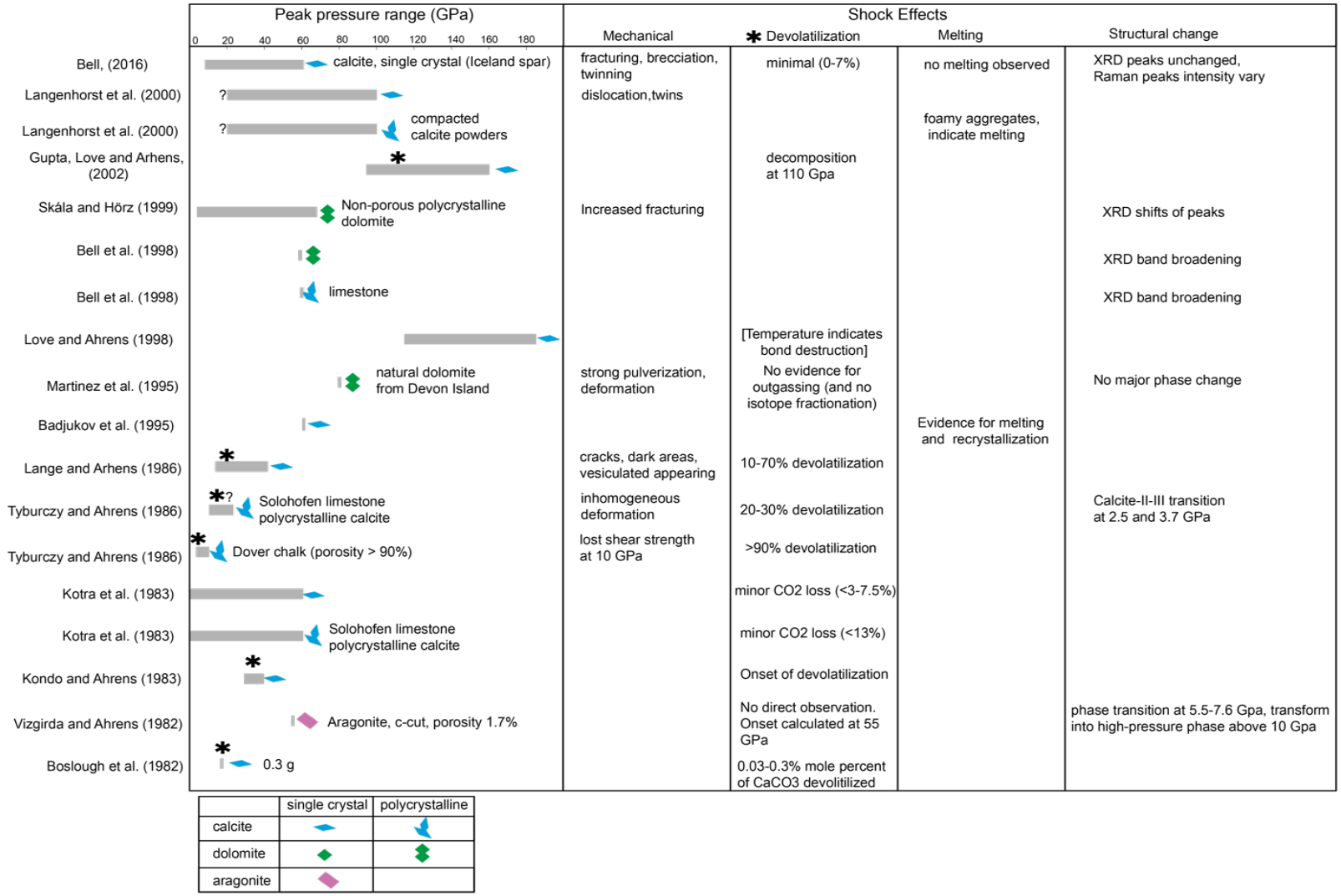

Figure 5: Summary figure of impact shock experiments on carbonate rocks and the shock effects observed in these experiments.

3. Carbonate rocks in shock environment

Many of the carbonate detections on Mars are found to be associated with impact craters (e.g. Leighton crater [Michalski and Niles, 2010], McLaughlin crater [Michalski et al., 2013], Auki crater [Carrozzo et al., 2017], Lucaya crater [Wray et al., 2016]) and have been suggested to represent an uplifted deep carbonate reservoir. However, spectral interpretation of these materials may be affected by the high peak pressure and temperature experienced in meteoric impacts. Here, I summarize the effect of impact on carbonate rocks in terrestrial impact structures and in shock experiments (Figure 5).

Shock effects on carbonate materials include mechanical change, devolatilization, melting and structural change. Mechanical and physical effects, including fracturing, brecciation and mechanical twinning, and peak broadening in X-ray diffraction patterns, are commonly found in terrestrial impact rocks [Skála, 2002] and are reproduced in experiments [e.g. Langenhorst, 2002].

Impact-related melting of carbonates is documented by the coexistence of carbonate and silicic impact-glass spherules in Chixulub ejecta [Schulte et al., 2010] and has been observed in carbonate rocks and calcite-bearing sandstone in the Haughton impact structure [Osinski, 2001; Osinski, 2005; Osinski, 2007].

Dissociation of carbonates into oxides and CO_2 can occur at high temperature (~ 840 °C for $CaCO_3$, lower for $MgCO_3$). The decomposition of carbonates may have the potential climate impact of releasing large amount of CO_2 into the atmosphere by large craters (e.g. Chixuclub crater). Early impact shock experiments [e.g. Tyburczy and Arhens, 1986; Lange and Arhens, 1986] found carbonate decomposition starting at peak pressure of ~10 GPa. However, later experiments on natural dolomite showed limited outgassing at peak pressure as high as 60-80 GPa [Martinez et al., 1995; Bell, 2016]. Theoretical considerations indicate that the dissociation of $CaCO_3$ into CO_2 gas requires high residual temperatures and also enough free space to allow expansion of the released CO_2 and diffusion out of the system [Deutsch and Langenhorst 2007]. Back-reaction [Agrinier et al., 2001] may also be important in natural impacts. In the field, evidence for the product of

decomposition of Mg-carbonate has been found as a solid residual phase (periclase, MgO) in the Haughton impact structure [Martinez et al., 1994].

Carbonates also undergo structural changes in static high-pressure experiments [Liu and Mernagh, 1990; Grzechnik, et al., 1999; Santillán, 2003; 2005] but as these phase transitions occur at a different time scale, they are less relevant to the context of natural impact events.

The shock effects on carbonates inferred from both study of terrestrial field samples from impact craters and shock-recovery experiments may influence the near-infrared spectroscopy of these shocked samples. Here we will present the investigation of the spectral characteristics of natural samples from six different impact craters (Table 1), with a focus on Haughton impact crater and discuss the spectral variability in comparison with Earth carbonates in other environments. We also conduct a shock experiment to characterize effects on spectra at 5 and 10 GPa respectively, if any.

4. Analytical Methods

4.1 Sample description

Carbonate impact clasts from breccia and melt rocks in six Earth impact structures were collected, including 41 impact clasts from Haughton structure, six limestone from Ries (courtesy of H. Newsom, University of New Mexico and G. Pösges, the Ries Crater Museum), and 16 clasts from Tunnunik, Crooked creek, Sierra Madera and Decaturville impact structures (courtesy of G. Osinski, Western University). The information on the crater and sample description summarized in Table 1. A set of carbonate samples (courtesy of D. Quinn, California Institute of Technology) including unshocked carbonates from Naukluft Mountains, Namibia, a marble from Paros, Greece and an oolite sample from Death Valley, California, have been used for comparison to the impact shocked rocks.

4.2 Visible and near-infrared spectroscopy

Visible and near-infrared spectra of all samples were measured with an ASD (Analytical Spectral Devices, Boulder, Colorado) FieldSpec 3 spectrometer (350–2500 nm, spectral resolution 3 nm at 700 nm and 10 nm at 1400 and 2100 nm) at the California Institute of Technology. Hand specimens were measured using the contact probe attachment with an

internal light source and at a viewing geometry of approximately 0° incidence and 30° emission angles. All of these spectral measurements were made relative to Spectralon® (Labsphere, North Sutton, New Hampshire) and corrected for the absolute reflectance properties of Spectralon®.

4.3 Attenuated Total Reflectance spectroscopy

Two select carbonate clasts were broken up using a mortar and pestle, and then were fully ground into powders in a Shatterbox®. Reflectance spectroscopy of the powdered samples were then measured using the Fourier Transform Infrared Spectroscopy (FTIR) instrument at California Institute of Technology under the Attenuated Total Reflectance mode. The spectra of a blank (air), a single calcite crystal, and powders of Haughton carbonate clasts were measured to identify spectral features other than that of pure calcite in the carbonate samples.

4.4 SEM-EDS analysis

Rock chips of carbonate clasts from Haughton impact were mounted and analyzed under a ZEISS 1550VP Field Emission Scanning Electronic Microscope (SEM) at California Institute of Technology, coupled with energy dispersive spectroscopy (EDS). The analysis provides high-resolution imagery of carbonate texture and qualitative compositional mapping.

4.5 Total organic carbon measurement.

To characterize the amount of organic carbon in the Haughton impact carbonates, we measured the total organic carbon in two select carbonate clasts. Powdered samples from Haughton impact were weighed and put in 40 mm vials for reaction. We then added 1M HCl to the sample in small increments until effervescence stops. Although the use of HCl may dissolve a small amount (~2-10%) of organic carbon compounds leading to a carbon loss prior to sample combustion [Galy et al., 2007], we expect the dissolution to be minimal since our samples are dominantly carbonate and the HCl will be much diluted after full reaction with carbonate materials. The samples remain in the solution for more than four hours for complete reaction, and then we centrifuge the vials and decant the remaining solution three times. Afterwards, the samples are freeze-dried and 200-250 μm of each

sample is weighed and run in a Costech Elemental Analyzer (EA) instrument coupled with mass spectrometer for combustion analysis to measure the total count for carbon in each sample.

4.6 Light gas gun shock recovery experiment

A magnesite sample from Lewis Ward mineral collection (Sample No. 346-4825) was cored for a shock-recovery experiment on the 20 mm light gas gun in the Lindhurst Laboratory for Experimental Geophysics. We performed two shots on two targets with velocities of 783.55 m/s and 1284 m/s, respectively, using an Al-flyer projectile. The peak shock pressures reached are ~5GPa and ~10GPa, respectively. After successful experiments, the metal chambers containing magnesite cores were cut open on an electrical discharge machine (EDM) and lapped on a rotating disc until the full recovery the shocked sample. Due to the fact the footprint of contact probe on ASD spectrometer was larger than the sample, we obtained the spectra of pre- and post-shock magnesite samples using a) ASD spectrometer with external light source and bare fiber optics on a goniometer and b) Headwall Photonics Inc. High Efficiency Hyperspec® visible–near-infrared (VNIR) E-series and High Efficiency Hyperspec® shortwave infrared (SWIR) X-series pushbroom systems imaging spectrometers.

5. Results

In this part I will first present a detailed spectral analysis of 41 carbonate clasts (Table 2) from the Haughton impact structure in the high Arctic in Canada, in combination with chemical analysis. Then the specific characteristics of these impact clasts are compared to samples from other terrestrial craters, as well as Mars data.

5.1 Case study: Investigation of the spectral slope of carbonates at the Haughton impact structure

The Haughton impact structure is a relatively well-preserved 23-km impact structure situated on Devon Island in the Canadian Arctic Archipelago (75^{o}22' N, 89^{o}41' W) [Osinski et al., 2005]. The Haughton impact disrupted target rocks which comprise Paleozoic sedimentary rocks of the Arctic Platform with a metamorphic basement of the Canadian Shield. In outcrop, impact shocked carbonate clasts are present in impact melt and breccia

and have been collected in the 2016 Haughton field campaign. Here we report the spectral measurements of the carbonate clasts that may be relevant to Mars.

5.1.1 Spectral characterization of carbonate clasts from Haughton impact structure

All carbonate clasts from the Haughton impact structure are light- to dark- grey in color, sometimes with white, yellow, or orange coatings. The carbonate clasts in Haughton are freshly exposed and include both pristine impact breccia and hydrothermally altered samples. Typical spectra of Haughton carbonates are shown in Figure 6 (here the spectra

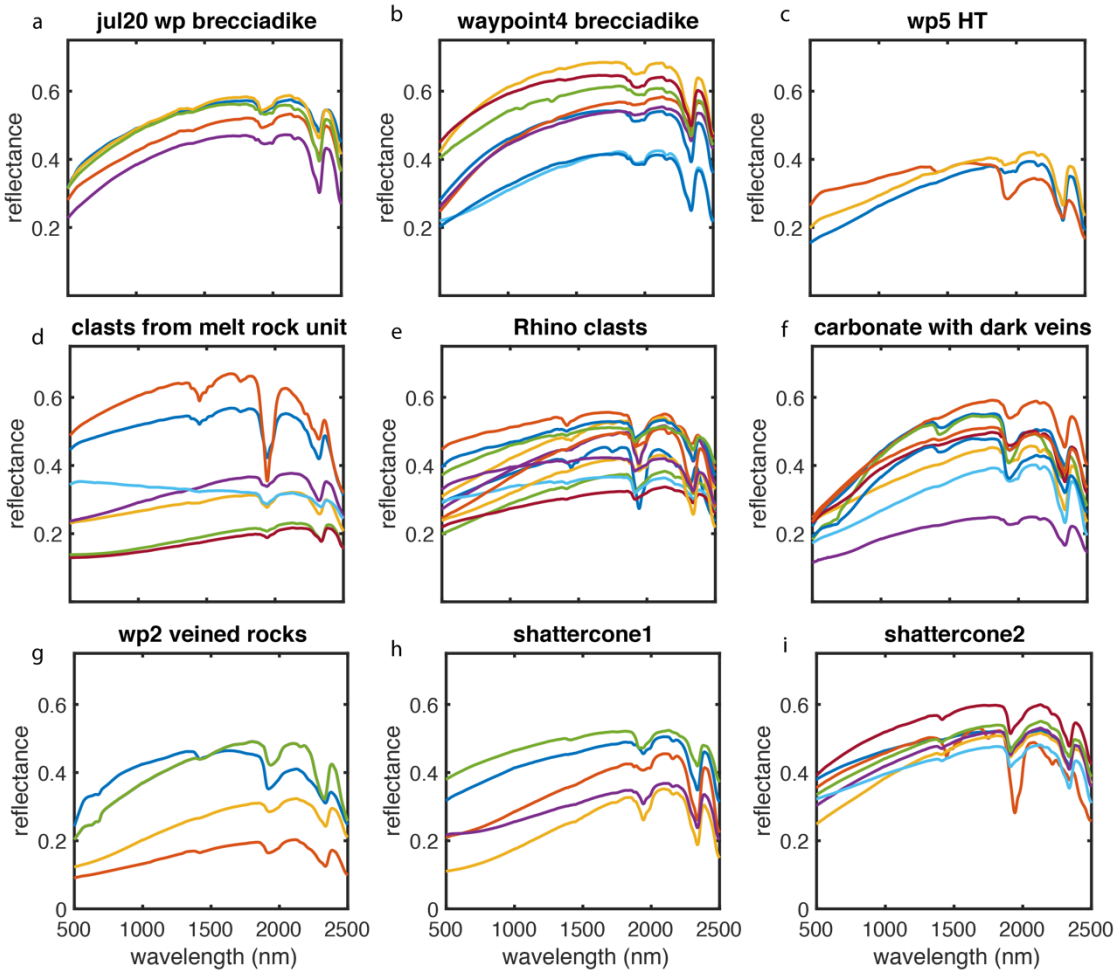

Figure 6: Visible-near-infrared spectra of relatively pristine carbonate clasts from the Haughton impact structure.

with apparent coatings that mask underlying carbonate features have been excluded). Carbonate clasts from Haughton typically show the overtones of CO_3^{2-} at slightly shorter wavelengths (2.32 μm and ~2.5 μm) than typical calcite, commonly associated with 1.4 and 1.9 μm bands due to H_2O overtones and combination. The 1.9-μm absorption is often broad enough to mask the 1.8 and 2.0 μm weaker bands of carbonates. In some cases, e.g. the two bright spectra in clasts from the melt rock unit (Figure 6d). the triplet at 1.4 is spatially associated with white-colored coatings due to gypsum, an alteration phases commonly found in the region. In fresh carbonate samples, a weak 2.18 μm feature due to higher order combination tones of CO_3 is present (Figure 6a, 6b, 6c, 6h).

In all the carbonate samples shown in Figure 6, where spectra are not dominated by coatings, an enhanced spectral slope at 0.5-1.7 μm is observed. The curvature of the 0.5-1.7 μm slope varies across different samples but does not match the broad absorptions expected from the electronic transitions due to Fe in siderite or Fe in Fe(III) oxides, and no other obvious absorption features are found in this region, except for the occasionally present 1.4-μm feature due to water and/or hydroxyl. The origin of the spectral slope is puzzling. The spectral slope may be due to a specific physical texture or chemical component in the sample that results in more enhanced absorption at shorter wavelengths and will be further discussed in Section 6.1 based on other measurements.

5.1.2 SEM-EDS analysis

Three carbonate clasts (rhino clast No. 8 and 9; shattercone1) with positive spectral slope are selected in the set of Haughton samples to be further studied under scanning electron microscope coupled with energy dispersive spectroscopy. Typically, pure calcium carbonate ($CaCO_3$) composition is found in the majority of the samples, with less than 5-10% of small particles of sulfate or clay (probably illite from Si, Al, and K correlations) on the surface of the samples, consistent with the results of ASD spectra. No particular Fe-bearing carbonate minerals have been identified in the EDS measurements. The calcite crystals typically exhibit pyramidal stacks of trigonal crystals approximately 1-2 μm on a side in all three samples, while the clay and sulfate mineral grains do not have a clear crystal form.

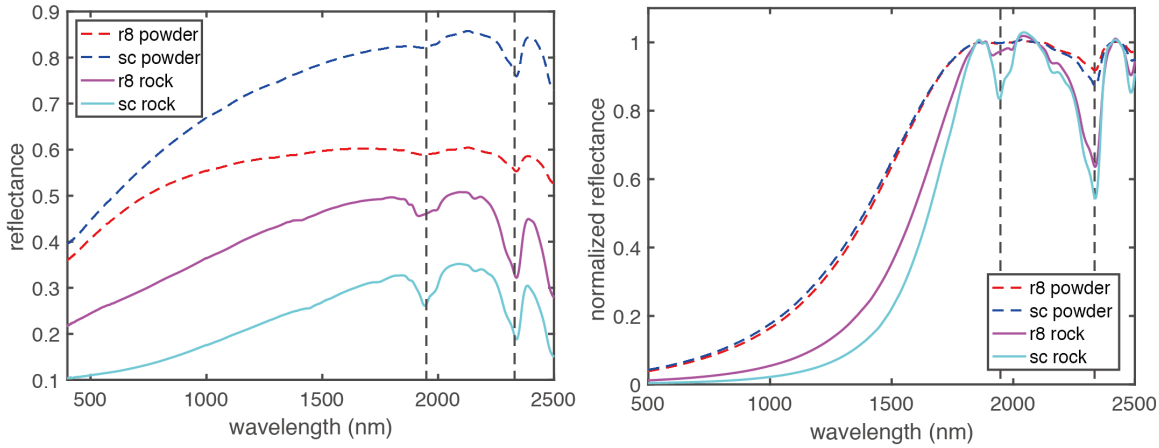

Figure 7: Left: Visible-near-infrared spectra of rock and powder of two samples from Haughton (r8: Rhino8, sc: shattercone). Right: All four spectra continuum-removed based on a 4-degree polynomial fit to reflectance at ~1.7, 2.1 and 2.4 μm. The normalization shows the decrease in absorption band strength of all major absorptions in the carbonates after powdering the rocks.

5.1.3 Macroscale textural effect on reflectance spectra in whole rock and powders

Comparing the reflectance spectra in whole rock and powders gives clues to the effect of physical texture and chemical components on the spectral slope, since the optical path is decreased and the surface texture is disrupted when a rock clast is ground into powders. We find the total reflectance is enhanced compared to rock measurements (Figure 7a), and all the absorption features are weakened in the powdered sample (Figure 7b). The spectra of powders still have a positive spectral slope, but rather the curvature is enhanced and the continuum-removed absorption at visible wavelengths is weakened (Figure 7b). To be more specific, the positive slope feature in 0.35 to 0.85 μm region remained unchanged while the slope between 1 μm and 1.7 μm is reduced in the powder spectra, resulting in a slightly different, reduced curvature compared to whole rock data.

5.1.4 Total organic carbon (TOC) in Haughton impact clasts

Total organic carbon was measured on powdered samples of two shocked carbonate clasts from the Haughton impact structure (Table 3). We find carbonate is the dominant component in both clasts, but the non-carbonate residual portion is higher in the shattercone sample (sc; ~ 7.86 %) and much less in the rhino clast (r8; ~0.62%). The weight percent of total organic carbon in the residual portion insoluble to HCl is 9.48% for shatter cone and 8.43% for Rhino 8. So the total organic carbon in the carbonate sample is ~0.75 wt % in the shatter cone sample and ~0.05 wt % in the Rhino clast. Given the uncertainty of HCl potentially dissolving some minor organic materials, these numbers represent a lower limit of the organic carbon content in these rocks. Nevertheless, the small amount of organics is consistent with the ATR spectra taken of both powders, where strong C-H stretching band around 2850-3000 cm^{-1} is not present (through two bands at 2870 and 2980 cm^{-1} are probably present in all three carbonate samples with minimal strength) and the powdered spectra have absorptions that are identical to pure calcite crystal (Figure 8). The amount of silicates and organics in the carbonate clasts may have had an impact on the infrared spectra and will be discussed in later sections.

5.2 Spectral variability of other terrestrial craters–*first results*

Carbonates from 6 impact craters (including Haughton) of diameters ranging from 6-30 km (Table 1) were collected and their spectra were measured and compared to understand if the spectral features observed in Haughton is applicable to broader scale. All

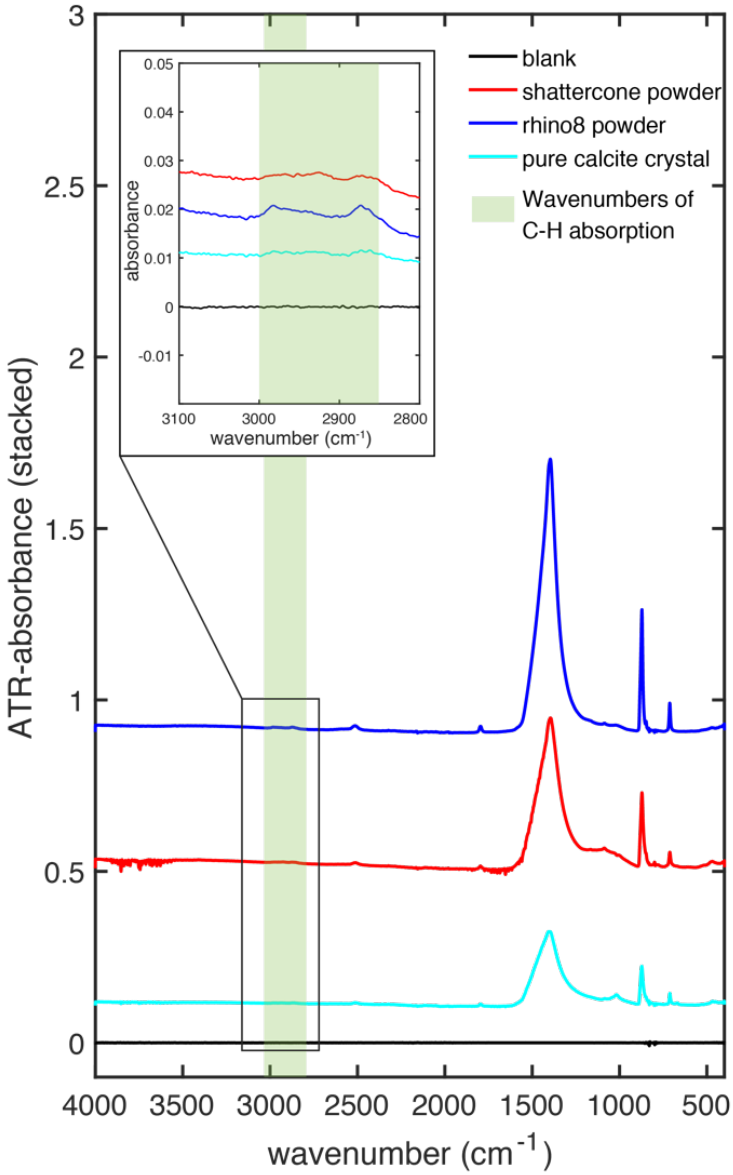

Figure 8: Attenuated total reflection spectra of two powdered samples from Haughton compared to a blank measurement and the spectrum of a pure calcite crystal. Green shaded region indicates the location of an absorption due to C-H stretching, expected for organic materials.

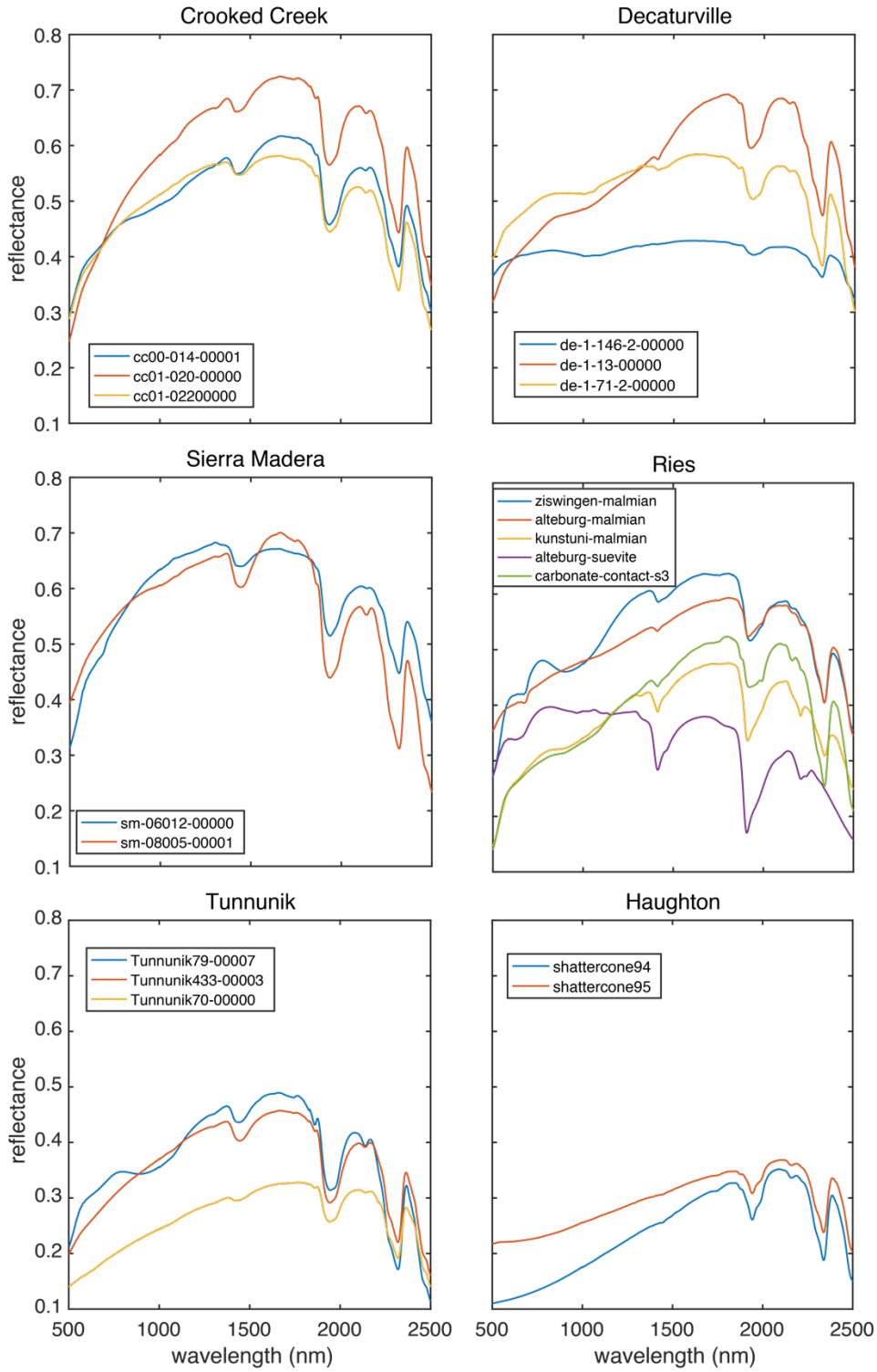

Figure 9: Visible-near-infrared spectra of relatively pristine carbonate clasts from six terrestrial impact structures (with information given in Table 1).

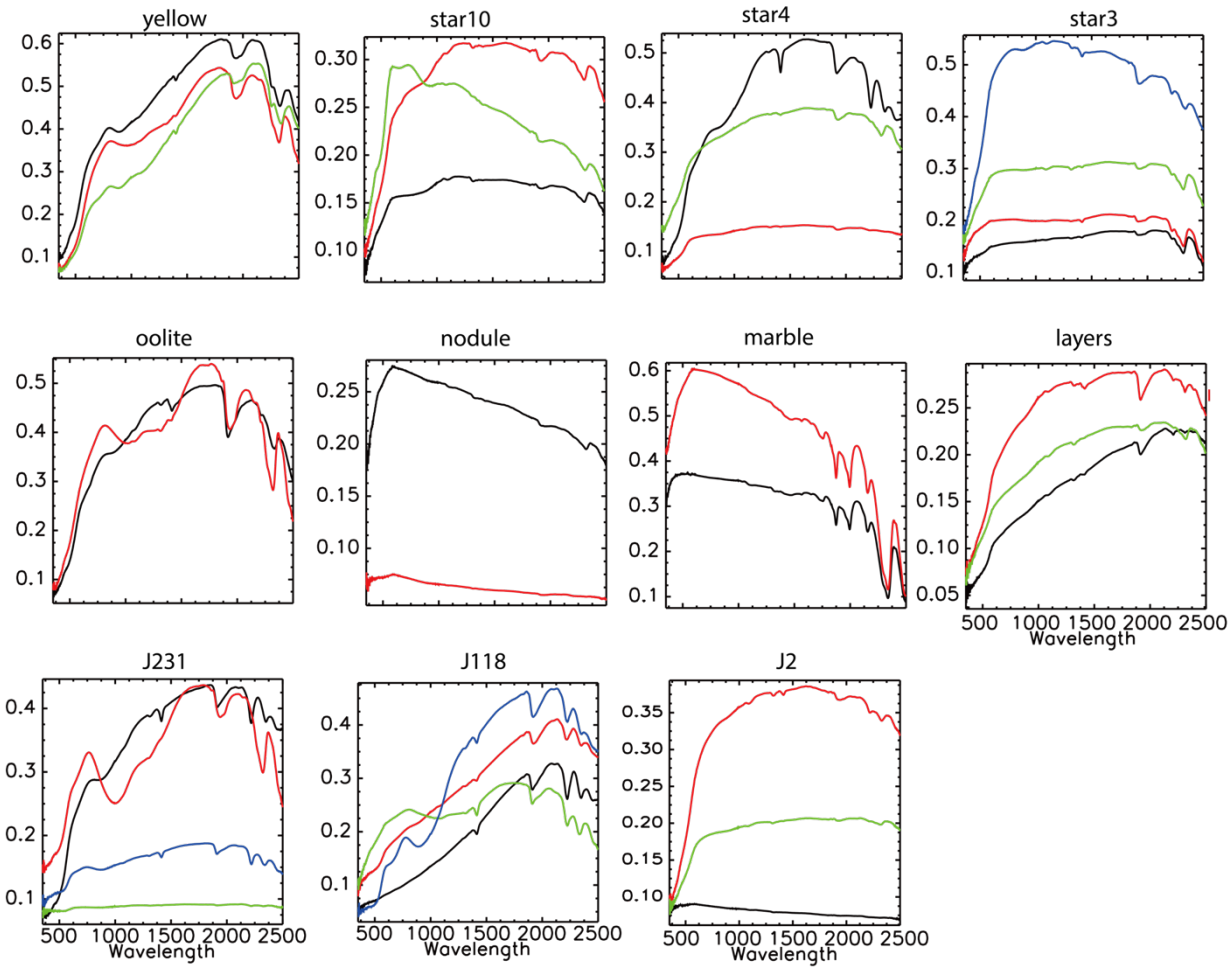

Figure 10: Visible-near-infrared spectra of carbonate from terrestrial unshocked samples.

the spectra taken of samples from impact-shocked carbonates show strong 2.3- and 2.5-μm absorption features typical of Ca- and Mg carbonate minerals (Figure 9). In all craters, there exists a weak 2.16-2.18 μm feature due to higher order combination in carbonate [Hunt and Salisbury, 1971, Gaffey, 1986]. Like those in the Haughton samples, all have a 1.9-μm band due to H_2O molecule and have a 1.4-μm H_2O/OH feature of varying relative strength. Select samples from Crooked Creek and Ries have absorptions at 650 and 900 nm in the visible-near-infrared and an absorption in the ultraviolet, extending to visible wavelength due to coating of Fe oxides, which are spatially correlated to the brownish/yellow weathering rind on the hand samples. The only suevite sample from Ries crater with some carbonate clasts did not show spectral features of carbonate rocks at 2.3 and 2.5 μm. All the carbonate samples except one clast from Decaturville possess a positive spectral slope to varying degrees, but the curvature varies in different samples. In the case of Crooked Creek (cc-01-014), Decaturville (de-1-13), Tunnunik (Tunnunik79), and three of five Ries spectra, a broad 1-μm absorption band due to Fe-oxide coating is present, and has an effect of enhancing the spectral slope. In Sierra Madera, Tunnunik, and Haughton, the slope is not associated to any specific feature and is indeed ubiquitous.

5.3 Analysis between terrestrial and Mars spectra *–first results*

Spectra with carbonate features are extracted and spectral parameters have been calculated and the rationale for each spectral parameter is summarized in Table 4. We compute the spectral features of carbonates from terrestrial impact craters (Figure 9) and natural carbonates (Figure 10) to Mars spectra (Figure 3). We exclude any samples with apparent weathering rinds or clay features or which do not exhibit any absorptions in the 1-2.6 μm range and compare the spectral parameters for samples with dominantly carbonate features. The Mars spectra used in this analysis are ratioed CRISM I/F spectra, so the band depth of Mars data measures the enhancement of a certain absorption compared to the denominator pixels, derived from spectrally featureless nearby areas (usually Mars dust). Consequently, all the band depths in Mars ratioed spectra are small compared to Earth data (Figure 11).

The slope in the 1-1.7 µm wavelength range is enhanced in Mars spectra compared to Earth rocks. All the Mars data and all samples (except two) in terrestrial impact craters show a positive spectral slope, while other Earth carbonates could have a negative spectral

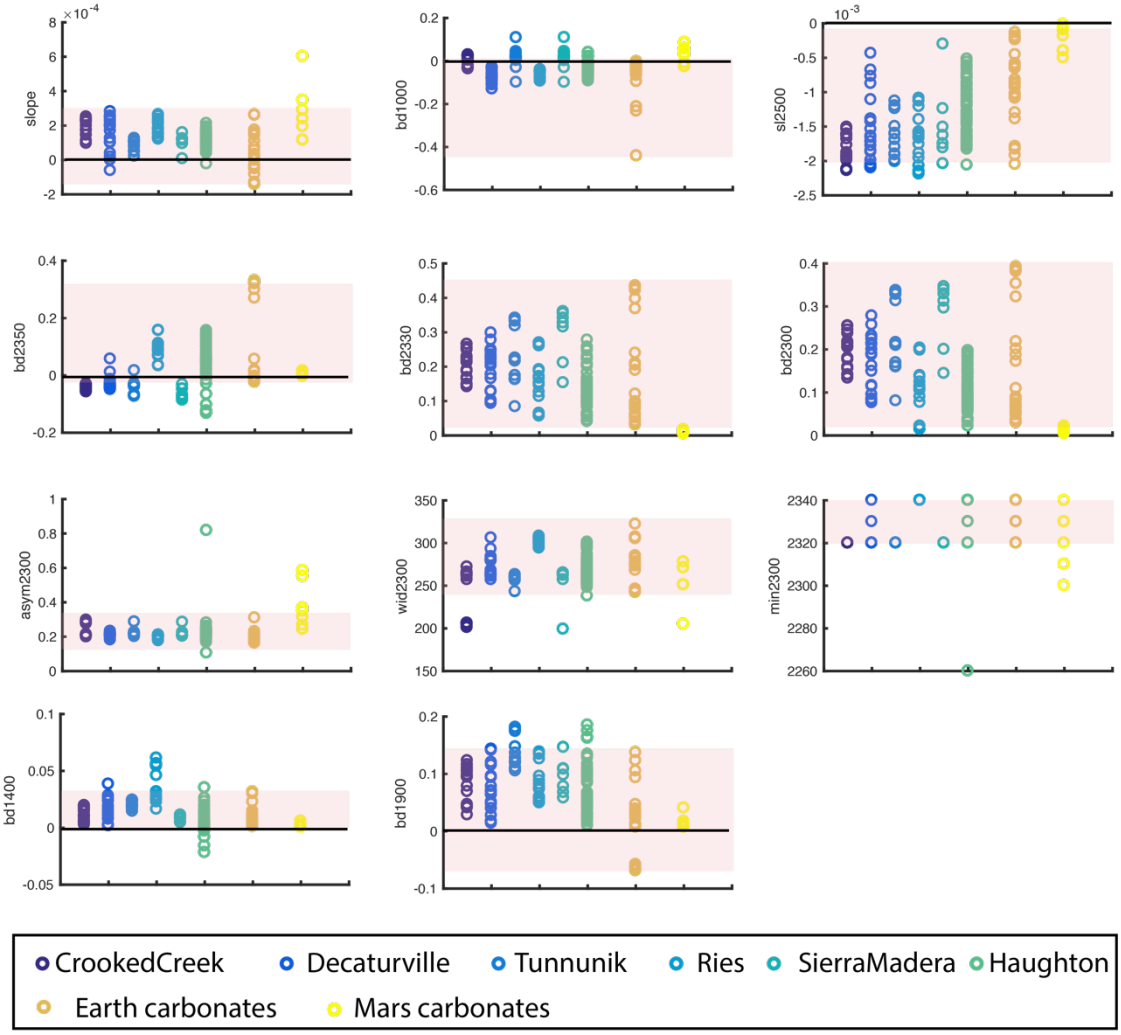

Figure 11: Spectral parameters computed from spectra of earth impact rocks, earth carbonates, and Mars carbonate spectra. Dark solid line at 0 value of each spectral parameter is plotted where applicable (e.g., zero band depth). Pink shaded region shows the variability of Earth natural carbonates. Dark grey region in the min2500 parameter indicates this parameter for Earth rocks cannot extend beyond 2.5 µm due to the limit of the ASD spectrometer used to take data.

slope, as seen in some of the laboratory data (e.g. the aragonite spectra in Figure 3). There is no significant variation between Earth and Mars in terms of the band depth of 1.0 μm band due to Fe substitution in carbonate. Some of the Earth carbonates have negative values due to non-detection of Fe and a negative slope. Parameterization of the curvature and shape of this wavelength will be needed to better characterize the variability in the spectral features in this wavelength region.

The band depth of water features exhibits a wide range, but the impact-shocked samples have slightly stronger water absorptions compared to terrestrial carbonates data in at both 1.9 μm and 1.4 μm. The band depth of 1.9-μm and 1.4-μm features are not correlated. For example, Tunnunik crater has the strongest 1.9 μm feature but only an average 1.4 μm band depth compared to other craters.

The band depth of the 2.3-μm and 2.5-μm absorption features can correlate with either the abundance of carbonate minerals in the sample (increasing depth with increasing abundance) and grain size of the sample (increasing depth with increasing grain size). Though there are differences among different impact sites, they generally fall within the range of terrestrial sedimentary carbonate. The band width and position of the 2.3 μm and 2.5 μm bands are comparable across Earth and Mars spectra. In a minority of detections in Earth impact samples and Mars data, the 2.3 μm can be narrower than natural terrestrial carbonates. Band centers are also sometimes at shorter wavelength in Mars data. The 2.3 μm absorption band is asymmetric in all of the data acquired (asym2300<1) but is significantly more asymmetric (0.15<asym2300<0.37) in all Earth samples than in Mars data.

5.4 Shock recovery experiment *–first results*

Here we present near-infrared spectra taken on the natural magnesite sample before and after the shock recovery experiment measured using Headwall Photonics Inc. imaging spectrometer (Figure 12). In addition to typical C-O bands at 2.316 and 2.515 μm, the natural magnesite sample used in the impact experiment show absorption due to H_2O and OH in the structure at 1.415 μm and 1.914 μm, the latter forming a doublet with an associated C-O band at 1.968 μm. The C-O bands are unchanged after the shock experiment, but we observe both the 1.415 and 1.914 μm bands are weakened compared

to other absorptions due to C-O, presumably resulted from the loss of H_2O and OH. Weaker combinations in the carbonates at 1.866 and 2.136 µm are present before the shock. These absorption features remain unchanged at 5 GPa but seem to be weakened after the 10 GPa shock. The magnesite samples show no particular short wave infrared slope before or after the shock, though in all cases, there is a slight drop off at ~0.5 µm. These results suggest at relevant shock pressure (5 and 10 GPa), there is no structural change to the magnesite in the natural sample but there may be minor changes probably related to water.

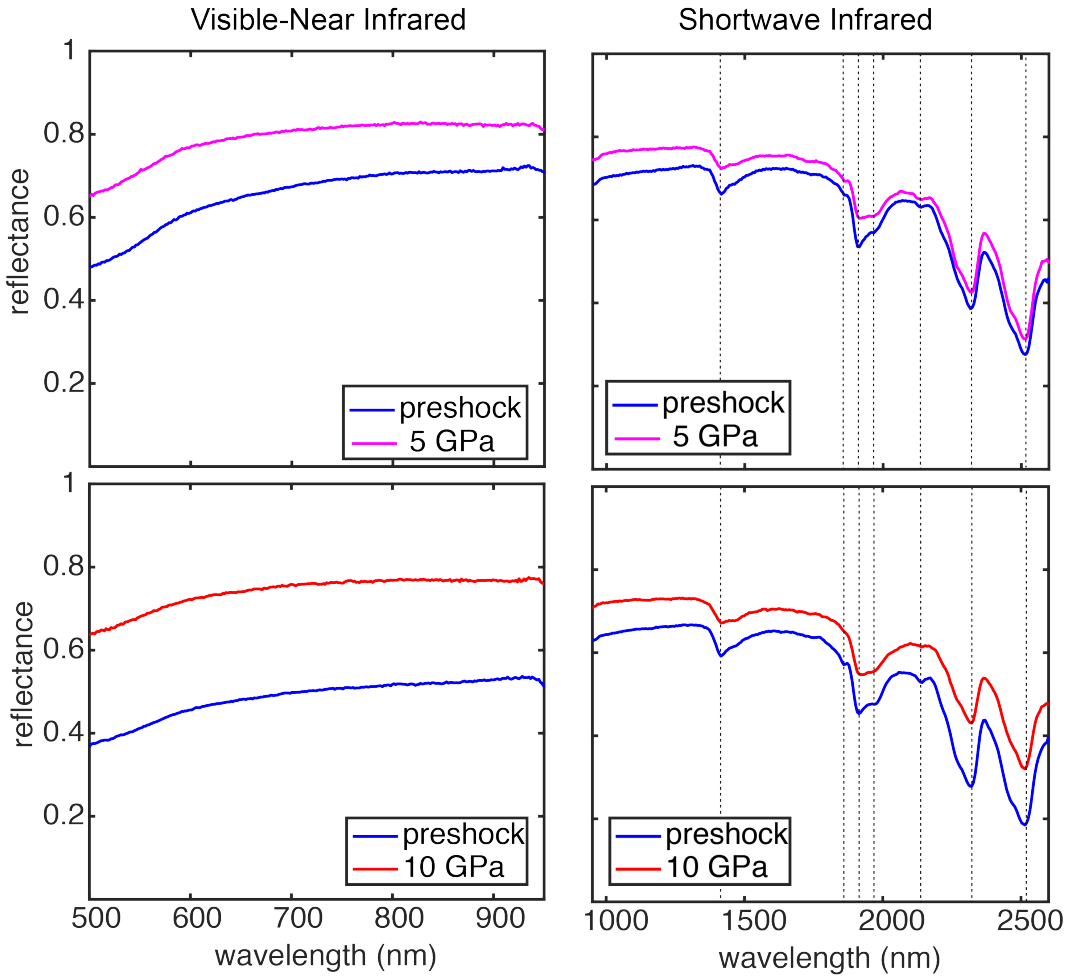

Figure 12: Spectra of magnesite before and after shock experiment. a-b) Spectra of Sample A at shock pressure of ~5 GPa measured with both VNIR and SWIR detector; c-d) Spectra of Sample B at shock pressure of ~10 GPa measured with both VNIR and SWIR detector.

6. Discussion

6.1 Cause of spectral slope in Haughton samples

The red slope in the 0.5-1.7 μm region is found to be ubiquitous in samples from Haughton impact structure and is also found in carbonates in a number of other impact structures and some unshocked carbonates. This same smooth drop-off with no Fe^{3+} bands has been observed previously in dolomite and limestone from the Mississippian Lodgepole Formation and the origin is not understood (Figure 13) [Gaffey, 1986]. Theoretically, this sloping feature can be caused by a darkening agent strongly absorbing in the visible and extending the absorption into the infrared or a light-trapping texture effect at the scale of the relevant wavelength (~0.5-2μm).

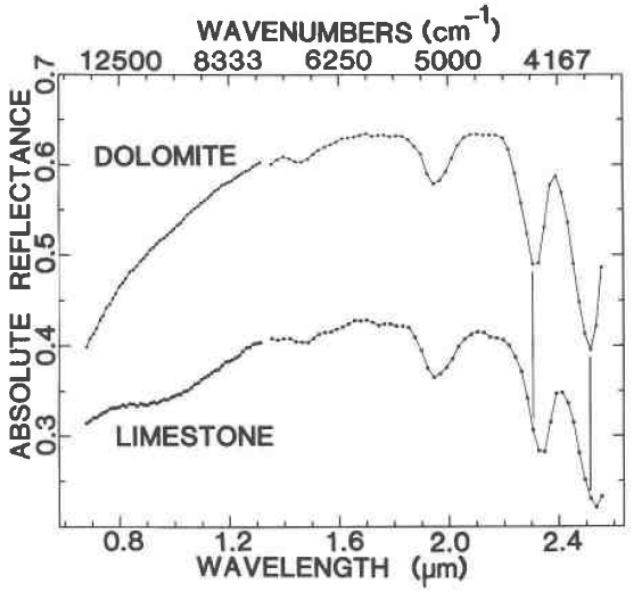

Figure 13: Dolomite and limestone spectra from Mississippian Lodgepole Formation [Gaffey, 1987].

Comparing the spectra of Haughton samples, we find enhanced total reflectance when the rock is ground into powders. This is consistent with scattering theory, since light travels further into the whole rock sample before encountering an interface, resulting in an increase in the optical path length for absorption, and thus a decrease in absolute reflectance. The

positive slope still is preserved in the spectra of fine-grained powder of the sample, which indicates that the surficial texture of the whole rock is not the main cause the slope.

Rather, the change in 0.5-1.7 μm can be explained mixing of a chemical component that absorbs strongly in the visible. The absorption in the visible is weakened in the powdered samples compared to whole rocks because of the smaller particle size and reduced optical path length for powdered samples.

We fit the curves of powder and whole rock on a plot with logarithm of the intensity of reflectance, in accordance with Lambert's law, which states absorbance of a material sample is directly proportional to its thickness (path length):

$$A = \log\left(\frac{I_0}{I}\right) = kx$$

where I_o is the original light intensity, I is the outgoing intensity, x is the thickness of the mineral light has passed through, and k is the effective absorption coefficient. We assess if the slope can be characterized as an absorption feature that changes with grain size. If the samples follow a Beer-Lambert's law, we expect the scattered points to be linearly correlated, as shown in previous examples [Gaffey, 1986]. Here we find in wavelength 1700-2500 nm, the data approximately can be fit linearly, consistent with the prediction of Beer-Lambert law (Figure 14). However, in wavelengths from 350 nm to 1700 nm the fit cannot be obtained with a simple line (Figure 15), which means the reflectance behavior does not obey Beer's law. This implies that the effective absorption coefficient in these wavelengths changes when the rock is ground into powders. The powder is darker that predicted by the linear relationship at the visible wavelengths, indicating nonlinear effects of mixing. The Haughton target samples are known to contain solid bitumen and liquid hydrocarbons within fluid inclusions [Parnell et al., 2003], which is a potential source of the darkening agent.

The measured concentration of carbon-bearing organic compounds can be as high as 7.8%, which might have been the cause for the spectral slope in these samples. However, the exact species and spectral behavior of these organics need to be further confirmed through analysis of a larger set of samples. Based on previous work [Parnell et al., 2003],

solid bitumen and liquid hydrocarbons are potential candidates in the sample. For example, asphaltite dust has a positive spectral slope from 0.4 to 0.8 µm [Moroz et al., 2003].

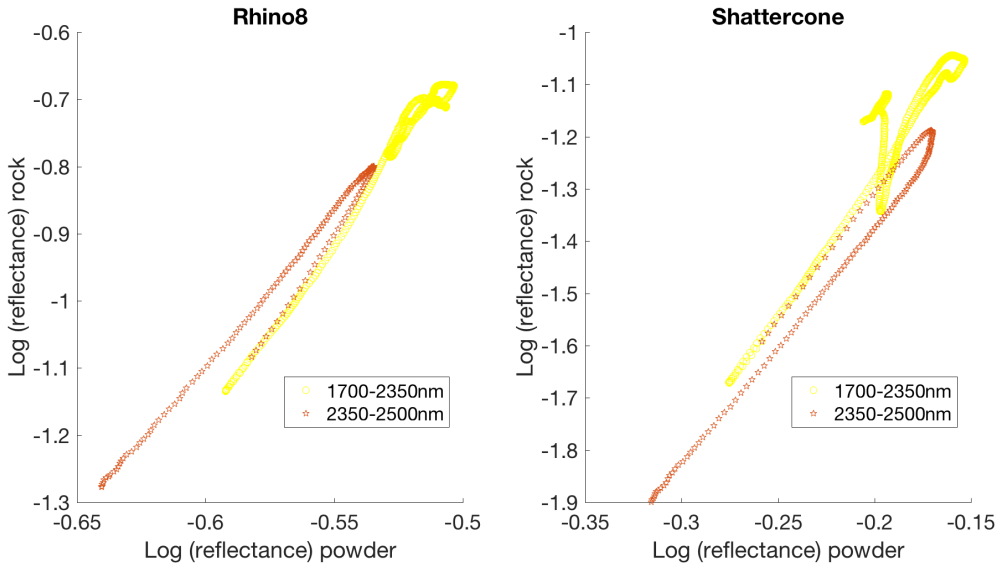

Figure 14: Log-log plot of the reflectance spectra of rock and powder for both rhino8 and shattercone samples with wavelength range of 1700 nm to 2500 nm.

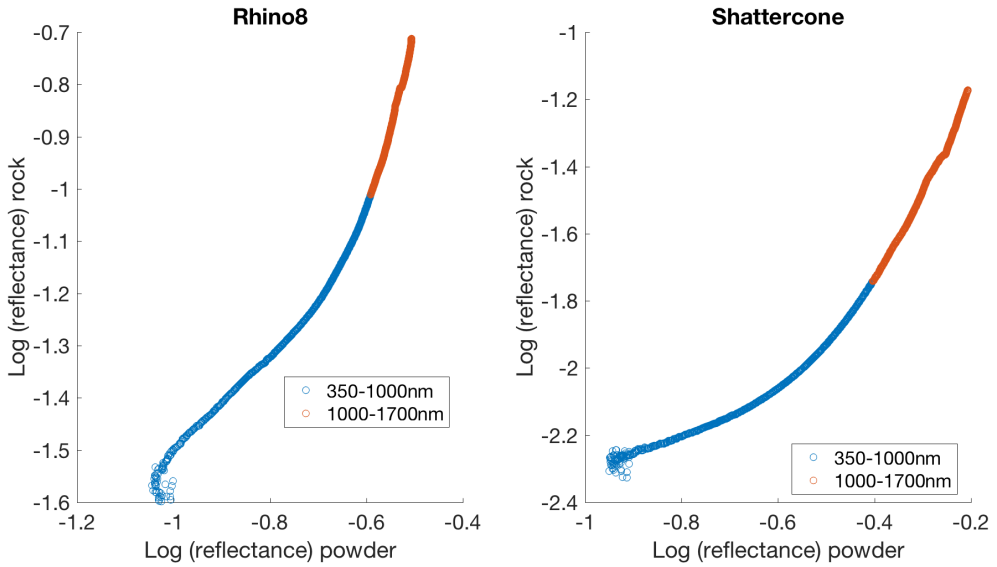

Figure 15: Log-log plot of the reflectance spectra of rock and powder for both rhino8 and shattercone samples with wavelength range of 350 nm to 1700 nm.

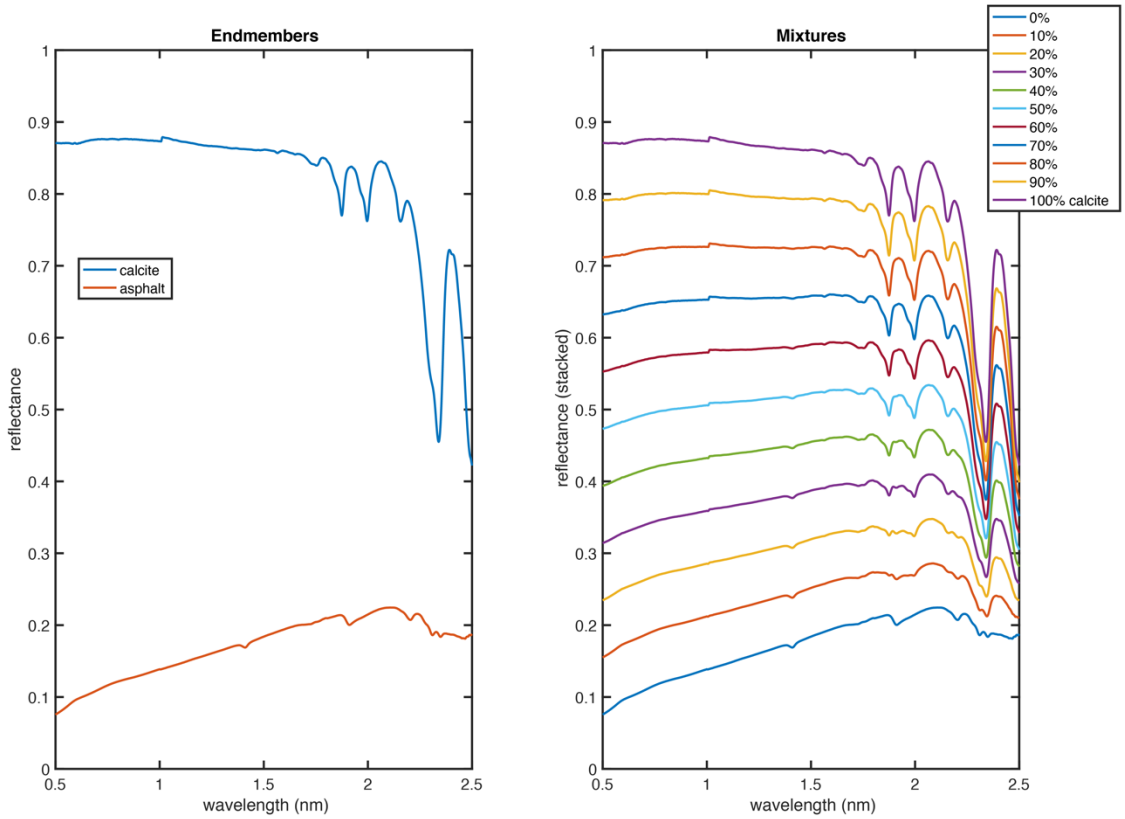

Figure 16: Linear mixing results of mixture of calcite (calcite_gds304.4124) and asphalt (black_old_asphaltroof_gds376.27384). Both spectra are from splib06 from Unites States Geological Survey (USGS).

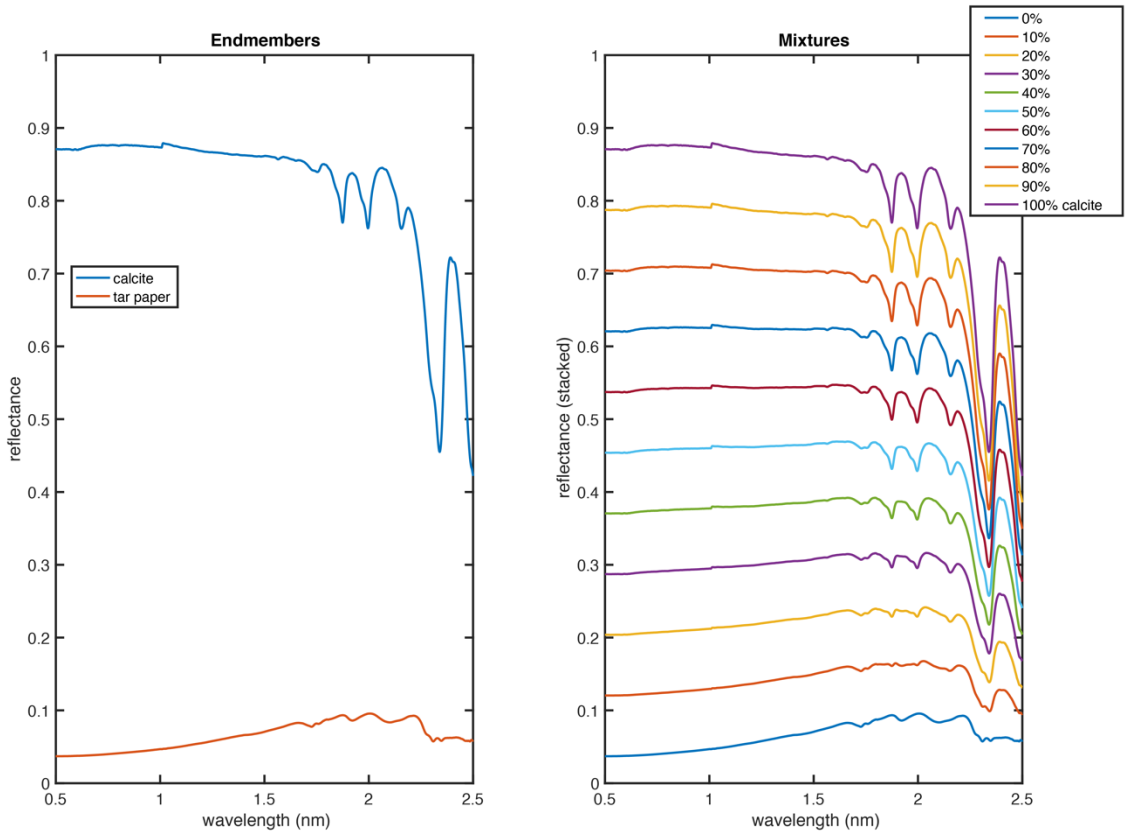

Figure 17: Linear mixing results of mixture of calcite (calcite_gds304.4124) and tarpaper (tarpaper_gds285a.29421). Both spectra are from splib06 from Unites States Geological Survey (USGS).

Using spectra from the USGS spectral library we test a linear mixture of calcite and different darkening agents, including carbon black, lichen, asphalt, and tarpaper. We find it is hard to reproduce the smooth spectral slope without introducing multiple absorption bands in the lichen mixture. The carbon black did not recreate the spectral slope. Here we show the mixture of asphalt (Figure 16) and tarpaper (Figure 17), in which the positive slope feature can be reproduced in mixture of carbonate with 30-40% of asphalt and 80-90 % of tarpaper. In summary, it is highly probable that the slope feature is caused by solid or liquid hydrocarbon in the samples. However, how the small amount of hydrocarbon created the enhanced spectral slope in Haughton samples is still not very well-understood. Non-linear mixing models (e.g. Hapke, [1981]) can be applied to confirm if the spectral feature can be reproduced in the case of intimate mixing. The mixing effect when the organics are present in liquid form in the samples needs to be further examined.

6.2 Spectral variability in terrestrial carbonates and implications for Mars

In terrestrial carbonate samples, weathering rinds and coatings of several millimeters can completely mask the spectral features of the underlying carbonate rocks (Figure 10). But for rocks with a fresh surface, there are variations in the spectral properties, including the red slope, presence/absence of 1.4 μm and 1.9 μm water bands, broad 1 μm absorption, and the width and band position of both 2.3 and 2.5 μm absorptions.

The existence of water bands in the carbonate rocks is due to the aqueous inclusions in the carbonate deposition environment as suggested by [Gaffey, 1986]. The features of the water bands remain unchanged or enhanced in the impact shocked samples, which may indicate these inclusions survived the pressure and temperature of the impact or that they are more susceptible to post-impact alteration that introduces water.

When compared to Mars spectra, the most significant difference is the enhanced red slope in the 1-1.7 μm range. As discussed above, the slope in the Haughton impact rocks are probably due to a small amount of solid or liquid hydrocarbons in the samples, though the actual mechanism of mixing that results in the darkening needs to be further examined. Indeed, there is no known source of organics on Mars, but it is possible that organic materials can be delivered by asteroids and comets. Alternatively, the feature we observe in Martian spectra could be due to a minor component with similar darkening effect, e.g.

small melt pocket from impact. This still remains an open question and needs to be addressed in a more systematic way.

We also observe a rather symmetric behavior of the 2.3 μm band in Mars data compared to terrestrial carbonates. The more symmetric band shape of 2.3 μm feature is probably due to mixture with Fe/Mg phyllosilicate with a strong 2.3 μm absorption, which is quite widespread on Mars.

Regardless of the changes in spectral slope and band shapes, the 2.3 and 2.5 μm are strong in all freshly exposed carbonate rocks as observed in terrestrial samples, despite being shocked in meteoric impact. Thus, unless carbonates are always obscured by coatings or buried in great depth on Mars, the distribution of carbonate on the surface of Mars is likely representative of the carbonate reservoir in the Martian upper crust.

6.3 Carbonates in impact shock experiment

To first order, the spectral features of magnesite samples did not change significantly after impact shock at ~5 GPa and ~10 GPa. For the two strong carbonate bands at ~2.3 and ~2.5 μm in this wavelength region, the locations of the absorption minimum, band width and absorption strength remain unchanged. These results indicate that the carbonate mineral structure stayed intact in the presence of relevant shock pressure for the majority of terrestrial target rock.

Except for the slight drop off in the visible wavelength (probably related to iron), there is no observed visible-near-infrared spectral slope in the natural magnesite sample before or after the shock, indicating the spectral slope observed in some other terrestrial impact structures is probably unrelated to the impact event.

Interestingly, we do observe weakening in the water bands at 1.415 and 1.916 μm in both shock experiments. Previous works suggested that bands due to the H_2O and OH are often present in carbonate rocks due to water in fluid inclusions [Gaffey, 1986]. Our first results show that during impact events, these minor components of water in the carbonate rocks could be partially released or mobilized at relevant pressure and temperature.

7 Summary and future work

Through a series of spectral analyses, we found spectral variability in carbonates from different settings on Earth and proposed possible causes for different spectral features and their implications for Mars. We find absorption features of carbonates as previously reported in terrestrial sedimentary carbonate and carbonates in impact structures. A positive slope in the wavelength region of 1-1.7 μm is found in both Mars spectra and some terrestrial shocked samples, which could be due to a small amount of organics dispersed in the carbonate samples from Haughton impact structure, but the actual darkening mechanism or compound responsible is unclear. Carbonate detections on Mars share the same features, which could be due to a minor component of similar darkening effect, e.g. small melt pockets or hydrocarbons delivered by asteroids or comets. Spectral features of Martian carbonates also have a narrower and more symmetric 2.3 μm than typical carbonates on Earth, which could be due to mixture with clay. Through a different approach, we obtained data from a controlled shock recovery experiment on a 20 mm light gas gun. The results suggest that at relevant shock pressures (~5 and 10 GPa), the visible-near-infrared slope and the major carbonate absorptions at 2.3 and 2.5 μm remain unchanged, while absorptions related to water and hydroxyl are weakened. These analyses suggest, despite the complexity in variations in the spectral continuum, that the 2.3 and 2.5 μm absorption features of carbonate minerals remain unchanged in shocked carbonate rocks on Earth and could be observed on Mars if exposed on the surface.

For future work, mixing models of multiple spectral endmembers, and different grain sizes can be tested to reproduce spectral properties in Haughton impact rocks. Systematic characterization of the bulk chemistry and mineralogy of the terrestrial samples will help resolve the spectral variability regarding the water features in the carbonate rocks. Shock experiments at higher pressures and further chemical analysis of shocked samples will help resolve the effects of different shock pressures on minor components in carbonate rocks. The spectral variability observed in terrestrial samples and lab experiments will be more systematically compared to Mars data and shed new light on the carbonate reservoir on Mars.

Table 1: Summary table of information for samples from 6 terrestrial impact craters in this study.

Impact crater	Location	Diameter (km)	Age (Ma)	Lat	Lon	Sample description	Sample name	Reference
Haughton	Nunavut, Canada	23	23	75°22'N	89°41'W	Mostly dark limestone clasts in impact melt units and breccia. A few with dark veins cutting through. Two clasts have shattercone texture indicating minimal shock pressure of 2 GPa.	e.g. Rhino_8, Shattercone. See Table 2 (identifier)	e.g. Bischoff et al., 1988; Osinski et al., 2001
Ries	Nordlingen, Germany	20	15	48°53'N	10°37'W	4 brown-grey Malmian limestones from different quarries; 1 suevite sample with carbonate lithic clasts; 1 light-colored limestone in Bunte breccia in contact with suevite	ziswingen-malmian, alteburg-malmian, kunstuni-malmian, kunstuni-malmian2, alteburg-suevite, limestone-contact.	e.g. Hörz, 1983; Newsom et al., 1986
Tunnunik	Victoria island, Canada	25 exposed	>130 <450	72°28'N	113°58'W	Three dark grey clasts with dark coating and one (79) with yellowish weathering surface	Tunnunik70, Tunnunik79, Tunnunik166, Tunnunik433	Dewing et al., 2013
Crooked creek	Missouri, United States	7	~320	37°50'N	91°23'W	Small carbonate clasts: including a yellowish crumbly limestone (017)	cc00-014, cc01-020, cc01-022, cc017.	e.g. Amstutz, 1965; Kenkmann, 2002
Sierra Madera	Texas, United States	13	<100	30°36'N	102°55'W	Two clasts: a fine grained light-grey, porous with shattercone-like texture (06-012); a clast with curvilinear fractures, dense, light-colored (08-005).	sm-06-012, sm-08-005.	e.g. Howard et al, 1972; Goldin, 2006; Huson et al., 2011
Decaturville	Missouri, United States	6	<300	37° 54'N	92°43'W	Six pieces of clast-rick melt rocks with carbonate	de-01-006, de-01-013, de-1-71-2, de-1-146-2, de-1-428-2, de-1-2339-2	e.g. Offield et al., 1977; Nickerson et al., 2001

Table 2: Sampling location and description of the carbonate clasts from Haughton impact structure.

Way-point	Lat	Lon	Field notes / Outcrop	identifier	# of clasts
2	75.36	-89.57	Darker rock with boxwork orange/white; on top of Eleanor R Formation	waypoint2_veined	3
4	75.36	-89.57	Small breccia dike in Eleanor River with missing clasts	waypoint4_brecciadike	3
5	75.36	-89.56	Very fine grained homogenous outcrop with amazing shattercones	waypoint5_HT	1
6	75.36	-89.56	Polymict/lithic breccia dike	jul20_wp_brecciadike	1
8	75.34	-89.64	No outcrop; melt rock hill with most cobbles in place/eroded	clasts_from_melt_rock_unit	8
11	75.34	-89.61	Bay Fiord formation	21jul2016bayfiordblack_white	1
14	75.35	-89.59	Non-gypsiferous Bay Fiord or Eleanor River with great shattercones	shattercone	2
15	75.41	-89.62	Rhino east	Dark clay-rich rock with gypsum coating	1
18	75.41	-89.63	Rhino	22jul2016_rhino_outcrop_clasts (rhino1-12)	12
30	75.39	-89.68	Layered sandstone	Layered sandstone	1
41	75.35	-89.55	Hydrothermal vein of sulfide/sulfate; altered breccia	carbonate with dark veins	6
1	75.37	-89.55	Dike of dark material within Eleanor River uplift	middlehill	2

Table 3: Results from total organic carbon measurements of 2 powdered samples from Haughton impact structure.

	total weight (g)	Residual after HCl dissolution (mg)	Residual after HCl dissolution (wt %)	Total organic carbon in residual (wt %)	Total organic carbon in rock (mg)	Total organic carbon in rock (wt %)	$d^{13}C/^{12}C$ (per mil)	$d^{18}O^{16}O$ (per mil)
shattercone	3.00	235.57	7.86	9.48	22.34	0.75	-6.52	-20.07
Rhino 8	1.03	6.39	0.62	8.43	0.54	0.05	-28.46	-20.83

Table 4: Spectral parameters analyzed in this work, with rationale and formula used in calculation. Here "R" represents the reflectance data at a given wavelength, "R_C" represents the reflectance of the continuum at that wavelength, and "wvl" represents the wavelength of a minimum or maximum position in reflectance spectra.

Spectral parameter	Rationale	Formula
VNIRslope	red slope from 1.7 to 1 µm	(R1700-R1000)/(1700-1000)
bd1000	Band depth of the broad 1 µm absorption band, due to Fe-substitution	(1-R1054/RC1054)*0.1+(1-R1211/RC1211)*0.1+(1-R1329/RC1329)*0.4+(1-R1474/RC1474)*0.4
bd1400	Band depth of 1.4 µm, absorption due to OH	1-R1400/RC1400
bd1900	Band depth of 1.9 µm, absorption due to water	1-R1900/RC1900
bd2330	Band depth at 2.33 µm, due to Ca- or Fe- carbonate	1-R2327/RC2327
bd2300	Band depth at 2.30 µm, due to Mg-carbonate and/or Fe/Mg phyllosilicate	1-R2300/RC2300
bd2350	Band depth at 2.35 µm, due to Ca- or Fe- carbonate, chlorite, illite, muscovite	1-R2364/RC2364
wid2300	Band width of 2.3 µm	wvl(maxR) – wvl(minR)
min2300	Absorption center of 2.3-2.35 µm, correlated with carbonate cation chemistry	wvl[min(~R2300)]
asym2300	Asymmetric parameter of the 2.3 µm band (1 being symmetric), distinguishing clay from carbonate	(RMax - min2300)/(min2300 - LMax)
sl2500	Slope of the shorter wavelength side of the 2.5 µm absorption band, proxy for band position of 2.5 µm carbonate feature. (ASD spectra do not extend to wavelengths beyond 2.5 µm)	(R2510-R2400)/(2510-2400)
min2500	Absorption center of 2.5-2.55 µm, correlated with carbonate cation chemistry.	wvl[min(~R2500)]

References:

Agrinier, P., A. Deutsch, U. Schärer, and I. Martinez (2001), Fast back-reactions of shock-released CO2 from carbonates: An experimental approach, Geochim. Cosmochim. Acta, 65(15), 2615–2632, doi:10.1016/S0016-7037(01)00617-2.

Amstutz, G. C. (1965), A morphological comparison of diagenetic cone-in-cone structures and shatter cones, Ann. N. Y. Acad. Sci., 123(2), 1050–1056.

Badjukov, D. D., Y. P. Dikov, T. L. Petrova, and S. V. Pershin (1995), Shock behavior of calcite, anhydrite, and gypsum, in LPS XXVI, pp. 63–64.

Bandfield, J. L., T. D. Glotch, and P. R. Christensen (2003), Spectroscopic identification of carbonate minerals in the martian dust., Science, 301(5636), 1084–1087, doi:10.1126/science.1088054.

Bell, M. S., F. Horz, and A. Reid (1998), Characterization of experimental shock effects in calcite and dolomite by X-ray diffraction, in Abstracts with Programs - Geological Society of America, vol. 30, p. 289.

Bell, M. S. (2016), CO2 release due to impact devolatilization of carbonate: Results of shock experiments, Meteorit. Planet. Sci., 51(4), 619–646, doi:10.1111/maps.12613.

Bischoff, L., and W. Oskierski (1988), The surface structure of the Haughton impact crater, Devon Island, Canada, Meteorit. Planet. Sci., 23(3), 209–220.

Bishop, J. L. et al. (2013), Mineralogy and morphology of geologic units at Libya Montes, Mars: Ancient aqueously derived outcrops, mafic flows, fluvial features, and impacts, J. Geophys. Res. E Planets, 118(3), 487–513, doi:10.1029/2012JE004151.

Booth, C., and H. H. Kieffer (1978), Carbonate Formation in Marslike Environments, Jouranl Geophys. Res., 83(B4), 1809–1815, doi:10.1029/JB083iB04p01809.

Borg, L. E., J. N. Connelly, L. E. Nyquist, C.-Y. Shih, H. Wiesmann, and Y. Reese (1999), The Age of the Carbonates in Martian Meteorite ALH84001, Science (80-.)., 286(5437), 90–94, doi:10.1126/science.286.5437.90.

Boslough, M. B., T. J. Ahrens, J. Vizgirda, R. H. Becker, and S. Epstein (1982), Shock-induced devolatilization of calcite, Earth Planet. Sci. Lett., 61(1), 166–170, doi:10.1016/0012-821X(82)90049-8.

Boynton, W. V et al. (2009), Evidence for calcium carbonate at the Mars Phoenix landing site., Science, 325(5936), 61–64, doi:10.1126/science.1172768.

Bultel, B., C. Quantin-Nataf, M. Andréani, H. Clénet, and L. Lozac'h (2015), Deep alteration between Hellas and Isidis Basins, Icarus, 260, 141–160, doi:10.1016/j.icarus.2015.06.037.

Carrozzo, F. G., G. Di Achille, F. Salese, F. Altieri, and G. Bellucci (2017), Geology and mineralogy of the Auki Crater, Tyrrhena Terra, Mars: A possible post impact-induced hydrothermal system, Icarus, 281, 228–239, doi:10.1016/j.icarus.2016.09.001.

Carter, J., and F. Poulet (2012), Orbital identification of clays and carbonates in Gusev crater, Icarus, 219(1), 250–253, doi:10.1016/j.icarus.2012.02.024.

Carter, J., F. Poulet, J. P. Bibring, N. Mangold, and S. Murchie (2013), Hydrous minerals on Mars as seen by the CRISM and OMEGA imaging spectrometers: Updated global view, J. Geophys. Res. E Planets, 118(4), 831–858, doi:10.1029/2012JE004145.

Deutsch, A., and F. Langenhorst (2007), On the fate of carbonates and anhydrite in impact processes - evidence from the Chicxulub event, Geol. Föreningen Förhandingar, 129(2), 155–160, doi:http://dx.doi.org/10.1080/11035890701292155.

Dewing, K., B. R. Pratt, T. Hadlari, T. Brent, J. BÉDard, and R. H. Rainbird (2013), Newly identified "Tunnunik" impact structure, Prince Albert Peninsula, northwestern Victoria Island, Arctic Canada, Meteorit. Planet. Sci., 48(2), 211–223.

Edwards, C. S., and B. L. Ehlmann (2015), Carbon sequestration on Mars, Geology, 43(10), 863–866, doi:10.1130/G36983.1.

Ehlmann, B. L. et al. (2008), Orbital Identification of Carbonate-Bearing Rocks on Mars, Science (80-.)., 322(5909), 1828–1832, doi:10.1126/science.1164759.

Forget, F., R. Wordsworth, E. Millour, J. Madeleine, V. Eymet, and R. M. Haberle (2010), 3d Modeling Of The Early Martian Climate And Water Cycle, Am. Astron. Soc. DPS Meet. #42, #45.02; Bull. Am. Astron. Soc. Vol. 42, 1047.

Gaffey, S. J. (1986), Spectral reflectance of carbonate minerals in the visible and near infrared (0.35-2.55 microns): calcite, aragonite, and dolomite., Am. Mineral., 71(1–2), 151–162.

Gaffey, S. J. (1987), Spectral reflectance of carbonate minerals in the visible and near infrared (0.35–2.55 um): Anhydrous carbonate minerals, J. Geophys. Res., 92(B2), 1429, doi:10.1029/JB092iB02p01429.

Galy, V., J. Bouchez, and C. France-Lanord (2007), Determination of Total Organic Carbon Content and δ 13 C in Carbonate-Rich Detrital Sediments, Geostand. Geoanalytical Res., 31(3), 199–207, doi:10.1111/j.1751-908X.2007.00864.x.

Goldin, T. J., K. Wunnemann, H. J. Melosh, and G. S. Collins (2006), Hydrocode modeling of the Sierra Madera impact structure, Meteorit. Planet. Sci., 41(12), 1947–1958.

Grzechnik, A., P. Simon, P. Gillet, and P. McMillan (1999), An infrared study of MgCO3 at high pressure, Phys. B Condens. Matter, 262(1–2), 67–73, doi:10.1016/S0921-4526(98)00437-2.

Gupta, S. C., S. G. Love, and T. J. Ahrens (2002), Shock temperature in calcite (CaCO3) at 95-160 GPa, Earth Planet. Sci. Lett., 201(1), 1–12, doi:10.1016/S0012-821X(02)00685-4.

Hörz, F., R. Ostertag, and D. A. Rainey (1983), Bunte Breccia of the Ries: Continuous deposits of large impact craters, Rev. Geophys., 21(8), 1667–1725.

Howard, K. A., T. W. Offield, and H. G. Wilshire (1972), Structure of Sierra Madera, Texas, as a guide to central peaks of lunar craters, Geol. Soc. Am. Bull., 83(9), 2795–2808.

Hunt G. R. and Salisbury, J. W., (1971). Visible and near infrared spectra of minerals and rocks. II. Carbonates. Modern Geology. Vol. 2, p. 23-30.

Huson, S., M. Pope, A. J. Watkinson, and F. Foit (2011), Deformational features and impact-generated breccia from the Sierra Madera impact structure, west Texas, Geol. Soc. Am. Bull., 123(1–2), 371–383.

Jain, N., and P. Chauhan (2015), Study of phyllosilicates and carbonates from the Capri Chasma region of Valles Marineris on Mars based on Mars Reconnaissance Orbiter-Compact Reconnaissance Imaging Spectrometer for Mars (MRO-CRISM) observations, Icarus, doi:10.1016/j.icarus.2014.11.018.

Kenkmann, T. (2002), Folding within seconds, Geology, 30(3), 231–234.

Kondo, K., and T. J. Ahrens (1983), Heterogeneous shock-induced thermal radiation in minerals, Phys. Chem. Miner., 9(3), 173–181, doi:10.1007/BF00308375.

Korn, L. K., and M. S. Gilmore (2015), Possible carbonate minerals within an unnamed gullied crater in Eridania basin, Mars, Lunar Planet. Sci., XLVI, Abstract 2224.

Kotra, R. K., T. H. See, E. K. Gibson, F. Horz, M. J. Cintala, and R. S. Schmidt (1983), Carbon dioxide loss in experimentally shocked calcite and limestone, in Lunar and Planetary Science Conference, pp. 401–402.

Lange, M. A., and T. J. Ahrens (1986), Shock-induced CO2 loss from CaCO3; implications for early planetary atmospheres, Earth Planet. Sci. Lett., 77(3–4), 409–418, doi:10.1016/0012-821X(86)90150-0.

Langenhorst, F., A. Deutsch, B. A. Ivanov, and U. Hornemann (2000), On the shock behavior of CaCO3: dynamic loading and fast unloading experiments - modeling - mineralogical observations, in Lunar and Planetary Science XXXI, pp. 3–4.

Langenhorst F. (2002) Shock metamorphism of some minerals: Basic introduction and microstructural observations. Bulletin of the Czech Geological Survey 77: 265-282

Langenhorst, F., and A. Deutsch (2012), Shock metamorphism of minerals, Elements, 8(1), 31–36, doi:10.2113/gselements.8.1.31.

Lapen, T. J., M. Righter, A. D. Brandon, V. Debaille, B. L. Beard, J. T. Shafer, and A. H. Peslier (2010), A younger age for ALH84001 and its geochemical link to shergottite sources in Mars, Science, 328, 347–351, doi:10.1126/science.1185395

Lin-Gun Liu, and T. P. Mernagh (1990), Phase transitions and Raman spectra of calcite at high pressures and room temperature, Am. Mineral., 75(7–8), 801–806.

Love, S. G., and T. J. Ahrens (1998). Measured shock temperatures in calcite and their relation to impact-melting and devolatilization. Abstracts of Papers Submitted to the Twenty-Ninth Lunar and Planetary Science Conference., 29, 2–3.

Martinez I., U. Schärer and F. Guyot, (1994) Experimental and theoretical investigation of shock induced outgassing of dolomite. Abstracts of Papers Submitted to the Twenty-Fifth Lunar and Planetary Science Conference., 839.

Martinez I., A. Deutsch, U. Schärer, P. Ildefonse, F. Guyot and P. Agrinier (1995) Shock recovery experiments on dolomite and thermodynamical calculations of impact induced decarbonation. Journal of Geophysical Research. Vol. 100, No. B8, 15,465-15,476.

Michalski, J. R., and P. B. Niles (2010). Deep crustal carbonate rocks exposed by meteor impact on Mars. Nature Geoscience, 3(11), 751–755. http://doi.org/10.1038/ngeo971

Michalski, J. R., Cuadros, J., Niles, P. B., Parnell, J., Rogers, A. D., & Wright, S. P. (2013). Groundwater activity on Mars and implications for a deep biosphere. Nature Geoscience, 6(2), 133-138.

Morris, R. V et al. (2010), Identification of Carbonate-Rich Outcrops on Mars by the Spirit Rover, Science (80-.)., 329(5990), 421–424, doi:10.1126/science.1189667.

Moroz, L. V., et al. "Ion irradiation of asphaltite: optical effects and implications for trans-Neptunian objects and centaurs." The First Decadal Review of the Edgeworth-Kuiper Belt. Springer Netherlands, 2004. 279-289.

Newsom, H. E., G. Graup, T. Sewards, and K. Keil (1986), Fluidization and hydrothermal alteration of the suevite deposit at the Ries crater, West Germany, and implications for Mars, J. Geophys. Res. Solid Earth, 91(B13).

Nickerson, G. A. J., J. G. Spray, and L. A. Mayer (2000), Investigation of integrated geologic and geophysical data using GIS: Crooked Creek and Decaturville impact structures, Missouri,

Offield, T. W., and H. A. Pohn (1977), Deformation at the Decaturville impact structure, Missouri, in Impact and Explosion Cratering: Planetary and Terrestrial Implications, pp. 321–341.

Osinski, G. R., and J. G. Spray (2001), Impact-generated carbonate melts: Evidence from the Haughton structure, Canada, Earth Planet. Sci. Lett., 194(1–2), 17–29, doi:10.1016/S0012-821X(01)00558-1.

Osinski, G. R., P. Lee, J. G. Spray, J. Parnell, D. S. S. Lim, T. E. Bunch, C. S. Cockell, and B. Glass (2005), Geological overview and cratering model for the Haughton impact structure, Devon Island, Canadian High Arctic, Meteorit. Planet. …, 40(12), 1759–1776, doi:10.1111/j.1945-5100.2005.tb00145.x.

Osinski, G. R. (2007), Impact metamorphism of CaCO3-bearing sandstones at the Haughton structure, Canada, Meteorit. Planet. …, 42(11), 1945–1960, doi:10.1111/j.1945-5100.2007.tb00552.x.

Pan L., B. L. Ehlmann, J. Carter, C. M. Ernst. "The Stratigraphy and History of Mars' Northern Lowlands Through Mineralogy of Impact Craters: A Comprehensive Survey." Journal of Geophysical Research: Planets. in revision.

Parnell, J., G. R. Osinski, P. Lee, P. F. Green, and M. J. Baron (2005), Thermal alteration of organic matter in an impact crater and the duration of postimpact heating, Geology, 33(5), 373–376, doi:10.1130/G21204.1.

Pollack, J. B., J. F. Kasting, S. M. Richardson, and K. Poliakoff (1987), The case for a wet, warm climate on early Mars, Icarus, 71(2), 203–224, doi:10.1016/0019-1035(87)90147-3.

Santillán, J., Q. Williams, and E. Knittle (2003), Dolomite-II: A high-pressure polymorph of CaMg(CO 3) 2, Geophys. Res. Lett., 30(2), 1–4, doi:10.1029/2002GL016018.

Santillán, J., K. Catalli, and Q. Williams (2005), An infrared study of carbon-oxygen bonding in magnesite to 60 GPa, Am. Mineral., 90(10), 1669–1673, doi:10.2138/am.2005.1703.

Schulte, P. et al. (2010), The Chicxulub Asteroid Impact and Mass Extinction at the Cretaceous-Paleogene Boundary, Science (80-.)., 327(5970), 1214–1218, doi:10.1126/science.1177265.

Skala, R., and F. Hoerz (1999), Mineralogical Studies of Experimentally Shocked Dolomite: Implications for the Outgassing of Carbonates.

Skála, R. (2002), Shock-induced phenomena in limestones in the quarry near Ronheim, the Ries Crater, Germany, Bull. Czech Geol. Surv., 77(4), 313–320.

Tyburczy, J. A., and T. J. Ahrens (1986), Dynamic compression and volatile release of carbonates, J. Geophys. Res., 91(B5), 4730, doi:10.1029/JB091iB05p04730.

Vizgirda, J., and T. J. Ahrens (1982), Shock compression of aragonite and implications for the equation of state of carbonate, J. Geophys. Res., 87, 4747–4758.

Viviano-Beck, C. E., and S. L. Murchie (2014), Phyllosilicates in the walls of Valles Marineris and the tectonic evolution of the greater Tharsis region, Eighth Int. Conf. on Mars, Abstract 1220.

Wray, J. J., S. L. Murchie, J. L. Bishop, B. L. Ehlmann, R. E. Milliken, M. B. Wilhelm, K. D. Seelos, and M. Chojnacki (2016), Orbital evidence for more widespread carbonate-bearing rocks on Mars, J. Geophys. Res. Planets, 121, 652–677, doi:10.1002/2015JE004972.

Chapter 6

SUMMARY, IMPLICATIONS, AND OUTSTANDING QUESTIONS

In Chapters 2-5, I have presented analyses of near-infrared spectral data in the northern lowlands of Mars and spectral measurements of carbonates in impact environments that are potentially relevant to Mars. From recent efforts to better characterize mineralogy of the northern lowlands of Mars [e.g. Gross et al., 2014; Turner et al., 2016; Pan et al., in revision], it is found that aqueous alteration is more widespread in the northern lowlands than previously thought. Hydrated minerals representative of the Noachian crust, including Fe/Mg phyllosilicates, chlorite, and illite/muscovite, are also commonly found in exposures in the northern lowlands. Hydrated silica found in the knobby terrains of Acidalia [Pan and Ehlmann, 2014], in small impact craters [Pan et al., in revision] and Utopia Planitia [Carter et al., 2013] are likely associated with a later episode of hydrated alteration related to younger sediments in the northern lowlands.

The extent of volcanic plains in the lowlands indicated by mafic mineralogy is more than doubling the Hesperian ridged plains [Head et al., 2002], and implies enhanced CO_2 emission from volcanoes. The mineralogy of the northern lowlands also revealed different, basin-specific geological processes, including discovery of concentrated aqueous minerals in Lyot crater vicinity. In-depth analysis showed that these hydrated minerals probably formed pre-impact in Noachian-Hesperian in a hydrothermal system, while post-impact processes in the vicinity did not lead to mineralization.

We also find lack of detection of carbonate minerals and evaporative salts in the northern lowlands. On Earth, past oceans leave carbonate or gypsum deposits as tracers of their presence. If there were standing bodies of water in the northern lowlands in the geologic past, it probably had limited water-rock interaction or low ionic strength, similar to a transient lake in localized basins in the northern lowlands, instead of the picture of a global ocean like that of Earth.

Though localized liquid water may be involved in the formation of morphologic features like pitted cones hypothesized to be mud volcanoes and fluvial channels in the

vicinity of Lyot crater, we find mineralization is limited in the Amazonian, as in the southern highlands. Although intriguingly, we have discovered some inverted channels made with phyllosilicate-rich sediments close to the dichotomy boundary in Tempe Terra [Pan and Ehlmann, 2015], but it is yet unclear whether these are diagenetic or detrital.

The lack of carbonate detections in the northern lowlands can be complicated by factors like impact shock, coating, dust cover, non-linear mixing and other effects. Through comparison with spectral data of terrestrial analogs, we find an interesting spectral slope in the 1-1.7 μm region on Mars data as well as some carbonates from impact craters on Earth, which could be due to a minor component of similar darkening effect, but the carbonate absorptions should be present. This implies that with the global statistics (including northern lowlands) of mineral distribution should be representative and a much larger carbonate reservoir in Mars' crust is not anticipated.

An emerging theme of the mineralogical record of Mars northern lowlands indicates the majority of aqueous minerals, including Fe/Mg phyllosilicates, chlorite, prehnite, and illite/muscovite, formed early in Mars' history, and the extent and intensity of aqueous alteration is diminished through time. Geologic processes involving liquid water are found locally in the Amazonian but probably with insufficient water-rock interaction for mineralization. The history of the northern lowlands is thus similar to the southern highlands, except for the large scale deposition of sediments with poorly-crystalline phases (e.g. silica coatings) [Kraft et al., 2003; Horgan and Bell, 2012] in the Amazonian.

The near infrared spectroscopy data from orbital missions revealed a great deal about the geologic history and aqueous environment on Mars, but also open new questions regarding the relationship of hydrated minerals to the geomorphologic features including valley networks, outflow channels and canyons. The nature of the widespread chemical alteration process needs to be better addressed through investigation of the formation mechanisms for these different aqueous alteration minerals with future orbital and in-situ investigations. Mineralogical data with higher spatial resolution on key geologic contacts of a well-preserved stratigraphy is needed to understand the timing of the aqueous mineral formation and its relationship to other geologic events. Detailed study on the micro-scale textures and correlation with mineralogy is needed to better address the ambiguities in the

formation of these minerals, e.g. whether these widespread phyllosilicates may form through impact-induced hydrothermal environments [e.g. Schwenzer and Kring, 2013]; groundwater upwelling [e.g. Ehlmann et al., 2011]; top-down surface weathering [Carter et al., 2015], or the alteration of primary crust via outgassing of a magma ocean [Cannon et al., 2017]. While these geological observations are crucial to deciphering the evolution of Mars climate, other lines of evidence for Mars' distant past may come from isotopic measurements of current volatile reservoirs, including atmosphere and the polar caps of Mars. Many of the future missions to Mars, including orbiters, rovers, landers, and possible sample return, are scheduled to further explore the red planet and will hopefully resolve the long-lasting debates about the geologic and climate history of early Mars and its potential habitability.

Reference:

Cannon, K. M., Parman, S. W., & Mustard, J. F. (2016, March). Hot and Steamy: Alteration of the Primordial Martian Crust by Supercritical Fluids During Magma Ocean Cooling. In Lunar and Planetary Science Conference (Vol. 47, p. 1265).

Carter, J., Poulet, F., Bibring, J. P., Mangold, N., & Murchie, S. (2013). Hydrous minerals on Mars as seen by the CRISM and OMEGA imaging spectrometers: Updated global view. Journal of Geophysical Research: Planets, 118(4), 831-858.

Carter, John, et al. "Widespread surface weathering on early Mars: A case for a warmer and wetter climate." Icarus 248 (2015): 373-382.

Ehlmann, B. L., Mustard, J. F., Murchie, S. L., Bibring, J. P., Meunier, A., Fraeman, A. A., & Langevin, Y. (2011). Subsurface water and clay mineral formation during the early history of Mars. Nature, 479(7371), 53-60.

Gross, C., Carter, J., Sowe, M., & Bishop, J. L. (2014, April). Excavation of Altered Sediments in the Northern Plains of Mars. In European Planetary Science Congress 2014, EPSC Abstracts, Vol. 9, id. EPSC2014-365 (Vol. 9).

Head, J. W., Kreslavsky, M. A., & Pratt, S. (2002). Northern lowlands of Mars: Evidence for widespread volcanic flooding and tectonic deformation in the Hesperian Period. Journal of Geophysical Research: Planets, 107(E1).

Horgan, B., & Bell III, J. F. (2012). Widespread weathered glass on the surface of Mars. Geology, 40(5), 391-394.

Kraft, M. D., Michalski, J. R., & Sharp, T. G. (2003). Effects of pure silica coatings on thermal emission spectra of basaltic rocks: Considerations for Martian surface mineralogy. Geophysical Research Letters, 30(24).

Turner, S. M., Bridges, J. C., Grebby, S., & Ehlmann, B. L. (2016). Hydrothermal activity recorded in post Noachian-aged impact craters on Mars. Journal of Geophysical Research: Planets, 121(4), 608-625.

Pan, L., & Ehlmann, B. L. (2014). Phyllosilicate and hydrated silica detections in the knobby terrains of Acidalia Planitia, northern plains, Mars. Geophysical Researc

Pan, L., & Ehlmann, B. L. (2014). Geology of the Eastern Margin of Tempe Terra with Implications for Mars Dichotomy Modifications. LPI Contributions, 1791, 1273.

Pan L. et al. (2017), "The Stratigraphy and History of Mars' Northern Lowlands Through Mineralogy of Impact Craters: A Comprehensive Survey." *Journal of Geophysical Research: Planets*. in revision.

Schwenzer, S. P., & Kring, D. A. (2013). Alteration minerals in impact-generated hydrothermal systems–Exploring host rock variability. Icarus, 226(1), 487-496.